

Signals and Communication Technology

Hemant Kumar  
E. S. Gopi *Editors*

# RF, Microwave and Millimeter Wave Technologies

 Springer

# **Signals and Communication Technology**

## **Series Editors**

Emre Celebi, Department of Computer Science, University of Central Arkansas,  
Conway, AR, USA

Jingdong Chen, Northwestern Polytechnical University, Xi'an, China

E. S. Gopi, Department of Electronics and Communication Engineering, National  
Institute of Technology, Tiruchirappalli, Tamil Nadu, India

Amy Neustein, Linguistic Technology Systems, Fort Lee, NJ, USA

Antonio Liotta, University of Bolzano, Bolzano, Italy

Mario Di Mauro, University of Salerno, Salerno, Italy

This series is devoted to fundamentals and applications of modern methods of signal processing and cutting-edge communication technologies. The main topics are information and signal theory, acoustical signal processing, image processing and multimedia systems, mobile and wireless communications, and computer and communication networks. Volumes in the series address researchers in academia and industrial R&D departments. The series is application-oriented. The level of presentation of each individual volume, however, depends on the subject and can range from practical to scientific.

Indexing: All books in “Signals and Communication Technology” are indexed by Scopus and zbMATH

For general information about this book series, comments or suggestions, please contact Mary James at [mary.james@springer.com](mailto:mary.james@springer.com) or Ramesh Nath Premnath at [ramesh.premnath@springer.com](mailto:ramesh.premnath@springer.com).


Hemant Kumar • E. S. Gopi  
Editors

# RF, Microwave and Millimeter Wave Technologies

 Springer

### *Editors*

Hemant Kumar  
Department of Electronics and  
Communication Engineering  
National Institute of Technology  
Tiruchirappalli  
Tiruchirappalli, Tamil Nadu, India

E. S. Gopi   
Department of Electronics and  
Communication Engineering  
National Institute of Technology  
Tiruchirappalli  
Tiruchirappalli, Tamil Nadu, India

ISSN 1860-4862

ISSN 1860-4870 (electronic)

Signals and Communication Technology

ISBN 978-3-031-62525-1

ISBN 978-3-031-62526-8 (eBook)

<https://doi.org/10.1007/978-3-031-62526-8>

© The Editor(s) (if applicable) and The Author(s), under exclusive license to Springer Nature Switzerland AG 2024

This work is subject to copyright. All rights are solely and exclusively licensed by the Publisher, whether the whole or part of the material is concerned, specifically the rights of translation, reprinting, reuse of illustrations, recitation, broadcasting, reproduction on microfilms or in any other physical way, and transmission or information storage and retrieval, electronic adaptation, computer software, or by similar or dissimilar methodology now known or hereafter developed.

The use of general descriptive names, registered names, trademarks, service marks, etc. in this publication does not imply, even in the absence of a specific statement, that such names are exempt from the relevant protective laws and regulations and therefore free for general use.

The publisher, the authors and the editors are safe to assume that the advice and information in this book are believed to be true and accurate at the date of publication. Neither the publisher nor the authors or the editors give a warranty, expressed or implied, with respect to the material contained herein or for any errors or omissions that may have been made. The publisher remains neutral with regard to jurisdictional claims in published maps and institutional affiliations.

This Springer imprint is published by the registered company Springer Nature Switzerland AG  
The registered company address is: Gewerbestrasse 11, 6330 Cham, Switzerland

If disposing of this product, please recycle the paper.

# Summary

This book provides in-depth exposure to emerging technologies and recent advancements in RF, Microwave, and Millimeter Wave Technologies. It covers the basic concepts along with the recent advancements in designing and developing antennas and circuits for the latest technologies. The concepts of mode compression, Full Duplex communication, massive MIMO, frequency selective surfaces, reflectarrays, and metasurfaces have been discussed in detail. Various types of antennas such as electrically small antennas, textile antennas, dielectric resonator antennas, etc., to be used for the latest wireless devices, RFID applications have been thoroughly explored. The concept of machine learning to develop data-driven models for antenna design is discussed briefly to provide readers with an introduction to ML algorithms.

The readers will be able to understand the theoretical concepts and practical design aspects of various antennas and high-frequency circuits. The target audience includes but is not limited to undergraduates, postgraduates, research scholars, academicians, scientists, and professionals who are interested in getting up-to-date with the latest knowledge in the field of RF, Microwave, and Millimeter Wave Technologies.

# Contents

<b>Introduction to Important Concepts of RF, Microwaves, and mm Waves Technologies</b> .....	1
K. P. Ray	
<b>Finite Circular Ground Plane Effects: A Case Study of Monopole Antenna</b> .....	17
Hemant Kumar and Girish Kumar	
<b>Mode Compression Theory: Dipole Antennas</b> .....	29
Rajbala Solanki	
<b>Multiple Resonator –Loaded Electrically Small Antennas for Wireless Devices</b> .....	45
Jyotibhusan Padhi and G. Shrikanth Reddy	
<b>Textile Antennas for RFID Applications</b> .....	65
Rajesh K. Singh	
<b>Recent Trends in the Design and Development of Dielectric Resonator Antennas</b> .....	83
Pragati Patel	
<b>A Low-Profile Perturbed Convex Conformal CDRA</b> .....	93
Manshree Mishra, Pramod Kumar Gupta, Garima Tiwari, Atul Kumar, and Biswajeet Mukherjee	
<b>Reflectarray Antenna Designs</b> .....	107
Ravi Kumar Arya	
<b>Antennas for Full-Duplex Communication: State of the Art and Way Forward</b> .....	119
Jogesh Chandra Dash and Debdeep Sarkar	

<b>Understanding Metasurface-Based Microwave Absorbers Using Transmission Line Theory .....</b>	<b>147</b>
Debdeep Sarkar	
<b>Frequency-Selective Surface and Its Applications in Radome Technology .....</b>	<b>165</b>
Saptarshi Ghosh	
<b>Algorithmic Applications for Massive MIMO Technology .....</b>	<b>175</b>
Sai Mitheran, T. N. Ram, Debrup Mukherjee, and Hemant Kumar	
<b>Regression Model for Antenna Design .....</b>	<b>187</b>
E. S. Gopi	
<b>Index .....</b>	<b>197</b>



# Introduction to Important Concepts of RF, Microwaves, and mm Waves Technologies



K. P. Ray

## 1 Introduction

In the conceptual period of the development of wireless systems, only the lower-frequency band was utilized because of various limitations. Later, researchers became more cognizant of higher-frequency spectrum for efficient transmission/reception, which includes radio frequency (RF), microwaves, and mm waves. In very generic terms, RF, microwaves, and mm waves are used to describe electromagnetic waves with frequency range from 1 MHz to 300 GHz. The corresponding wavelengths range is from 300 m to 1 mm [1, 2].

The whole electromagnetic spectrum is shown in Fig. 1 [3, 4]. Starting from the power supply band to cosmic rays, various bands with their frequency range and corresponding wave lengths are depicted in the diagram. From here, the relative position of various bands can be estimated. There is an important band of terahertz ( $10^{12}$  Hz), which is sandwiched between mm wave and optical region. Terahertz waves have become popular in recent years for their distinct features. In this chapter, terahertz will not be discussed further and is treated as higher end of mm waves. This figure also shows electromagnetic interference (EMI) shielding range for electromagnetic compatibility (EMC) of electronic systems [3, 4]. Though the position of high frequency waves, radio waves, and microwaves are indicated in the Figure, it requires further discussions and quantification (high-frequency waves are not meant here as “HF,” which will be elaborated later).

---

K. P. Ray (✉)

Electronics Engineering Department, Defence Institute of Advanced Technology (DIAT) DRDO,  
Pune, Maharashtra, India  
e-mail: [kpray@diat.ac.in](mailto:kpray@diat.ac.in)

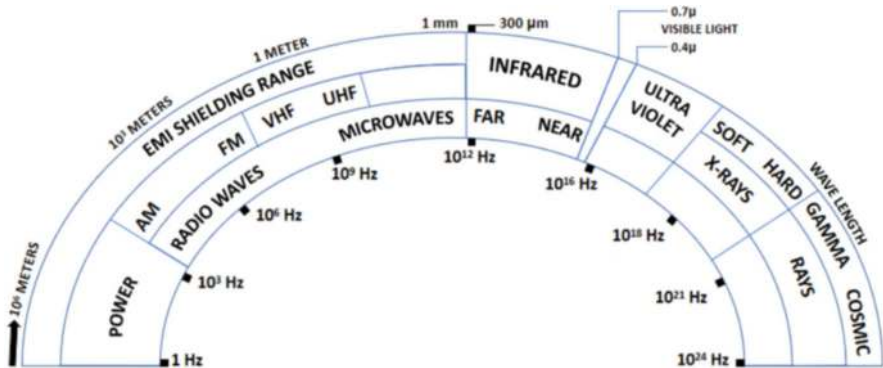


Fig. 1 Electromagnetic spectrum

2 RF, Microwaves and mm Waves

Wireless communication systems from amplitude modulation (AM) broadcast to mm wave communication employ radio waves, operating from 1 MHz to 300 GHz. The term radio frequency (RF) is derived from radio waves; thus, in general terms, the entire frequency range is referred to as RF band. However, various researchers have defined frequency range of RF, microwaves, and mm waves differently. There are no distinct boundaries between these frequency bands, which are discussed in the following section.

Vendelin has put these frequency bands as [5]:

RF:	1 MHz (or less) to 1 GHz
Microwave:	1–30 GHz
Millimeter wave:	30–300 GHz (or higher)

D. M. Pozar has categorized RF and microwave frequencies range from 30 MHz to 3000 MHz (3GHz) and 3 GHz to 300 GHz, respectively. The higher end of the microwave with wavelengths of the order of millimeters is referred to as mm waves. mm Waves are just below the optical region, wherein radio wave overlaps with light wave, and thus, these are also known as quasi-optical waves [6].

R. E. Collin describes microwaves as electromagnetic waves with frequency range of 300 MHz to 30 GHz, whereas frequency ranging from 30 GHz to 300 GHz are called mm waves [7].

Out of these three high-frequency regions, the microwave frequency range has been extensively researched, perhaps because of its application in radars during World War II and has become a fairly mature area. A few important researchers have defined it slightly differently. K. C. Gupta has set the approximate range from 1 GHz to 30 GHz, sometimes extending up to 600 GHz, without explaining the higher-

**Table 1** High-frequency band designation and corresponding wavelength

Band designation	Nominal frequency range	Wavelength range
MF	0.3–3 MHz	1000–100 m
HF	3–30 MHz	100–10 m
VHF	30–300 MHz	10–1 m
UHF	300 MHz–3 GHz	1–0.1 m
SHF	3 GHz–30 GHz	0.1–0.01 m
L	1–2 GHz	30–15 cm
S	2–4 GHz	15–7.5 cm
C	4–8 GHz	7.5–3.75 cm
X	8–12 GHz	3.75–2.5 cm
Ku	12–18 GHz	2.5–1.66 cm
K	18–27 GHz	1.66–1.11 cm
Ka	27–40 GHz	11.1–7.5 mm
V	40–75 GHz	7.5–4 mm
W	75–110 GHz	4–2.72 mm
mm	Up to 300 GHz	2.72–1 mm
THz	300 GHz–3THz	1000–100 $\mu$ m

frequency range [8]. Samuel Y. Lio mentioned microwave frequencies roughly from 1 GHz to 300 GHz and further opines that microwave means the wavelengths is in the micron ranges and thus frequencies extend up to optical regions [9]. Another interesting definition of microwave, based on its features, is given by Thomas S. Laverghetta [10]. He describes it as “A radiowave operating in the frequency range of 500 MHz to 20 GHz that requires printed circuit components be used instead of conventional lumped components.” We will further elaborate this definition in next section, when salient feature of microwave will be discussed, but it can be noted that frequency range of microwave is again different.

It is noted from the above deliberation that there is no unanimity among different schemes of classifications to designate frequency bands of RF, microwaves, and mm waves. Without loss of generality, it can be summarized that RF approximately starts from 1 MHz, covers full of HF (high frequency), VHF (very high frequency), and a portion of UHF (ultrahigh frequency) up to 1 GHz. Microwave starts from 1 GHz (L-band) and goes slightly beyond K- band up to 30 GHz, covering full band of super high frequency (SHF) band. Finally, mm wave ranges from 30 GHz to 300 GHz [6, 11].

Table 1 shows commonly designated frequency bands with their ranges and corresponding wavelengths, which are used for most of the applications including radar and communication. For three bands of high frequency, the wavelength varies from 300 m to 0.3 m for RF and 30 cm to 1 cm for microwaves, whereas for mm wave, it is from 10 mm to 1 mm. One very important observation is made here that when wavelength is in meter, it is called meter-wave, and for mm wave, the wavelength is in mm; likewise, a technically correct name of microwave would have been centi-meter wave!

### 3 Characteristic Features of High-Frequency Waves

In high-frequency waves, particularly microwaves, there exist several interesting and unusual features, which are not seen in other electromagnetic frequency bands. These unique features, as elaborated below, make high-frequency waves suitable for various useful applications [6–8].

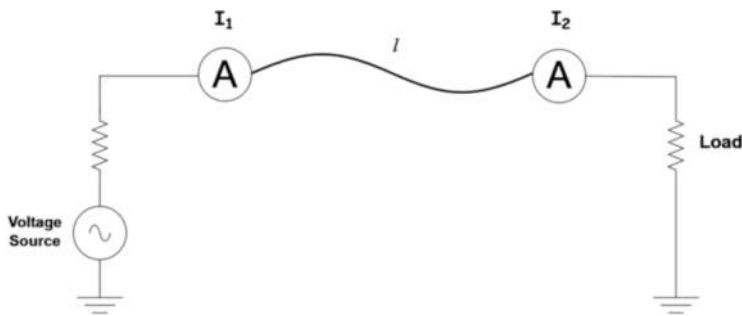
#### 3.1 Wider Bandwidth

When the usage of wireless communication system became more extensive, the lower-frequency range became overpopulated leading to EMI (electromagnetic interference) issues. It became inevitable to move toward higher-frequency range. This yielded wider bandwidth, facilitating full utilization of technological advancements in improved techniques and components. Wider bandwidth leads to higher data rate of communication systems. For example, 10% bandwidth at 1 MHz is 100 kHz, which can provide a transmission/reception data rate of 100 kbps, whereas for the same percentage bandwidth at 10 GHz is 1 GHz, which in turn will provide much improved data rate of 1Gbps [6, 8, 13]. This characteristic of high frequency will be further elucidated when wireless applications will be covered.

#### 3.2 Insertion Phase of Components/Interconnects

One of the important characteristic features of high-frequency waves stem from the fact that with increase in frequency, wavelength becomes smaller and smaller and, thus, becomes comparable or smaller than the sizes of commonly used electronic components, devices, and interconnects. This leads to rapid-phase variation of the signal passing through them, necessitating modifications in commonly used low-frequency circuit theory based on voltage-current.

To bring out this important concept of high-frequency waves, Fig. 2 is considered, wherein a small length of a metallic wire connects a voltage source to a load through two ammeters [12]. At low frequency, the current reading  $I_1$  and  $I_2$  would be the same, which is in consonance with conventional circuit theory, whereas at high frequency starting from RF, readings  $I_1$  and  $I_2$  will not be equal! It is not that the circuit theory is wrong, but some additional parameters have to be taken into account at high frequency. This variation of  $I_1$  and  $I_2$  over the length  $l$  is explained using the characteristic of amplitude-distance variation, which is known as wavelength. Assuming sinusoidal signal, when wavelength is much larger than the circuit dimension  $l$ , there will not be any noticeable variation of amplitude of the signal, whereas when  $l$  is comparable to the wavelength, there will be appreciable amplitude variation. This high-frequency circuit behavior is further explained in Fig. 3.



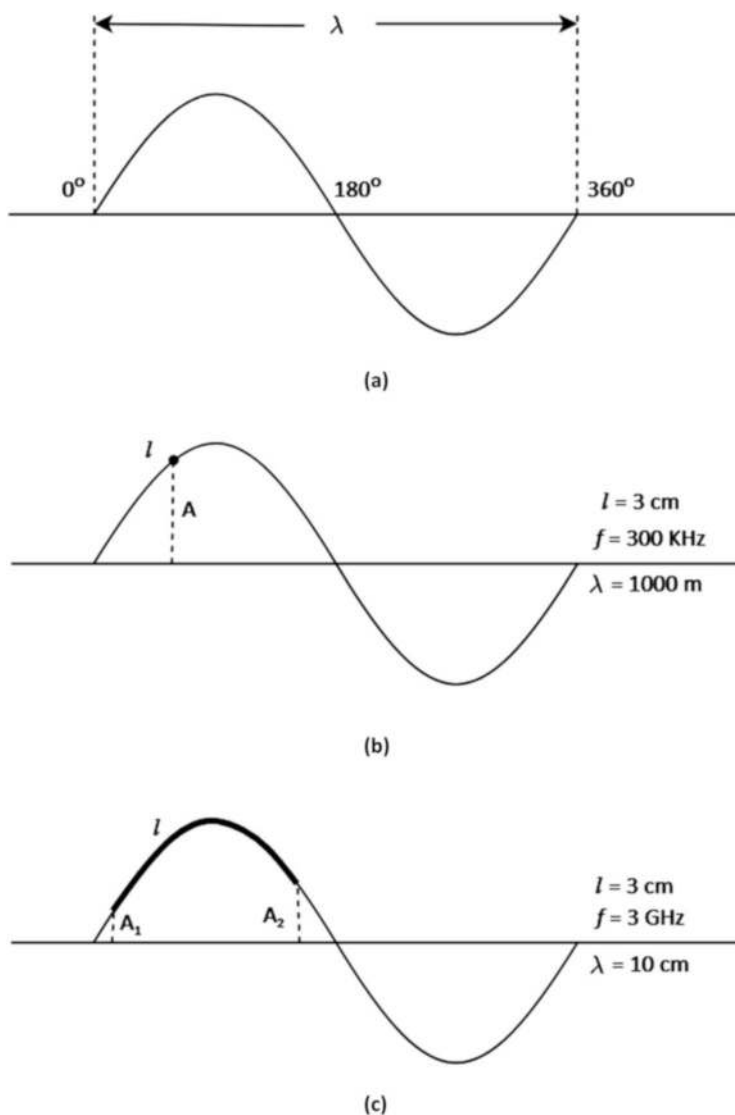
**Fig. 2** Wire connecting a voltage source to a load; current flow

Figure 3a shows one cycle variation of the signal over the length, which is known as wavelength ( $\lambda$ ). It corresponds to  $360^\circ$  phase difference and time period  $T$ . At low frequency of 300 kHz,  $\lambda = 1$  km. Assuming that the wire length  $l$  as shown in Fig. 2 equals to 3 cm, when it is mapped on wavelength of 1 km, it appears as a dot on the wavelength, as shown in Fig. 3b. The electrical path length travelled by the signal through  $l$  is negligibly small; thus, amplitude remains constant as 'A', and both the ammeters read same value of current. Next, we move to another example of higher frequency of 3 GHz with  $\lambda = 10$  cm and map the same wire length of  $l = 3$  cm around the same position as that of low-frequency case of Fig. 3b. The length covers around one third of  $\lambda$  indicating the insertion phase of the wire as  $108^\circ$  and amplitude changes from  $A_1$  to  $A_2$ . This is the reason for different readings of two ammeters in Fig. 2.

To sum up the discussions, at lower frequencies,  $\lambda$  is very large that the phase change is insignificant across the dimensions of an element/component. One deals with only magnitude of voltage-current in the low-frequency circuit theory based on Kirchhoff's Law. At high frequencies, there is significant variation of the phase of voltage-current over the physical dimensions of the element/device, as they are of the order of the  $\lambda$ . Consequently, Kirchhoff's law-based analysis and concept of voltage-current are inadequate to represent the high frequency circuit behavior [6–10].

In other words, short  $\lambda$  means that for electrical effects, the propagation time from one end in a circuit to another end is comparable to the time period  $T$  of the exciting oscillating voltage-currents. It again means that conventional circuit theory no longer holds good to describe the high-frequency electrical phenomena [6–8].

Variations of amplitude and phase of the signal while passing through the component represent its wave nature. Therefore, it is necessary to perform the analysis in terms of the associated electric and magnetic fields with circuit elements/device. In essence, high-frequency engineering deals with Maxwell's equations, rigorous solutions of which provide the wholistic description of electromagnetic fields at every point in the circuit [14–17]. The standard low-frequency circuit theory then becomes an approximation of these broader electromagnetic theory based on Maxwell's



**Fig. 3** Wire length ' $l$ ' on wavelength; (a) wavelength (b) ' $l$ ' represented on wavelength at 300 kHz (c) ' $l$ ' represented on wavelength at 3 GHz

equations. Transmission line theory works as the transition between Kirchoff's law-based circuit theory and Maxwell's equation-based field theory, wherein instead of considering only magnitude of voltage and current, their special variation (phase) is brought in. Here, voltage-current waves, forward moving (incident) and reverse moving (reflected), are considered to get terminal characteristics of circuits.

### 3.3 *Higher Antenna Gain*

At high frequencies, wavelengths are shorter, which facilitates the development of high-directivity antennas. Antenna directivity, which is inversely proportional to beamwidths, in terms of its aperture (area)  $A$ , is given as:

$$D = \frac{4\pi A}{\lambda^2} \quad (1)$$

As can be noted from Eq. (1) that antenna directivity is proportional to its electrical area/size, at high frequencies, more directivity (smaller beamwidth) is obtained for a given physical antenna area. In other words, for the same directivity, antenna size becomes much larger as compared to that at high frequency. Also, antennas radiate efficiently if their size is comparable to the wavelength, which in turn yields higher gain. Further, at higher frequencies, antennas become compact, which is convenient for mobile applications. Additionally, high-frequency signals get reflected from perfect metallic surfaces, which can be very effectively utilized to develop highly efficient radiator/receptors for wireless system. Further, it enhances retrodirective reflections increasing the radar cross-section (RCS) of the target. These aspects have very important consequences while realizing various high-frequency systems.

### 3.4 *Distributed Elements/Components*

Lumped elements, such as the carbon resistors, mica-capacitors, and compact inductors are used in low-frequency circuits. Because of the advancement in the field of microelectronics, some high-frequency resistors, capacitors, and inductors have also been realized, but their usage in high frequencies is limited because of smaller wavelength. Consequently, in high-frequency systems, distributed circuit elements are often employed, wherein the phase of the signal (voltage-current) varies significantly over the physical extent of the device as these are comparable to the wavelength. These elements are realized using small sections of transmission lines. For example, a short-circuited transmission line with length less than  $\lambda/4$  realizes an inductor, whereas in an open-circuited transmission line, same length would be a capacitor [7–10].

Another way of interpretation why lumped elements cannot be used at higher frequency is that the energy does not penetrate into the component and travels only on the outside surface/skin of the conductor. This high-frequency-related phenomenon is known as skin effect. The corresponding depth inside the conductor up to which the high-frequency energy penetrates is known as skin depth ( $\delta$ ). The formula for skin depth is given as:

$$\delta = \frac{1}{\sqrt{\pi \sigma f \mu}} \quad (2)$$

where  $\sigma$  is the conductivity and  $\mu$  is the permeability of the material and  $f$  is the frequency of operation.

As is noted from Eq. (2), the  $\delta$  depth is dependent on the frequency and the material used. The value of  $\delta$  for a commonly used metal copper at 3 GHz is 0.000115 mm, which indicates that the energy truly travels along the top surface of the metal. This is the reason for realizing various high-frequency circuits on a printed circuit board (PCB) with copper, the thickness of which is 0.0356 mm (for 1 oz of copper). Sometimes, gold plating of similar thickness is done for obtaining higher conductivity.

### 3.5 Characteristic Impedance

Characteristic impedance (in ohms) determines the flow of high-frequency energy through a transmission line or in a system. It is dynamic impedance that does not represent an ohmic loss and entirely depends on the physical and electrical characteristics of the transmission line. Most often, the value of characteristic impedance used in high frequency is 50  $\Omega$ , which is not an arbitrary value but has semblance of order in it [6, 8, 10, 18]. Considering Fig. 4, it is noted that for a particular transmission line, 30  $\Omega$  gives the maximum power handling capability, whereas 77  $\Omega$  yields the lowest attenuation. Therefore, the compromise between 30  $\Omega$  and 77  $\Omega$  is chosen as 50  $\Omega$  for ideal characteristic impedance.

The characteristic impedance becomes the reference parameter for high-frequency systems as most of the input-output ports have the same value of impedance (50  $\Omega$ ). Measurements are performed in terms of signal/field amplitudes, phase differences, and power carried by waves with ports impedance of 50  $\Omega$  and unused ports terminated in 50  $\Omega$ . Here, the relative power or their ratio is expressed in decibel (dB), whereas absolute power is quantified with reference to 1 milliwatt (mW), which in decibels is denoted as dBm. It represents an absolute number in milliwatts. Commonly used power levels, starting from 1 microwatt to a megawatt, are represented in dBm in Table 2.

At low frequencies, the maximum power transfer theorem gives the power delivered to the load, which, at high frequency, takes the form of impedance matching of the load with respect to the characteristic impedance of 50  $\Omega$ . If the load is not matched to 50  $\Omega$ , there will be reflected signal. The ratio of reflected signal to the incident signal is known as reflection coefficient. It is the voltage ratio that is derived from power. The superimposition of reflected and incident signal gives rise to the standing wave pattern along the transmission line. High-frequency measurements are based on this standing wave pattern. The amplitudes and phase relationship of the reflection coefficient determine the impedance characteristics of circuits/components.



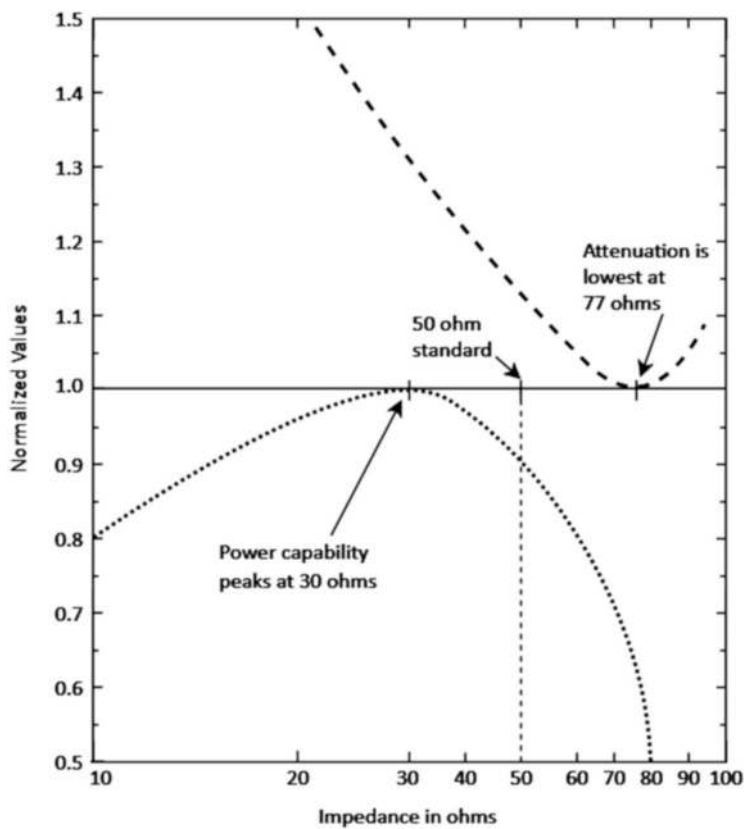


**Fig. 4** Choice of characteristic impedance based on attenuation and power handling capability [18]

**Table 2** Commonly used power levels in dBm

Power	1 $\mu$ W	1 mW	1 W	1 kW	1 MW
dBm	−30	0	30	60	90

The reflection coefficient varies between 0 and 1, where the former indicates no reflection and hence perfectly matched condition; the latter represents extreme mismatch. The standing wave amplitude depends on how well the port is matched with the transmission line. When there is no reflection (for perfect matching condition), standing waves will not get formed, which means the standing wave ratio (SWR) will be 1. In the case of 100% mismatch, SWR will be infinity.

The reflection coefficient, when expressed in dB, is known as return loss (RL), which indicates the reflected power (loss) from the device due to mismatch. Thus, for a perfectly matched condition, the return loss will be a large negative number in dB, the corresponding values of reflection coefficient and SWR will be 0 and 1, respectively. The value of RL for a large mismatch would be 0 dB with respective values of reflection coefficient and SWR of 1 and infinity.

### 3.6 *Resonance Phenomena*

High frequencies exhibit interesting feature of various atomic, molecular, and nuclear resonances, creating variety of applications in domains of basic science, industrial processing/monitoring, bulk heating/drying, medical diagnostics and treatments, etc.

As is evident from elaborations in preceding sections, there are challenges in dealing with high-frequency waves starting from the analysis itself, where one has to employ field theory based on Maxwell's equations that has mathematical rigor. Secondly, as the components size is comparable or bigger than the wavelength, their realization with tight tolerances becomes that much complex. Thirdly, the main challenge exists for generation of high-frequency signals as the transit time of carriers through devices becomes comparable to the time period of the wave. Some of these challenges have been overcome by totally novel ideas and technological innovations. Moreover, complexities bring challenges and rewards hand in hand, providing unique opportunities to employ high-frequency domain for various applications.

## 4 Applications

Research and study in the area of high-frequency waves (RF, microwaves, and millimeter waves) have led to several useful applications. Most of these applications are in the field of radars, wireless networking and communication systems, security systems, environmental remote sensing, industrial and domestic processing, and medical systems.

The majority of applications are on wireless systems, and its detailed electromagnetic spectrum is shown in Fig. 5. It covers some of the important wireless applications for all the three high-frequency wave signals [6, 8, 10]. The main applications are broadcast systems, cellular/mobile phones, global positioning systems (GPSs), PCSs, direct broadcast satellites (DBSs), radars, etc. Many more applications are added in recent past in this chart [10], making these systems all pervasive. Only the important applications of high-frequency waves are discussed in the following sections.

### 4.1 *Radar*

Radar is a short form of radio detection and ranging (Radar), which was extensively researched and used during World War II. It is a high-frequency electromagnetic system used to detect the existence and location of the object/target [6, 8, 10].

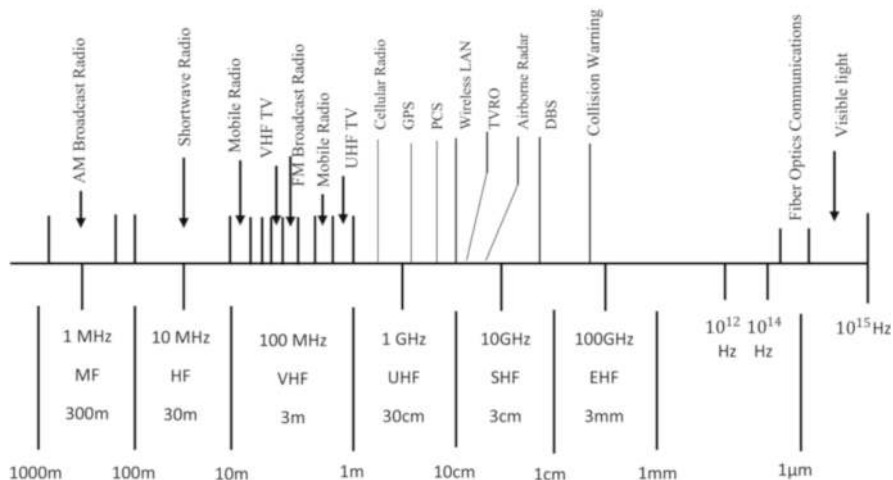


Fig. 5 Electromagnetic spectrum for wireless applications [10]

The increased reflection (RCS) of objects/targets because of their increased electrical size, coupled with higher gain and compact phased array antennas with fast electronic beam scanning, makes high frequencies preferred for developing radar systems. Radars have been developed across high-frequency bands. Starting from the lower end of RF band 3–30 MHz, where signal is bent from the ionosphere, long-distance over-the-horizon (OTH) radars are developed. On the extreme higher end of mm wave, W-band active Seeker and mm wave imaging radars have been realized.

Radar systems find applications in various military, commercial, and scientific areas. In the field of military applications, radars have been developed for detection/tracking of airborne objects like drones, aircraft, spacecraft, and missiles, navigation of air and marine, guidance of missile, Fire control, weapon fuses, etc. Radars play very important and increasing roles in modern-day electronics warfare (EW) and, therefore, national security of various countries.

The main civilian application of radars are weather radars, surveillance and landing at airports, navigation, speed guns, security alarms, etc. Radars are also used in scientific applications such as remote sensing, astronomy, imaging/mapping, level and distance measurements, etc.

## 4.2 Wireless Communication System

Various wireless communication systems are depicted in the chart given in Fig. 5. Out of these systems, the cellular telephone has become indispensable in our day-to-day life. It enables functionalities such as mobile communication, voice/video call,

data sharing, messages, emails, etc. between people nearby or far away or in another part of the globe. It has been literally providing voice and data access to “everyone, everywhere, and every time.” Cellular networks have really revolutionized the telecommunication systems and the way in which human beings communicate with each other.

The rapidly growing consumer demands, increasing business, and constant advancements in wireless miniaturized/improved components and efficient technology have put cellular telephones and data systems in constant evolution mode. It involves the use of both old and new technologies, existing and newly allotted frequencies, advanced multiple access techniques, and international agreements between service providers/governments/regulatory agencies.

The earliest cellular telephone system is usually referred to as first-generation systems, or 1G, which brought in mobile devices. Second-generation cellular systems (2G) yielded improved performance employing various digital modulation schemes. This network also brought the ability to text and receive/send data across mobile devices. Then 3G brought in the mobile Web, and 4G made it faster, which was further improved by introducing the 5G. It is responsible for making more people connected than ever. Telecom carriers will redefine high-speed wireless communications in 6G networks [19, 20].

Some of the important features of various generations of mobile communication technologies have been compared in Table 3. Each generation is an upgrade in the cellular network with an improvement over the older generation. It was discussed earlier in Sect. 3.1 that to take advantage of technological advancements, operating frequencies were increased in each wireless systems, not forgetting that lower frequency had quickly become overcrowded because of increased applications. It is noted from the table that for each generation, increased operating frequency brought in higher bandwidth, which in turn increased speed and data rate, and a host of other featural improvements.

### ***4.3 Satellite Wireless System***

Except for lower end of RF, high-frequency signals are neither bent nor absorbed by the ionospheric layers and travel in sight line. This makes them suitable for satellite communication/broadcast, space communication, and radio astronomy. Satellite communication with a small group of satellites can cover the whole globe, including far-flung areas such as sea, mountain, desert, etc., where cellular and conventional wireless systems cannot be deployed. Satellites were launched to provide voice, video, and data connectivity worldwide. But this service was closed down as it could not be made profitable. On the other hand, satellite systems providing navigational global positioning systems (GPS) and direct broadcast systems (DBS) are highly popular and successful [6, 8].

**Table 3** Comparison of features of various generations of mobile communication technologies

Technologies	Year introduced	New feature introduced	Frequency	Bandwidth	Channel capacity
1G	1979	Analog cell phone, calling	150–900 MHz	~30 KHz	~2.4 kbps
2G/2.5G	1991	Digital, SMS, conference, MMS, long-distance call tracking, internet (in 2.5G)	1.8 GHz	~ 200 kHz	~64 kbps
3G	2001	Cheap data, GPS, broadband internet, SD video, streaming	1.6–2 GHz	~100 MHz	~2 mbps
4G	2009	Cheaper data, HD streaming, smart wearables, secured communication	2–8 GHz	100 MHz	~100Mbps
5G	2019	Internet of things, MIMO, cloud storage, cloud computing	3–30 GHz	100 × BW/unit area	10 GBPS
6G (expected)	2030s	High system capacity, global coverage, AI	20 GHz–10 THz	Undefined now	Up to 3 Tbps

## ***4.4 Scientific Applications***

When materials are subjected to high-frequency periodic electromagnetic fields, their atomic, molecular, and nuclear systems show different resonance phenomena. Many of the resonance absorption lines fall under microwave/millimeter-wave frequency range. These resonant lines are characteristic of molecular structure and intramolecular levels of energies. Hence, high-frequency waves become powerful tools to study basic characteristics of various materials experimentally. These are used extensively to quantify the density/concentration of various gases. For example, for control of pollution, emission of pollutants from the exhaust chimneys can be continuously measured. Likewise, there are many applications related to the resonance phenomenon [6, 8].

## ***4.5 Industrial/Medical Applications***

Materials having polar molecular structures absorb high-frequency energy and get heated. Heat generated inside the material is because of molecular friction; thus, it is generated inside-out and is uniform. This aspect of high-frequency heating has been adopted for numerous industrial applications. Some of these are:

1. For agro-industries: drying of seeds; grains; blanching of vegetables; drying of fruits; making fruit powder; drying of spices; dehydration of grains/fruits/food products, soyabean, pulses, etc.; seed germination; increasing shelf life of food products including milk; converting butter into ghee; tea drying; oil extraction/separation, etc.
2. Processing of ores/minerals
3. Metal extraction
4. Metal welding
5. Processing of chemicals, polymers, nanomaterials, etc.
6. Rubber vulcanization, etc.
7. For medical applications: hyperthermia, irradiation, medical LINAC, disinfection of hospital waste, neutralization of COVID-19 virus, sterilization of medical instruments/tapes/cottons/laundry, etc.

This list keeps increasing every year, indicating the usefulness of high-frequency waves.

There are several other new and traditional applications of high frequency waves such as power beaming, RF identification (RFID) system, ultra-wideband (UWB) systems, radiometry, plasma effects, etc.

## References

1. A.A. Oliner, Historical perspectives on microwave field theory. IEEE Trans. Microw. Theory Tech. **MTT-32**, 1022–1045 (1984)
2. T.K. Sarkar, R.J. Mailloux, A.A. Oliner, M. Salazar-Palma, D. Sengupta, *History of Wireless* (Wiley, Hoboken, 2006)
3. D.R.J. White, *Electromagnetic Shielding Design: Materials and performs*, MSEE/PE (Interference Control Technologies, Don White Consultants Inc., Gainesville, 1986)
4. International Journal of EMC<sup>TM</sup>, Interference Technology Engineers' Master, 1976–2001
5. G.D. Vendelin, A.M. Pavio, U.L. Rohde, *Microwave Circuit Design using Linear and Non-linear Techniques*, 2nd edn. (Engineering Rockwell Collins Phoenix Design Center Synergy Microwave Corporation, 2021)
6. D.M. Pozar, *Microwave and RF Design of Wireless Systems* (Wiley, Hoboken, 2001)
7. R.E. Collin, *Foundations for Microwave Engineering*, 2nd edn. (Wiley-IEEE Press, Hoboken, 2001)
8. K.C. Gupta, *Microwaves* (New Age International, New Delhi, 1979)
9. S.Y. Lio, *Microwave Devices and Circuits* (Prentice Hall, Englewood Cliffs, 1990)
10. T.S. Laverghetta, *Microwaves and Wireless Simplified* (Artech House, Boston/London, 2005)
11. M.L. Skolnik, *Introduction to Radar Systems* (McGraw-Hill Book Company, New Delhi, 1981)
12. D. Roddy, *Microwave Technology* (Prentice-Hall, Englewood Cliffs, 1986)
13. D.K. Mishra, *Radio-Frequency and Microwave Communication Circuits* (Wiley Inter- Science, 2004)
14. J.D. Kraus, D.A. Fleisch, *Electromagnetics* (McGraw-Hill, New York, 1999)
15. F. Ulaby, *Fundamentals of Applied Electromagnetics* (Prentice-Hall, Upper Saddle River, 2010)
16. S. Ramo, T.R. Whinnery, T. van Duzer, *Fields and Waves in Communication Electronics* (Wiley, New York, 1994)
17. C.A. Balanis, *Advanced Engineering Electromagnetics* (Wiley, New York, 1989)
18. T.S. Laverghetta, *Modern Microwave Measurements and Techniques* (Artech House, Norwood, 1988)
19. <https://www.ieee.org/searchresults/index.html?q=3g+cellular+network#gsc.tab=0&gsc.q=3g%20cellular%20network&gsc.page=1>
20. <https://www.emfexplained.info/?ID=25196>

# Finite Circular Ground Plane Effects: A Case Study of Monopole Antenna



Hemant Kumar and Girish Kumar

## 1 Introduction

One of the most popular antennas employed in mobile communication systems is the monopole antenna. Monopole antennas are unbalanced and can be matched with  $50\ \Omega$  coaxial feed. This eliminates the need for a balun, which is required for a dipole antenna [1, 2].

For a monopole antenna mounted on an infinite ground plane, the analysis and empirical formula for finding the resonant length and wire radius from a given resonance frequency are available [1]. However, monopole antennas are generally mounted on a finite-sized ground plane. The size and shape of the ground plane may vary based on the application and space restrictions. There are some applications where monopole antennas are mounted on a very small ground plane, such as a walkie-talkie, cell phone, etc. There are some other applications that can provide large ground planes, such as monopole antennas mounted on cars, trucks, aircraft, etc. Hence, it is important to study the effect of the finite ground plane on the characteristics of a monopole antenna.

---

This work was done at EE Dept, IIT Bombay

---

H. Kumar (✉)

Electronics and Communication Engineering Department, National Institute of Technology  
Tiruchriappalli, Tiruchirappalli, Tamil Nadu, India  
e-mail: [hemant@nitt.edu](mailto:hemant@nitt.edu)

G. Kumar

Electrical Engineering Department, Indian Institute of Technology Bombay, Powai, Mumbai,  
Maharashtra, India  
e-mail: [gkumar@ee.iitb.ac.in](mailto:gkumar@ee.iitb.ac.in)



Some papers are available for monopole antennas on a finite ground plane [3–13]. Different techniques based on the size and shape of the finite ground plane are given for variation of the input impedance of the monopole antenna [3–9]. These techniques are different in their complexity, accuracy, and assumptions considered based on the shape and size of the finite ground plane. Some of the techniques assume effects of magnetic edge current [3], vertex diffraction [5], physical surface current [9], etc. The effect on the radiation pattern of a monopole antenna mounted on a finite ground plane with circular and rectangular shapes is presented [9–11]. In [12, 13], the effect of thickness and conductivity of finite ground plane has been analyzed, respectively. In the literature, the main focus of the work was the input impedance and radiation pattern variation of the monopole antenna with respect to the shape and size of the finite ground plane.

In this chapter, the effect of the finite circular ground plane on various characteristics of a monopole antenna, such as reflection coefficient, resonance frequency, input impedance, bandwidth, directivity, and radiation pattern, is analyzed. A finite circular ground plane with infinite conductivity and negligible thickness has been considered. An approximate design equation for calculating the resonant length of a monopole antenna mounted on a small circular ground plane for a given resonance frequency is proposed. The analysis is done using a commercially available IE3D software based on the method of moments (MoM) [14]. The characteristics of a monopole antenna on a finite ground plane and infinite ground plane are also compared.

## 2 Design Specifications

A monopole antenna mounted on a finite circular ground plane is shown in Fig. 1. A cylindrical wire of radius  $r$  and length  $l$  has been considered as a monopole mounted on a finite circular ground plane of radius  $R$ . Initially, the parameters of a monopole antenna such as length and radius of monopole have been chosen based on the formula for the infinite ground plane as given below [1]:

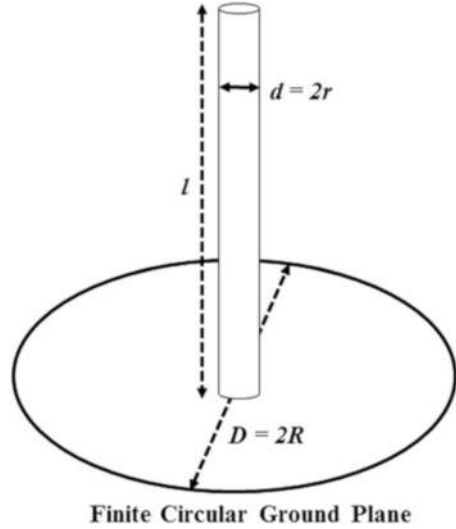
$$l + r = 0.24\lambda_i \quad (1)$$

where  $\lambda_i$  is the wavelength corresponding to the resonance frequency,  $f_i$  of a monopole antenna mounted on the infinite ground plane.

## 3 Parametric Analysis

In this section, the effect of varying the radius of the circular ground plane ( $R$ ) for a fixed value of length ( $l$ ) and radius ( $r$ ) of a monopole on various characteristics

**Fig. 1** Monopole antenna on a finite circular ground plane



of the antenna, viz., reflection coefficient, resonance frequency, input impedance, bandwidth, radiation pattern, and directivity, has been analyzed.

Initially, fixed values of length,  $l = 90$  mm, and wire radius,  $r = 2$  mm, have been chosen, and corresponding resonance frequency and wavelength are obtained using Eq. (1) as  $f_i = 783$  MHz and  $\lambda_i = 383$  mm, respectively.

### 3.1 Effect on the Resonance Frequency of a Monopole Antenna

Figure 2 shows the reflection coefficient,  $|S_{11}|$ , of the monopole antenna versus frequency for different sizes of the ground plane. The radius of the circular ground plane is varied from a very small value of 11 mm ( $0.028\lambda_i$ ) to a value that is comparable to the wavelength.

For comparison, simulation is also done for the infinite ground plane. The curves are plotted for two different regions based on the size of the ground plane. In Fig. 2a, the reflection coefficient versus frequency plot is shown for the ground plane radius values (11, 18, 36, and 90) mm, which are less than or equal to the length of the monopole antenna. As the ground plane radius increases from 11 mm ( $0.028\lambda_i$ ) to 90 mm ( $0.235\lambda_i$ ), the resonance frequency decreases from 1.22 GHz to 0.8 GHz. For the ground plane radius greater than the length of the monopole antenna, the variation in the resonance frequency is small, which can be observed in Fig. 2b. As the radius of the ground plane increases from 144 mm ( $0.376\lambda_i$ ) to infinite size ground plane size, the resonance frequency first decreases to 0.76 GHz and then saturates to nearly a constant value of 0.783 GHz (value for the infinite ground plane).

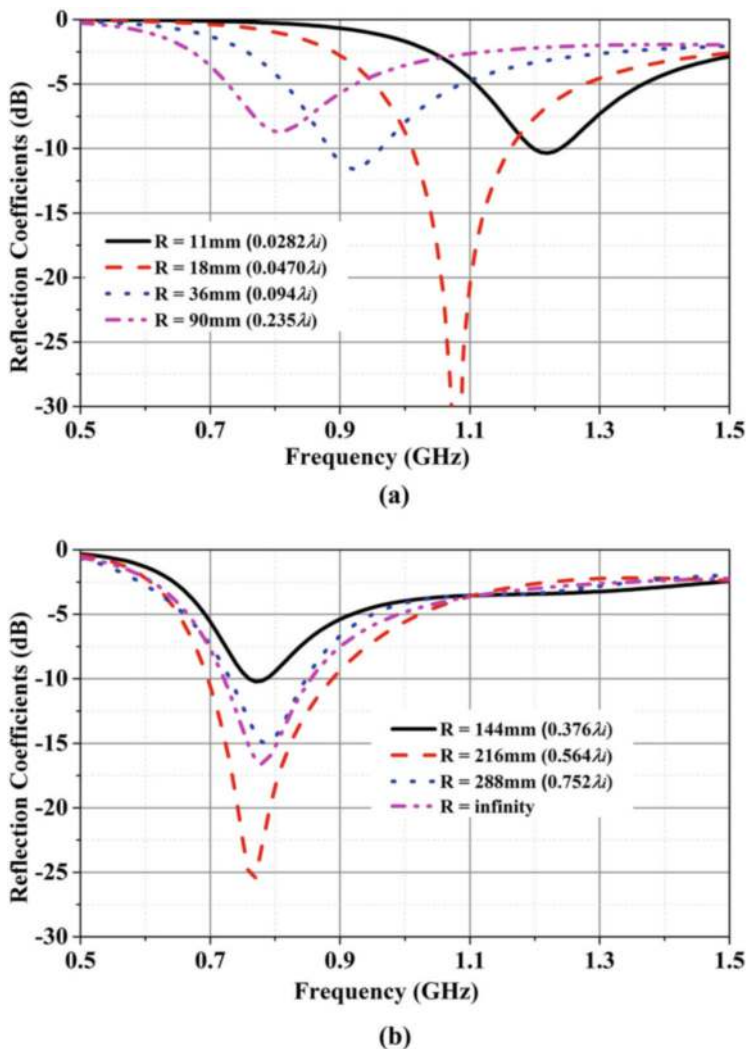


**Fig. 2** Reflection coefficient versus frequency for different values of ground plane radius (a) less than or equal to and (b) greater than the monopole length,  $l = 90$  mm, for  $r = 2$  mm ( $0.0052\lambda_i$ )

The resonance frequency variation with respect to variation in the ground plane radius by keeping the constant value of monopole radius,  $r = 2$  mm, is plotted in Fig. 3. For a small ground plane, as its size increases, the effective length of the antenna (from monopole tip to periphery of circular ground plane) increases, so resonance frequency decreases. For larger ground planes, the effect on resonance frequency is small. It can be observed from Fig. 3 that as the ground plane radius increases from 11 mm ( $0.028\lambda_i$ ) to 198 mm ( $0.5\lambda_i$ ), the resonance frequency decreases from 1.22 GHz to 0.76 GHz. Further increase in ground plane radius shows comparatively

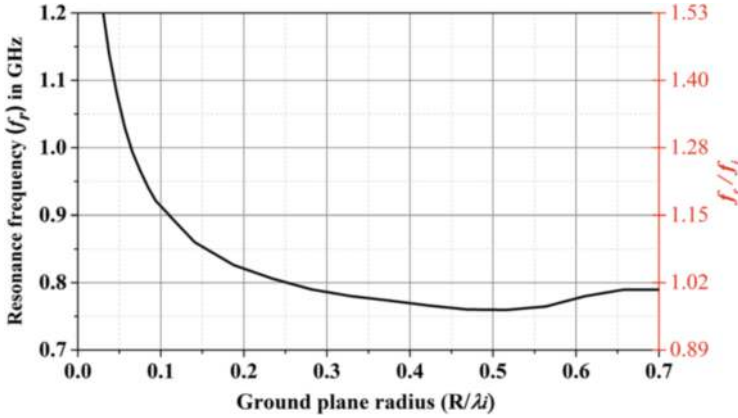


**Fig. 3** Variation of the resonance frequency of monopole antenna with the ground plane radius for  $l = 90$  mm and  $r = 2$  mm ( $0.0052\lambda_i$ )

lesser variation in the resonance frequency, and then it settles to a constant value of  $f_i = 0.783$  GHz, which is the resonance frequency as calculated from Eq. (1) for infinite ground plane size.

A similar analysis has been carried out for other values of wire radius for monopole antenna mounted on the finite ground plane. Based on these analyses and by using the curve fitting technique, the expression for approximately calculating the resonance frequency of a monopole antenna mounted on a finite circular ground plane with wire radius,  $r < 0.016\lambda_i$ , is given as:

$$l + r + xR = 0.48\lambda_r \quad (2)$$

where  $\lambda_r$  represents wavelength corresponding to the resonance frequency of the monopole antenna on a finite ground plane of radius,  $R$ , and  $x$  is given by:

$$x = \begin{cases} 2.2 & \text{for } R < 0.04\lambda_i \\ -0.76 \ln(R) + 4.4 & \text{for } 0.04\lambda_i \leq R < 0.45\lambda_i \end{cases} \quad (3)$$

For ground plane radius,  $R > 0.45\lambda_i$ , Eq. (1) can be used to calculate the approximate value of resonance frequency.

Percentage error versus ground plane radius plot is shown in Fig. 4. The approximate error between the value calculated from Eq. (2) and the simulated value is within  $\pm 3\%$ .

For a given resonance frequency,  $f_r$ , for a monopole antenna on finite circular ground plane with radius ( $R$ ), the length of monopole antenna ( $l$ ) can be obtained using the following equation:

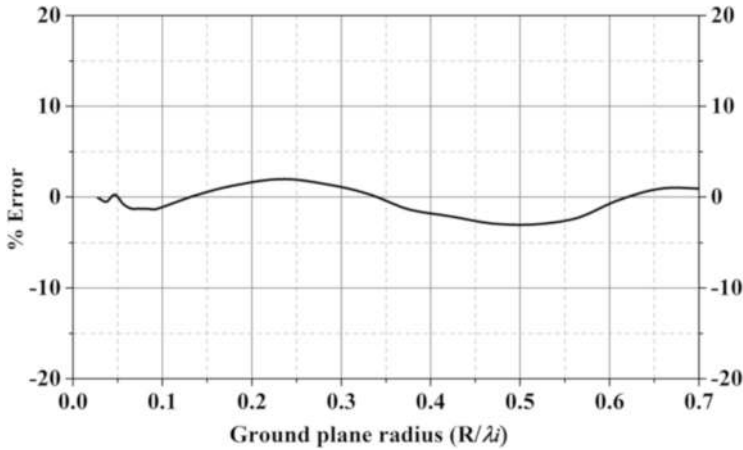


**Fig. 4** Percentage error in resonance frequency of monopole antenna versus ground plane radius for  $l = 90$  mm and  $r = 2$  mm ( $0.0052\lambda_i$ )

$$l = 0.48 \left( \frac{c}{f_r} \right) - r - xR \quad (4)$$

where  $c$  is the velocity of light in air.

### 3.2 Effect on the Input Impedance of Monopole Antenna

Figure 5 shows the variation of input impedance with ground plane radius for  $l = 90$  mm and  $r = 2$  mm ( $0.0052\lambda_i$ ). Here also the plots are split into two regions depending on the size of the ground plane. Figure 5a shows the input impedance variation for the ground plane radius less than or equal to the length of the monopole. As the radius of the ground plane increases from 11 mm to 90 mm, the input impedance of the monopole antenna shifts toward the left side, and its real part decreases from approximately  $100 \Omega$  to  $21 \Omega$ , and it is matched with  $50 \Omega$  for  $R = 18$  mm ( $0.047\lambda_i$ ). Figure 5b shows the input impedance plot for the radius of the ground plane greater than the length of the monopole. As the ground plane radius increases from 144 mm to 216 mm, the input impedance first decreases, and then it increases with a further increase in ground plane radius. Finally, the real part of input impedance approaches a value of approximately  $36 \Omega$ , which is obtained for infinite ground plane size.

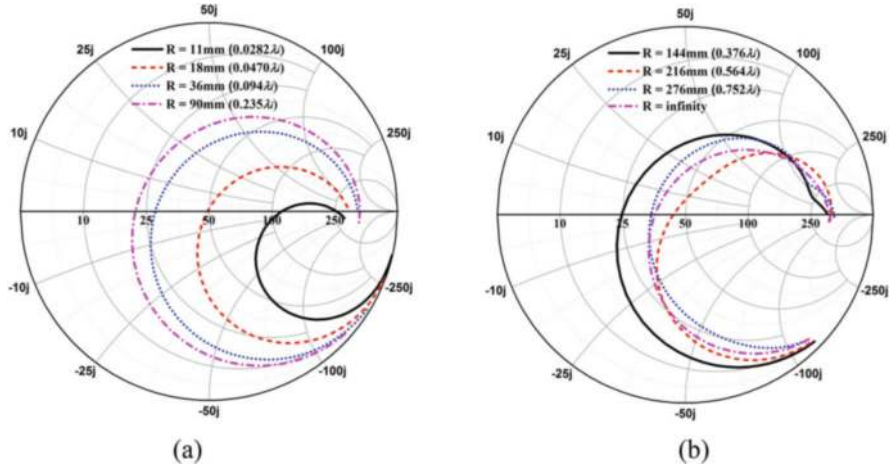


**Fig. 5** Input impedance variation with respect to ground plane radius (a) less than or equal to and (b) greater than the monopole length,  $l = 90\text{ mm}$ , for  $r = 2\text{ mm}$  ( $0.0052\lambda i$ )

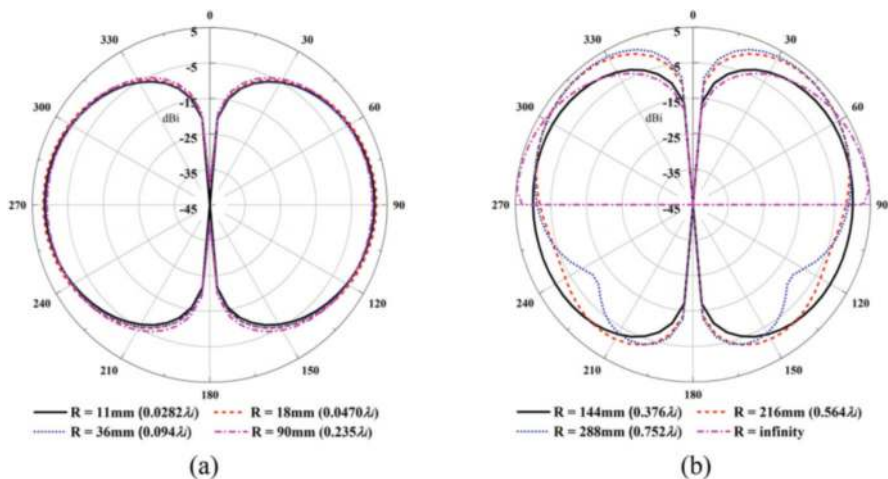
### 3.3 Effect on the Radiation Pattern of a Monopole Antenna

Figure 6 shows the radiation pattern of a monopole antenna for different ground plane sizes at their corresponding resonance frequency obtained from Fig. 2 for  $r = 2\text{ mm}$ . For a smaller ground plane size ( $R < \lambda i/4$ ), the radiation pattern of the monopole antenna is similar to that of a dipole antenna, and the maximum radiation occurs in the direction perpendicular to the monopole, as shown in Fig. 6a. As the ground plane size increases ( $R > \lambda i/4$ ), the radiation pattern changes, and the maximum radiation occurs at an angle “ $\theta$ ” with respect to the ground plane, as shown in Fig. 6b. For infinite ground plane radius, the radiation is only at the top hemisphere with maxima in the direction of the ground plane. For all the ground plane sizes, the radiation pattern is uniform (circular) in the horizontal plane.

### 3.4 Effect on the Directivity of a Monopole Antenna

Figure 7 shows the variation of directivity for different values of the ground plane radius. For ground plane radius,  $R < 0.1\lambda i$ , the variation in the directivity is less than 0.1 dB, but for ground plane radius equal to or greater than the length of the monopole, the variation in the directivity value is large from approximately 1 dBi to 4 dBi. For the infinite ground plane, simulated directivity is 5.1 dBi at the resonance frequency, which matches with the theoretical value of a  $\lambda i/4$  monopole.

For a finite ground plane with a larger radius, there is constructive and destructive interference between the main current component and the reflected current compo-

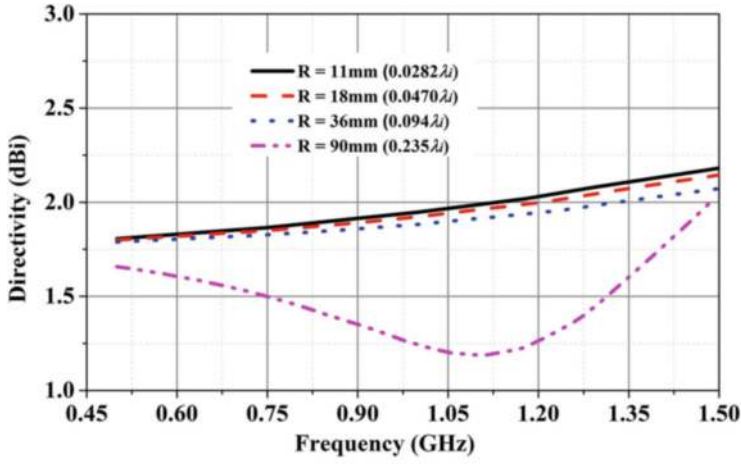


**Fig. 6** Radiation pattern variation with the ground plane radius (a) less than and (b) greater than the monopole length,  $l = 90$  mm, for  $r = 2$  mm ( $0.0052\lambda_i$ )

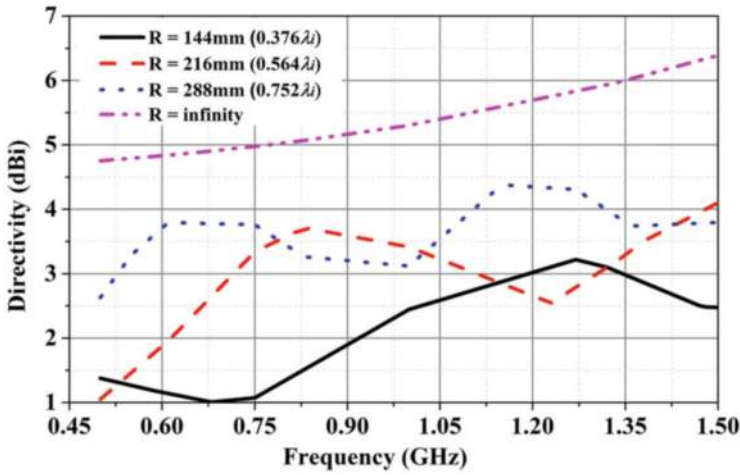
nent from the periphery of the circular ground plane, which behaves as an open circuit at the end. The waves, which are reflected for the radius of odd integer multiples of  $\lambda_i/4$ , will be  $180^\circ$  out of phase at the feed point, which will lead to destructive interference, and those which are reflected for the radius of even integer multiples of  $\lambda_i/4$  will be in phase at the feed point, resulting in constructive interference. A similar phenomenon can be observed in the current distribution. Current distributions for a monopole antenna at different frequencies, 0.6, 0.9, 1.2, and 1.5 GHz for  $R = 288$  mm ( $0.752\lambda_i$ ),  $l = 90$  mm, and  $r = 2$  mm, are shown in Fig. 8. The blue concentric rings on the ground plane appeared at a distance of integer multiple of  $\lambda_i/4$  from the center of monopole antenna showing the destructive interference, which is the cause of standing wave pattern in the directivity plot for a finite ground plane of  $R \geq \lambda_i/4$ .

## 4 Conclusions

A monopole antenna mounted on a finite circular ground plane is studied. The effect of varying the radius of a circular ground plane on the various characteristics of a monopole antenna such as reflection coefficient, resonance frequency, bandwidth, input impedance, radiation pattern, and directivity has been analyzed. A simple approximate expression for finding the resonant length of monopole antenna mounted on a finite circular ground plane for a given resonance frequency is proposed. Also, the normalized value of ground plane radius is given for impedance matching with  $50 \Omega$  coaxial feed.



(a)

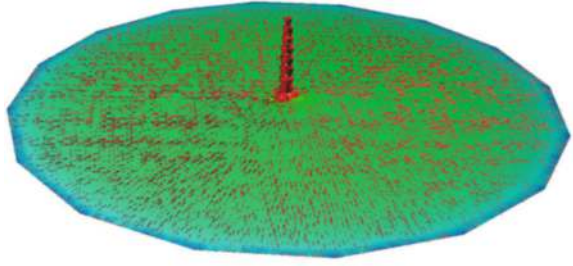


(b)

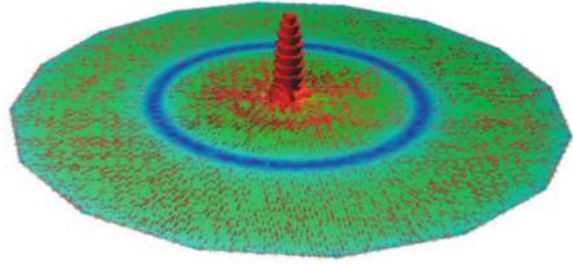
**Fig. 7** Directivity versus frequency for different values of ground plane radius (a) less than or equal to and (b) greater than the monopole length,  $l = 90$  mm, for  $r = 2$  mm ( $0.0052\lambda_i$ )



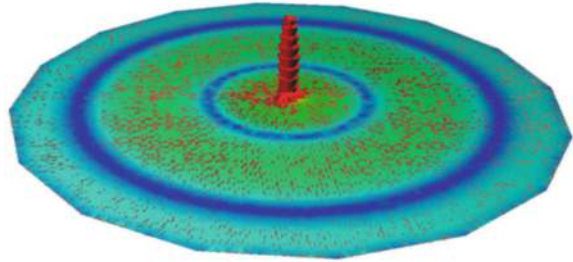
**Fig. 8** Current distribution of monopole antenna at (a) 0.6, (b) 0.9, (c) 1.2, and (d) 1.5 GHz for  $R = 288$  mm ( $0.752\lambda_i$ ),  $l = 90$  mm, and  $r = 2$  mm



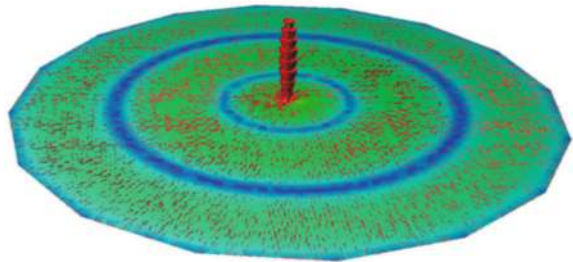
(a)



(b)



(c)



(d)

## References

1. C.A. Balanis, *Antenna Theory: Analysis and Design* (Wiley-Interscience, 2005)
2. T.A. Milligan, *Modern Antenna Design* (McGraw-Hill, Inc., New York, 2005)
3. K. Awadalla, T. Maclean, Input impedance of a monopole antenna at the center of a finite ground plane. *IEEE Trans. Antennas Propag.* **26**(2), 244–248 (1978)
4. P.E. Zimourtopoulos, J.N. Sahalos, G.A. Thiele, Input impedance of a monopole antenna on a finite polygonal ground plane. *IEE Proc. H Microw. Opt. Antennas* **130**(4), 276–280 (1983)
5. M. Hassan, Solution of a monopole antenna over a circular finite disk, in *1986 Antennas and Propagation Society International Symposium, Philadelphia, PA, USA*, (1986), pp. 133–136
6. M. Weiner, Monopole element at the center of a circular ground plane whose radius is small or comparable to a wavelength. *IEEE Trans. Antennas Propag.* **35**(5), 488–495 (1987)
7. J. Richmond, Monopole antenna on circular disk. *IEEE Trans. Antennas Propag.* **32**(12), 1282–1287 (1984)
8. J. Richmond, Monopole antenna on circular disk over flat earth. *IEEE Trans. Antennas Propag.* **33**(6), 633–637 (1985)
9. K. Awadalla, T. Maclean, Monopole antenna at center of circular ground plane: Input impedance and radiation pattern. *IEEE Trans. Antennas Propag.* **27**(2), 151–153 (1979)
10. Z. Živković, D. Senić, C. Bodendorf, J. Skrzypczynski, A. Šarolić, Radiation pattern and impedance of a quarter wavelength monopole antenna above a finite ground plane, in *Soft-COM 2012, 20th International Conference on Software, Telecommunications and Computer Networks, Split*, (2012), pp. 1–5
11. L. Kibona, Analysis of the effects of rectangular ground plane on radiation pattern of the monopole antenna. *Int. J. Sci. Res. Publ.* **3**(11), 1–4 (2013)
12. Z. Shen, R.H. MacPhie, Input impedance of a monopole over a circular ground-plane of finite thickness, in *IEEE Antennas and Propagation Society International Symposium. 1998 Digest. Antennas: Gateways to the Global Network. Held in Conjunction with: USNC/URSI National Radio Science Meeting Atlanta, GA, USA*, vol. 3, (1998), pp. 1726–1729
13. C. Balanis, D. DeCarlo, Monopole antenna patterns on finite size composite ground planes. *IEEE Trans. Antennas Propag.* **30**(4), 764–768 (1982)
14. IE3D Mentor Graphics, ver. 15.3, USA (2015)

# Mode Compression Theory: Dipole Antennas



Rajbala Solanki 

## 1 Introduction

In modern portable communication systems, integrating multiple communication technologies within the same system has elevated the demand for compact and wideband antennas. Dipole antennas, favored for their omnidirectional radiation, find suitability in numerous wireless applications. However, dipole antennas with a small width-to-length ratio inherently offer narrow bandwidth. To address this limitation, various methods outlined in the literature aim to broaden the bandwidth.

As the width of dipole antennas increases, so does the bandwidth, albeit at the expense of fluctuating radiation patterns across the impedance bandwidth, heightened cross-polarization levels, and increased antenna size. Diverse shapes of dipole arms have been explored to augment dipole width and subsequently broaden the bandwidth [1–5]. Additionally, the introduction of parasitic resonators [6, 7], stubs [8], slots [9], stubs combined with slots [10], and passive elements [11] has been reported to enhance bandwidth, albeit often accompanied by variations in radiation pattern and larger antenna dimensions.

Over the past decade, a notable technique known as mode compression has emerged as an effective means to broaden the bandwidth of various antenna types, including slot antennas [12, 13], microstrip antennas [14, 15], and dipole antennas [16–24]. In this approach, one mode is compressed in proximity to another mode, resulting in an expanded bandwidth. For instance, in a slot antenna configurations

---

This research was conducted at IIT Bombay.

---

R. Solanki (✉)  
National University of Singapore, Singapore, Singapore  
e-mail: [rajbala@nus.edu.sg](mailto:rajbala@nus.edu.sg)

reported in [12], the fundamental mode is shifted up and combined with a third-order mode to achieve increased bandwidth. Similarly, in patch antennas, modes are manipulated through various means such as loading vias or shorting pins [14] to achieve similar bandwidth expansion. In the realm of dual-mode dipole antennas, innovative strategies have been employed to broaden the bandwidth while maintaining compactness. Techniques such as loading electrically small loop resonators [16–18], vias [19], stubs [20–22], capacitive loading [23], and combination of stub and loop [24] have been utilized to manipulate mode frequencies, effectively widening the bandwidth.

In brief, the pursuit of wideband antennas in modern communication systems has spurred the development of various techniques, including mode compression, to address the challenges of limited bandwidth within compact form factors. These advancements hold promise for the continued evolution of wireless communication technologies.

## 2 Dipole Antenna

Initially, a dipole antenna is designed to operate at approximately 3.3 GHz in its fundamental mode, serving as a benchmark for comparison. The antenna is constructed on a substrate featuring specific parameters: a dielectric constant of  $\epsilon_r = 2.55$ , a substrate thickness  $h$  of 60 mil (1.524 mm), and a loss tangent  $\tan \delta$  of 0.018. Through the application of dipole design equation, the dipole's dimensions are determined, resulting in a length ( $L$ ) of 34 mm and a width ( $W_d$ ) of 4 mm. Given the requirement for a balanced feed in dipole antennas, simulations entail the connection of a “Discrete Port” between the top and bottom arms of the dipole antenna. This configuration allows for the examination of the antenna parameters' effects in isolation, devoid of any connector influence. In preparation for antenna prototype fabrication, the design encompasses a balun, realized through a tapered microstrip line, alongside a coaxial-SMA connector using CST-MWS software.

The schematic representation of the antenna and its simulated outcomes are illustrated in Fig. 1. Herein, the dark- and light-colored dipole arms signify the top and bottom arms, respectively. Here, the dipole is fed at the center. Therefore, even harmonics do not get excited due to impedance mismatch as shown in Fig. 1b. The input impedance pertaining to the first- and third-order modes approximates  $50\Omega$ , while for the second-order mode, it escalates significantly to approximately  $300\Omega$ . Consequently, the  $|S_{11}|$  plot exhibits no traces of even harmonics (second order), as illustrated in Fig. 1c. The fundamental mode frequency of the antenna is 3.3 GHz, while the third-order mode frequency is 9.2 GHz.

Figure 2 illustrates the radiation patterns and current distributions of the antenna at the first- and third-order modes. A notable distinction in the radiation patterns of these modes lies in the presence of side lobes, as evident in Fig. 2a,b, thereby constraining the practical applications of the third-order mode. This divergence in radiation patterns arises from differences in the current distributions at these

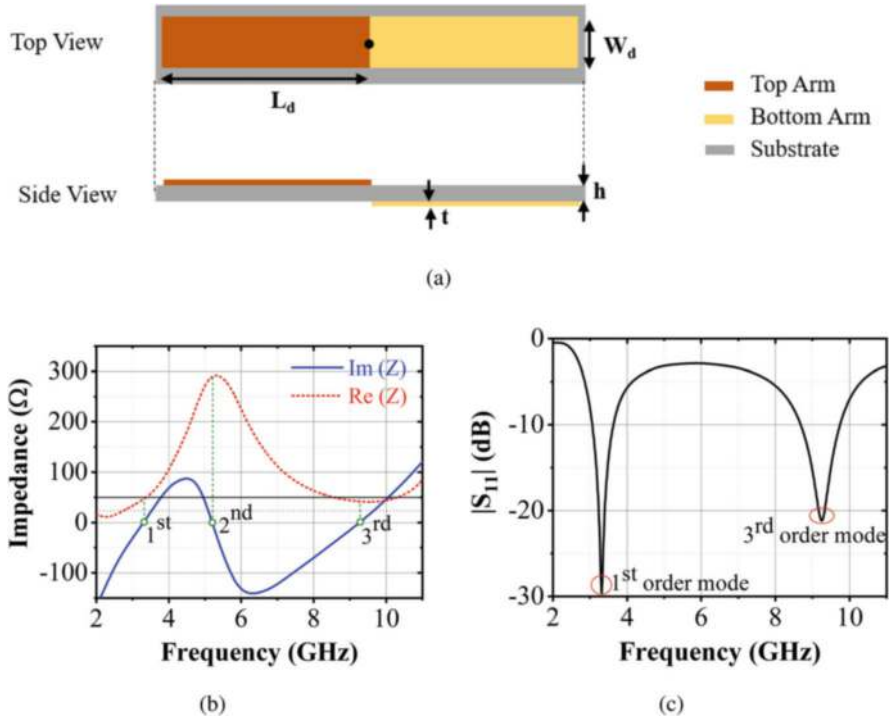


**Fig. 1** (a) Schematic and simulated (b) input impedance and (c)  $|S_{11}|$  plots of a dipole antenna

two modes, as depicted in Fig. 2c,d. Nevertheless, by refining the manipulation of current distributions, it becomes feasible to enhance the radiation patterns at higher order modes.

### 3 Stub-Loaded Dual-Mode Dipole Antenna

#### 3.1 Need and Concept of Stub Loading

As observed in Fig. 1b,c, the  $|S_{11}|$  plot exhibits traces of two resonances: the first-order mode resonance at 3.3 GHz and the third-order mode resonance at 9.2 GHz. If we can manipulate the third-order mode to align it closer to the first-order mode, their combined effect may lead to a wider bandwidth. To achieve this, the designed dipole antenna is loaded with stubs, as depicted in Fig. 3. The stubs effectively lengthen the total path for the third-order mode while leaving the main path unaffected. Consequently, the third-order mode is shifted toward lower frequencies. The size and placement of the stubs determine the shifted frequency

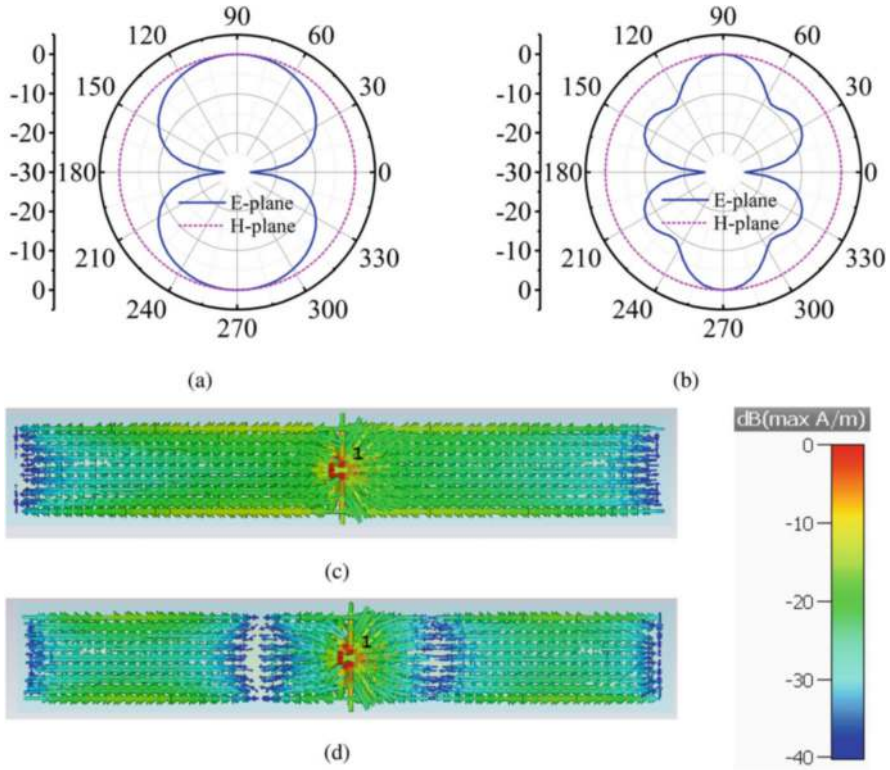
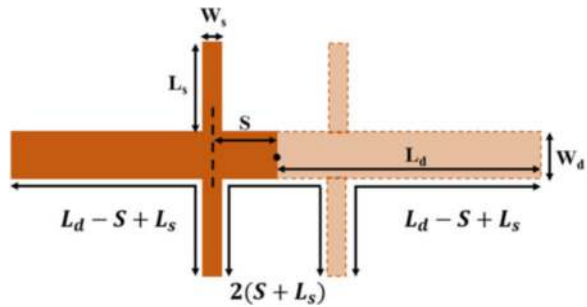


**Fig. 2** Normalized radiation patterns at (a) 3.3 GHz and (b) 9.2 GHz and current distributions at (c) 3.3 GHz and (d) 9.2 GHz

**Fig. 3** Electric path lengths on the stub-loaded dipole antenna (dark color: top arm; light color: bottom arm)



of the third-order mode. The calculation of stub parameters relies on the following concepts and equations:

1. The stubs are loaded at the current null points of the shifted third-order mode. Consequently, the location of the stubs (or the distance from the center of the dipole:  $S$ ) can be determined by equating the lengths of each  $\lambda/2$  section of the shifted third-order mode.

$$2(S + L_s) = L_d - S + L_s = \frac{1}{2}\lambda_{3new} \quad (1)$$

$$S = L_d + L_s - \frac{1}{2}\lambda_{3new} \quad (2)$$

or

$$S = \frac{1}{4}\lambda_{3new} - L_s \quad (3)$$

or

$$\boxed{S = \frac{L_d - L_s}{3}} \quad (4)$$

2. The path length for the shifted third-order mode is the sum of the dipole length and the lengths of the stubs. Therefore, the stub length will be given by

$$2L_d + 4L_s = \frac{3}{2}\lambda_{3new} \quad (5)$$

$$\frac{3}{2}\lambda_3 + 4L_s = \frac{3}{2}\lambda_{3new} \quad (6)$$

$$\Rightarrow \boxed{L_s = \frac{3}{8}(\lambda_{3new} - \lambda_3)} \quad (7)$$

where  $\lambda_3$  represents the wavelength of the original third-order mode,  $\lambda_{3new}$  denotes the wavelength of the new or shifted third-order mode, and  $L_s$  stands for the stub length. Thus, depending on the desired frequency of the new or shifted third-order mode, the stub length can be calculated.

In these calculations, the stub width is neglected due to its relatively smaller size compared to other parameters. However, the stub length, width, and position influence antenna performance. Hence, a parametric analysis is presented in Sect. 3.2 to assess the effects of these parameters.

### 3.2 Antenna Geometry and Parametric Analysis

Figure 4 illustrates the schematic of the stub-loaded dipole antenna for third-order mode compression. The antenna consists of a rectangular dipole and a symmetric pair of stubs loaded at an appropriate distance from the center of the dipole. A substrate with dielectric constant  $\epsilon_r = 2.55$ , thickness  $h = 1.524$  mm, and loss tangent  $\tan \delta = 0.018$  is utilized to design the antenna. Printed in the  $xy$ -plane,

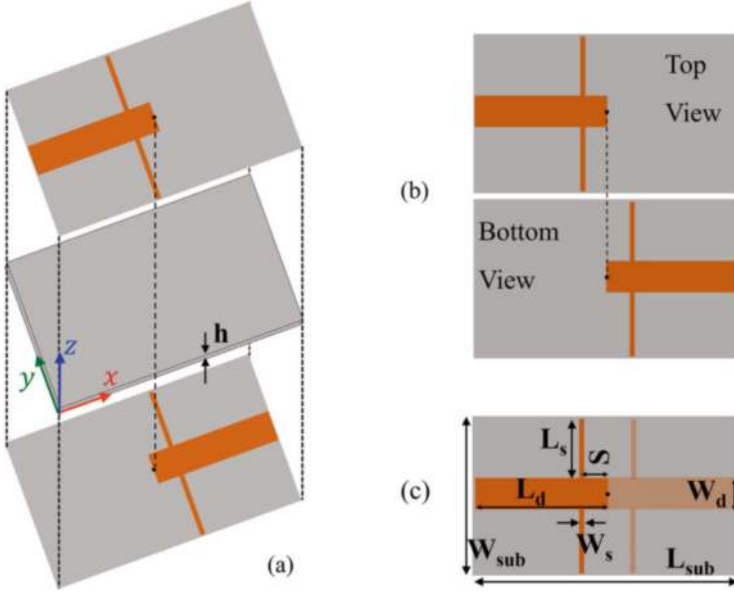


**Fig. 4** (a) Layered and (b) top and bottom views of the stub-loaded dipole antenna (Antenna 1) and (c) its geometrical parameters

the antenna exhibits two-dimensional symmetries, one along the  $y$ -axis and another along the  $x$ -axis. As depicted in Fig. 4a,b, the two symmetric arms of the dipole are printed on the top and bottom sides of the substrate. In Fig. 4c, the dark- and light-colored arms of the dipole represent the top and bottom sides of the substrate, respectively. Each dipole arm is loaded with two symmetric stubs of length  $L_s$  and width  $W_s$ , positioned at a distance  $S$  from the center of the dipole. The length and width of the dipole are consistent with those described in Sect. 2, i.e.,  $L_d = 17$  mm and  $W_d = 4$  mm. The length of the stubs is calculated using equation (7) to achieve a desired new third-order mode frequency of approximately 5.5 GHz. Subsequently, the length  $L_s$  is determined to be approximately 8 mm. Next, the stub position is calculated using equation (4), resulting in  $S = \frac{17-8}{3} = 3$  mm. The stub width is set to 1 mm.

To investigate the effects of stub parameters, a parametric analysis of the stub length, width, and position is conducted using CST-MWS 2017. Each parameter is varied independently while keeping the others fixed.

### 3.2.1 Variation in Stub Length $L_s$

Initially, the stub length ( $L_s$ ) is varied from 7 mm to 9 mm while keeping  $W_s = 1$  mm and  $S = 3$  mm constant. The simulated  $|S_{11}|$  and input impedance vs. frequency plots for three values of stub length  $L_s = 7$  mm, 8 mm, and 9 mm are illustrated in Fig. 5.



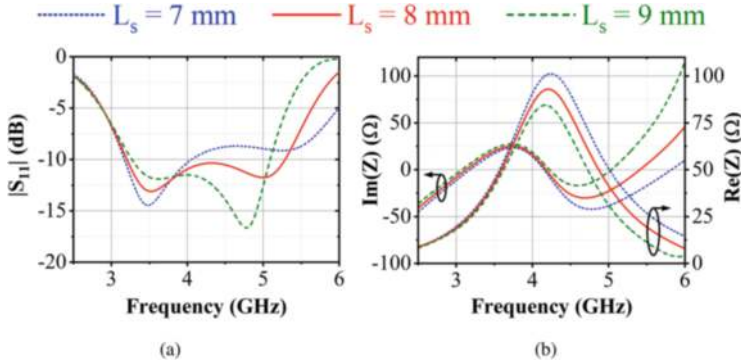


**Fig. 5** Simulated (a)  $|S_{11}|$  and (b) input impedance vs. frequency plots of a stub-loaded dual-mode dipole antenna for three different stub lengths  $L_s = 7$  mm, 8 mm, and 9 mm

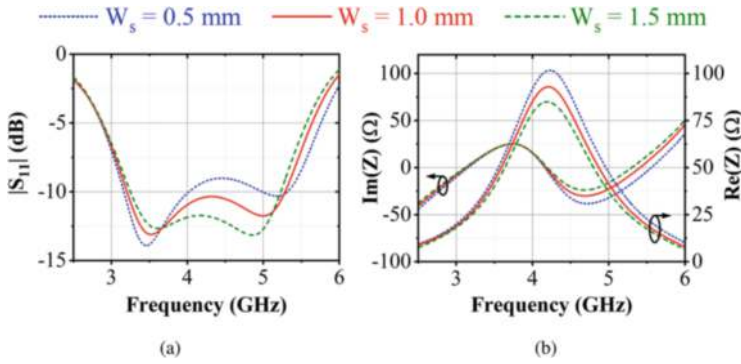


**Fig. 6** Simulated (a)  $|S_{11}|$  and (b) input impedance vs. frequency plots of a stub-loaded dual-mode dipole antenna for three different stub widths  $W_s = 0.5$  mm, 1.0 mm, and 1.5 mm

Observing the  $|S_{11}|$  plot, there is no significant effect on the first-order mode frequency, whereas the third-order mode frequency decreases due to the increased path length. This observation aligns with the reactance null points in the input impedance vs. frequency plot. There is no significant effect on the first-order reactance null point, whereas the third-order reactance null point decreases with an increase in  $L_s$ .

The impact of stub length on the input resistance is negligible in the first-order mode region. However, the input resistance decreases with an increase in  $L_s$  at higher frequencies or in the third-order mode region. Consequently,  $L_s = 8$  mm is chosen for further parametric analysis.

### 3.2.2 Effect of Variation in Stub Width $W_s$

Subsequently, the stub width ( $W_s$ ) is varied from 0.5 mm to 1.5 mm while keeping  $L_s = 8$  mm and  $S = 3$  mm constant. Figure 6 depicts the simulated  $|S_{11}|$  and input

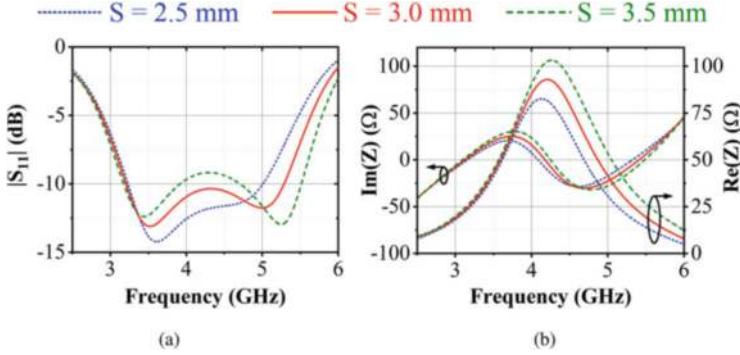


**Fig. 7** Simulated (a)  $|S_{11}|$  and (b) input impedance vs. frequency plots of a stub-loaded dual-mode dipole antenna for three different stub locations  $S = 2.5$  mm,  $3.0$  mm, and  $3.5$  mm

impedance vs. frequency plots for three values of stub width  $W_s = 0.5$  mm,  $1.0$  mm, and  $1.5$  mm.

As the stub width increases, the first-order mode frequency remains almost unchanged, while the third-order mode frequency decreases. This observation is confirmed by the input reactance plot. The impact of  $W_s$  on the input resistance is negligible in the first-order mode region. However, the input resistance decreases with an increase in  $W_s$  at higher frequencies or in the third-order mode region. Consequently, stub width  $W_s = 1$  mm is selected for further parametric analysis.

### 3.2.3 Variation in Stub Location $S$

Next, the stub location ( $S$ ) is varied from  $2.5$  mm to  $3.5$  mm with a step size of  $0.5$  mm. The simulated  $|S_{11}|$ , resistance, and reactance vs. frequency plots for three values of stub location  $S = 2.5$  mm,  $3.0$  mm, and  $3.5$  mm are depicted in Fig. 7.

As the stubs move closer to the center of the dipole, the first-order mode frequency remains nearly unchanged, while the third-order mode frequency decreases. As shown in the input resistance curve, there is no significant change in the resistance at lower frequencies (i.e., first-order mode region). However, at higher frequencies (i.e., third-order mode region), the input resistance decreases as the stubs move closer to the center of the dipole.

Given that the size and location of the stubs can alter or shift the third-order mode frequency without notably affecting the fundamental frequency, it follows that a wideband dipole antenna can be engineered by incorporating optimally sized stubs at a suitable distance from the center of the dipole.

**Table 1** Geometrical parameters of the stub-loaded dual-mode dipole antenna

Parameter	Value (mm)	Parameter	Value (mm)
$L_{sub}$	35	$W_{sub}$	21
$L_d$	17	$W_d$	4
$L_s$	8	$W_s$	1
S	3		

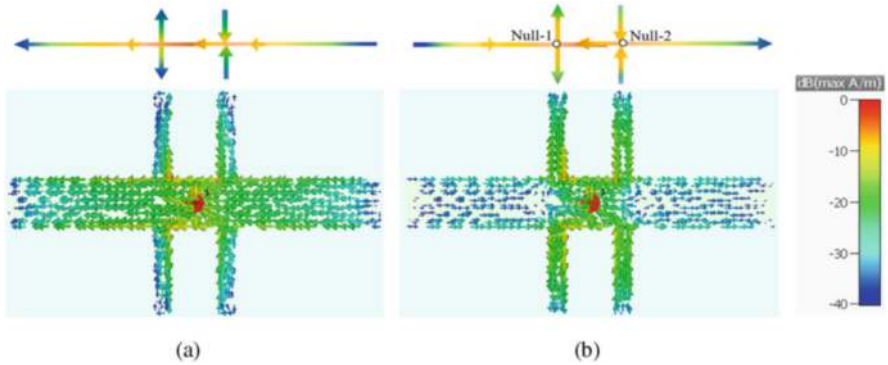


**Fig. 8** Current distributions of the stub-loaded dual-mode dipole antenna at (a) 3.2 GHz and (b) 5.2 GHz

**3.3 Optimized Stub-Loaded Dual-Mode Dipole Antenna**

After undergoing a parametric study, the stub-loaded dipole antenna has been optimized. The dimensions of the optimized antenna are summarized in Table 1. Current distributions of the antenna at 3.2 GHz and 5.2 GHz are presented in Fig. 8. Antenna modes can be distinguished by the total number of forward and reverse currents or by the presence of nulls. At 3.2 GHz, the current exhibits a half sinusoidal variation along the dipole length (with zero nulls), indicating radiation in its fundamental or first-order mode. Conversely, at 5.2 GHz, two nulls are observed on the dipole, indicating radiation in the third-order mode. In the third-order mode, the maximum current is concentrated on the stubs and the middle part of the dipole. The direction of current on the stubs and the middle part of the dipole is consistent, thereby enhancing the radiation characteristics of the dipole at the shifted third-order mode.

The simulated gain, efficiency, and radiation pattern of the antenna are illustrated in Fig. 9. The gain varies from 1.62 dBi to 2.57 dBi over the impedance bandwidth. Both radiation efficiency and total efficiency surpass 98% and 89%, respectively, across the entire impedance bandwidth. This indicates that the proposed antenna radiates effectively throughout the bandwidth.

Radiation patterns at the lowest, highest, and center frequencies are presented in Fig. 9b–d. The radiation pattern exhibits a figure-of-eight shape and omnidirectional

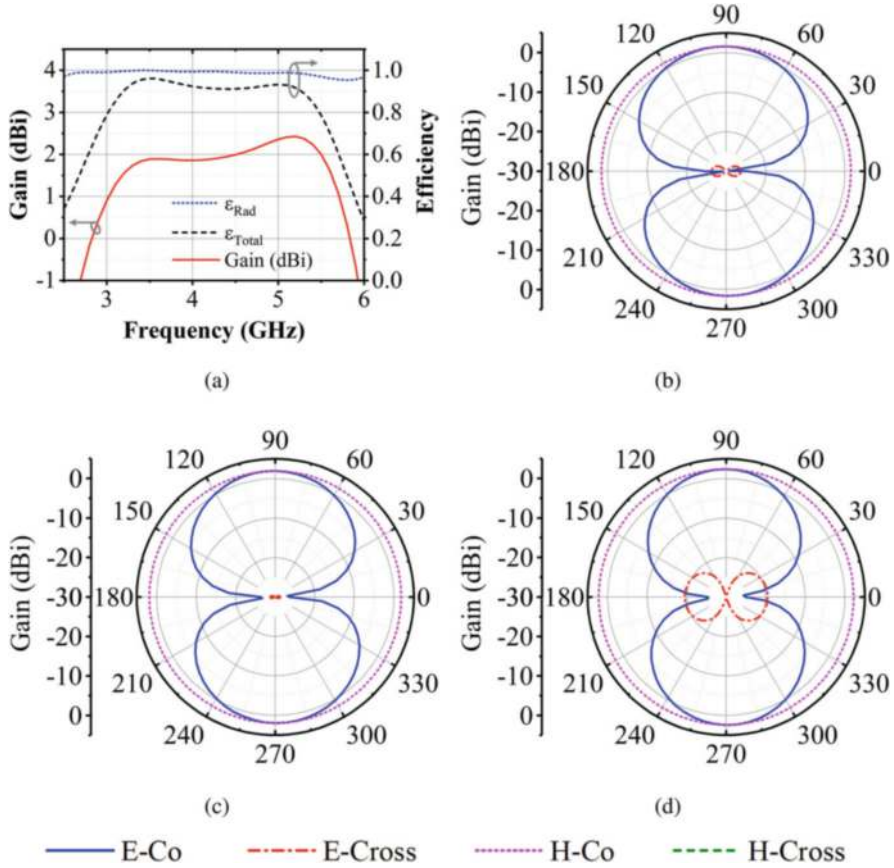


**Fig. 9** Simulated results of the stub-loaded dual-mode dipole antenna: (a) gain and efficiency plots and radiation patterns at (b) 3.2 GHz, (c) 4.25 GHz, and (d) 5.3 GHz

characteristics in the E- and H-planes, respectively, with cross-polarization levels below  $< -22$  dB over the bandwidth.

#### 4 Bent Stub-Loaded Dual-Mode Dipole Antennas

The stub-loaded dipole antenna discussed in Sect. 3.3 exhibits dimensions of  $35 \text{ mm} \times 21 \text{ mm}$ , which corresponds to approximately  $0.37\lambda_L \times 0.22\lambda_L$  at its lowest operating frequency. To enhance the antenna's compactness and reduce its width, two alternative configurations are proposed, employing bent stub loading technique as shown in Fig. 10. In both proposed configurations, labeled as Antenna 2 and Antenna 3, the basic dimensions of the dipole and the placement of the stubs remain

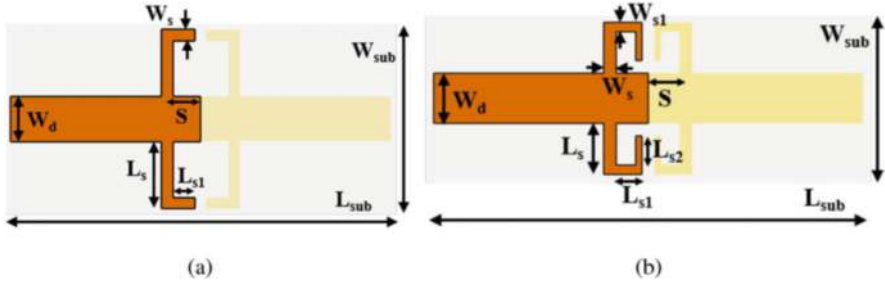


**Fig. 10** Bent stub-loaded dual-mode dipole antennas with (a) single bend (Antenna 2) and (b) double bends (Antenna 3)

consistent with the optimized design outlined in Table 1. For Antenna 2, the stub parameters are adjusted to achieve a reduction in width. By setting  $L_s = 6$  mm,  $L_{s1} = 2$  mm, and  $W_s = 1$  mm, the overall dimensions are reduced to 35 mm  $\times$  17 mm, marking a reduction of approximately 19% in width compared to the original design. Antenna 3 further optimizes the design by introducing additional modifications to the stub parameters. With  $L_s = 4$  mm,  $W_s = 1$  mm,  $L_{s1} = 2$  mm,  $W_{s1} = 0.75$  mm,  $L_{s2} = 2$  mm, and  $W_{s2} = 0.5$  mm, the antenna size is further reduced to 35 mm  $\times$  13 mm, achieving a notable 38% reduction in width compared to the original configuration (Fig. 4). An important aspect to highlight is that despite the variations in stub configurations and resulting antenna sizes, the total length of the stubs remains consistent across all designs, maintaining at 8 mm. This ensures that the performance of the antennas remains almost consistent while achieving the desired reduction in width.

The performance of Antennas 1, 2, and 3 is compared in Fig. 11. The first-order mode frequency remains almost identical across all three antennas due to the consistent dipole parameters. However, a slight shift in the third-order mode frequency is observed, attributable to variations in stub shape and width. The impedance bandwidths for Antennas 1, 2, and 3 are measured at 49.2% (3.2–5.29 GHz), 50.6% (3.22–5.40 GHz), and 52.8% (3.22–5.53 GHz), respectively. Despite these slight differences, the variation in gain over the respective impedance bandwidths remains approximately the same. Based on these observations, it can be concluded that the performance of Antennas 1, 2, and 3 is largely similar, with Antenna 3 exhibiting a slight advantage.

Figure 12 displays the current distribution of Antenna 3 at frequencies of 3.25 GHz and 5.0 GHz. At 3.25 GHz, the current exhibits a single half sinusoidal variation along the length of the dipole, indicative of the first-order mode. Conversely, at 5.0 GHz, the current distribution manifests three half sinusoidal variations or two nulls along the length of the dipole, characteristic of the third-order mode. Notably, the maximum current is observed on the stubs and the central portion of the dipole, with the direction of the currents aligned. This configuration effectively enhances

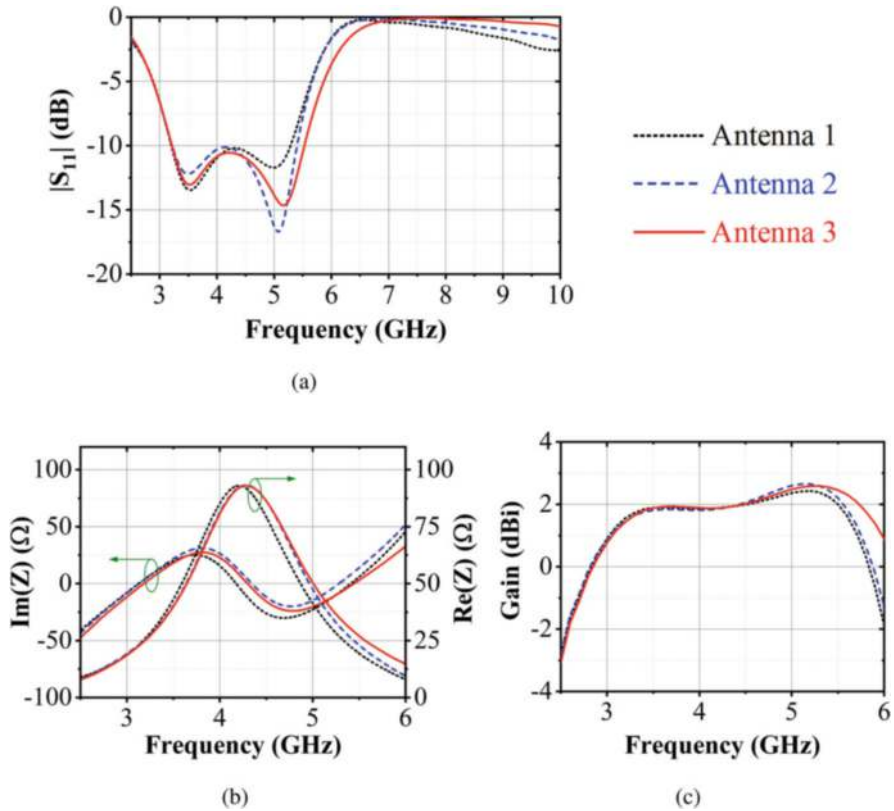


**Fig. 11** (a) Simulated  $|S_{11}|$ , (b) input impedance, and (c) gain plots of the stub-loaded dual-mode dipole antennas: Antennas 1, 2, and 3

the radiation characteristics of the dipole antenna at the shifted third-order mode frequency.

The simulated plots of efficiencies and radiation patterns of Antenna 3 are depicted in Fig. 13. The radiation efficiency and total efficiency exceed 96% and 87%, respectively, across the entire impedance bandwidth, indicating effective radiation performance throughout. Comparatively, the efficiency of Antenna 3 is slightly lower than that of Antenna 1, which may be attributed to the bending of the stubs. The radiation pattern is plotted at three frequencies: the lowest frequency  $f_L = 3.22$  GHz, the center frequency  $f_0 = 4.375$  GHz, and the highest frequency of operation for  $|S_{11}| \leq -10$  dB,  $f_H = 5.53$  GHz. The pattern exhibits a figure-of-eight shape in the E-plane and an omni pattern in the H-plane. It remains stable over the bandwidth, with cross-polarization levels of  $\leq -23$  dB.

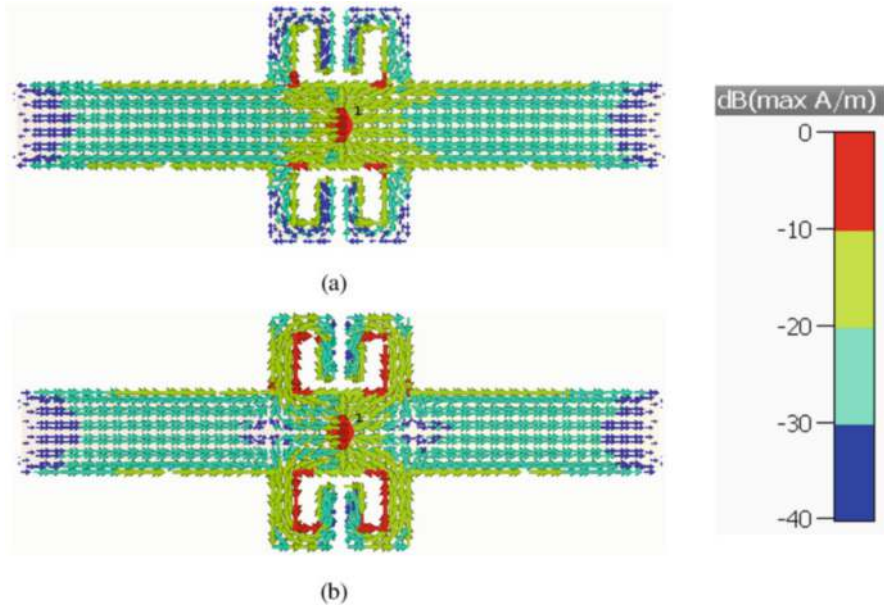


**Fig. 12** Surface currents of Antenna 3 at (a) 3.25 GHz, and (b) 5.0 GHz

## 5 Summary

In this chapter, we explore a technique aimed at compressing the third-order mode of a dipole antenna closer to its fundamental mode. Through this process, we introduce and discuss three configurations of wideband dual-mode dipole antennas. In the first configuration, a pair of symmetric stripline stubs is strategically loaded at the current null points of the third-order mode. We derive equations to calculate the optimal stub length and distance from the center of the dipole. These stub parameters effectively shift the third-order mode frequency without significantly impacting the fundamental frequency. As we vary the stub length, we observe a corresponding decrease in the third-order mode frequency, while the fundamental frequency remains relatively stable. Similar effects are noted when adjusting the stub width, while the third-order mode frequency increases as the stubs move away from the dipole center. The optimized stub-loaded dipole antenna resulting from this configuration exhibits an electrical size of  $0.37\lambda_L \times 0.22\lambda_L$ . It delivers a substantial 49.2% bandwidth, along with a peak gain of 2.6 dBi and cross-polarization levels lower than  $-22$  dB across the band. However, the introduction of stubs increases the overall width of the antenna. To address this, in configurations 2 and 3, we introduce single and double bends in the stubs, respectively, to effectively reduce the antenna's width. In the case of the double-bent stub-loaded dual-mode dipole antenna in configuration 3, we achieve an impressive 52.8% bandwidth, maintaining a peak gain of 2.6 dBi and cross-polarization levels lower than  $-23$  dB over the



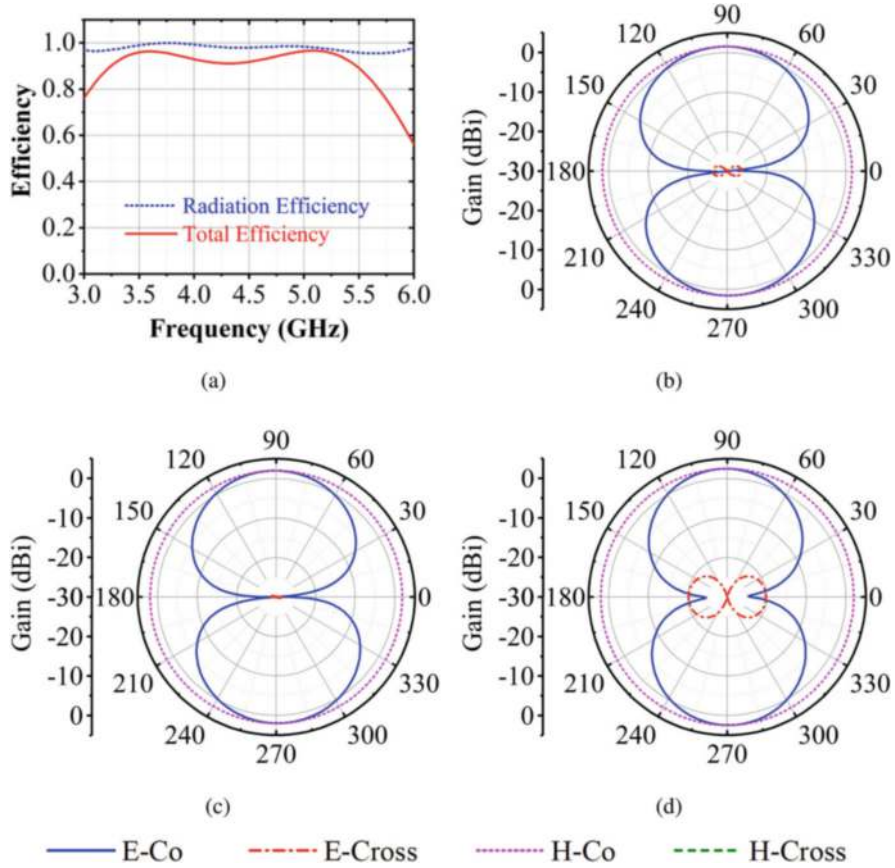


**Fig. 13** Simulated (a) efficiencies and radiation patterns of Antenna 3 at (b) 3.22 GHz, (c) 4.375 GHz, and (d) 5.53 GHz

band. This antenna possesses an electrical size of  $0.38\lambda_L \times 0.14\lambda_L$ , demonstrating a significant reduction in width (by approximately 38%) as compared to the initial stub loaded dipole antenna configuration.

## References

1. T. Olsson, H.E. Nilsson, Bow-tie and dipole antenna feed robustness mechanisms. *IEEE Antennas Wirel. Propag. Lett.* **5**(1), 163–167 (2006)
2. W.S. Yeoh, K.L. Wong, W.S.T. Rowe, Wideband miniaturized half bowtie printed dipole antenna with integrated balun for wireless applications. *IEEE Trans. Antennas Propag.* **59**(1), 339–342 (2011)
3. J. Lu, S. Lin, Y. Tian, L. Jing, M. Liu, Z. Zhao, The simulation and experiment of a UWB printed dipole antenna. *Prog. Electromagn. Res. Lett.* **36**, 21–30 (2013)



4. B. Feng, S. Li, W. An, S. Yin, J. Li, T. Qiu, U-shaped bow-tie magneto-electric dipole antenna with a modified horned reflector for ultra-wideband applications. *IET Microwaves Antennas Propag.* **8**(12), 990–998 (2014)
5. S.X. Ta, H. Choo, I. Park, Broadband printed-dipole antenna and its arrays for 5g applications. *IEEE Antennas Wirel. Propag. Lett.* **16**, 2183–2186 (2017)
6. R. Wu, Q.X. Chu, Resonator-loaded broadband antenna for LTE700/GSM850/GSM900 base stations. *IEEE Antennas Wirel. Propag. Lett.* **16**, 501–504 (2017)
7. D. Wen, Y. Hao, H. Wang, H. Zhou, Design of a wideband antenna with stable omnidirectional radiation pattern using the theory of characteristic modes. *IEEE Trans. Antennas Propag.* **65**(5), 2671–2676 (2017)
8. W.J. Lu, J. Yu, L. Zhu, On the multi-resonant antennas: Theory, history, and new development. *Int. J. RF Microwave Comput. Aided Eng.* **29**(9), e21808 (2019)
9. A.T. Mobashsher, A. Abbosh, Slot-loaded folded dipole antenna with wideband and unidirectional performance for L-band applications. *IEEE Antennas Wirel. Propag. Lett.* **13**, 798–801 (2014)
10. W. Hu, X. Liu, S. Gao, L. Wen, Q. Luo, P. Fei, Y. Yin, Y. Liu, Compact wideband folded dipole antenna with multi-resonant modes. *IEEE Trans. Antennas Propag.* **67**(11), 6789–6799 (2019)
11. S. Shadrokh, Y.Q. Yu, F. Jolani, Z. Chen, Ultra compact end-loaded planar dipole antenna for ultra-wideband radar and communication applications. *Electron. Lett.* **50**(21), 1495–1496 (2014)
12. W.J. Lu, L. Zhu, Planar dual-mode wideband antenna using short-circuited-strips loaded slotline radiator: Operation principle, design, and validation. *Int. J. RF Microwave Comput. Aided Eng.* **25**(7), 573–581 (2015)
13. W.J. Lu, L. Zhu, Wideband stub-loaded slotline antennas under multi-mode resonance operation. *IEEE Trans. Antennas Propag.* **63**(2), 818–823 (2015)
14. N.W. Liu, L. Zhu, W.W. Choi, A differential-fed microstrip patch antenna with bandwidth enhancement under operation of TM<sub>10</sub> and TM<sub>30</sub> modes. *IEEE Trans. Antennas Propag.* **65**(4), 1607–1614 (2017)
15. Z. Gan, Z.H. Tu, Dual-mode conjoint patch-pair for 5G wideband patch antenna array application. *IEEE Antennas Wirel. Propag. Lett.* **20**(2), 244–248 (2021)
16. W. Zhang, Y. Li, Z. Zhou, Z. Zhang, Dual-mode compression of dipole antenna by loading electrically small loop resonator *IEEE Trans. Antennas Propag.* **68**(4), 3243–3247 (2020)
17. R. Solanki, Compact and broadband dual-mode dipole antenna. *Prog. Electromagn. Res. Lett.* **106**, 21–29 (2022). <https://doi.org/10.2528/PIERL22060102>
18. R. Solanki, S. Moharir, Compact and broadband loop-loaded dual-mode dipole antenna. *IETE J. Res.* (2023). <https://doi.org/10.1080/03772063.2023.2210091>
19. Y. Shi, J. Liu, Investigation of a via-loaded microstrip magnetic dipole antenna with enhanced bandwidth and gain. *IEEE Trans. Antennas Propag.* **67**(7), 4836–4841 (2019)
20. Y. Luo, Z.N. Chen, K. Ma, Enhanced bandwidth and directivity of a dual-mode compressed high-order mode stub-loaded dipole using characteristic mode analysis. *IEEE Trans. Antennas Propag.* **67**(3), 1922–1925 (2019)
21. Y. Luo, X. Ma, N. Yan, W. An, K. Ma, Sidelobe suppression of dual-mode compressed high-order-mode dipole by loading bent stubs. *IEEE Antennas Wirel. Propag. Lett.* **20**(6), 898–902 (2021)
22. R. Solanki, Stub loaded dual-mode dipole antenna for wide bandwidth in a compact size, in *2022 IEEE Microwaves, Antennas, and Propagation Conference (MAPCON)*, Bangalore, India, 2022, pp. 923–927. <https://doi.org/10.1109/MAPCON56011.2022.10047301>
23. H. Li, Y. Li, Mode compression method for wideband dipole antenna by dual-point capacitive loadings. *IEEE Trans. Antennas Propag.* **68**(8), 6424–6428 (2020)
24. R. Solanki, Third- and fifth-order mode compression of a dipole antenna. *IEEE Trans. Antennas Propag.* **70**(12), 12294–12298 (2022). <https://doi.org/10.1109/TAP.2022.3209649>

# Multiple Resonator–Loaded Electrically Small Antennas for Wireless Devices



Jyotibhusan Padhi and G. Shrikanth Reddy

## 1 Introduction

Electrically small antennas (ESAs) possess several inherent characteristics, such as compact size, cost-effectiveness, lightweight design, and ease of integration [1]. Due to these benefits, ESAs are widely preferred for integration into miniaturized wireless devices, including mobile phones, laptops, routers, dongles, indoor base stations, biomedical sensors, RFID technology, and various other Internet of Things (IoT)-enabled devices [2–4]. Several techniques, like reactive element loading, metamaterial-inspired structures loading, and external matching circuit loading techniques, have been reported in the literature to design ESAs. Although these techniques are useful, they have some limitations, such as scalability issues, dependence on the ground plane, complicated designs, etc. In addition, it is very challenging to incorporate multiple reactive elements and external matching circuits with antennas without increasing their overall surface area while maintaining low-quality factors, acceptable bandwidth, gain, efficiency, etc. This thesis explores the scalable techniques to mitigate the above challenges for designing multiband/wideband efficient electrically small antennas while maintaining a small surface area [4–6]. This chapter discusses multiple stub resonators [4], parasitic resonators, and [5] loading techniques to design single/multiband/wideband ESAs. The method proposed in this chapter enables a 50% reduction in the electrical size of the antenna. Configurations presented in this chapter are characterized by adopting fundamental properties of electrically small antennas, as discussed in [7–17]. All antennas proposed meet Chu’s criteria for an ESA, i.e., electrical size  $K \times a < 1$ .

---

J. Padhi · G. S. Reddy (✉)

School of Computing and Electrical Engineering, Indian Institute of Technology Mandi, Mandi, Himachal Pradesh, India

e-mail: [gopishrikanth@iitmandi.ac.in](mailto:gopishrikanth@iitmandi.ac.in)

Prototypes of all the proposed antennas were fabricated to validate the theoretical design techniques and their outcomes, and the measure results were verified with theoretical analysis. All the measured/experimental results match well with the theoretical results, which validate the proposed techniques.

## 2 Multiple Stub Resonator–Loaded Triple-Band Electrically Small Antenna

In this section, a compact triple-band electrically small antenna (ESA) is designed to cater sub-6 GHz 5G NR band applications, namely, n78 (3.3 GHz to 3.8 GHz) band or n77 (3.3 GHz to 3.4 GHz) band, mobile WiMAX band (IEEE 802.16e), and DCS1800 MHz band. To design the proposed antenna, a simple impedance matching technique through stubs is used, which is easy to fabricate and scalable.

### 2.1 Design of Compact Triple-Band Antenna

This section discusses the design process of multiple stub–loaded triple-band ESA. The proposed antenna consists of a bent monopole with added stub/resonator to achieve triple-band responses. In this work, fundamental limits of an ESA, as discussed in [7–9], are considered to evaluate the performance of the proposed antenna. Theoretical and experimental analyses are used to characterize the proposed antenna and ensure its suitability for wireless device.

#### 2.1.1 Designs to Achieve Resonance Within the DCS Band

The antenna presented in Fig. 1a is a basic printed monopole whose length is nearly quarter wavelength corresponding to 1.825 GHz. The resonance within the desired DCS band is achieved through three stage design process as discussed below. The proposed antenna is designed on a 1.6-mm-thick FR-4 substrate with loss tangent ( $\tan \delta$ ) of 0.025 and dielectric constant ( $\epsilon_r$ ) = 4.3. Here, a 50- $\Omega$  CPW transmission line is used as a feed line for all the configurations shown in Fig. 1. The surface area of antenna\_1 with CPW feed is  $50 \times 12.08 \text{ mm}^2$ .

To reduce the overall size of the antenna, in the next stage, Antenna-1 is bent at five locations to reduce its surface area, as shown in Fig. 2. Here, the electrical length of the bent is nearly equal to the quarter wavelength at 1.825 GHz. It can be seen in Fig. 2 that though the bending has reduced the surface area of the monopole, it disturbed impedance characteristics at the desired frequency band. It can be seen in the impedance response in Fig. 2b; point “B” represents the inductive behavior.

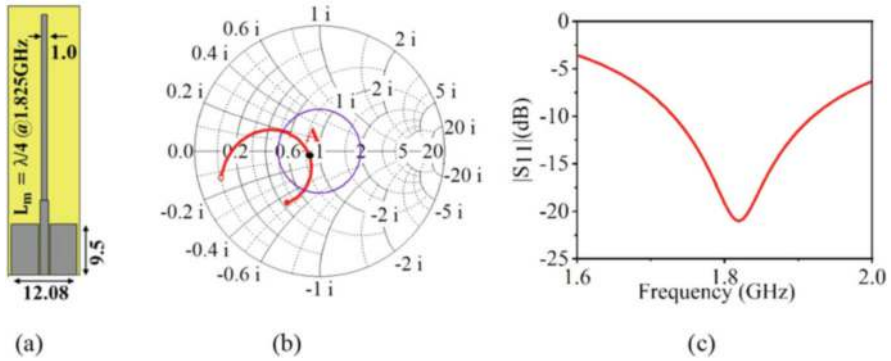


**Fig. 1** Basic printed monopole (Antenna-1). (a) Structure representation, (b) impedance response 1.5–2 GHz, (c) simulated  $|S_{11}|$  response (all dimensions are in mm)

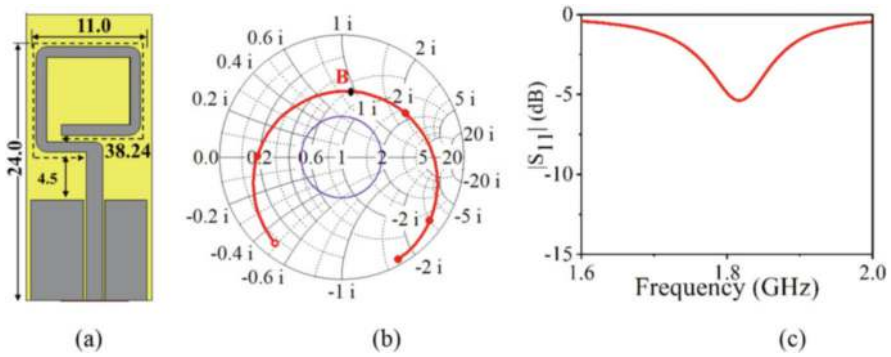


**Fig. 2** Bent monopole (Antenna-2). (a) Structure representation, (b) impedance response 1.5–2 GHz, (c) simulated  $|S_{11}|$  response (all dimensions are in mm)

To improve the impedance response at 1.825 GHz, an impedance matching technique as discussed in [18, 19] is implemented. In stage 3, to nullify the inductive impedance, an appropriate stub length is calculated, and correspondingly, a meander line (stub-1) of length  $L_{m1} = 8.35$  mm ( $0.05\lambda$ ) is added in series with the feed line of Antenna-2 as shown in Fig. 3a.

The meander line stub-1 of length ( $L_{m1}$ )  $0.05\lambda$  is responsible for the movement of impedance points from B to C as shown in Fig. 3b. The meander line of length  $0.05\lambda$  also corresponds to a minimum possible distance between impedance point B and a position/location on the Smith chart, which lies on unity impedance circle. Considering dimensional constraints, the initial width of the meander line is kept as  $W_2 = 0.28$  mm. The impedance response of the proposed antenna in stage 3 depicts that the input impedance of the antenna is  $51 + j64 \Omega$ . It can be observed from Fig. 3b that the impedance response for Antenna-3 at 1.825 GHz is inductive and still far from the unity impedance point (D). To get impedance matching, a shunt stub (inverted L-shaped stub) is used to move impedance point C to D. The

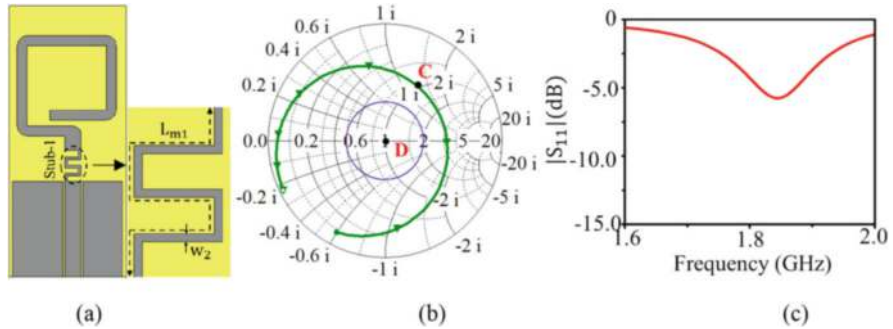


**Fig. 3** Bent monopole with meander line stub (Antenna-3). (a) Structure representation, (b) impedance response 1.5–2 GHz, (c) simulated  $|S_{11}|$  response (all dimensions are in mm)

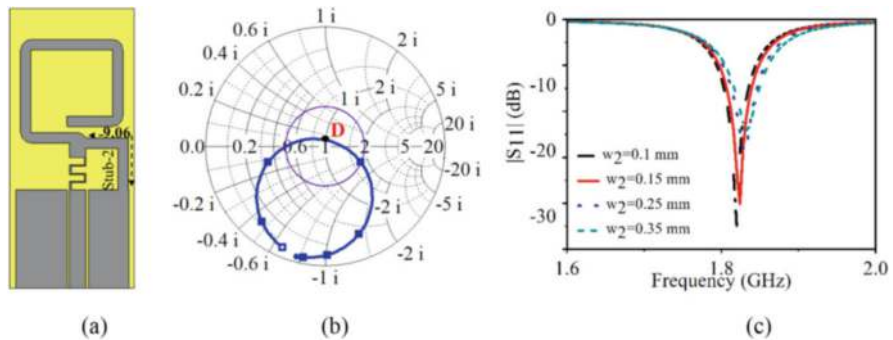


**Fig. 4** Bent monopole with shunt stub (stub-2) (Antenna-4): (a) structure representation, (b) impedance response 1.5–2 GHz, (c) simulated  $|S_{11}|$  response for different width of meander line  $W_2$  (all dimensions are in mm)

proposed stub of length  $0.055\lambda$  (9.06 mm) is loaded between the ground plane and the bended monopole to minimize inductive reactance as shown in Fig. 4a, b. The antenna configuration along with two stubs is termed as Antenna-4. The gaps between successive turns in the meander line are optimized to tune the impedance response at 1.825 GHz, as shown in Fig. 4c. It is observed that the capacitive effect increases by increasing the line width ( $W_2$ ) of the meander line ( $L_{m1}$ ). This effect aids to fine-tune the impedance response at 1.825 GHz.

### 2.1.2 Design to Achieve Resonance at WiMAX and 5G New Radio-n77/n78 Bands

The impedance characteristic of Antenna-4 is further analyzed to seek possibilities of a multiband response. The admittance chart presented in Fig. 5 indicates that an open-ended stub, i.e., stub-3, is suitable for achieving impedance matching at

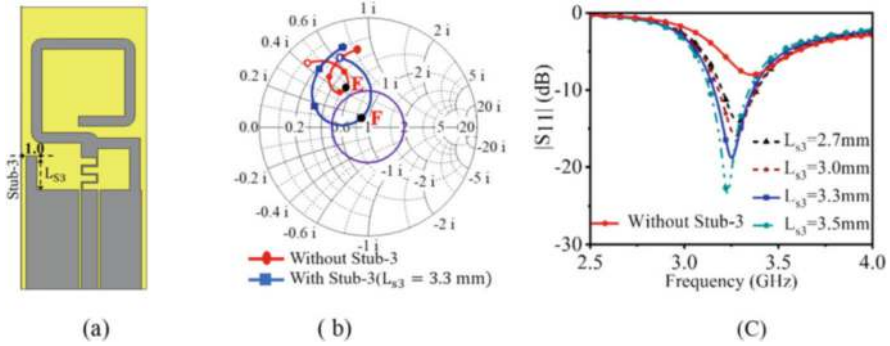


**Fig. 5** Bent monopole with open-circuited stub (stub-3) (Antenna-5). (a) Structure representation, (b) impedance response 2.5–4 GHz with and without stub-3, (c) simulated  $|S_{11}|$  response for different stub length  $L_{S3}$  (all dimensions are in mm)

3.3 GHz. Admittance curves E and F (Fig. 5) present the effects of adding the stub-3 with the antenna. Here, the initial length of stub-3 is calculated through a similar process used for stub-1 and stub-2. The length for stub-3, i.e.,  $L_{S3}$ , is further optimized to tune the impedance bandwidth as shown in Fig. 5.

Further, another resonator is added (or branched) at the space inside the bent structure as shown in Fig. 6a, to achieve additional resonance intended at 3.58 GHz. The impedance for Antenna-5 at 3.58 GHz (referring to point G in Fig. 6b) is  $18.4 + j7.6\Omega$ , which indicates an unmatched condition. Hence, by using the transmission line equivalence-stub matching technique as discussed in [20, 21], an inductive meander line ( $L_{m2}$ ) of length  $\cong 0.106\lambda$  in series with a capacitive rectangular patch of perimeter  $\cong 0.116\lambda$  is loaded (branched) with bent monopole to achieve impedance matching at 3.58 GHz band. This addition brought the impedance point of 3.58 GHz from G to H, as shown in Fig. 6b (point H). As shown in Fig. 6a, the rectangular patch (capacitive stub) is arranged to facilitate fringing capacitances between the edges of the rectangular patch and the bent monopole. As a result, the proposed antenna shows good impedance matching at the 3.58 GHz band. The lower frequency of the desired operating band  $f_L$  is approximated by using the dimensional values of  $W_S$  and  $L_S$  as given in Eq. 1, where  $C$  is the speed of light in free space and  $W_S$  and  $L_S$  are the dimensions of the capacitive stub.

$$f_L \cong \frac{C}{4 \left[ L_{m2} + 2(L_S + W_S) \right]} \quad (1)$$

The effect of  $W_S$  on the third resonance of Antenna-6 is summarized in Table 1. It is observed that the third resonant frequency shifts toward the lower bound with the increase in the width of the capacitive stub ( $W_S$ ).

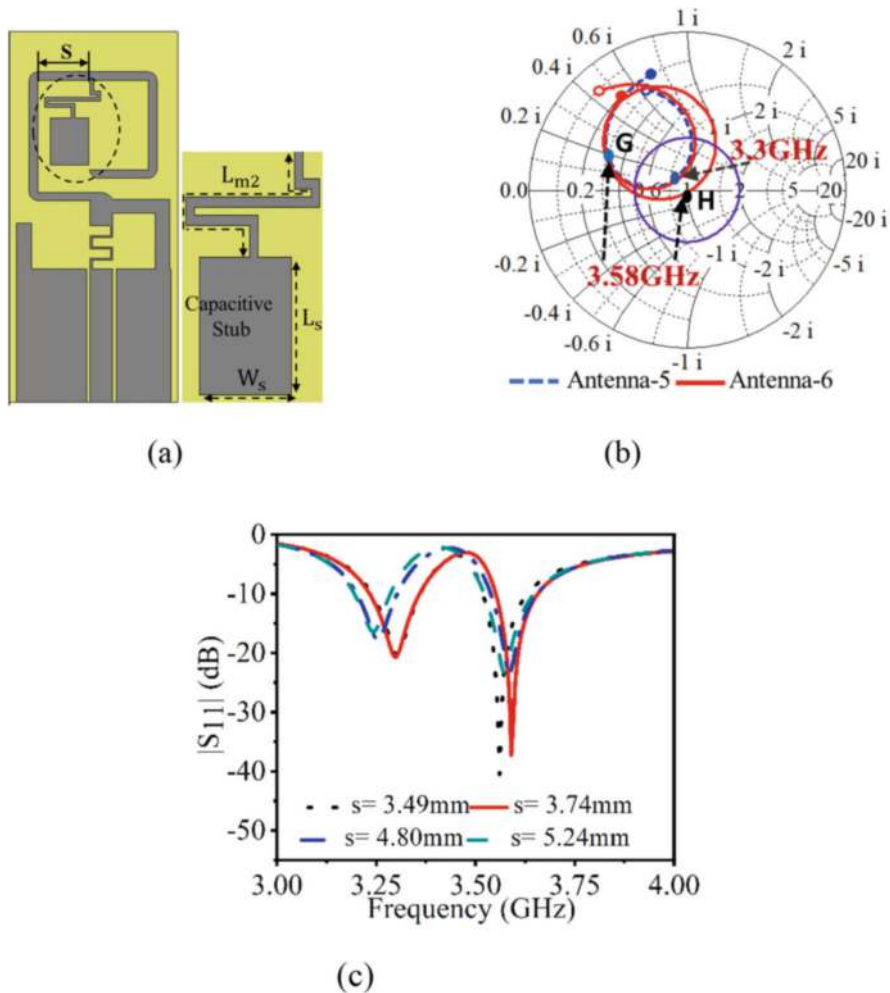


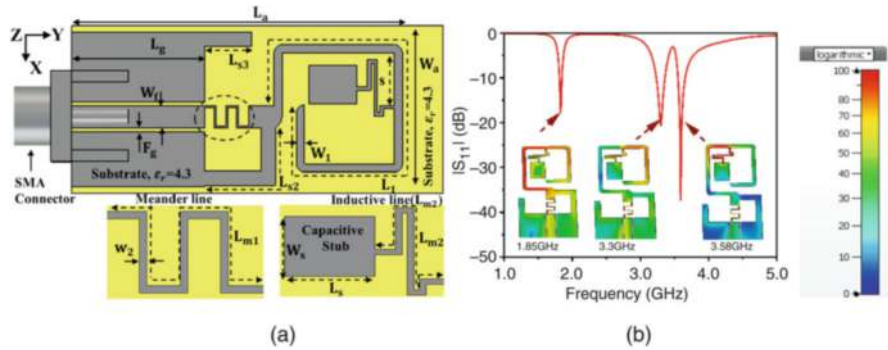
**Fig. 6** Bent monopole loaded with inductive meander line and capacitive resonator (Antenna-6). (a) Structure representation, (b) impedance response 2.5–4 GHz, (c) simulated  $|S_{11}|$  response for different values of “ $S$ ” (all dimensions are in mm)

As shown in Fig. 6, the third resonator is placed at a distance  $S = 3.74$  mm such that it does not affect the first and or second operating band(s). However, it can be seen in Fig. 6c that there is a slight shift in the resonance point for the second and third frequency bands. The offset in the resonance point is attributed to the change in the real part of the impedance response, especially for the bent monopole. Hence, the width of the bent monopole is reduced from 1 mm to 0.6 mm to optimize the real value of impedance.



**Table 1** Comparison of third resonance for different values of “ $W_S$ ”

$L_S$ (mm)	$W_S$ (mm)	$L_{m2} + 2(L_S + W_S)$	$f_L$ (GHz) for third resonance
3.36	1.25	18.15	4.0
3.36	1.75	19.15	3.85
3.36	2.25	20.15	3.695
3.36	2.75	21.15	3.55

**Fig. 7** Multiple stub–loaded ESA: (a) complete structural layout and (b) simulated  $|S_{11}|$  response and surface current distribution

## 2.2 Working Principle of Multiple Stub–Loaded Triple-Band ESA

The working principle of the proposed antenna is further analyzed by observing the surface current distribution. The simulated impedance response of the antenna with the corresponding current distribution is presented in Fig. 7. It can be observed from the current distribution that quarter-wavelength bent metallic strip along with stub-1 and 2 is responsible for the resonance at the DCS1800 band. Here, stub-1 and stub-2 are the matching elements for first resonance at 1.8 GHz band. The current on the rightmost part of the metallic strip corresponds to the first harmonic at 3.3 GHz, as shown in Fig. 7b, where the open-ended stub (i.e., stub 3) adds the capacitance to the input impedance of the antenna to generate matched response over the 3.3 GHz band. In addition, the capacitive stub-loaded meander line structure provides resonance at a higher operating band, i.e., at 3.58 GHz. The electrical length of the capacitive stub-loaded meander line is  $[2(L_S + W_S) + L_{m2}] \cong \lambda/4$ , where  $\lambda$  is the wavelength corresponding to 3.58 GHz. It can be observed that the achieved bandwidths for respective bands are acceptable for DCS1800-, WiMAX-, and 5G NR (n77, n78)-based wireless applications. All the optimized dimensions of the proposed antenna, which sufficiently cater for the impedance-matching requirements for triple band operation, are given in Table 2. It can be observed from the optimized dimensional values that the length of the final proposed



**Table 2** Optimized dimensions of proposed multiple stub-loaded ESA

Name	Value (mm)	Name	Value (mm)	Name	Value (mm)
$L_a$	24	$L_1$	31.8	s	3.74
$W_a$	11	$W_1$	0.6	$w_2$	0.15
$W_f$	1.6	$L_{S2}$	9.06	$F_g$	0.25
$L_{S3}$	3.3	$W_S$	2.75	$L_g$	9.9
$L_{m1}$	8.35	$L_{m2}$	8.93	$L_S$	3.36

antenna shown in Fig. 7 is almost 50% less compared to Antenna-1. The overall surface area of the proposed antenna is suitable for a wireless dongle or small router devices.

### 2.3 Compact Triple-Band ESA: Impedance and Radiation Characteristics Measurements

To validate the theoretical analysis, a prototype of the proposed antenna is fabricated using (on) FR\_4 substrate of 1.6 mm thickness. The overall dimension of the fabricated antenna is  $24 \times 11 \times 1.6 \text{ mm}^3$ . The fabricated prototype is tested for its reflection parameter response, radiation characteristics, antenna gain, and efficiency characteristics. The  $S_{11}$  response of the fabricated antenna is measured using N5232B PNA Network Analyzer in an anechoic chamber, as shown in Fig. 8a. It can be observed from Fig. 8b that the proposed antenna offers -10 dB impedance bandwidth of 30 MHz (1.8 GHz to 1.83 GHz) for the first band, 200 MHz (3.18 GHz to 3.38 GHz) for the second band, and 240 MHz (3.47 GHz to 3.71 GHz) for third band. It is also noted that for  $VSWR \leq 3$ , the measured impedance bandwidths are 151 MHz (1.699–1.85 GHz) for the DCS1800 band and 810 MHz (3.06–3.87 GHz) for the 3.3 GHz band.

The proposed ESA(AUT) is tested for its radiation pattern characteristics and antenna gain in an anechoic chamber environment at a far field distance, as shown in Fig. 8a. The current distribution presented in Fig. 7 indicates that the surface current on the loop structure (i.e., on the bent monopole) induces a strong magnetic field in the XZ plane, whereas the strength of the electric field is maximum in the XY plane. As a result, the proposed antenna offers an omnidirectional radiation pattern in the XZ plane and a monopole-type pattern in the XY plane shown in Fig. 9.

The current distribution in correlation with radiation characteristics indicates that the proposed antenna is linearly polarized for all bands and suitable for applications like DCS, WiMAX, and 5G communication. The bent monopole exhibits  $\lambda/4$  resonance at 1.825 GHz, and first harmonic is observed at 3.3 GHz as shown in Fig. 7b. Divergence in current distribution and filed distribution at 1.825 GHz and 3.3 GHz leads to a shift in phase center, and the maxima and minima of the radiation pattern of the proposed antenna at 3.3 GHz are not aligned with the radiation pattern

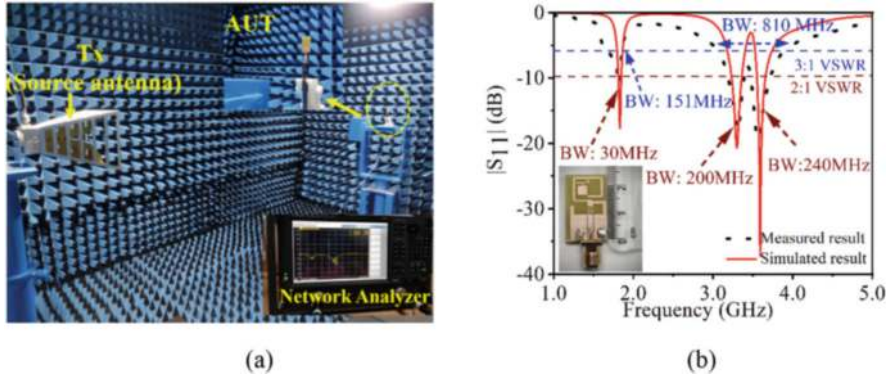


**Fig. 8** Multiple stub–loaded ESA: (a) measurement setup and (b) measured reflection coefficient response ( $|S_{11}|$ ) and fabricated prototype

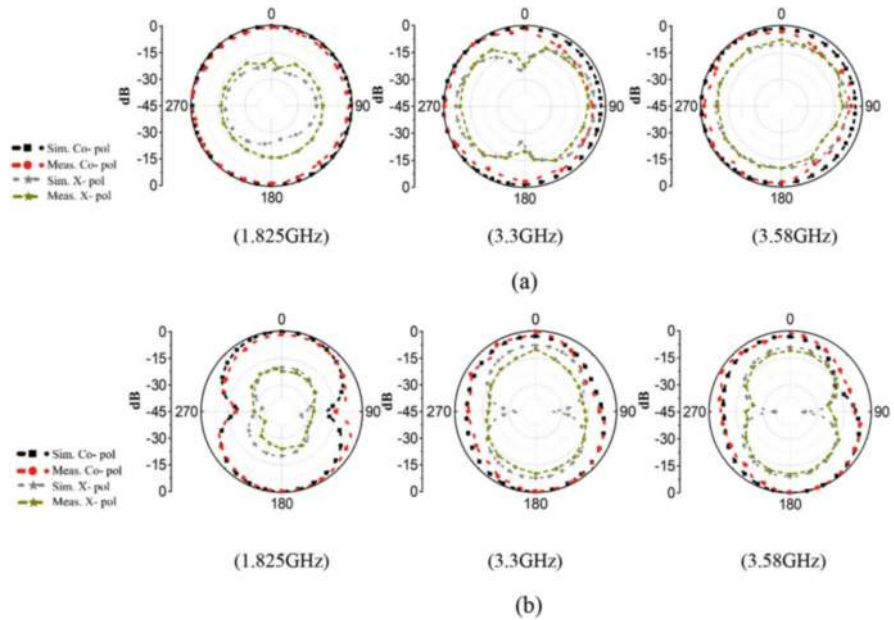
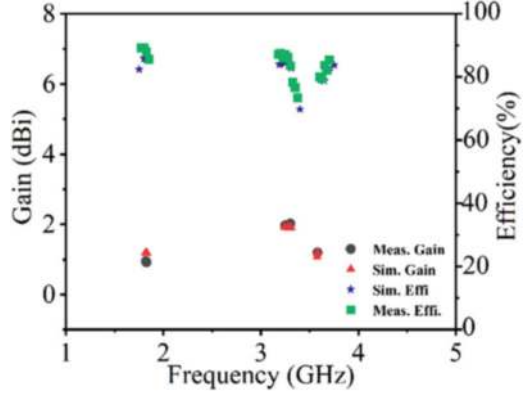


**Fig. 9** Measured radiation pattern multiple stub–loaded ESA in (a) XZ and (b) XY plane

observed at 1.825 GHz. Likewise, for 3.58 GHz, the position of the resonator and orientation of the current lead to maximum radiation in the -XY plane. From surface current distribution, it is observed that the magnitude of the X-axis-oriented current (at the top edges of the CPW structure) is less at all resonating modes. Hence, a low-cross-pol level is maintained below  $-15$  dB in the direction of maxima at all resonant frequencies. The measured gain and efficiency of the proposed antenna are presented in Fig. 10. This antenna exhibits gain of 0.95dBi, 1.92dBi, and 1.2dBi at

**Fig. 10** Simulated and measured gain (dBi) and radiation efficiency of multiple stub-loaded ESA



1.825 GHz, 3.3 GHz, and 3.58 GHz, respectively, whereas the maximum radiation efficiency of the antenna is 88%, 83%, and 80% over the operating bandwidth(s). It is noted that the proposed antenna's measured gain and efficiency characteristics are sufficient to cater to the radiation requirements at desired frequency bands.

Further, the proposed antenna is subjected to the dimensional limits of ESA, as reported in [7–17]. It is observed that at 1.825 GHz, the free space wave number, i.e.,  $K = 0.038$  rad/mm, whereas the radius of the smallest radian sphere “ $a$ ” is 13.2 mm. Hence, at 1.825 GHz, the value of  $K \times a = 0.5$ . Similarly, the values of  $(K \times a)$  at 3.3 GHz and 3.58 GHz are 0.9 and 0.97, respectively. The calculated value of “ $K \times a$ ” for all the intended frequency bands is less than “1,” indicating that the proposed antenna can be classified as an electrically small antenna (ESA). This antenna's estimated lower-bound quality factor ( $Q_{lb}$ ) is 8.8, 34, and 817 for 1.825 GHz, 3.3 GHz, and 3.58 GHz bands, respectively. The proposed multiple stub-loaded ESA is a highly miniaturized antenna. Hence, the quality factor for ESAs is usually high over the intended bands, and the same is reported for antennas with reduced electrical dimensions [7–17]. Due to this, the impedance bandwidth of the ESA of miniaturized antennas is low. However, the design technique ensured that the radiation efficiency at the intended bands remained high.

### 3 Multiple Resonator–Loaded Wideband ESA

In this section, efficient parasitic element-loaded electrically small antenna is discussed. Here, ESA is designed to cover 2.4 GHz Bluetooth/Wi-Fi, 5G new radio (n79), and 5 GHz WLAN band. Another important purpose of this work is to demonstrate that a wideband electrically small antenna can be designed by merging two adjacent resonating modes within a single passband. The design of the parasitic element-loaded configuration is flexible enough to be scaled for the desired frequency band and to provide frequency reconfigurability by means of integrating the antenna with parasitic elements. This work discusses an electrically

small antenna loaded with a parasitic loop resonator for dual-band and wideband operations. The antenna consists of a parasitic loop resonator, a driven element, and open-ended stubs. Here, the dimensional parameter of the open-ended stub plays a crucial role in impedance matching independently at the 5 GHz WLAN band, whereas the loop resonator is parasitically coupled with the driven element to achieve resonance at the lower frequency at 2.4 GHz. In this section, the design process of the antenna is discussed in multiple stages. The antenna is designed on an FR4 substrate, and it is theoretically analyzed using CST microwave studio. The proposed antenna offers an impedance bandwidth at 2.4 GHz and 4.3–5.8 GHz frequency bands with an efficiency of more than 80%.

### 3.1 Compact Antenna for 5 GHz WLAN Band

A CPW feed printed monopole is designed for 5.4 GHz at the initial stage, as shown in Fig. 11. This printed monopole is designed on the 1.6-mm-thick FR-4 substrate with a dielectric constant( $\epsilon_r$ ) and loss tangent( $\delta$ ) of 4.3 and 0.025, respectively. For reference, the conventional printed monopole is termed as Antenna-0.

#### 3.1.1 Tuning Impedance for 5 GHz WLAN Band

The monopole (Antenna-0) is remodeled to an inverted “L” shape as shown in Fig. 12a. This type of arrangement can induce a fringing field and extend beyond the top edge of the structure along the Y-axis. So, the proposed inverted L-shaped structure can be used further to excite (drive) another parasitic resonator. Here, the electrical length of the inverted L-shaped monopole is kept at approximately quarter-wavelength to achieve resonance at 5.4 GHz. The width of the projection

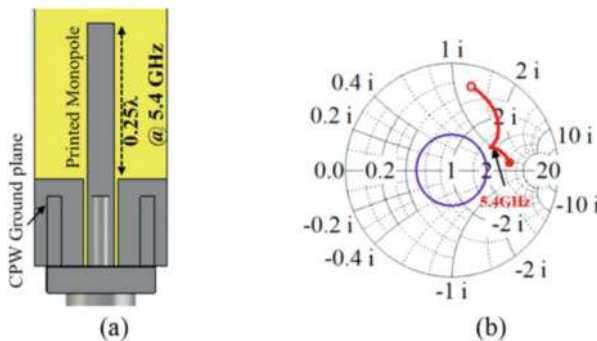


**Fig. 11** CPW feed printed monopole antenna. (a) Structural representation of Antenna-0, (b) impedance response 4 GHz to 6 GHz of conventional monopole (Antenna-0)

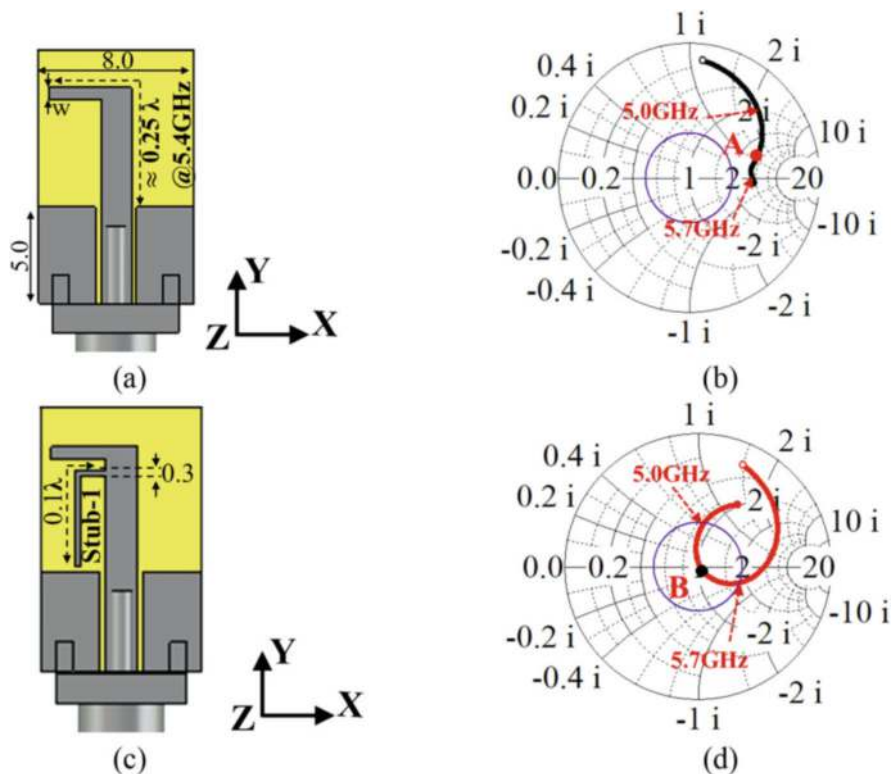


**Fig. 12** Inverted L-shaped monopole: (a) structure of Antenna-1, (b) impedance response of Antenna-1, (c) L-shaped monopole with stub (Antenna-2), and (d) impedance response of Antenna-2

in the driven element is kept narrow, as shown in Fig. 1b, to maintain maximum current(excitation) along the edges of the driven element.

The impedance response of Antenna-1, as shown in Fig. 12b, indicates that it is highly inductive over the 5.0–5.7 GHz band. Here, the impedance response is improved (or inductive reactance reduced) by attaching an open-circuited stub (stub-1) of length  $6.3 \text{ mm} = 0.1\lambda$  (where  $\lambda$  corresponds to the wavelength of 5.4 GHz frequency). The stub is added in series with the antenna to bring the impedance of 5.4 GHz from position A to B, as shown in Fig. 12c, d. This configuration with an open stub is termed as Antenna-2.

### 3.2 Dual-Band Compact ESA (Antenna-2)

To introduce another operating band to Antenna-2, a parasitic element is loaded with the proposed antenna, as shown in Fig. 13. The quarter-wavelength parasitic

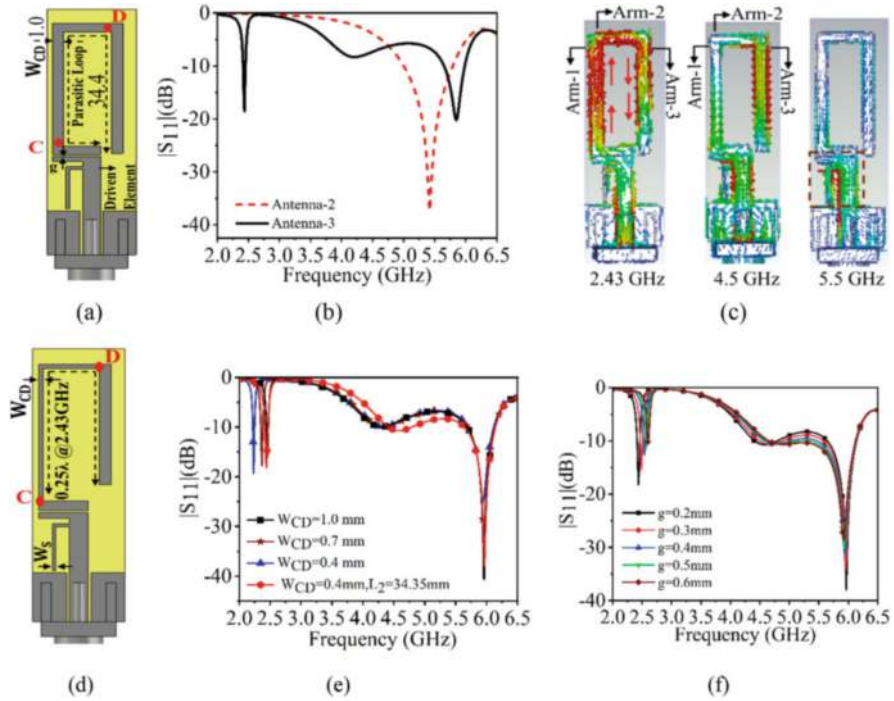


**Fig. 13** Parasitic loop–loaded ESA (Antenna-3): (a) structural geometry; (b) simulated  $|S_{11}|$  response; (c) surface current distribution at 2.43 GHz, 4.5 GHz, and 5.5 GHz; (d) ESA with modified loop (Antenna-4); (e)  $|S_{11}|$  response for different value of  $W_{CD}$ ; and (f)  $S_{11}$  response for different value of  $g$

loop resonator is capacitively coupled (or loaded) with a driven element to achieve an additional resonance within the 2.4 GHz–2.48 GHz ISM band with an impedance bandwidth of 48 MHz. This configuration is termed Antenna-3. Figure 13b shows that after adding a parasitic loop, the resonant frequency/impedance bandwidth is observed within the 5 GHz band, whereas an additional resonating mode (harmonic of the first band) appears near the 4.5 GHz. The resonating behavior of Antenna-3 is further analyzed through surface current distribution at different frequencies.

The surface current distributions shown in Fig. 13c are re-analyzed to understand the operating mechanism. It indicates that the quarter-wavelength parasitic loop resonator provides resonance at two frequencies, one at 2.43 GHz and another at 4.5 GHz. The surface current distribution also indicates that at 2.43 GHz, the surface current at arm-1 is  $180^\circ$  out of phase to the current at arm-3, leading to current cancellation at the desired operating band. To minimize current cancellation, the spacing between arm-1 and arm-3 is increased by reducing the width for arm-1 and arm-2. Here, the width “ $W_{CD}$ ” (for arm-1 and arm-2) within Antenna-3 is reduced to 0.4 mm, as shown in Fig. 13d. It can be observed from Fig. 13e (the  $S_{11}$  response) that with the reduction of  $W_{CD}$ , the resonance at 2.4 GHz band shifts further to a



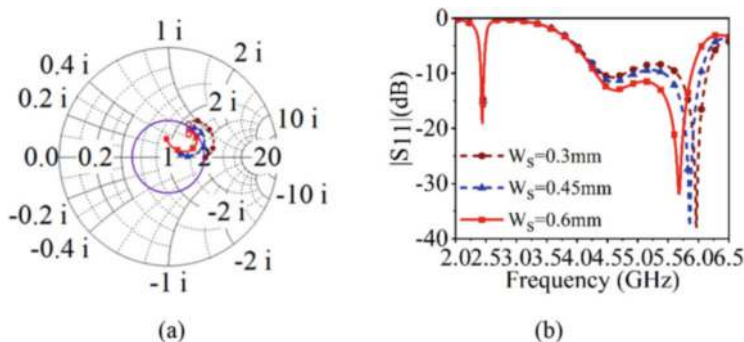


**Fig. 14** Parasitic element-loaded ESA (Antenna-4) for different stub widths ( $W_s$ ). (a) Smith chart-impedance response from 4.5 to 5.6 GHz and (b) simulated  $|S_{11}|$  response from 2 to 6 GHz

lower bound. To maintain resonance within the 2.4 GHz WLAN band, the length of the loop resonator ( $L_2$ ) is considered to be 30.45 mm. The  $|S_{11}|$  response for different values of gap “ $g$ ” is also analyzed to observe its effects on 2.4 GHz band. It is observed from Fig. 13f that a strong capacitive coupling exists between the parasitic loop and driven elements for a lower value of “ $g$ .” Hence, an optimum spacing “ $g$ ” of 0.2 mm is considered to maintain resonance at 2.4 GHz.

### 3.2.1 Bandwidth Improvement by Merging Resonating Modes

The above analysis shows that Antenna-3 exhibits three resonating modes at 2.4 GHz, 4.5 GHz, and 5.8 GHz. It is observed from Fig. 13b, c that the antenna with a loop resonator produces additional resonance at the 4.5 GHz band. Meanwhile, impedance mismatching condition arises from 4.7 to 5.6 GHz due to the parasitic load. Hence, current distributions (Fig. 13c) on the radiating elements at 4.5 GHz and 5.5 GHz are re-analyzed before merging two resonating modes (i.e., 4.5 GHz and 5.5 GHz). The existence of a coupling effect at 5.5 GHz is observed between the open-ended stub and the driven element.

The dimension of Stub-1, especially its width “ $W_s$ ,” is further optimized to stabilize/improve the impedance response between the 4.7 and 5.6 GHz band. It can be observed in Fig. 14a that at  $W_s = 0.3$  mm, the impedance response for 4.7 to 5.6 GHz is inductive, and as the value of “ $W_s$ ” is increased, the resonant curve moves toward VSWR = 2 circles as shown in Fig. 14a. It can be observed from Fig. 14b that for  $W_s = 0.6$  mm, the proposed antenna offers impedance bandwidth ( $|S_{11}| \leq -10$  dB) of 60 MHz (2.4–2.46 GHz) and 1.58 GHz (4.3–5.88 GHz), which is suitable for Bluetooth/Wi-Fi/WLAN and 5G new radio ( $n=79$ ) applications, respectively.

The structural layout of the optimized antenna is shown in Fig. 15. The overall dimension of the proposed antenna is  $0.06\lambda \times 0.2\lambda$ , where  $\lambda$  is the wavelength at 2.43 GHz. The parasitic loop resonator-loaded electrically small antenna (ESA)

**Fig. 15** Parasitic element–loaded ESA: (a) antenna configuration, (b) dimensional layout

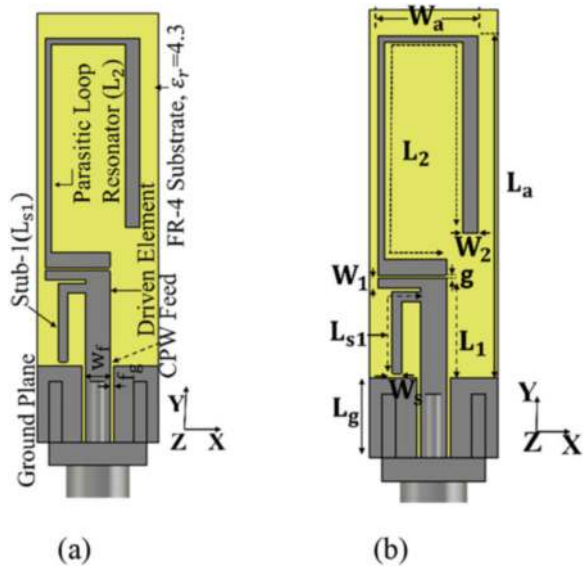


**Table 3** Optimized dimensional parameters of parasitic element–loaded ESA

Parameters	$L_{S1}$	$W_S$	$W_1$	$L_1$	$L_2$
Value(mm)	6.8	0.6	0.6	6.2	30.45
Parameters	$W_2$	$W_a$	$L_g$	$W_f$	$f_g$
Value(mm)	1.0	6.3	5.0	1.6	0.25

offers 60 MHz and 1580 MHz impedance bandwidth ( $|S_{11}| \leq -10$  dB). The optimized dimension of the final prototype is listed in Table 3.

### 3.3 Compact Dual-Band ESA: Impedance and Radiation Characteristics Measurement

The prototype of the proposed antenna is fabricated on the 1.6-mm-thick FR-4 substrate, where the total surface area occupied by the antenna is  $26.4 \times 8 \text{ mm}^2$ , as shown in Fig. 16a.

The fabricated antenna is tested for its impedance and radiation characteristics. The measured  $|S_{11}|$  response presented in Fig. 16b shows that the fabricated prototype of the proposed antenna offers impedance bandwidth ( $|S_{11}| \leq -10$  dB) of 60 MHz (2.4 GHz to 2.46 GHz) and 1580 MHz (4.3 to 5.88 GHz) for the first and second bands, respectively. A minor deviation in the magnitude of measured  $|S_{11}|$  results in comparison to the simulated results can be attributed to fabrication tolerance.

The measured and simulated radiation patterns shown in Fig. 17 indicate that the antenna offers stable radiation characteristics over the entire operating



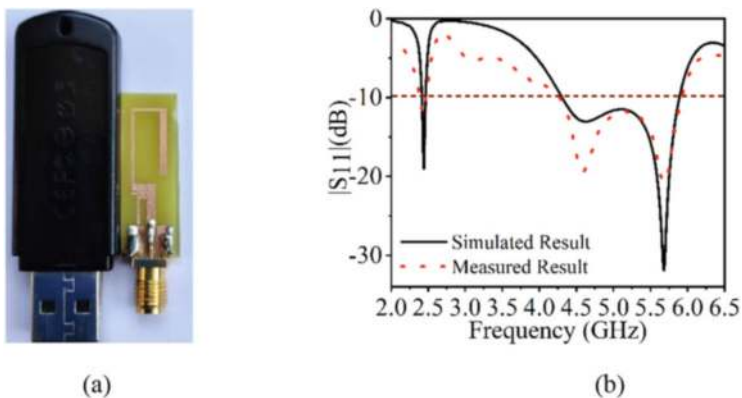


**Fig. 16** Parasitic element-loaded ESA: (a) fabricated prototype and (b) measured reflection coefficient

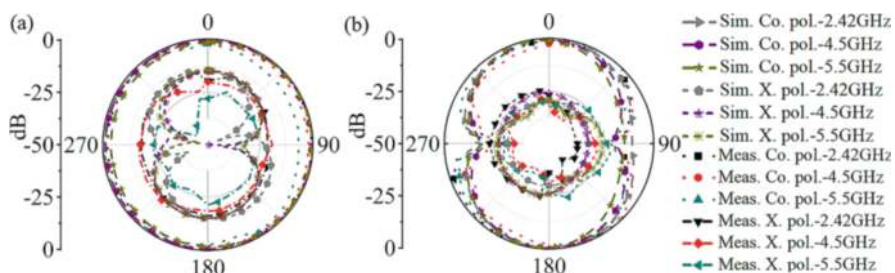


**Fig. 17** Measured radiation pattern of parasitic element-loaded ESA: (a) ZX plane and (b) ZY plane

band(s). The current distribution at 4.5 GHz and 5.5 GHz on the driven element contributes conventional monopole type E and H field variation along the antenna. Hence, at higher frequencies, the proposed parasitic element-loaded ESA exhibits omnidirectional radiation patterns in ZX and ZY planes, respectively. However, the current variation on the quarter-wavelength parasitic loop at 2.4 GHz generates a magnetic dipole-type radiation pattern in the ZY plane and an omnidirectional pattern in the ZX plane, as shown in Fig. 17. The cross-polarization level is less (i.e., <15 dB) than the co-polarization level of the antenna in both ZX and ZY planes. Figure 18 shows that the designed antenna exhibits a maximum gain of 1 dBi and 3.8 dBi over 2.43 GHz and 5 GHz bands, respectively. As discussed in the previous section, the dimensional parameters of the radiating element and open-ended stub of the proposed ESA are optimized to improve its impedance matching. The proposed parasitic loop resonator-loaded ESA exhibits significantly better radiation efficiency, i.e., 78–82% over the 2.4 GHz band and 80–95% over the 5.0 GHz band, respectively.

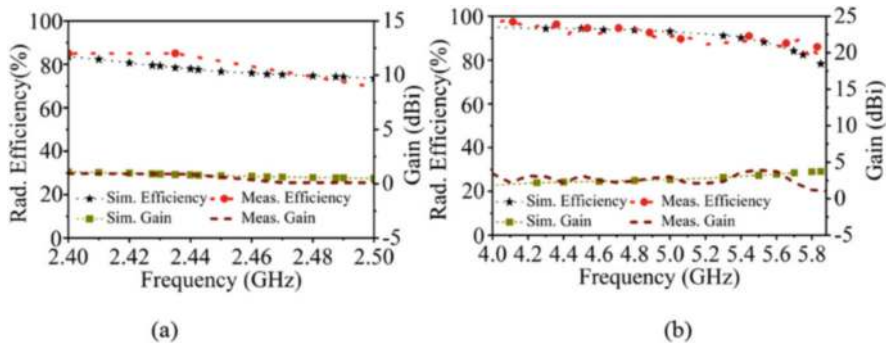


**Fig. 18** Measured gain (dBi) and efficiency response of parasitic element–loaded ESA: over (a) 2.4–2.5 GHz band and (b) 4–6.0 GHz band

The proposed parasitic element–loaded antenna is further analyzed for its ESA characteristics [7–17]. It is calculated that the free space wavenumber ( $K$ ) at 2.43 GHz is 0.05, whereas the radius of the smallest radian sphere “ $a$ ” enclosing the antenna is 13.5 mm. Hence, for 2.43 GHz, the value of “ $K \times a$ ” = 0.6 is less than 1, which indicates that the proposed loop resonator–loaded antenna is electrically small. The design technique for the proposed is scalable to implement, and it can be used to design an ESA at any frequency band.

## 4 Conclusion

This chapter presents multiple resonator–loaded multiband and wideband antenna. In one of the configurations, multiple resonators are directly attached to the base  $\lambda/4$  length monopole antenna to generate resonance at a lower frequency, whose operating wavelength is larger than the size of the antenna. As a result, the antenna is more compact than the conventional quarter-wavelength printed monopole. In addition to this, due to the reduction in overall sizes of the antenna, the input impedance becomes highly reactive. Hence, this chapter discusses scalable impedance matching techniques to achieve matched impedance response while maintaining an electrically small antenna size.

Further in another section, an electrically small antenna loaded with a parasitic loop resonator is discussed. Loading the parasitic loop with the driven element exhibits resonance lower than the resonance frequency of the driven element. In addition to this, an efficient bandwidth improvement technique, i.e., by merging resonating modes, is presented. Here, to improve the impedance bandwidth of the proposed loop resonator–loaded ESA, two higher-order methods are merged into a single passband by tuning the stub dimension without increasing the specified dimension of the antenna. The measured reflection coefficient response indicates that the proposed antenna offers impedance bandwidth of 60 MHz for the

2.4 GHz (Bluetooth/Wi-Fi) band and 1580 MHz for 5G-NR (n79)/WLAN/Wi-Fi band. The antenna offers a stable radiation pattern with more than 80% radiation efficiency over the operating bands. Overall dimension, simple design technique, and stable radiation characteristics make the proposed antenna suitable for indoor Wi-Fi/WLAN applications.

## References

1. C. Zhu, T. Li, K. Li, et al., Electrically small metamaterial-inspired tri-band Antenna with meta-mode. *IEEE Antennas Wirel. Propag. Lett.* **14**, 1738–1741 (2015). <https://doi.org/10.1109/LAWP.2015.2421356>
2. A. Gupta, R.K. Chaudhary, The metamaterial Antenna: A novel miniaturized dual-band coplanar waveguide-fed Antenna with backed ground plane. *IEEE Antennas Wirel. Propag. Lett.* **60**(4), 41–48 (2018). <https://doi.org/10.1109/MAP.2018.2839894>
3. B.J. Niu, Q.Y. Feng, P.L. Shu, Epsilon negative zeroth- and first-order resonant antennas with extended bandwidth and high efficiency. *IEEE Trans. Antennas Propag.* **61**(12), 5878–5884 (2013)
4. G. Jyotibhusan Padhi, S. Reddy, A. Kumar, Multiple stubs loaded efficient electrically small antenna for DCS/WiMAX/5G NR-n77/n78 applications. *J. Electromagn. Waves Appl.* (2022). <https://doi.org/10.1080/09205071.2022.2131470>
5. J. Padhi, A. Kumar, G.S. Reddy, Parasitic element loaded efficient electrically small Antenna for indoor wireless applications. *Microw. Opt. Technol. Lett., Wiley* **64**(10), 1793–1799 (2022)
6. J.B. Padhi, G.S. Reddy, Electrically small surface mountable chip antenna for 5G WiMAX/WLAN applications, in *2021 IEEE International Symposium on Antennas and Propagation and USNC-URSI Radio Science meeting (APS/URSI), 021*, (2021), pp. 1635–1636
7. R.C. Hansen, R.E. Collin, *Small Antenna: Handbook* (Wiley/IEEE Press Publications, 2011)
8. H.A. Wheeler, Fundamental limitations of small antennas. *Proc. IRE* **35**(12), 1479–1484 (1947). <https://doi.org/10.1109/JRPROC.1947.226199>
9. L.J. Chu, Physical limitations of Omni-directional antennas. *J. Appl. Phys.* **19**(12), 1163–1175 (1948). <https://doi.org/10.1063/1.1715038>
10. R.F. Harrington, Effect of Antenna size on gain, bandwidth, and efficiency. *J. Res. Natl. Bureau Stand. D Radio Propag.* **64D**(1), 1 (1960)
11. R.E. Collin, S. Rothschild, Evaluation of antenna Q. *IEEE Trans. Antennas Propag.* **12**(1), 23–27 (1964). <https://doi.org/10.1109/TAP.1964.1138151>
12. R.C. Hansen, Fundamental limitations in antennas. *Proc. IEEE* **69**(2), 170 (1981)
13. J.S. Mclean, A re-examination of the fundamental limits on the radiation Q of electrically small antennas. *IEEE Trans. Antennas Propag.* **44**, 672 (1996)
14. D.F. Sievenpiper et al., Experimental validation of performance limits and design guidelines for small antennas. *IEEE Trans. Antennas Propag.* **60**(1), 8–19 (2012). <https://doi.org/10.1109/TAP.2011.2167938>
15. A.D. Yaghjian, S.R. Best, Impedance, bandwidth, and Q of antennas. *IEEE Trans. Antennas Propag.* **53**(4), 1298–1324 (2005). <https://doi.org/10.1109/TAP.2005.844443>
16. S.R. Best, D.L. Hanna, A performance comparison of fundamental small-antenna designs. *IEEE Antennas Propag. Mag.* **52**(1), 47–70 (2010). <https://doi.org/10.1109/MAP.2010.5466398>
17. G.A. Mavridis, D.E. Anagnostou, M.T. Chryssomallis, Evaluation of the quality factor, Q, of electrically small microstrip-patch antennas. *IEEE Antennas Propag. Mag.* **53**(4), 216–224 (2011). <https://doi.org/10.1109/MAP.2011.6097329>
18. D.M. Pozer, *Microwave Engineering*, 4th edn. (Wiley, 2013)

19. G. Gonzalez, *Microwave Transistor Amplifiers*, 2nd edn. (Wiley, 1996), p. 506
20. J.S. Hong, M.J. Lancaster, *Microstrip Filters for RF/Microwave Applications* (Wiley, 2001)
21. G.N. Satish, K.V. Srivastava, A. Biswas, D. Kettle, A via-free left-handed transmission line with radial stubs, in *APMC 2009 – Asia Pacific Microwave Conference 2009*, vol. 1, (2009), pp. 2501–2504. <https://doi.org/10.1109/APMC.2009.5385214>

# Textile Antennas for RFID Applications



Rajesh K. Singh

## 1 Introduction

An antenna is a key component of RFID communication, it exists both at the reader and tag sides. In the past few years, the development of novel and compact antennas for readers and tags has been gaining attention to fulfill the increasing requirements of wireless industries. Nowadays, RFID has become one of the promising technologies being used for various applications. Previously, it was being used for short-range communication, but now, it is being used for long-range communications (typically in meters). Depending on the communication range and frequencies, different shapes and types of antennas are being realized to fulfill the needs. Different frequency bands of the electromagnetic spectrum, such as 130 kHz (low frequency); 13.5 MHz (high frequency); 865–867 MHz, 900 MHz, and 920 MHz (ultrahigh frequency); and 2.4 GHz, 5.8 GHz, and 24 GHz (microwave frequency), are allocated for RFID applications [1–3]. Three-dimensional, two-dimensional (planar), conformal, and textile antennas are being developed for various RFID applications. Three-dimensional antennas have high gain and efficiencies compared to planar antennas, while planar antennas are suitable for compact (low-volume) RFID systems where 3D antennas can't fit. In the era of 5G, 6G, and IOT, flexible (realized on thin substrates or cloths) antennas became popular and sometimes are the only solution. Low-profile and lightweight antennas are required to be integrated into cloths. The low cost could be another feature of the flexible antennas when they are commercialized. Significant work has

---

R. K. Singh (✉)

Electronics Engineering Department – DIAT, Pune, Maharashtra, India

e-mail: [rajesh\\_singh@diat.ac.in](mailto:rajesh_singh@diat.ac.in)

been done to realize 3D and planar antennas in the last decade. 3D antennas can be realized on thick substrates or made from metal sheets like copper, aluminum, etc. Planar antennas can be realized using thin substrates. Textile antennas come under planar antennas, which enhance the flexibility of the system and provide extra features. However, planar (2D) antennas have low radiation efficiency and narrow bandwidth; these radiation characteristics of the antenna can be enhanced using existing techniques.

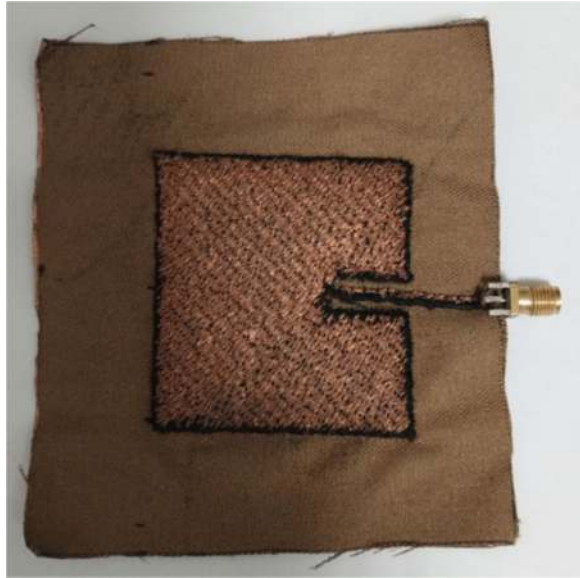
Nowadays, wearable antennas are extensively used in various industrial and medical devices. In supporting the increasing interest in antenna research for body-centric communications, the IEEE 802.15 standardization group has been established to standardize applications intended for off-body, on-body, or in-body communication [4–6]. Modern applications require wearable antenna to be lightweight, low-cost, flexible, and maintenance-free. Textile is being used in developing flexible antennas. The textile material is proven to be a promising material for wearable antennas. Different conductive and dielectric fabrics are available in the market, but developing antennas with such fabrics requires knowledge of the electrical properties of such materials such as conductivity, permittivity, loss tangent, etc. Conventional antennas that include printed dipoles, monopoles, inverted-Fs (PIFAs), and microstrip patches have been used previously for developing wearable antennas [7–10]. Among them, microstrip antennas have planar geometry and a simple feeding method. These antennas can be easily etched on a printed circuit board (PCB).

Textile materials have been studied and tested by many researchers, but there is a lot of scope in exploiting them to get the best-optimized performance. Flexible (textile) materials can be studied to achieve better performance with low-cost devices.

Connection strategy (RF feeding to the textile antenna) is another area in which one can improve the performance of textile antennas. To feed RF signal in such antennas is not an easy task; it must be studied through some standard tests. One such issue is explained in [11]. There were cracks on the surface of the uncoated screen-printed textile antennas washed 20 times [11]. The RF feed connector may detach from the antenna (shown in Fig. 1) after many washes, which may increase the ohmic losses. Additionally, soldering is not possible for the fabric materials.

To overcome the issue, coating can be done on top of the structure, but it doesn't significantly improve the performance. The use of snap buttons may be the solution for such issues. A few wearable antennas have been realized on thin substrates. Although these antennas are wearable, it may degrade the antenna performance while bending. A flexible material is needed for an antenna to be developed for body-centric communication. If the placement of such wearable devices is in proximity to the human body, then it is mandatory to overcome the issue of the human body's effect on the performance of antennas.

**Fig. 1** RF connector detachment issue in textile-based antennas



## 2 3D Antennas

Active RFIDs can detect or identify objects at a larger distance; hence, the read range is large, whereas passive RFIDs have a short read range of up to 10–15 m (typically); again, it depends on the transmitting power and gain of the reader and tag antennas. Additionally, the tags can be fixed on metallic and non-metallic objects for identification and tracking. There are different mechanisms (methods) to realize tags for metallic and non-metallic objects. 3D antennas for RFID readers and tags were realized to increase the read range of the system. The UHF RFID 3D solenoid antenna has been discussed in [12]. Solid and segmented solenoid antennas were presented to detect objects in the near-field zone of the RFID system as shown in Fig. 2. The reflection coefficients are plotted for both configurations as illustrated in Figs. 3a and b.

Another 3D UHF RFID tag mounting on metallic surfaces for IoT indoor localization applications was presented in [13]. A 3D meander line narrow-band antenna for an RFID system for IOT application was realized in [14]. Various other 3D antennas were developed to increase read range [15–17]. A UHF RFID reader 3D antenna with high gain is presented in Fig. 4. Reflection coefficients and axial ratio are plotted. The antenna operates in the frequency range of 855–885 MHz. It is designed on an F4B substrate with a dielectric constant of 2.65 and a thickness of 1.5 mm. Both substrate layers are of the same thickness. An air gap of 22 mm is created between the patch and feed to increase the impedance bandwidth of the overall structure.

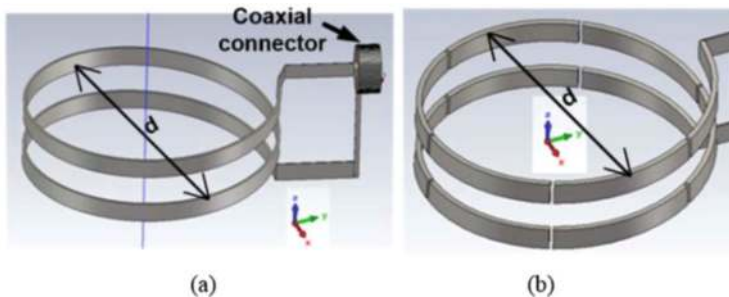


Fig. 2 3D UHF RFID reader antenna. (a) Solid solenoid and (b) segmented solenoid [12]

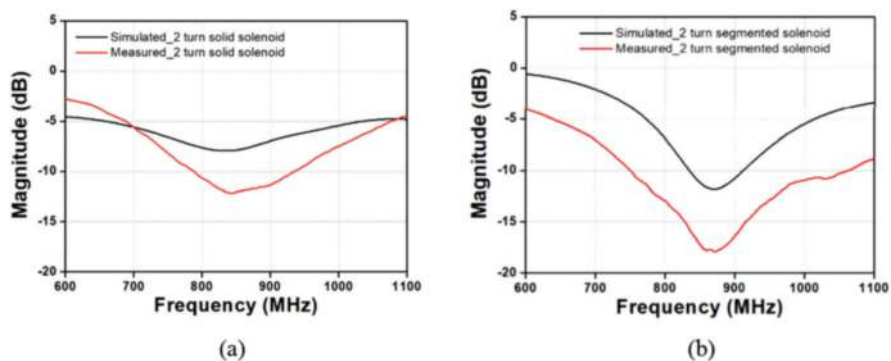


Fig. 3 Reflection coefficients of (a) solid solenoid and (b) segmented solenoid

### 3 2D or Planar Antennas

Several papers were reported on RFID planar antennas for both passive and active RFID readers and tags. It includes the slot [18], patch [19], PIFA [20], dipole [21], etc. An overview of passive RFID tag antenna design is presented in [22]. Broadband antennas were also realized to cover the frequency bands of UHF RFID for various countries [23]. The operating frequencies of UHF RFID are different in different countries. To cover all bands, a single wideband antenna can be realized. A dual monopole planar antenna is presented in [24]. It operates at two frequency bands, i.e., 2.4 and 5.8 GHz bands.

Another tag antenna was developed to be used for metallic products or packages with metal material inside [25]. A few RFID planar antennas were also realized for the RFID reader. A compact RFID reader antenna for UHF near-field and far-field operations was realized in [26]. It achieved a good impedance bandwidth of 31 MHz, which covers the USA RFID band. There is enough space in the case of developing reader antennas compared to tag antennas. An array of radiating elements were also used to enhance the gain and to get a large read range. One such antenna was realized in [27].



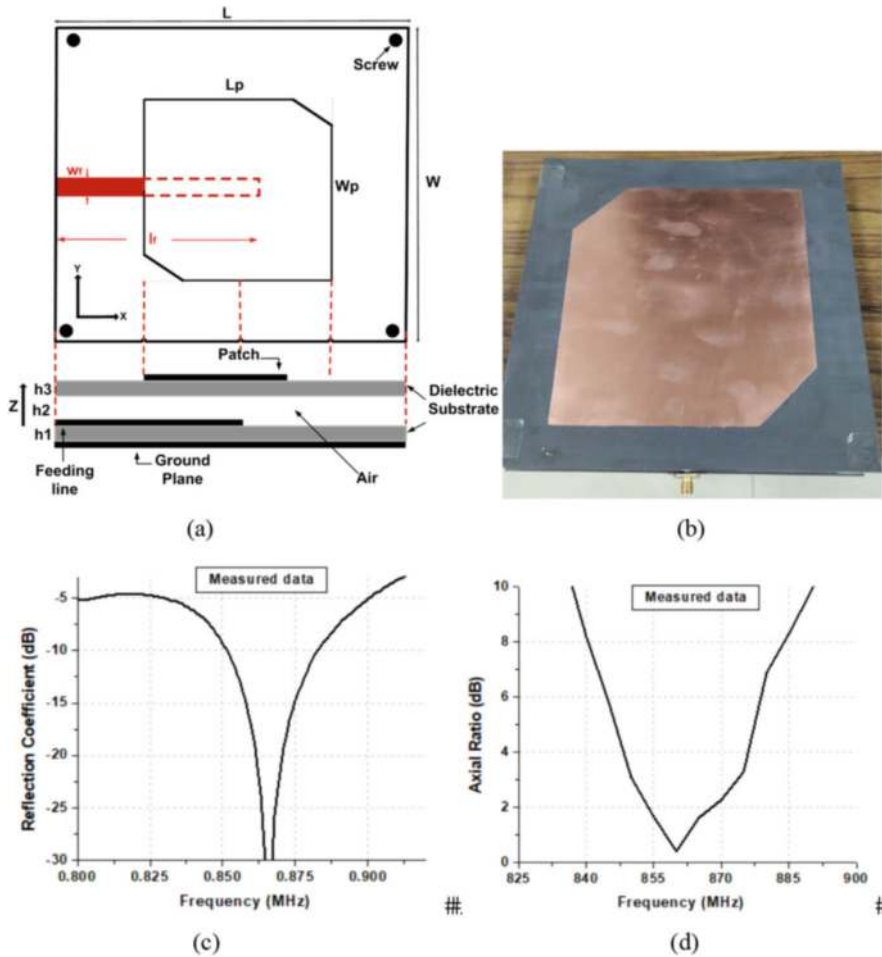


**Fig. 4** Circularly polarized UHF RFID reader antenna. (a) Geometry. Dimensions:  $W = L = 165$  mm,  $W_p = 138$  mm,  $L_p = 132$  mm,  $L_f = 130$  mm,  $W_f = 3.8$  mm. (b) Photograph. (c) Reflection coefficient. (d) Axial ratio

Another UHF RFID reader antenna design having multi-tag identification for medical systems was realized in [28]. It may operate in various countries because of the different operating RFID frequencies. Various other reader and tag antennas were realized in the past. All the discussed antennas were realized on thick substrates.

## 4 Conformal Antennas

When RFID tags are packaged in labels, antennas must be conformed to their surface. The requirements for unconventional shapes of the tag antenna may arise on demand. For example, RFID tags can be embedded inside pipes, bottles, bottle caps, and any irregularly shaped products; antennas can be conformal to those shapes. A few conventionally and unconventionally shaped tag antennas were developed in [29–35]. Unconventionally shaped tags were realized in [29]. A flexible anti-metal RFID based on a high-conductivity graphene film was presented in [34]. A compact conformal/flexible dipole antenna designed to be integrated into a soldier's beret was discussed in [35] as shown in Fig. 5. The antenna was designed to be operated at the UHF RFID frequency of 866 MHz.

An FSS AMC structure was used to block radiation toward the head of the soldier, and performance in terms of reflection coefficient and radiation pattern was reported. The reported antenna involves foam in between the AMC and dipole structure so it is not fully flexible.

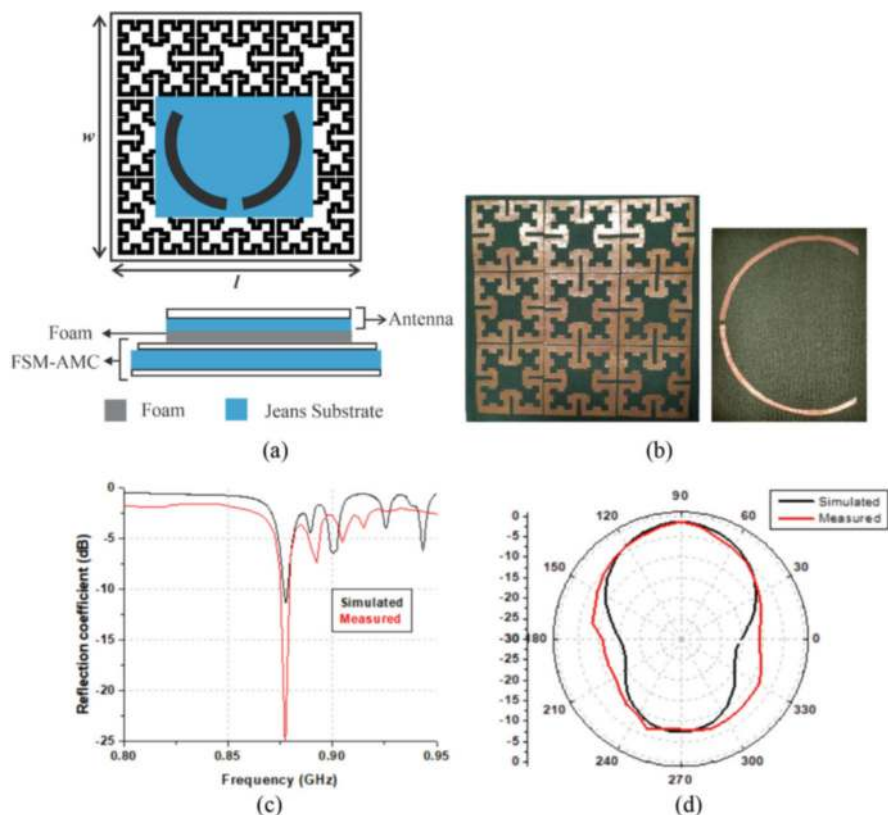


Fig. 5 Conformal dipole antenna with FSM-AMC structure [35]

## 5 Textile Antennas

Wearable devices are continuously receiving more attention in the research community for on-body communication or WBAN as well as for connecting wireless networks. It has various applications in medicine, sports, military, and space. Although there are various issues in developing wearable devices due to the lossy behavior of the human body that affects the performance of the antenna, devices are used extensively for various applications. There are various types of antennas developed as body-worn antennas.

Best-suited materials that may give better performance when used in antennas must be studied. Additionally, connection strategies or RF feed becomes important in the case of textile-based antennas.

### 5.1 *Materials for Textile-Based Antennas*

The attraction toward textile-based antennas urged researchers to study the characteristics of dielectric and conductive fabric that helps in selecting the suitable material for a particular application because the antenna needs to be conformal to the surface of the body and also the antenna performance should not be changed when mounted on a human body. Additionally, materials with different electrical properties give different results. It is essential to study the material's properties so that the material may be exploited to achieve better results. Various other properties like conformability, durability, etc. must be studied to obtain reliable and robust solutions. Different textile fabrics have been discussed in the next section.

The materials used to realize flexible antennas and affect their performance are conductive and dielectric fabrics. Conductive materials have electric conductive abilities, while dielectric materials have certain dielectric properties and tolerance to mechanical deformation (including bending, stretching, and twisting). The selection of material is done based on the abovementioned properties to ensure better characteristics of the antenna such as gain, radiation efficiency, and bandwidth. Conductive fabrics with high electrical conductivity are preferred to ensure the high efficiency of the antenna. Various conductive materials have been used and reported in the scientific literature. A few of them are listed in Table 1.

A variety of conductive fabrics are embedded inside polydimethylsiloxane (PDMS) to realize a robust flexible conductive layer for wearable/body-worn antennas. The embedded conductive fabric is also allowed to improve the adhesion of PDMS metal [36]. Table 2 shows various fabrics used to get a better combination.

All the embedded fabric has undergone some kind of mechanical testing; the performance of the embedded conductive fabric is better compared to the fabric without encapsulation because the conductive fabric detaches from the substrate (PDMS).

**Table 1** List of conductive materials

Conductive material	Conductivity (S/m)
PEDOT: PSS	100–1500
Polyaniline	5
Polypyrrole	40–200
Polyacetylene	200–1000
Silver nanoparticles	$6.173 \times 10^7$
Gold nanoparticles	$4.098 \times 10^7$
Copper nanoparticles	$5.813 \times 10^7$

**Table 2** Different conductive fabrics (CFs) with different conductivities

Composition	$t$ (mm)	$\sigma$ (S/m)
Nickel-copper-silver-coated nylon ripstop	0.13	$7.7 \times 10^5$
Copper-coated polyester taffeta	0.08	$2.5 \times 10^5$
Nickel-copper-coated ripstop	0.08	$4.2 \times 10^5$
Silver-coated ripstop	0.05	$8 \times 10^4$

**Table 3** Dielectric fabrics (textile) and their properties

S. no.	Substrate	Dielectric constant	Loss tangent
1	Cotton	1.50	0.023
2	PDMS	2.65	0.02
3	Jeans	1.54	0.03
4	Felt	1.22	0.016
5	Kapton polyimide	3.5	0.003
6	Silk	1.75	0.012
7	Panama	2.12	0.05
8	100% polyester	1.90	0.0045
9	Cordura	1.90	0.0098

Body-worn antennas for medical sensors are based on embroidered conductive polymer fiber (e-fibers) on textiles [37]. Challenges and opportunities in embroidery and related manufacturing techniques for wearable antennas have been explained in [38]. During embroidering, an assistant yarn is used to couch the e-fibers onto one side of the textile’s surface.

Substrate materials with low dielectric constant, low dielectric loss, low coefficient of thermal expansion, and high thermal conductivity can be ideal materials for developing flexible antennas. A low dielectric constant gives better efficiency, but it costs a large antenna size, whereas a high dielectric constant provides a compact geometry but with low gain. The substrate with features such as flexibility, strength, washability, and stretchability tends to be the most popular and attractive to be used by researchers. Table 3 lists some of the used dielectric substrates (textile) in the past literature. Various other fabrics are used to realize antennas for RFID [39–43].

**Fig. 6** Male snap button fitted on a microstrip transmission line



## 5.2 Feeding/Connection Strategies for Textile-Based Antennas

Realize an antenna on a textile fabric such as cloth. It is impossible to solder a feed connector on it. There are different connections used to feed textile-based antennas. The use of snap buttons may be the better solution in such antennas, but it gives more losses at high frequencies. The design/geometry of the snap button is simple; it is attached to the substrate using machine-washable glue [44].

The RF connector (SMA) used in a single-use wearable antenna can be replaced by a coaxial-to-microstrip transition via low-cost snap buttons [45]. The transition from coaxial to microstrip via snap buttons has already been tested. It is proven that snap buttons can be used up to 3 GHz with low losses. Figure 6 shows the male snap button fitted at the microstrip line end.

Snap buttons are used to connect the coaxial cable and textile patch antenna to a detachable feeding system [45, 46]. A pair of commercial snap buttons has been demonstrated as a detachable radio-frequency (RF) balanced connection between a garment-integrated textile dipole antenna and a passive sensor-enabled radio-frequency identification (RFID) tag in a wearable wireless system [47].

The best connection strategy is discussed in [48] after analyzing electrical performance, manufacturing complexity, and mechanical stability. Three different potential connection strategies on textile materials were presented—conductive epoxy, snap button, butterfly claps, and wing solution. The wing solution was suggested as an available alternative solution; it has more mechanical stability and is simpler in manufacturing than other methods.

## 5.3 Textile-Based Antennas for RFID

Several textile-based antennas were realized using these materials and connections. Textile antennas to be used for different applications of RFID are discussed here. A textile-based UHF RFID tag antenna comprising only textile materials (e-textile, textile substrate, and conductive yarn) has been presented in [49]. Screen-printed RFID antennas on two different fabrics and six different coating materials have been discussed in [50]. The reliability of the developed RFID tags was also tested after

applying a coating of glue-type material. Discontinuities and breaks were found due to the uneven surface; thus, hard coatings were suggested to keep the tag from breaking.

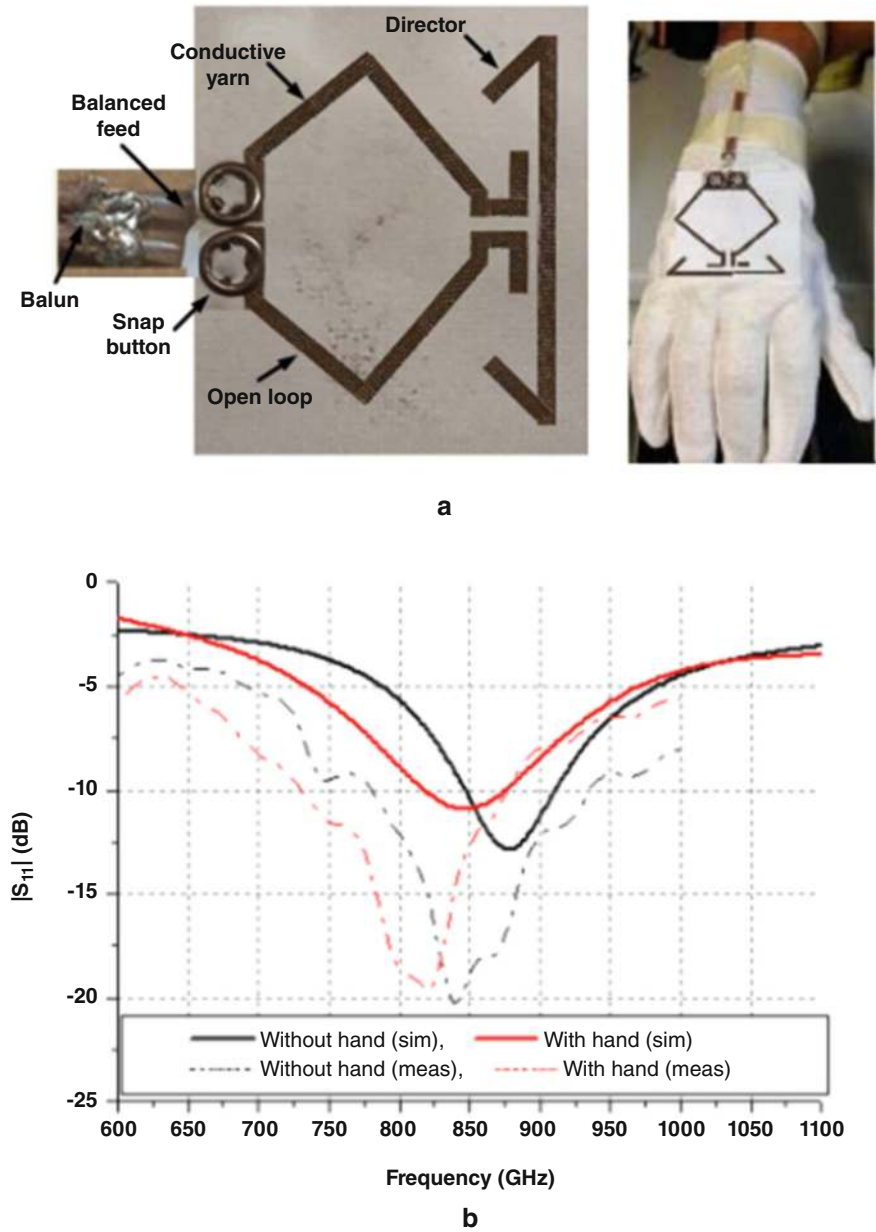
The flexible textile-concealed RFID tags for wearable applications were realized in [51]. It also showed the performance of the tag while bending. Several textile-based antennas were realized to be integrated into the smart glove for RFID applications [52–63]. Later, the frequency selective surface (FSS), electromagnetic band gap (EBG), artificial magnetic conductor (AMC) structures, etc. were realized using textile fabrics [64–67]. A fabric-based CPW antenna integrated with EBG-FSS structures was presented in [67]. It was also studied to determine its benefits and safety. A textile-based Yagi-like antenna was realized in [59] as shown in Fig. 7. It is made on a cloth fabric. Two different fabrics (a bi-elastic 3D and a quadri-elastic plain conductive fabric) have been tested and discussed. Human hand impact is considered here in Fig. 7b. When antennas are designed to be placed on the human body, bending, stretching, etc. analysis is compulsory to get the impact of its overall structure performance.

Figure 8 shows the different bending scenarios. The antenna is placed on the back of a hand palm. At different bending, reflection coefficients are plotted in Fig. 9. It does not have a significance on the performance, but it may not be true for all textile-based designs in proximity to the body. Here, the location of the antenna was chosen in such a way that it is less affected while bending and stretching. Another textile-based antenna to be fitted at the same place was reported in [61] as shown in Fig. 10. It is a dual-band antenna operating at 868 MHz and 2450 MHz.

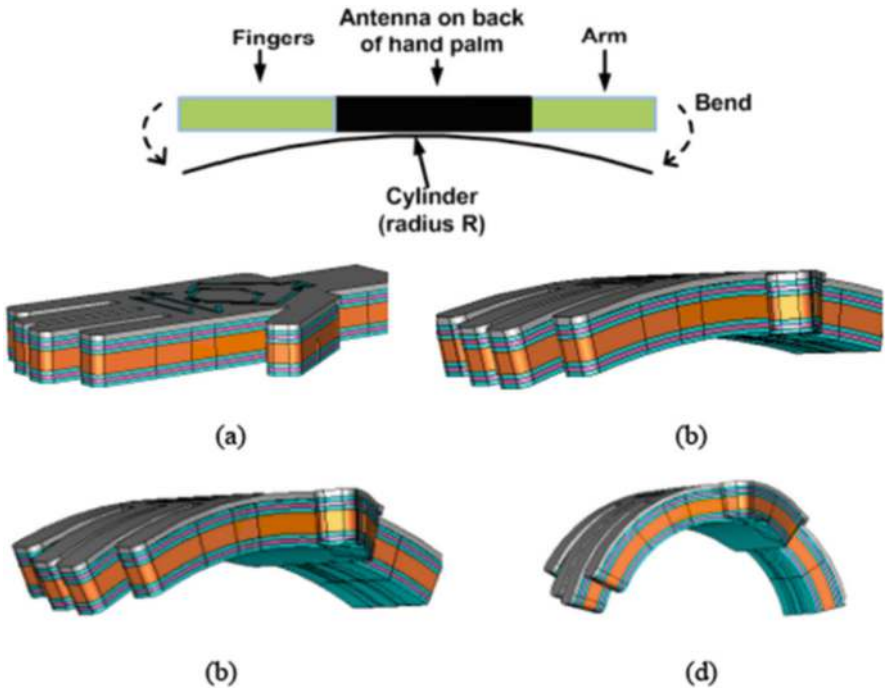
The reconfigurable textile-based antenna using the snap-on button concept is a promising practical engineering solution for reconfigurable textile antennas [44]. With an advancement in technology, research on realizing textile-based antennas, AMC, FSS, and EBG structures is ongoing.

## 6 Conclusion

Various antennas used for RFID applications have been covered in this chapter. The discussion started with the 3D antennas; later, planar and conformal antennas were discussed. When it comes to textile antennas, feeding arrangements and properties of textile materials must be discussed. The electrical and mechanical properties of the materials are key for textile antennas. A few textile-based antennas for different applications of near- and far-field RFID were discussed in detail.

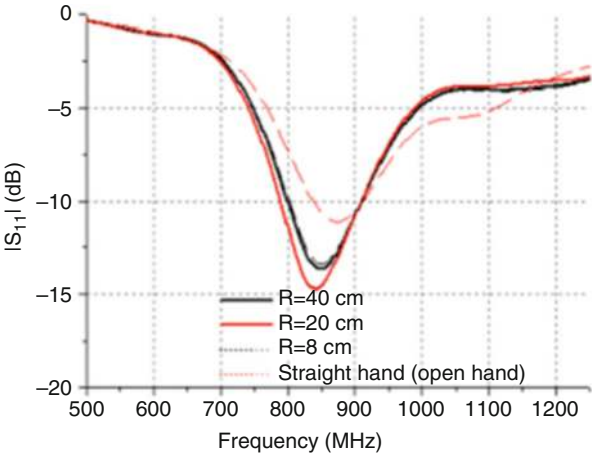


**Fig. 7** Textile-based Yagi-like flexible antenna for UHF RFID systems [59]. (a) Photograph of the antenna. (b) Reflection coefficient with and without hand



**Fig. 8** Bending analysis of textile-based antenna to be placed on the back of a palm. (a) Cylinder radius,  $R = \infty$  (no bending). (b)  $R = 40$  cm. (c)  $R = 20$  cm. (d)  $R = 8$  cm (almost closed hand) [59]

**Fig. 9** Reflection coefficients at different bending [59]





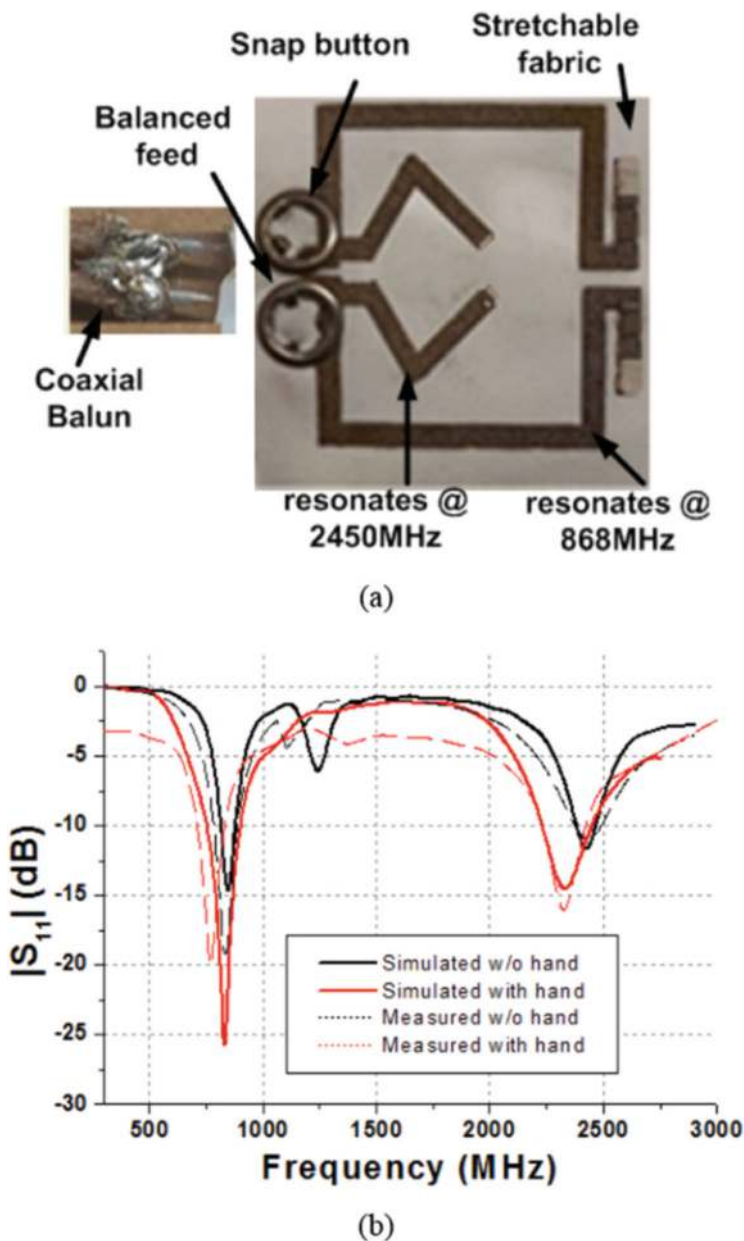


**Fig. 10** Textile-based Yagi-like flexible dual-band antenna for UHF RFID systems [61]. (a) Photograph of the antenna. (b) Reflection coefficients with and without hand

## References

1. S.S. Basat, K. Lim, J. Laskar, M.M. Tentzeris, Design and modeling of embedded 13.56 MHz RFID antennas, in *2005 IEEE Antennas and Propagation Society International Symposium, Washington, DC, USA*, vol. 4B, (2005), pp. 64–67. <https://doi.org/10.1109/APS.2005.1552740>
2. K. Jomaa, F. Ndagijimana, H. Ayad, M. Fadlallah, J. Jomaah, Near-field characterization for 13.56 MHz RFID antenna, in *2017 International Symposium on Electromagnetic Compatibility – EMC EUROPE, Angers, France*, (2017), pp. 1–4. <https://doi.org/10.1109/EMCEurope.2017.8094759>
3. X. Qing, C.K. Goh, Z.N. Chen, UHF near-field RFID reader antenna, in *Proceedings of Asia Pacific Microwave Conference, Singapore*, (2009), pp. 2383–2386
4. I. Gammoudi, M. Nedil, T.A. Denidni, L. Talbi, RFID off-body tag antenna for underground environment, in *2017 IEEE International Symposium on Antennas and Propagation & USNC/URSI National Radio Science Meeting, San Diego, CA, USA*, (2017), pp. 2435–2436. <https://doi.org/10.1109/APUSNCURSINRSM.2017.8073260>
5. J.D. Hughes, R. Horne, N. Brabon, J. Batchelor, An on-body UHF RFID tag with DDRR antenna for healthcare data streaming applications. *IEEE J. Radio Freq. Identif.* **6**, 680–687 (2022). <https://doi.org/10.1109/JRFID.2022.3216762>
6. A. Kiourti, RFID antennas for body-area applications: From wearables to implants. *IEEE Antennas Propag. Mag.* **60**(5), 14–25 (2018). <https://doi.org/10.1109/MAP.2018.2859167>
7. J. Alarcon, M. Egels, P. Pannier, A low profile circularly polarized antenna for UHF RFID readers, in *2011 IEEE International Conference on RFID-Technologies and Applications, Sitges, Spain*, (2011), pp. 469–472. <https://doi.org/10.1109/RFID-TA.2011.6068680>
8. L. Tian, H. Guo, X. Liu, Y. Wang, X. Yang, Novel 3D RFID antenna with low profile and low cost, in *ISAPE2012, Xi'an, China*, (2012), pp. 69–72. <https://doi.org/10.1109/ISAPE.2012.6408710>
9. P. Parthiban, B.-C. Seet, X.J. Li, Low-cost low-profile UHF RFID reader antenna with reconfigurable beams and polarizations, in *2017 IEEE International Conference on RFID (RFID), Phoenix, AZ, USA*, (2017), pp. 81–87. <https://doi.org/10.1109/RFID.2017.7945591>
10. M. El Bakkali, P. Singh, M. El Bakkali, L. Kansal, G.K. Sodhi, A low profile CPW-Fed Slot antenna for UHF-RFID readers, in *2021 International Conference on Computer Communication and Informatics (ICCCI), Coimbatore, India*, (2021), pp. 1–4. <https://doi.org/10.1109/ICCCI50826.2021.9402378>
11. I. Kazani, F. Declercq, M.L. Scarpello, C. Hertleer, H. Rogier, D. Vande Ginste, G. De Mey, G. Guxho, L. Van Langenhove, Performance study of screen-printed textile antennas after repeated washing. *Autex Res. J.* **14**(2), 47–54 (2014). <https://doi.org/10.2478/v10304-012-0049-x>
12. R.K. Singh, A. Michel, P. Nepa, A. Salvatore, Glove integrated solenoid antennas for near-field UHF RFID applications, in *2019 IEEE Indian Conference on Antennas and Propagation (InCAP), Ahmedabad, India*, (2019), pp. 1–4. <https://doi.org/10.1109/InCAP47789.2019.9134637>
13. M. Dhaouadi, F. Choubani, A novel 3D PILA-Type UHF RFID tag antenna mountable on metallic objects for IoT indoor localization. *Int. J. Antennas Propag.* **2021**, Article ID 7643941, 12 pages (2021). <https://doi.org/10.1155/2021/7643941>
14. A. Mohamed, S.N. Azemi, S.A. Suhaimi, A. Ezanuddin, 3D miniature antenna design for RFID applications in IoT environment. *Les Ulis: EDP Sci.* **97** (2017). <https://doi.org/10.1051/mateconf/20179701092>
15. D. Kaddour, S. Tedjini, A. Djamel, 3D antenna for UHF RFID Tag On Molded interconnect device, in *2013 IEEE Antennas and Propagation Society International Symposium (APSURSI), Orlando, FL, USA*, (2013), pp. 1502–1503. <https://doi.org/10.1109/APS.2013.6711410>
16. D.V. Kholodnyak, P.A. Turalchuk, A.B. Mikhailov, S.Y. Dudnikov, I.B. Vendik, 3D antenna for UHF RFID tags with eliminated read-orientation sensitivity, in *2006 Euro-*

- pean Microwave Conference, Manchester, UK*, (2006), pp. 583–586. <https://doi.org/10.1109/EUMC.2006.281459>
17. C.M. Kruesi, R.J. Vyas, M.M. Tentzeris, Design and development of a novel 3-D cubic antenna for wireless sensor networks (WSNs) and RFID applications. *IEEE Trans. Antennas Propag.* **57**(10), 3293–3299 (2009)
  18. S.-Y. Chen, P. Hsu, CPW-fed folded-slot antenna for 5.8 GHz RFID tags. *Electron. Lett.* **24**, 1516–1517 (2004)
  19. S.K. Padhi, N.C. Karmakar, C.L. Law, S. Aditya, A dual polarized aperture coupled circular patch antenna using a C-shaped coupling slot. *IEEE Trans. Antennas Propag.* **51**(12), 3295–3298 (2003)
  20. M. Hirvonen, P. Pursula, K. Jaakkola, K. Laukkanen, Planar inverted- F antenna for radio frequency identification. *Electron. Lett.* **40**, 848–850 (2004)
  21. Q. Xianming, Y. Ning, A folded dipole antenna for RFID. *Proc. IEEE Antennas Propag. Soc. Int. Symp.* **1**, 97–100 (2004)
  22. K.V.S. Rao, P.V. Nikitin, S.F. Lam, Antenna design for UHF RFID tags: A review and a practical application. *IEEE Trans. Antennas Propag.* **53**(12), 3870–3876 (2005). <https://doi.org/10.1109/TAP.2005.859919>
  23. Y. Shi, C. Fang, K. Qi, C.-H. Liang, A broadband design of UHF fractal RFID tag antenna. *Prog. Electromag. Res. Lett.* **58**, 45–51 (2016). <https://doi.org/10.2528/PIERL15100406>
  24. N. Ojaroudi Parchin, H. Jahanbakhsh Basherlou, R.A. Abd-Alhameed, J.M. Noras, Dual-band monopole antenna for RFID applications. *Future Internet* **11**, 31 (2019). <https://doi.org/10.3390/fi11020031>
  25. L. Mo, C. Li, Double loop inductive feed patch antenna design for Antimetal UHF RFID Tag. *Int. J. Antennas Propag.* **2019**, Article ID 2917619, 8 pages (2019). <https://doi.org/10.1155/2019/2917619>
  26. L.X. Zheng, X. Zeming, C. Xuanliang, A compact RFID reader antenna for UHF near-field and far-field operations. *Int. J. Antennas Propag.* **2013**, Article ID 961042, 5 pages (2013). <https://doi.org/10.1155/2013/961042>
  27. D. Xie, X. Liu, H. Guo, X. Yang, Novel design of high-gain planar dipole-array antenna for RFID 2.45 GHz. *Int. J. Antennas Propag.* **2014**, Article ID 704974, 6 pages (2014). <https://doi.org/10.1155/2014/704974>
  28. J.S. Jung, J.N. Lee, J.M. Kim, J.K. Park, An UHF RFID reader antenna with Multitag identification for extremely low-temperature medical systems. *Int. J. Antennas Propag.* **2020**, Article ID 2482961, 11 pages (2020). <https://doi.org/10.1155/2020/2482961>
  29. S. Wang, Y. Liu, T.T. Ye, “Unconventionally shaped” antenna design for UHF RFID tags. *Int. J. Antennas Propag.* **2021**, Article ID 9965252, 9 pages (2021). <https://doi.org/10.1155/2021/9965252>
  30. H. Rajagopalan, Y. Rahmat-Samii, A novel conformal all-surface mount RFID tag antenna design, in *2009 IEEE Antennas and Propagation Society International Symposium, North Charleston, SC, USA*, (2009), pp. 1–4. <https://doi.org/10.1109/APS.2009.5171872>
  31. H. Rajagopalan, Y. Rahmat-Samii, Conformal RFID antenna design suitable for human monitoring and metallic platforms, in *Proceedings of the Fourth European Conference on Antennas and Propagation, Barcelona, Spain*, (2010), pp. 1–5
  32. J. Xi, T.T. Ye, Conformal UHF RFID tag antenna mountable on winebottle neck, in *Proceedings of the 2012 IEEE International Symposium on Antennas and Propagation, Chicago, IL, USA*, (2012), pp. 1–2. <https://doi.org/10.1109/APS.2012.6349252>
  33. S. Sajal, B.D. Braaten, A conformal antenna on a passive UHF RFID tag using 97% carbon content graphene-based conductors and paper substrates, in *2017 IEEE International Symposium on Antennas and Propagation & USNC/URSI National Radio Science Meeting, San Diego, CA, USA*, (2017), pp. 2427–2428. <https://doi.org/10.1109/APUSNCURSINRSM.2017.8073256>
  34. B. Zhang, C. Zhang, Y. Wang, Z. Wang, C. Liu, D. He, Z.P. Wu, Flexible anti-metal RFID tag antenna based on high-conductivity graphene assembly film. *Sensors* **21**, 1513 (2021). <https://doi.org/10.3390/s21041513>

35. S. Palani, R.K. Singh, K.P. Ray, M. Singh, A compact and flexible dipole antenna to be integrated into military berets, in *2022 IEEE Microwaves, Antennas, and Propagation Conference (MAPCON), Bangalore, India*, (2022), pp. 1774–1778. <https://doi.org/10.1109/MAPCON56011.2022.10047703>
36. R.B.V.B. Simorangkir, Y. Yang, R.M. Hashmi, T. Björninen, K.P. Esselle, L. Ukkonen, Polydimethylsiloxane-embedded conductive fabric: Characterization and application for realization of robust passive and active flexible wearable antennas. *IEEE Access* **6**, 48102–48112 (2018). <https://doi.org/10.1109/ACCESS.2018.2867696>
37. L. Zhang, Z. Wang, J.L. Volakis, Textile antennas and sensors for body-worn applications. *IEEE Antennas Wirel. Propag. Lett.* **11**, 1690–1693 (2012). <https://doi.org/10.1109/LAWP.2013.2239956>
38. A. Tsolis, W.G. Whittow, A.A. Alexandridis, J.C. Vardaxoglou, Embroidery and related manufacturing techniques for wearable antennas: Challenges and opportunities. *Electronics* **3**, 314–338 (2014). <https://doi.org/10.3390/electronics3020314>
39. Z. Wang, L. Zhang, D. Psychoudakis, J.L. Volakis, Flexible textile antennas for body-worn communication, in *Proceedings of the IEEE International Workshop on Antenna Technology, Tucson, AZ, USA*, (2012), pp. 205–208
40. Toyobo Co., LTD., Osaka, Japan, PBO Fiber Zylon Technical Information, (2005)
41. P. Salonen, J. Kim, Y. Rahmat-Samii, Dual-band E-shaped patch wearable textile antenna. *Proc. IEEE Antennas Propag. Soc. Int. Symp.* **1A**, 466–469 (2005)
42. Y. Ouyang, W.J. Chappell, High frequency properties of electro-textiles for wearable antenna applications. *IEEE Trans. Antennas Propag.* **56**(2), 381–389 (2008)
43. S. Bashir, A. Chauraya, R.M. Edwards, J. Vardaxoglou, A flexible fabric metasurface for on-body communication applications, in *Proceedings of the Antennas Propagation Conference, Loughborough, UK., November 16–17*, (2009), pp. 725–728
44. S.J. Chen, D.C. Ranasinghe, C. Fumeaux, A robust snap-on button solution for reconfigurable wearable textile antennas. *IEEE Trans. Antennas Propag.* **66**(9), 4541–4551 (2018). <https://doi.org/10.1109/TAP.2018.2851288>
45. T. Kellomäki, Snaps to connect coaxial and microstrip lines in wearable systems. *Int. J. Antennas Propag.* **2012**, Article ID 659287 10 pages (2012). <https://doi.org/10.1155/2012/659287>
46. I. Belov, M. Chedid, P. Leisner, Investigation of snap-on feeding arrangements for a wearable UHF textile patch antenna, in *Proceedings of the Ambience 08 Smart Textiles Technology and Design, Borås, Sweden*, (2008)
47. S.J. Chen, C. Fumeaux, D.C. Ranasinghe, T. Kaufmann, Paired snap-on buttons connections for balanced antennas in wearable systems. *IEEE Antennas Wirel. Propag. Lett.* **14**, 1498–1501 (2015). <https://doi.org/10.1109/LAWP.2014.2363852>
48. S.P. Pinapati, T. Kaufmann, I. Linke, D. Ranasinghe, C. Fumeaux, Connection strategies for wearable microwave transmission lines and antennas, in *2015 International Symposium on Antennas and Propagation (ISAP), Hobart, TAS, Australia*, (2015), pp. 1–4
49. J. Virkki, Z. Wei, A. Liu, L. Ukkonen, T. Björninen, Wearable passive E-Textile UHF RFID tag based on a slotted patch antenna with sewn ground and microchip interconnections. *Int. J. Antennas Propag.* **2017**, Article ID 3476017, 8 pages (2017). <https://doi.org/10.1155/2017/3476017>
50. T. Kellomäki, J. Virkki, S. Merilampi, L. Ukkonen, Towards washable wearable antennas: A comparison of coating materials for screen-printed textile-based UHF RFID tags. *Int. J. Antennas Propag.* **2012**, Article ID 476570, 11 pages (2012). <https://doi.org/10.1155/2012/476570>
51. M. Wagih, Y. Wei, A. Komolafe, R. Torah, S. Beeby, Reliable UHF long-range textile-integrated RFID tag based on a compact flexible antenna filament. *Sensors* **20**, 3435 (2020). <https://doi.org/10.3390/s20123435>

52. S. Ahmed, S.M.M. Rehman, L. Ukkonen, T. Björninen, Glove-integrated slotted patch antenna for wearable UHF RFID reader, in *2018 IEEE International Conference on RFID Technology & Application (RFID-TA)*, Macau, Macao, (2018), pp. 1–5. <https://doi.org/10.1109/RFID-TA.2018.8552817>
53. R.K. Singh, A. Michel, P. Nepa, A. Salvatore, Design of a compact Yagi-Uda Antenna for near field UHF RFID smart gloves, in *IEEE International Conference on RFID Technology and Applications (RFID-TA)*, Pisa, Italy, (2019), pp. 1–4
54. S. Ahmed, A. Mehmood, L. Sydänheimo, L. Ukkonen, T. Björninen, 2019 IEEE International Conference on RFID Technology and Applications (RFID-TA), Pisa, Italy, in *Glove-integrated textile antenna with reduced SAR for wearable UHF RFID reader*, (2019), pp. 231–235. <https://doi.org/10.1109/RFID-TA.2019.8892251>
55. S. Ahmed, S.T. Qureshi, L. Sydänheimo, L. Ukkonen, T. Björninen, Comparison of wearable E-textile split ring resonator and slotted patch RFID reader antennas embedded in work gloves. *IEEE J. Radio Freq. Identif.* **3**(4), 259–264 (2019). <https://doi.org/10.1109/JRFID.2019.2926194>
56. R.K. Singh, A. Michel, P. Nepa, A. Salvatore, Glove integrated dual-band Yagi reader antenna for UHF RFID and Bluetooth application, in *International Workshop on Antenna Technology (iWAT)*, Bucharest, Romania, (2020), pp. 1–4
57. R.K. Singh, A. Michel, P. Nepa, A. Salvatore, Modified Yagi-Uda reader antenna for UHF RFID smart-glove, in *14th European Conference on Antennas and Propagation (EUCAP)*, Copenhagen, Denmark, (2020), pp. 1–4
58. R.K. Singh, A. Michel, P. Nepa, A. Salvatore, Compact Quasi-Yagi reader antenna for UHF RFID smart-glove, in *IEEE International Conference on Smart and Sustainable Technologies, Croatia, September 23–26*, (2020)
59. R.K. Singh, A. Michel, P. Nepa, A. Salvatore, M. Terraroli, P. Perego, Compact and wearable Yagi-like textile antennas for near-field UHF-RFID readers. *IEEE Trans. Antennas Propag.* **69**(3), 1324–1333 (2021). <https://doi.org/10.1109/TAP.2020.3030944>
60. A. Michel, R.K. Singh, P. Nepa, G. Manara, Smart glove for near-field UHF RFID applications, in *URSI General Assembly and Scientific Symposium, Rome, Italy*, (2021), pp. 1–1
61. R.K. Singh, A. Michel, P. Nepa, A. Salvatore, Wearable dual-band quasi-Yagi antenna for UHF-RFID and 2.4 GHz applications. *IEEE J. Radio Freq. Identif. (RFID)* **4**(4), 420–427 (2020). <https://doi.org/10.1109/JRFID.2020.3000298>
62. A. Michel, R.K. Singh, P. Nepa, G. Manara, A smart glove for near-field UHF RFID applications. *URSI Radio Sci. Lett.* **3**, 1–4 (2022). <https://www.ursi.org/Publications/RadioScienceLetters/Volume3/RSL21-0046-final.pdf>
63. A. Michel, R.K. Singh, On the use of power-transfer efficiency to analyze the performance of a 3D-printed wearable UHF-RFID antenna. *URSI Radio Sci. Bull.* **2021**(377), 38–45 (2022)
64. H.R. Raad, A.I. Abbosh, H.M. Al-Rizzo, D.G. Rucker, Flexible and compact AMC based antenna for telemedicine applications. *IEEE Trans. Antennas Propag.* **61**(2), 524–531 (2013). <https://doi.org/10.1109/TAP.2012.2223449>
65. R.C. Hadarig, M.E. de Cos, F. Las-Heras, UHF dipole-AMC combination for RFID applications. *IEEE Antennas Wirel. Propag. Lett.* **12**, 1041–1044 (2013). <https://doi.org/10.1109/LAWP.2013.2279095>
66. S. Genovesi, F. Costa, F. Fanciulli, A. Monorchio, Wearable inkjet-printed wideband antenna by using miniaturized AMC for sub-GHz applications. *IEEE Antennas Wirel. Propag. Lett.* **15**, 1927–1930 (2016). <https://doi.org/10.1109/LAWP.2015.2513962>
67. A.Y.I. Ashyap et al., Highly efficient wearable CPW antenna enabled by EBG-FSS structure for medical body area network applications. *IEEE Access* **6**, 77529–77541 (2018). <https://doi.org/10.1109/ACCESS.2018.2883379>

# Recent Trends in the Design and Development of Dielectric Resonator Antennas



Pragati Patel

## 1 Introduction

An antenna is an important part of wireless communication systems. Efficient antenna design improves the overall performance of such a system. The main role of an antenna is to transmit or receive electromagnetic waves [1]. The types of antennas can be wire, aperture, microstrip, array, reflector, lens, or dielectric resonator. Among all, microstrip antennas had been popular due to their advantages such as lightweight, compact, conformal, and ease of fabrication [2]. The shape of such microstrip antennas can be square, circular, triangular, etc. The frequency of modern wireless communication system is scaling upward to millimeter waves to meet the demand of multitasking or fast communications. The conductor losses of microstrip or other metallic antennas become severe at such high frequencies due to skin effect. Increased losses degrade efficiency of the antenna significantly, which is undesired. Therefore, efficient antennas are required at millimeter- and near-millimeter-wave regions (10–300 GHz). Conversely, dielectric resonator antennas, or DRAs, became popular because of minimal conductor losses and absence of surface waves [3]. Dielectric resonators are popular as an energy-storing element in microwave circuits due to their compact size and high-quality factor. Application as efficient radiators or antennas started because of the availability of low-quality factor dielectric materials, which could retain wideband antenna characteristics. The additional inherent advantages of DRAs are wide bandwidth, high radiation efficiency, and compact size at high frequency [4]. The bandwidth offered by DRAs is more than that of microstrip antennas because in the former, all sides

---

P. Patel (✉)

Department of Electronics and Communication Engineering, National Institute of Technology  
Goa, Cuncolim, Goa, India  
e-mail: [pragati@nitgoa.ac.in](mailto:pragati@nitgoa.ac.in)

radiate, except for the grounded part, whereas in the latter, radiation takes place from two narrow radiating edges. Nevertheless, microstrip antennas and DRAs have many similar features. Both types of antennas behave like cavity resonators. Also, excitation techniques are similar for the two categories of antennas. In order to design DRA for modern wireless communications, the theory of dielectric resonators is first discussed briefly in the subsequent section.

### ***1.1 Dielectric Resonators***

Dielectric resonators consist of low-loss, high-permittivity, and thermally stable ceramic material. Shapes of such resonators can be cylindrical, spherical, parallelepiped, etc. The cost and size have been a challenge while designing microwave circuits, and miniaturization of such microwave circuits is possible due to the advancement in low loss temperature stable dielectric resonators. The first thermally stable, low-loss dielectric material reported was barium tetratitanate ceramics in 1970 [5]. After this breakthrough, many advanced dielectric resonators have been investigated. At resonant frequencies, an equal storage of electric or magnetic energies takes place. Therefore, input impedance is purely resistive at resonance.

The quality factor or Q factor is an important figure of merit in the resonant circuits [6]. It is defined as the ratio of electromagnetic energy stored to energy dissipated in the form of heat. The highest value of quality factor is around 10,000, which makes dielectric resonators suitable as an efficient energy-storing element rather than as a radiating element.

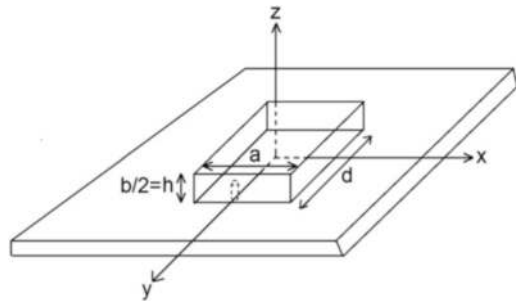
Due to aforementioned characteristics, dielectric resonators were popular as energy-storing elements in the shielded environment to prevent any radiation of energy until 1983. It was reported in the year 1983 that when shielding is removed and excited appropriately, they can behave as an efficient radiator.

### ***1.2 Dielectric Resonator Antennas (DRAs)***

The potential application of dielectric resonators as efficient radiators started in the year 1983 when cylindrical, rectangular, and hemispherical shapes were investigated. Detailed analysis of resonant modes, radiation characteristics, and techniques of excitation was reported in [7–9] for the three aforementioned basic geometries. Thereafter, an investigation of dielectric resonators as potential radiators started. DRAs operating at their fundamental modes irrespective of shape behave like a short horizontal magnetic dipole. They are designed to obtain certain characteristics such as compact size, wideband, circular polarization, gain enhancement, multiple input-multiple output (MIMO), and ultrawideband (UWB) [10]. The basic features and mode nomenclature are adopted from [11–13].



**Fig. 1** Geometry of a rectangular DRA



The main findings of investigations on basic shapes of DRAs can be summarized as follows [3]:

- The size of the DRA is proportional to  $\lambda_0/\epsilon_r$ , where  $\lambda_0$  is the free space wavelength and  $\epsilon_r$  is the dielectric constant.
- The resonant frequency and radiation quality factor are dependent on the aspect ratio of the DRA for fixed dielectric constant.
- Low-loss dielectric materials can offer high radiation efficiency up to millimeter-wave region because of minimal conductor losses and absence of surface waves.
- The physical size of the DRA and bandwidth can be controlled due to the availability of a wide range of dielectric constants for dielectric materials.
- The resonant frequency can vary from several MHz to several GHz.
- Various excitation techniques available for the excitation of DRAs make integration with MIC or MMIC technology possible.
- Different types of radiation patterns are possible depending upon resonant modes excited within the DRA, which can meet requirements of different applications.

Resonant modes play an important role in determining radiation characteristics of DRA. Therefore, analysis or understanding of different modes excited inside the DRA is important. The modal theory is taken from dielectric resonators and does not consider the effect of feed or the coupling method. Therefore, it may affect the resonant frequency, quality factor, and cross-polar patterns of the DRA. Modes for the three basic geometries will be discussed.

Rectangular-shaped DRAs shown in Fig. 1 excite two resonant modes, TE and TM. However, inclusion of ground plane in designing of rectangular DRA restricts the excitation of TM modes. Therefore, rectangular-shaped DRAs support TE modes only when mounted on a ground plane. The fundamental  $TE_{111}$  mode radiates like short horizontal magnetic dipoles. The three subscripts represent field variations along the x, y, and z axis.

Cylindrical-shaped DRAs shown in Fig. 2 excite  $TM_{01\delta}$  (radiate like short electric monopole),  $TE_{01\delta}$ , and  $HE_{11\delta}$  (radiate like a short horizontal magnetic dipole) modes. The three subscripts represent variations along azimuth, radial, and axial direction, whereas HEM refers to the hybrid mode. The value of  $\delta$  can vary from 0 to 1 and is equal to 1 for high dielectric constant material. Hemispherical-



**Fig. 2** Geometry of a cylindrical DRA

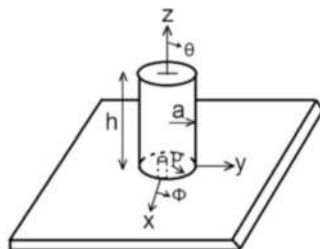
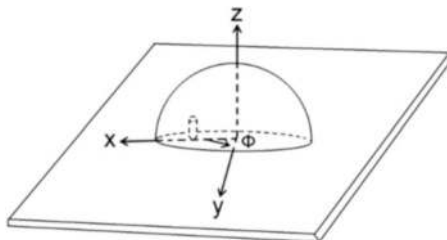


**Fig. 3** Geometry of a hemispherical DRA



shaped DRAs shown in Fig. 3 excite two resonant modes,  $TE_{111}$  and  $TM_{101}$  which radiate like a short horizontal magnetic dipole and short electric monopole, respectively. The three subscripts refer to field variations along radial, azimuth, and elevation direction, whereas TE refers to transverse electric, and TM refers to transverse magnetic.

## 2 Recent Trends in the Design and Development of Dielectric Resonator Antennas

Rectangular DRAs offer more degree of freedom than the other two geometries, viz., cylindrical and hemispherical DRAs. Thus, it has more flexibility in choosing the desired antenna profile. This means depending upon the application desired antenna profile can be selected. Therefore, tall and slender or thin and wide designs are possible for given dielectric constant and resonant frequency. The radiation quality factor varies with the profile and provides more design flexibility. Therefore, the design of compact and wideband rectangular DRAs is challenging particularly at low-frequency applications. Numerous rectangular DRAs have been proposed to meet stringent requirements of modern communication systems. However, antennas offer limited bandwidth due to the resonant nature. The main reason for restriction in the enhancement of bandwidth is the impedance of the antenna, which varies with frequency. Some techniques for enhancement of bandwidth are lowering of radiation quality factor, external matching networks, modified feed network, and stacking of multiple resonators [3, 4]. The rectangular DRAs discussed have enhanced bandwidth based upon method of reduction of radiation quality factor. This is

achieved by reducing effective dielectric constant, which is directly related to the radiation quality factor. It is worth mentioning that a low dielectric constant material ( $\epsilon_r < 10$ ) is not preferred while designing a rectangular DRA because to resonate, fields should be contained within the DRA.

The technique of edge grounding is used for size reduction in [15]. The field configuration within the half-rectangular DRA does not change if a PEC (or metal plate) is placed along the chopped edge [3, 4]. The PEC does not extend further than the edge dimensions. However, the major drawback is significant reduction in the bandwidth as reported in [3, 4, 15]. The asymmetry exists in the radiation patterns due to the effect of metal plate used. The metal plate acts as a shorting post for electric fields as mentioned in [3, 4]. This reduces volume by approximately half and thus makes the antenna compact. It is similar to the use of shorting posts for patch antennas to reduce length of patch from  $\lambda/2$  to  $\lambda/4$ . In [15], a rectangular DRA is designed first using dielectric waveguide model [3, 4] to resonate at 1.22 GHz. The coaxial probe feeding is used to excite the rectangular DRA. However, the impedance bandwidth is reduced significantly, and resonant frequency decreases. The resonant frequency shifted from 1.22 GHz to 918 MHz, and impedance bandwidth significantly reduced from 16% to 5.4%.

Next, the method of edge grounding along with lowering of effective dielectric constant is used to reduce size and improve impedance bandwidth [16–24]. The concept of designing compact rectangular and cylindrical DRAs involves incorporation of both perfect electric conductors (PEC) and perfect magnetic conductors (PMC) [16]. The perfect PMC condition is attained by utilizing a high dielectric constant interface. To enhance performance, a quarter-rectangular DRA is designed, offering a bandwidth of 26% and an impressive size reduction of 75%. Additionally, an innovative U-shaped DRA, inspired by rectangular DRA, has been proposed. This U-shaped design offers a broader bandwidth of 35% while achieving a size reduction of 50% when excited using a hook-shaped co-axial probe.

In [17], a compact wideband rectangular dielectric resonator antenna using perforations and edge grounding is proposed as shown in Fig. 4. First a rectangular DRA is designed using dielectric waveguide model [3, 4] to resonate at 2.39 GHz. For excitation offset, coaxial probe feeding is used. Size reduction is achieved with the edge grounding method, and impedance bandwidth is improved by incorporating perforations. Perforations reduce the effective dielectric constant and thus improves impedance bandwidth. The proposed perforated rectangular DRA is made compact by approximately half of the original size. Improved BW up to 56% is attained, and a shift in resonant frequency is observed from 2.39 GHz to 2.82 GHz as shown in Fig. 5. The radiation pattern is affected at the plane where metal plate is attached. The gain and radiation efficiency are in the acceptable limit.

Effective permittivity is calculated using [3]:

$$\epsilon_{\text{eff}} = \left(\frac{S}{p}\right)^2 + \epsilon_r \left[1 - \left(\frac{S}{p}\right)^2\right]$$

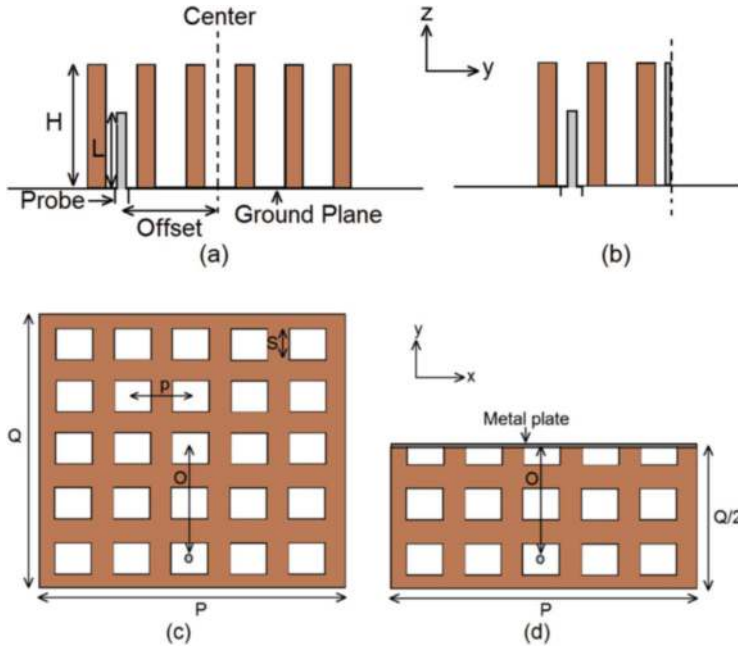


**Fig. 4** Side view and top view (without ground plane): (a, c) Perforated rectangular DRA. (b, d) Proposed half-perforated edge-grounded rectangular DRA ( $P = Q =$  length or width of RDRA). The markings show dimensions of the square slot  $S$ , height of rectangular DRA  $H$ , offset  $O$ , probe length  $L$ , and periodicity  $p$

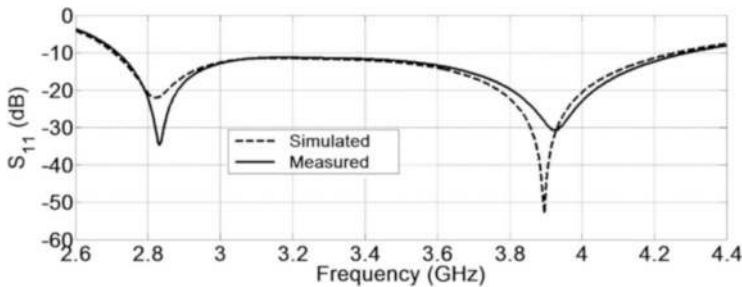


**Fig. 5**  $S_{11}$  response of the proposed rectangular DRA

where  $S$  represents dimension of the square slots,  $\epsilon_r$  dielectric constant,  $\epsilon_{\text{eff}}$  effective dielectric constant, and  $p$  periodicity. The optimum value of  $S = 4$  mm and  $S/p = 0.6$  for  $\epsilon_r = 10.2$ . The calculated value of  $\epsilon_{\text{eff}}$  is approximately 6.11, which is around 40% lower than the original dielectric constant. This will lower the quality factor and thus improves the bandwidth. This design is further made compact by reducing the size to quadrature of original size and maintaining impedance bandwidth of 47% [18]. The wideband, dual-band, and single band response can be obtained from

the perforated rectangular DRA. The effective dielectric constant is adjusted to attain different bandwidth response, which makes the antenna suitable for various applications [19]. In order to fill the slot with different dielectric constants, the feed is placed outside the rectangular DRA wall. In order to improve impedance matching, a rectangular microstrip patch is used between the wall of the DRA and the feeding probe. It should be noted that only one dielectric material at a time is used for filling the slots. The wideband design offers a bandwidth of 32.55% at a resonant frequency of 2.92 GHz (2.716–3.64 GHz) for air-filled slots. The dual-band designs offer a bandwidth of 11% (2.23–2.47 GHz) at 2.32 GHz; 3.2% (3.94–4.07 GHz) at 4.01 GHz for dielectric material with  $\epsilon_r = 9.2$ ; 8.7% (2.1–2.29 GHz) at 2.18 GHz; and 3% (3.70–3.81 GHz) at 3.76 GHz for  $\epsilon_r = 12.85$ . The single-band design offers a bandwidth of 12% (2.35–2.65 GHz) at 2.48 GHz for  $\epsilon_r = 6.15$ .

The circularly polarized (CP) antennas are favored over linearly polarized ones due to misalignment issues between transmitter- and receiver-side antenna. Additionally, they address multipath problems arising from reflections of buildings and the ground. These circularly polarized antennas play a crucial role in modern wireless communication, satellite communication, and radar systems. To achieve CP, researchers have explored rectangular DRAs. This polarization state can be achieved through dual- or single-feed methods. The stringent conditions involve exciting two orthogonal modes with equal amplitude and quadrature phase. While dual-fed CP rectangular DRAs offer a wide axial ratio bandwidth compared to single-fed designs, the dual-feed approach necessitates additional space to external feeds. Over time, numerous CP antennas have been proposed based on these two methods [3, 4]. A wideband CP rectangular DRA is designed with single feed to operate at 5.8 GHz. Initially, a square rectangular DRA is designed and excited with an offset coaxial probe. The wide bandwidth is achieved by a high aspect ratio [4] that excites two resonant modes,  $TE_{111}$  and  $TE_{113}$ , and merges them in the bandwidth of operation. This wide-band rectangular DRA is made CP through perturbation, achieved by strategically placing four square-shaped slots along the diagonals. The size of the slots is different along both diagonals, but the shape is symmetrical. They excite two orthogonal modes with a phase difference of  $90^\circ$ , which is a stringent condition to achieve CP. The measured 10 dB impedance bandwidth is 48% (4.7–7.7 GHz) while in simulations 41% (4.8–7.3 GHz) for  $S_{11} \leq -10$  dB. The axial ratio is simulated and measured in the boresight direction. The measured 3 dB axial ratio bandwidth is 11.5% (5.7–6.4 GHz) while in simulations 10% (5.6–6.2 GHz) as shown in Fig. 6. Experimental results are in close agreement with predicted results. However, small differences exist because of fabrication inconsistencies like placement of different dielectric layers, air gap formed between dielectric and ground plane, etc.

Next, a wideband circularly polarized rectangular DRA using two square-shaped slots along the diagonal is proposed and investigated to improve axial ratio bandwidth further. The square-shaped slots excite two orthogonal modes and provide a phase difference of  $90^\circ$  required to achieve circular polarization as mentioned earlier. Antenna prototype is experimentally verified and depicts

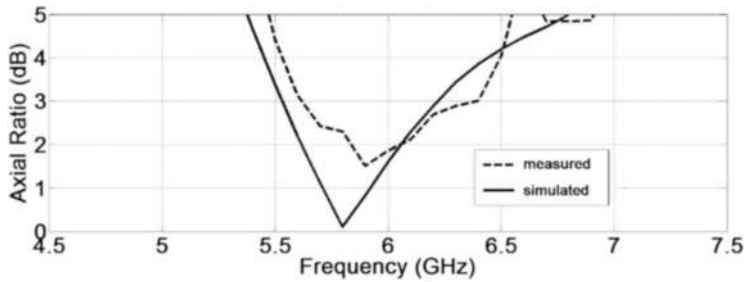


**Fig. 6** Axial ratio plot for four-slot CP rectangular DRA

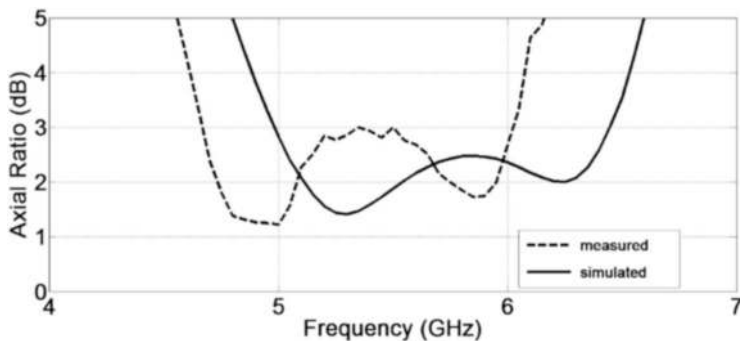


**Fig. 7** Axial ratio plot for two-slot CP rectangular DRA

reasonably good performance over the complete band. It offers 3 dB axial ratio bandwidth from 4.7 to 6 GHz as shown in Fig. 7. The 10 dB impedance bandwidth is attained from 4.6 to 7 GHz. Hence, a complete axial ratio band is usable. The maximum gain of 5.6 dBi is obtained for right-hand circularly polarized waves with the efficiency [14] of more than 85% over the complete band.

Further, new rectangular DRAs are proposed [21–24] to meet the requirement of modern communication systems. DRAs are designed mainly to achieve compactness and wide impedance bandwidth. In [21], a compact half H-shaped DRA inspired from rectangular DRA is designed and developed. It offered a bandwidth of 92% (4.3–8.9 GHz) at 5 GHz. A tuning fork-shaped DRA inspired from rectangular DRA is designed in [22]. It offers a wide impedance bandwidth of 154% (1.5–4.2 GHz) at 1.75 GHz. A novel low-profile stacked edge-grounded rectangular DRA with compact size is designed for UWB applications [23]. It almost covers ultrawideband (UWB) from 3.6 to 11.8 GHz. A novel golden ratio-aided fractal rectangular DRA for C-band applications has been proposed in [24]. The structure is derived from the Fibonacci series approach, meticulously maintaining the golden ratio. This innovative design based on the Fibonacci series and Minkowski fractal investigates rectangular DRA for the first time. To validate the concept, a prototype is developed and tested. Results reveal that the prototype offered a measured and

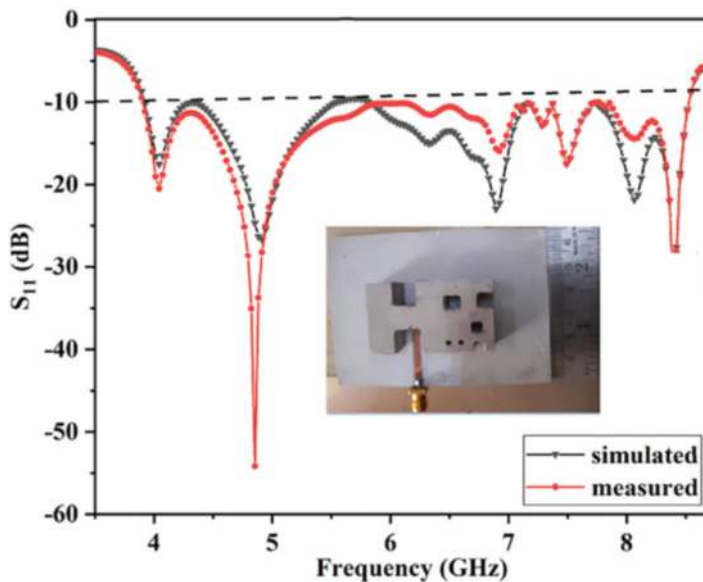


**Fig. 8**  $S_{11}$  response of the proposed fractal rectangular DRA with the inset view of prototype

simulated impedance bandwidth of 82% (3.80–8.70 GHz) as shown in Fig. 8. Additionally, a stable radiation pattern is observed over the desired frequency band with a peak measured gain of 7.62 dBi. Furthermore, the proposed fractal DRA exhibits excellent broadside directional radiation patterns, low cross-polarization levels, and favorable gain characteristics, making it a promising candidate for C-band communication.

### 3 Conclusion

Rectangular DRAs with high bandwidth and small size can be designed by using perforations and edge grounding techniques. These techniques enhance both bandwidth and size performance of the rectangular DRAs. The edge grounding technique with an extra metal plate lowers the efficiency of DRAs, which may not suit some applications. DRAs are better than conventional metallic antennas for modern wireless communication, which uses high-frequency bands. Satellite communication and radar systems need transmitter- and receiver-side antennas to align well. Circularly polarized DRAs do not depend on this alignment and also avoid multipath issues from reflections of buildings, grounds, etc. Using the perforation technique, we can design and develop circularly polarized rectangular DRAs as well.

## References

1. C.A. Balanis, *Antenna Theory, Analysis, and Design* (Wiley, 1997)
2. G. Kumar, K.P. Ray, *Broadband Microstrip Antennas* (Artech House, 2003)
3. A. Petosa, *Dielectric Resonator Antenna Handbook* (Artech House, 2007)
4. K.M. Luk, K.W. Leung, *Dielectric Resonator Antenna* (Research Studies Press Ltd., 2002)
5. D.J. Masse, R.A. Pucel, D.W. Readey, C.P. Hartwig, A new low-loss high-k temperature-compensated dielectric for microwave applications. *Proc. IEEE* **59**(11), 1628–1629 (1971)
6. D. Kajfez, P. Guillon, *Dielectric Resonators*, 2nd edn. (Noble Publishing Corporation, Atlanta, 1998)
7. S.A. Long, M.W. McAllister, L.C. Shen, The resonant cylindrical dielectric cavity antenna. *IEEE Trans. Antennas and Propag* **AP-31**(3), 406–412 (1983)
8. M.W. McAllister, S.A. Long, Resonant hemispherical dielectric antenna. *Electron. Lett.* **20**(16), 657–659 (1984)
9. A. Petosa, A. Ittipiboon, Dielectric resonator antennas: A historical review and the current state of the art. *IEEE Antennas Propag. Mag.* **52**(5), 91–116 (2010)
10. R.K. Mongia, P. Bhartia, Dielectric resonator antennas—A review and general design relations for resonant frequency and bandwidth. *Int. J. Microw. Millimeter Wave Comput. Aided Eng.* **4**, 230–247 (1994)
11. Y.M.M. Antar, D. Cheng, G. Seguin, B. Henry, M.G. Keller, Modified waveguide model (MWGM) for rectangular resonator antenna (DRA). *Microw. Opt. Technol. Lett.* **19**(2), 158–160 (1998)
12. R.K. Mongia, Theoretical and experimental investigations on rectangular dielectric resonators. *IEEE Proc.-H* **139**, 98–104 (1992)
13. R.K. Mongia, A. Ittipiboon, Theoretical and experimental investigations on rectangular dielectric resonator antennas. *IEEE Trans. Antennas Propag.* **45**(9), 1348 (1997)
14. H.A. Wheeler, The radiansphere around a small antenna. *Proc. IRE* **47**, 1325–1331 (1959)
15. M.T.K. Tam, R.D. Murch, Half volume dielectric resonator antenna designs. *Electron. Lett.* **33**(23), 1914–1916 (1997)
16. A.A. Kishk, H. Wei, Size reduction method for dielectric resonator antennas. *IEEE Antennas Propag. Mag.* **53**, 26–38 (2011)
17. P. Patel, B. Mukherjee, J. Mukherjee, Compact wideband rectangular dielectric resonator antenna using perforations and edge grounding. *IEEE Antennas Wirel. Propag. Lett.* **14**, 490–493 (2015)
18. P. Patel, G.S. Reddy, J. Mukherjee, B. Mukherjee, New wideband quadrature rectangular dielectric resonator antenna, in *2015 European Microwave Conference (EuMC), Paris*, (2015), pp. 1335–1338
19. E. Vernekar, P. Patel, M. Erramshetty, Perforated Rectangular Dielectric Resonator Antenna for Wideband, Dual Band and Single Band Application, in *2018 48th European Microwave Conference (EuMC), Madrid*, (2018), pp. 384–387
20. P. Patel, B. Mukherjee, J. Mukherjee, Wideband circularly polarized rectangular dielectric resonator antennas using square-shaped slots. *IEEE Antennas Wirel. Propag. Lett.* **15**, 1309–1312 (2016)
21. A. Gaonkar, P. Patel, Compact half H-shaped dielectric resonator antenna for wideband applications. *Microw. Opt. Technol. Lett.* **64**, 1849–1857 (2022)
22. A. Gaonkar, P. Patel, Novel compact and wideband tuning fork shaped DRA. *AEU Int. J. Electron. Commun.* **54**, 221–227 (2022)
23. A. Gaonkar, A. Nair, P. Patel, Novel low profile stacked edge grounded RDRA with compact size for UWB applications. *Microw. Opt. Technol. Lett.* **65**, 2011–2020 (2023)
24. A. Gaonkar, M. Ayyappan, P. Patel, A novel fractal RDRA for C-band applications. *IEEE Trans. Compon. Packag. Manuf. Technol.* **13**(7), 995–1002 (2023). <https://doi.org/10.1109/TCPMT.2023.3295480>

# A Low-Profile Perturbed Convex Conformal CDRA



**Manshree Mishra, Pramod Kumar Gupta, Garima Tiwari, Atul Kumar,  
and Biswajeet Mukherjee**

## 1 Introduction

Concerning the growing demand for wireless communication, researchers are currently interested in the design of antennas that incorporate a variety of qualities, including high gain, wide bandwidth, a small dimension, high efficiency, and negligible ohmic loss. Such requirements are fulfilled by dielectric resonator antennas (DRAs) [1, 2]. Investigating DRAs on level ground planes (GP) in various shapes, like cylindrical, rectangular, hemispherical, sector, annular, and triangle DRAs, is done using many theoretical and numerical methods [3–32].

Several efforts to broaden the antenna's bandwidth have been studied in [3–14]. In [3], the fundamental cylindrical dielectric resonator antenna (CDRA) perturbation excites higher-order modes, which also reduce the CDRA's effective permittivity, aiding in increasing the antenna's working frequency range by lowering the Q factor of the antenna. In [4], the study focuses on metallic perturbation within a DRA's body to improve modal field purity and drastically decrease undesired cross-polarized (XP) radiations.

---

M. Mishra · P. K. Gupta · G. Tiwari

Department of Electronics and Communication Engineering, PDPM IITDM Jabalpur, Jabalpur, Madhya Pradesh, India

A. Kumar

Department of Electronics and Communication Engineering, Maulana Azad National Institute of Technology, Bhopal, Madhya Pradesh, India

B. Mukherjee (✉)

Department of Electronic Science, University of Delhi, New Delhi, India



In [5], wideband and dual-band capabilities of the DRA are attained by incorporating modified Sierpinski structure into the DRA. A broad fractal rectangular dielectric resonator antenna (RDRA) for wireless communication is introduced in [6] and is based on the dipole with a hook shape. In [7], a coaxial probed symmetrical triangular notched lateral cylindrical dielectric resonator antenna (LCDRA) is described. The CDRA has its longitudinal axis parallel to and its lateral surface maintained on the GP. Compared to the CDRA, the LCDRA has a significantly broader impedance bandwidth and a lower resonant frequency. To further increase impedance bandwidth, two symmetrical triangular notches are added to two perpendicular edges of the LCDRA. In [8], the 4-element CDRA is excited by a tiny dielectric rod that serves as a field launching element with an extended probe feed. In [9], to get a broad frequency with minimal cross-polarization and directional gain, CDRA is stimulated using a dual feeding network. This is an example of a probe feed network with dual differential configuration for CDRA. With minimal cross-polarization and a wide bandwidth, this proposed structure provides directional gain. In [10], dielectric materials are shaped to create wideband DRAs. Conical-shaped DRAs are investigated experimentally, with certain findings being validated mathematically. Four distinct cone forms are taken into consideration. It is believed that the excitation is a coaxial probe that has been moved away from the cone axis. In [11], the air gap between a microstrip line and a CDRA affects the impedance bandwidth, unloaded Q-factor, resonant frequency, and directivity. An investigation on a compact, half CDRA constructed of a ceramic material with a high permittivity is carried out in [12]. Peak gains in the azimuth plane are 3.6 dBi, while the elevation plane is 5.5 dBi. The DRA exhibits wide and stable radiation characteristics throughout the frequency band of 2.32–2.5 GHz. In [13], excitation occurs via a microstrip feed line to an inverted half CDRA studied to achieve wideband. Surprisingly, the author discovered that the antenna's total radiating surface area increases. When the surface-area-to-volume (S/V) ratio of the antenna decreases, the antenna's Q factor also decreases, increasing the antenna's total bandwidth. In [14], it is recommended to generate a microstrip with an annular shape and a matching C-shaped-etched GP as a quad-band cylindrical DRA.

To increase the antenna's gain, various works are reported in [15–29]. A DRA is fitted with a corrugated circular ring-shaped meta superstrate in order to increase the peak gain to 11.9 dBi [15]. In [16], the substrate loading of a  $5 \times 5$  unit-cell SRR improves the DRA gain. Currents with opposing orientation develop in split rings when SRRs are connected with an RDRA in the near-field region; these currents effectively cancel the transverse fields. In [17], 50-unit metamaterial (MTM) cells are arranged to create an antenna. A dielectric substrate with two parallel, eight-shaped conducting strips etched across both faces results in a negative refractive index of 7.3–8.1 GHz constituting each unit cell of the RDRA. This allows the RDRA to cover its maximum bandwidth and enhance its gain. The high gain performance of the differentially coplanar-fed filtering DRA loaded

with metallic vias is designed in [18]. A rectangular filtering DRA with a broad bandwidth and high gain is studied in [19]. A bottom-side substrate excites a microstrip-connected slot in the microstrip feed line, which is intended to supply two radiation nulls in the frequency range for a filtering function. In [20], a metallic boundary configuration combined with DRA is used to amplify radiation in a certain direction in order to boost the gain for wideband wireless applications. In [21], at 340 GHz, a higher-order DRA achieves great gain. The low-loss dielectric resonator of the antenna is made of high-resistivity silicon material, and the necessary modes are activated by on-chip feeding-patch complementary metal-oxide-semiconductor (CMOS) technology. By excitation of  $TE_{017}$ , a higher-order mode, the antenna gain is significantly increased to 6.7 dBi. In [22], for high gain, circularly polarized two-layered RDRA is taken into consideration. The DRA and a dielectric coat layer with corresponding dielectric constants of  $\epsilon_r = 10$  and 3.5 are part of the design configuration. The outer layer has a high gain of 11 dBic and a larger impedance with CP bandwidths of 9.5% and 21%, respectively. In [23], using near-zero-index metamaterial, a higher-order-mode ( $TE_{031}$ ) dielectric resonator is employed to investigate the high gain of a quasi-Yagi magnetic dipole antenna. By using the higher-order  $TE_{031}$  mode as a magnetic-dipole driver, a high-gain quasi-Yagi antenna can be designed. In [24], it is successfully demonstrated that a  $2 \times 2$  CDRA array using a microstrip aperture feed technique may achieve a gain of 13.9 dBi between 6.62 and 7.15 GHz. For maximum gain, a unique aperture feeding arrangement with  $2 \times 2$  wideband dual-polarized DRAs is investigated in [25]. For millimeter-wave applications, an RDRA array with strong gain and bandwidth is demonstrated in [26]. In [27], uniaxial anisotropic materials are employed in RDRAs to improve boresight gain by enhancing side wall radiation. With a high broadside gain of 8.4 dBi, the DRA walls, various boundary conditions and electromagnetic wave interaction result in an impedance bandwidth of 20.65% (3.17–3.9 GHz).

In [28], employing equilateral triangular uniaxial anisotropic DRAs increases impedance bandwidth and gain in the boresight direction. Increase in sidewall radiations lead to gain enhancement and decrease in the structure's effective permittivity result in bandwidth enhancements. In [29], a different technique for creating grooves on an RDRA's side walls in order to achieve a 9.6 dBi gain is examined. The gain of the DRA is improved by increasing radiations from the side wall boundary by adding corrugated engraved grooves to the side walls.

In [30–32], various works are reported for the design and development of low-profile CDRA. A completely novel, miniature, low-profile stacked DRA for wideband applications, by also maintaining a high radiation efficiency with small electrical size is presented in [30]. A circular disc DR antenna, which is low profile and has a low resonant frequency, is constructed in [31] using a material with a very high dielectric permittivity. In [32], an extremely low aspect ratio less than or equal to 6 is chosen to construct a low-profile antenna.

In modern communication systems including RADAR systems, smart antennas, beam steering array antennas, wearable communication devices for body-area networks, spatial domain multiple access, Internet of Things (IoT), and aerospace applications, antennas on conformal structures have become essential components [33]. Flexible antennas are desirable because they may be employed on flexible surfaces. Conformal DRAs can offer more gain and a wider bandwidth. A conformal antenna has a radiating element installed on or incorporated into an evenly curved surface, which can be spherical, cylindrical, or any other shape. The conformal antenna has several benefits, including the ability for a 360-degree coverage, a low amount of undesired radiation, and lightweight. It is possible to review a summary of the body of research on conformal DRA in [34–38]. DRA with curved GP that are conformally concave and convex is suggested and examined in [34]. Using approximate models with a range of boundary conditions, the eigenmode approach and single-mode approximation are used to mathematically analyze their resonant frequencies and field distributions. In [35], on both flat and curved GP, the theory of homogeneity for stacked DRA is examined. To identify and assess the deficiencies of the widely used static capacitance models, a more thorough evaluation is conducted. To give better empirical equations, the effective medium theory is presented. High-dielectric-constant (HiK) patches and metal plates are used to load compact, arc-shaped conformal DRAs in [36]. Their concept of miniaturization is examined from several perspectives. The role of the conformal ground in size reduction is characterized by closed-form expressions that have been generated. In [37], ground effects are studied and used to accomplish various radiation performances on conformal arc-shaped. DRAs operating in the  $TE_{118}^Z$  mode. In [38], a low-profile conformal CDRA with perturbation excited by differential feed is presented and analyzed. At 7.7 GHz and 8.7 GHz, the  $TM_{118}$  and  $TM_{218}$  modes are observed respectively. High broadside gain is obtained at the bent angle of  $\varphi_1 = 24^\circ$ .

In this chapter, perturbed CDRA with convex conformal GP for X band application is presented and examined. Analysis is done on how bent GP affects DRA's radiation performance. To increase the bandwidth of the antenna, a higher electric field region is perturbed. A comparison is made between the proposed design and the perturbed flat CDRA. Design and simulation of the CDRA are done using CST Studio with transient domain solver.

## 2 Antenna Design and Analysis

The proposed CDRA structure is designed in CST Studio with transient domain solver as depicted in Fig. 1. Dimensions from a 3D perspective view are shown in Fig. 1a. Side and bottom views of the proposed work are shown in Fig. 1b, c, respectively. The cylindrical dielectric resonator (CDR) having a radius of

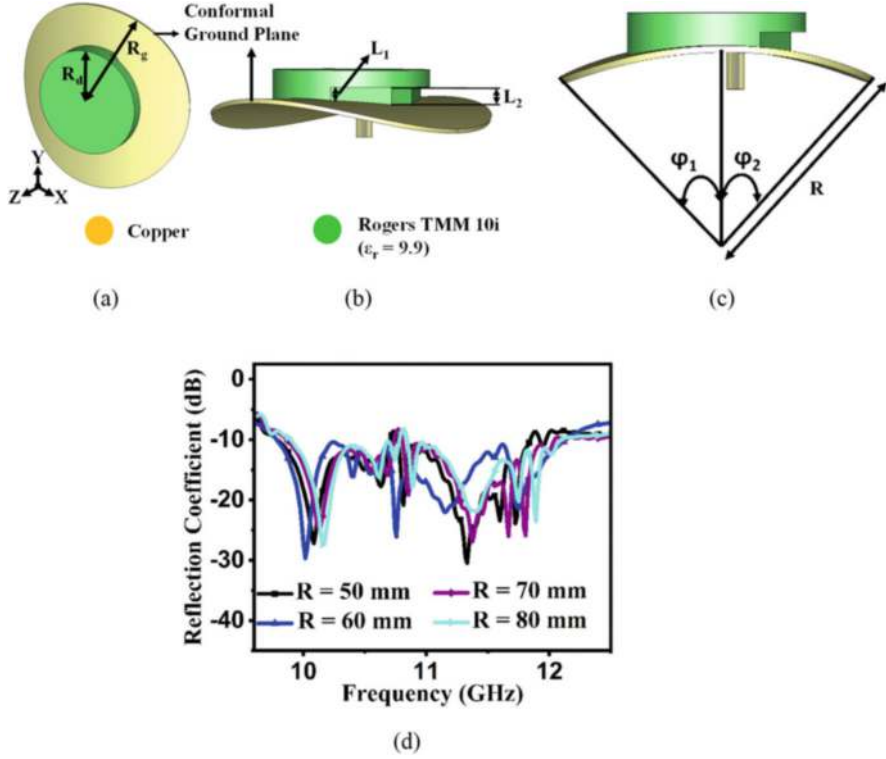


**Fig. 1** Convex conformal CDRA. (a) Dimensions from 3D perspective view  $R_d = 14$  mm,  $R_g = 50$  mm. (b) Side View  $L_1 = 2.3$  mm,  $L_2 = 3.1$  mm. (c) Bottom View  $\phi_1 = \phi_2 = 24.5^\circ$ ,  $R = 60$  mm. (d) Reflection coefficient at different radius  $R$

$R_d = 14$  mm and a height of  $H = 5$  mm is designed on Rogers TMM 10i having a permittivity of  $\epsilon_r = 9.9$ , mounted on the convex conformal GP of radius  $R = 60$  mm. The CDRA is excited using a  $50 \Omega$  coaxial cable. Initially, CDRA is designed to excite fundamental mode, by perturbing the basic CDRA higher-order modes generated, which results in the increase of antenna bandwidth. According to the perturbation theory, resonant frequency will increase if higher magnetic field ( $H$ ) portion is perturbed, and resonant frequency will decrease if higher electric field ( $E$ ) portion is perturbed [3]. The effect of this perturbation on the fundamental CDRA resonant frequency can be better understood using the following Eq. [3]:

$$\frac{\omega - \omega_0}{\omega_0} \approx \frac{\int \int \int_{\Delta \tau} (\mu |H_0|^2 - \epsilon |E_0|^2) d\tau}{\int \int \int_{\tau} (\mu |H_0|^2 + \epsilon |E_0|^2) d\tau} \quad (1)$$

The denominator is proportional to the total energy stored, whereas terms in the numerator are proportional to the electric and magnetic energies removed by the perturbation.

$$\frac{\omega - \omega_0}{\omega_0} \approx \frac{\Delta \bar{W}_m - \Delta \bar{W}_e}{W} \quad (2)$$

where  $W$  is the total energy contained within the original cavity and  $\Delta \bar{W}_m$  and  $\Delta \bar{W}_e$  are time-average electric and magnetic energies originally contained in  $\Delta \tau$ .

$$\frac{\omega - \omega_0}{\omega_0} \approx \frac{(\bar{w}_m - \bar{w}_e) \Delta \tau}{\hat{w} \tau} = C \frac{\Delta \tau}{\tau} \quad (3)$$

In the proposed work, a higher-electric field portion is perturbed to increase the bandwidth of the antenna.

The radiation properties of convex conformal DRA and CDRA are explained by the geometric theory of diffraction (GTD). The creeping wave appears to radiate out surface diffracted rays in the tangent direction and to move along curved surfaces as surface rays [37]. Diffracted rays can cause the power to be sent to the squint side, producing split, tilted, or even larger beams. Equation (4) supports the use of the (CST) solver to simulate the performance of CCCDRA with various GP configurations.

$$\begin{aligned} E_\varphi(\varphi) &= C(r) [E_{\text{Surf}}(\varphi) + E_{\text{Edge}}(\varphi)] \\ &= -j\omega \frac{\mu_0}{4\pi} \frac{e^{-jkr}}{r} \int_{-\varphi_1}^{\varphi_2} e^{jka \cos(\varphi - \varphi')} \times \left\{ \begin{aligned} &I_{\text{surf}}(\varphi') F_{\text{surf}}(\varphi - \varphi') + \\ &I_{\text{edge}}(\varphi') F_{\text{edge}}(\varphi - \varphi') \times \\ &[\delta(\varphi' + \varphi_1) + \delta(\varphi' - \varphi_2)] \end{aligned} \right\} d\varphi' \end{aligned} \quad (4)$$

where

$$\begin{aligned} I_{\text{surf}}(\varphi) &= I^+ - R \cdot I^- = I_0 \left[ \frac{e^{-\alpha|\varphi|} e^{-j\beta|\varphi|} -}{R e^{\alpha(|\varphi| - 2\varphi_{1,2})} e^{j\beta(|\varphi| - 2\varphi_{1,2})}} \right]; \\ I_{\text{edge}}(\varphi) &= D \cdot I_0 e^{-(\alpha + j\beta)|\varphi|}; \beta = \frac{\pi}{\varphi_{dr}}; D^2 + R^2 = 1; \\ F_{\text{surf}}(\varphi) &= \cos \varphi \cdot u\left(|\varphi| - \frac{\pi}{2}\right); F_{\text{edge}}(\varphi) = \cos \varphi \end{aligned}$$

where  $K$  is the free space wavenumber,  $C(r)$  the pattern factor,  $D$  the diffraction at two edges,  $R$  the reflection on both edges,  $\delta(x)$  the impulse function,  $u(x)$  the unit step,  $\beta$  the effective phase constant, and  $\alpha$  the surface diffraction.

On a curved ground, smooth convexity causes the emergence of surface and edge diffraction, whereas on planar GP edge, diffraction is observed. The GP of a CDRA is conformed at a radius of 60 mm for obtaining better performance of

the antenna. Here, the symmetrical ( $\varphi_1 = \varphi_2$ ) GP is chosen because co-polarization is influenced by the symmetrical GP and cross polarization remains constant. The maximum bandwidth of 21% is achieved at a radius of 60 mm as shown in Fig. 1d. At  $R = 50$  mm, 70 mm, and 80 mm, the bandwidth obtained is 1 GHz, 0.9 GHz, and 0.8 GHz, respectively.

### 3 Antenna Design Methodology

The CDRA is designed and simulated using CST Studio and a transient domain solver. The Rogers TMM 10i ( $\epsilon_r = 9.9$ ) is used in the design of the 14 mm radius cylindrical dielectric resonator (CDR). The GP has a radius of 25 mm. Figure 2 depicts the proposed antenna design methodology. Three steps are involved in the design of the CDRA. Figure 2a, b show the perspective and bottom views of Ant.1, Ant.2, and Ant.3, respectively. Initially, Ant.1 is first created with a basic coaxial probe without perturbation as shown in Fig. 2a, b. Further, Ant.2 is obtained by perturbing Ant.1 as depicted in Fig. 2a, b, which lowers the resonant frequency as shown in Fig. 2c. This is because, according to perturbation theory, when an electric field's higher radiating portion is perturbed, the resonant frequency decreases; however, when a strong magnetic field is present at the location of perturbation, the resonant frequency increases [3]. Based on the static capacitance model [3], the perturbation causes an approximate reduction in effective permittivity, which causes a drop in the quality factor and an increase in the bandwidth of the CDRA. The shape and position of the perturbation are selected to maximize the surface-area-to-volume (S/V) ratio. The CDRA's bandwidth increases as the S/V ratio reaches its maximum. Additionally, the appropriate frequency range is attained at this specific point. Finally, on Ant.2, convex conformal GP is introduced to obtain Ant.3, as illustrated in Fig. 2a. In the conformal DRA, there are TE and TM modes; in the bending DRA, there is no hybrid mode [34, 37]. The TE and TM modes' fields are axisymmetric and do not change in azimuth. Conversely, the hybrid modes' fields fluctuate in the azimuth direction [37].

When it comes to efficiency and bandwidth, CDRA provides better and more flexible results. As seen in Fig. 2c, the bandwidth acquired for the proposed CDRA is 21%, which is more than the bandwidth of Ant.1 and Ant.2. The perturbation causes the field to be spread asymmetrically, which lowers the antenna's gain for Ant.2 at lower frequencies. The gain of Ant.3 further decreases because the convex conformal GP cannot concentrate the fields in a particular region, but the antenna still has a high gain, which is greater than 5 dBi throughout the entire frequency band. Ant.3's peak gain is 7 dBi at 11.5 GHz frequency as shown in Fig. 2d.

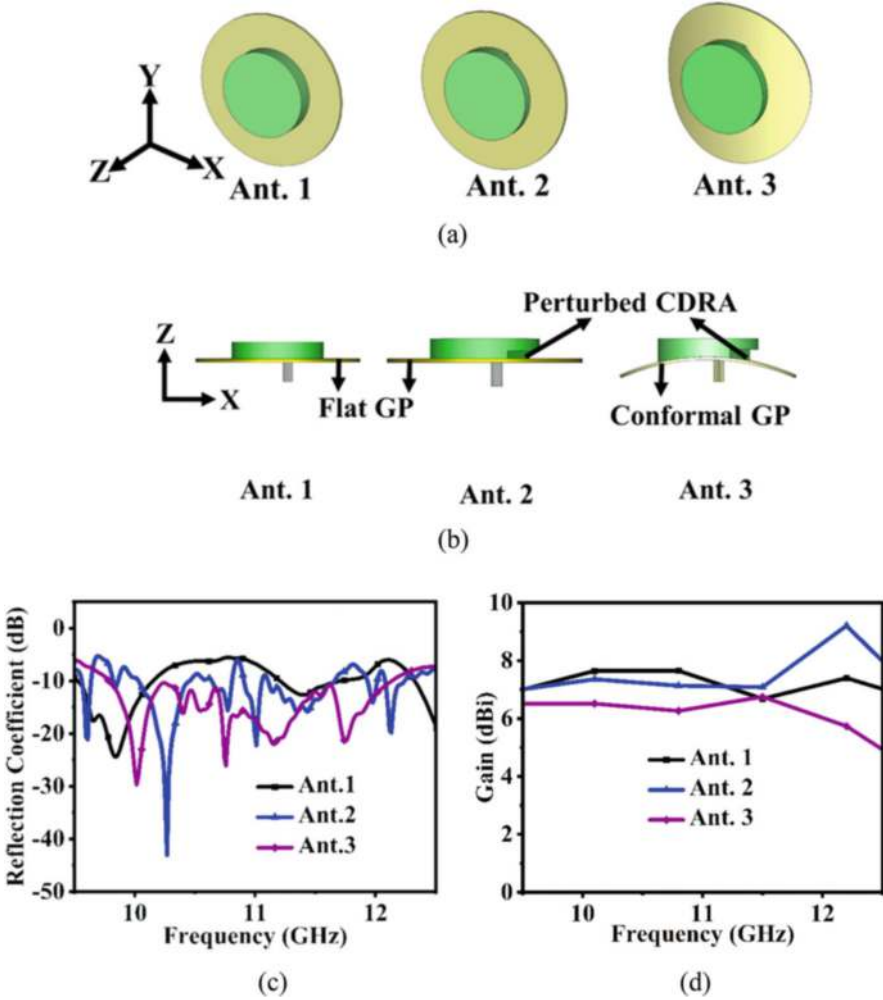


**Fig. 2** Antenna design methodologies. (a) Perspective view of CDRA. (b) Bottom view of CDRA. (c) Reflection coefficient comparison of all three-step antennas. (d) Gain comparison of all three-step antennas

## 4 Parametric Study

A parametric analysis of the height and radius of the CDRA is carried out. As seen in Fig. 3a, a maximum bandwidth of 21% (9.7–12.1 GHz) is attained at height  $H = 5$  mm, and as shown in Fig. 3b, a maximum peak gain of 7 dBi is attained at 11.5 GHz. At  $H = 3$  mm, 4 mm, and 6 mm, the maximum bandwidth of 0.1 GHz, 0.3 GHz, and 0.7 GHz is obtained, respectively, and a peak gain of 7.1 dBi, 7.3 dBi, and 7.2 dBi at 10.1GHz, 10.1 GHz, and 10.8 GHz is obtained, respectively.



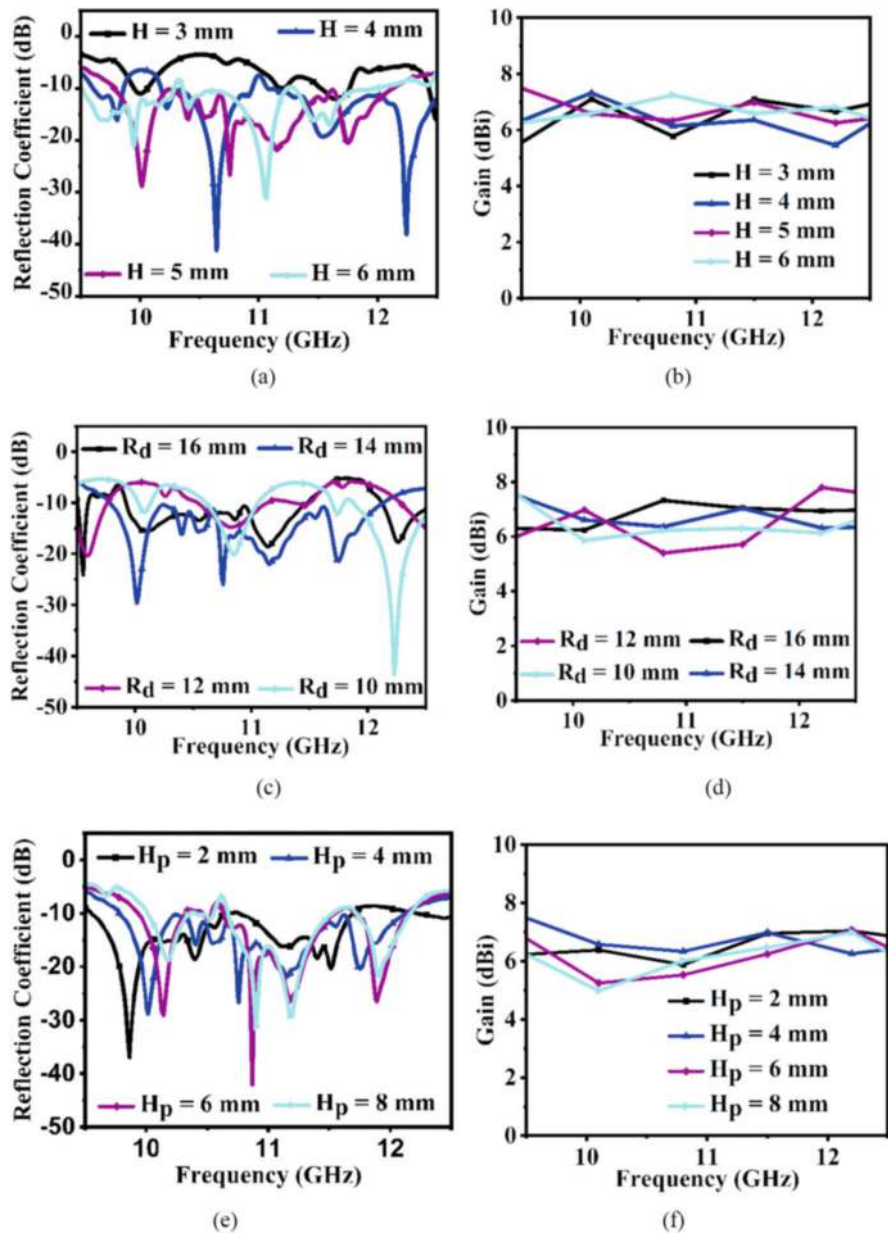


**Fig. 3** Parametric study on various parameters of CDRA. (a) Reflection coefficient at CDRA height (H), (b) gain at CDRA height (H), (c) reflection coefficient at CDRA radius ( $R_d$ ), (d) gain at CDRA radius ( $R_d$ ), (e) reflection coefficient at CDRA perturbed height ( $H_p$ ), (f) gain at CDRA perturbed height ( $H_p$ )



Antenna area increases in tandem with antenna height, leading to an increase in S/V ratio, a decrease in Q factor, and an increase in antenna band. Because the effective aperture area grows with CDRA height, the antenna gain also increases. The effect of the radius ( $R_d$ ) of the CDRA is shown in Fig. 3c and Fig. 3d and at  $R_d = 14$  mm maximum bandwidth of 21% and a peak gain of 7 dBi at 11.5 GHz frequency is achieved. At  $R_d = 10$  mm, 12 mm, and 16 mm, the maximum bandwidth of 1.1 GHz, 0.2 GHz, and 1.5 GHz, respectively, and a peak gain of 6.2 dBi, 7.7 dBi, and 7.3 dBi at 10.8 GHz, 12.2 GHz, and 10.8 GHz are obtained, respectively. Furthermore, the CDRA's height and radius are selected to make it a low-profile antenna. The proposed DRA has a low profile of  $0.16 \lambda_0$ , where  $\lambda_0$  is the wavelength of the lower cutoff frequency. A parametric study is performed on the height of the perturbation and at  $H_p = 4$  mm, maximum bandwidth of 21% is achieved, and a peak gain of 7 dBi at 11.5 GHz frequency is obtained as shown in Fig. 3e, f. Higher-order modes are generated by perturbing the basic CDRA, increasing the antenna's bandwidth. At  $H_p = 2$  mm, 6 mm, and 8 mm, the bandwidth obtained is 0.9 GHz, 0.6 GHz, and 0.3 GHz, respectively, as well as a peak gain of 7 dBi at 12.1 GHz.

## 5 Results and Discussion

The proposed antenna has an impedance bandwidth of 2.3 GHz, which ranges from 9.8 GHz to 12.1 GHz as shown in Fig. 4a. The peak gain of the proposed CDRA is 7 dBi at 11.5 GHz, and 94.5% efficiency is obtained at 10.8 GHz as shown in Fig. 4b. The radiation pattern for both  $\varphi = 0^\circ$  and  $\varphi = 90^\circ$  is shown in Fig. 5, and it can be observed that the cross polarization is below  $-20$  dB. Table 1 presents a comparison between the proposed work and the other simulated work, and it can be observed that both the bandwidth and gain is superior to the other reported work.

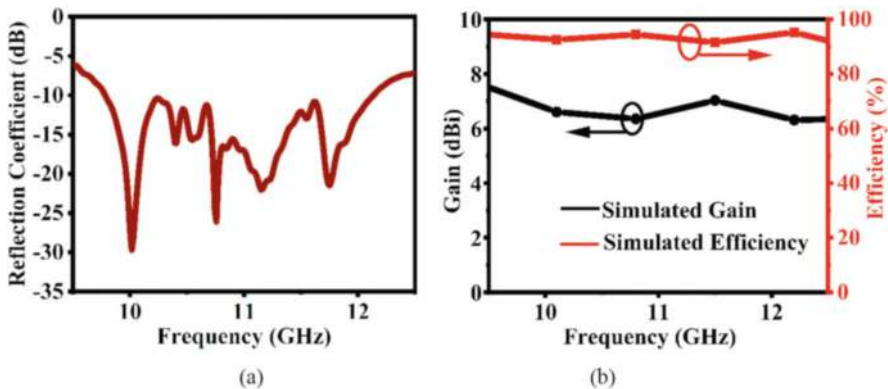


Fig. 4 Proposed work. (a) Reflection coefficient. (b) Gain and efficiency

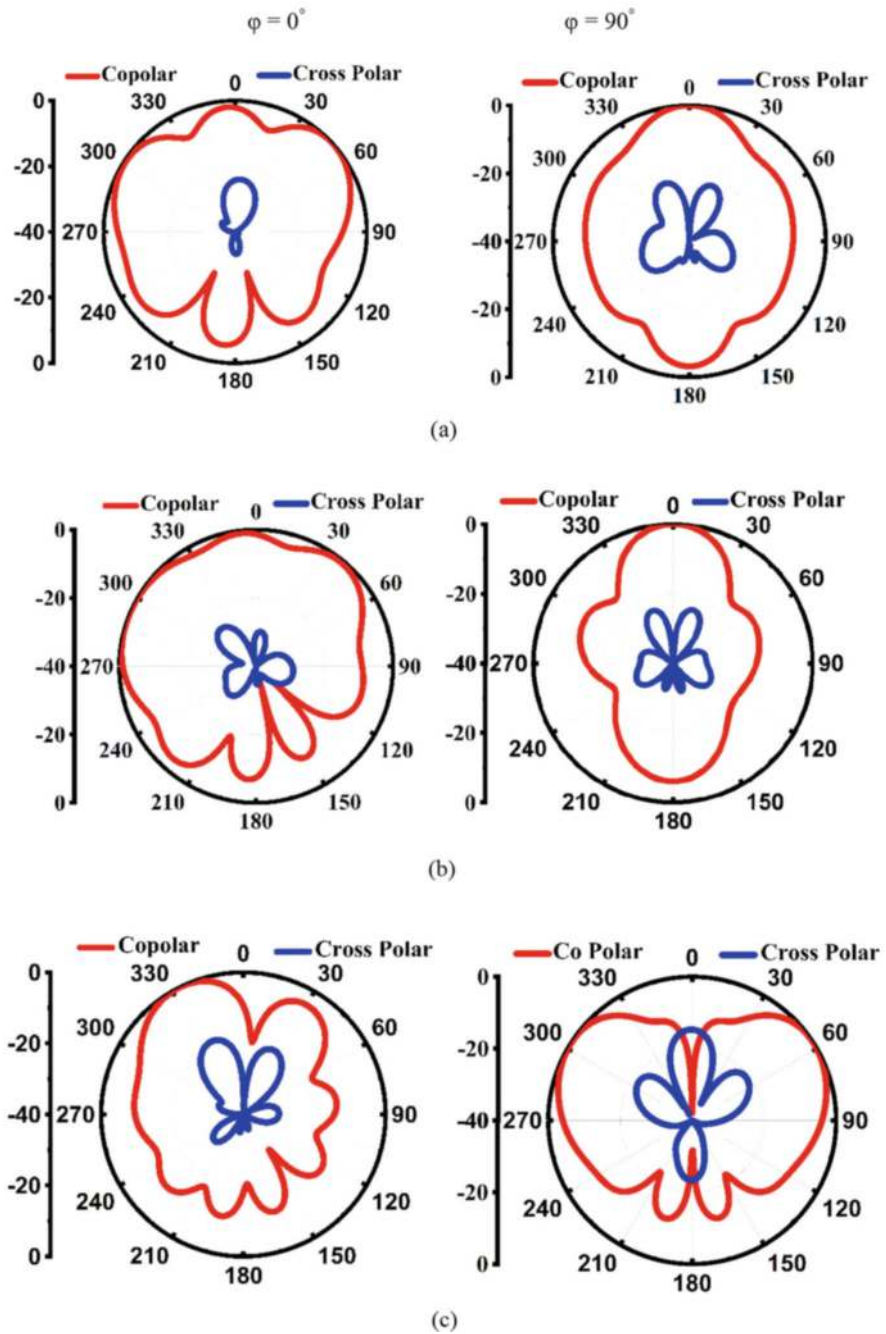


Fig. 5 Radiation pattern. (a) At  $f = 10$  GHz. (b) At  $f = 10.7$  GHz. (c) At  $f = 11.7$  GHz

**Table 1** Comparing the proposed work to already published research

Refs.	$H (\lambda_0)$	$\varepsilon_r$	B.W	P.G.	Antenna + feeding technique
[4]	0.14	10	8.5	6	CDRA+ CF
[6]	0.17	9.8	19	6.6	SIW Slot
[31]	0.09	9.9	18.4	7	CBDRA+ AC
[32]	0.1	9	26	5	CSDRA
[33]	0.08	9.9	16.5	6	CDRA
[34]	0.08	12.3	14.2	7	SFASDRA
P.S.	0.16	10.2	21	7	CCCDRA

*AC* Aperture coupled, *B.W* bandwidth in %, *CBDRA* conformal bent DRA, *CF* coaxial feed, *CSDRA* conformal stacked DRA, *H* CDRA height in terms of electrical length, *MF* microstrip feed, *P.G.* Peak gain (dBi), *P.S.* Proposed structure, *SFASDRA* Slot fed arc-shaped DRA

## 6 Conclusion

In this chapter, CDRA with convex conformal GP are investigated and presented. A CDRA with improved radiation performance at  $R = 60$  mm was consequently selected for the proposed work. An impedance bandwidth of 21% is achieved due to perturbation. The peak gain obtained is 7 dBi at 11.5 GHz. Applications for proposed antenna are found in the X-band. The topic on wearable DRAs and conformal, flexible electronic systems is expanded by this communication.

**Acknowledgments** The research described in this chapter is supported by the SERB, DST project No.-CRG/2020/000635.

## References

1. B. Mukherjee, M. Chauhan, *Dielectric Resonator Antennas* (Artech, 2021)
2. B. Mukherjee, P. Patel, J. Mukherjee, A review of the recent advances in dielectric resonator antennas. *J. Electromagn. Waves Appl.* **34**(9), 1095–1158 (2020)
3. M. Mishra, A. Rajput, P.K. Gupta, B. Mukherjee, Low profile, wideband, high gain CDRA with Microstrip feed for ISM and C band applications. *Prog. Electromagn. Res. C* **126**, 77–90 (2022)
4. D. Guha, H. Gajera, C. Kumar, Perturbation technique to improve purity of modal fields in dielectric resonator antenna resulting in reduced cross-polarized radiation. *IEEE Trans. Antennas Propag.* **63**(7), 3253–3257 (2015)
5. H. Liu, L. Ying, W. Ming, G. Shuxi, Dual-broadband dielectric resonator antenna based on modified Sierpinski fractal geometry. *Electron. Lett.* **51**(11), 806–808 (2015)
6. W. Luo, Y. Feng, Y. Ren, B. Yin, A novel wideband fractal rectangular dielectric resonator antenna with improved radiation performance. *AEU-Int. J. Electron. Commun.* **142**, 153984, ISSN 1434–8411 (2021)
7. D. Sankaranarayanan, V.K. Duggirala, B. Mukherjee, Laterally placed CDRA with triangular notches for ultra wideband applications. *Frequenz* **72**(1–2), 1–6 (2018)
8. D. Guha, Y.M.M. Antar, Four-element cylindrical dielectric resonator antenna for wideband monopole-like radiation. *IEEE Trans. Antennas Propag.* **54**(9), 2657–2662 (2006). <https://doi.org/10.1109/TAP.2006.880766>

9. A. Singh, S.K. Sharma, Investigation on wideband CDRA with directive radiation patterns and low cross-polarization. *IEEE Trans. Antennas Propag.* **58**(5), 1779–1783 (2010)
10. A.A. Kishk, Y. Yin, A.W. Glisson, Conical dielectric resonator antennas for wideband applications. *IEEE Trans. Antennas Propag.* **50**(4), 469–474 (2002)
11. G. Drossos, Z. Wu, L.E. Davis, The air gap effect on a microstrip-coupled cylindrical dielectric resonator antenna. *Microw. Opt. Technol. Lett.* **20**(1), 36–40 (1999)
12. A.V.P. Kumar et al., Microstripline-fed half cylindrical dielectric resonator antenna for 2.4-GHz WLAN application. *Microw. Opt. Technol. Lett.* **48**(4), 724–726 (2006)
13. A.V. Praveen Kumar et al., Microstripline fed cylindrical dielectric resonator antenna with a coplanar parasitic strip. *Prog. Electromagn. Res.* **60**, 143–152 (2006)
14. A. Sharma, R.K. Gangwar, Compact quad-band cylindrical dielectric resonator antenna with complementary C-shaped defected ground structure. *Microw. Opt. Technol. Lett.* **58**(3), 611–615 (2016)
15. M. Chauhan, A. Rajput, B. Mukherjee, Wideband circularly polarized low profile dielectric resonator antenna with meta superstrate for high gain. *AEU – Int. J. Electron. Commun.* **128**, 153524 (2021)
16. M. Sinha, V. Killamsetty, B. Mukherjee, Near field analysis of RDRA loaded with Split ring resonators superstrate. *Microw. Opt. Technol. Lett. (Wiley)* **60**(2), 472–478 (2018)
17. A.K. Pandey, M. Chauhan, V.K. Killamsetty, B. Mukherjee, High gain compact rectangular dielectric resonator antenna using metamaterial as superstrate. *Int. J. RF Microw. Comput. Aided Eng. Wiley* **29**(12), 1–10 (2019)
18. C. Tong et al., Differentially coplanar-fed filtering dielectric resonator antenna for millimeter-wave applications. *IEEE Antennas Wirel. Propag. Lett.* **18**(4), 786–790 (2019)
19. P.F. Hu et al., A compact filtering dielectric resonator antenna with wide bandwidth and high gain. *IEEE Trans. Antennas Propag.* **64**(8), 3645–3651 (2016)
20. R. Cicchetti et al., A high-gain mushroom-shaped dielectric resonator antenna for wideband wireless applications. *IEEE Trans. Antennas Propag.* **64**(7), 2848–2861 (2016)
21. C. Li, T. Chiu, 340-GHz low-cost and high-gain on-chip higher order mode dielectric resonator antenna for THz applications. *IEEE Trans. Terahertz Sci. Technol.* **7**(3), 284–294 (2017)
22. A.A. Abdulmajid, Y. Khalil, S. Khamas, Higher-order-mode circularly polarized two-layer rectangular dielectric resonator antenna. *IEEE Antennas Wirel. Propag. Lett.* **17**(6), 1114–1117 (2018)
23. L. Yang et al., High-gain magnetic-dipole Quasi-Yagi antenna using higher-order mode dielectric resonator with near-zero-index metamaterial. *Int. J. RF Microwave Comput. Aided Eng.* (2020). <https://doi.org/10.1002/mmce.22329>
24. C. Sarkar, D. Guha, C. Kumar, Advanced design of higher mode-based dielectric resonator antenna array featuring high-gain operation over a large frequency band. *Microw. Opt. Technol. Lett.* (2020). <https://doi.org/10.1002/mop.32621>
25. J. Kowalewski et al., A millimeter-wave broadband dual-polarized dielectric resonator antenna based on hybrid modes. *IEEE Antennas Wirel. Propag. Lett.* **19**(7), 1068–1072 (2020)
26. Z. Chen et al., Millimeter-wave rectangular dielectric resonator antenna Array with enlarged DRA dimensions, wideband capability, and high-gain performance. *IEEE Trans. Antennas Propag.* **68**(4), 3271–3276 (2020)
27. S. Fakhte, H. Oraizi, L. Matekovits, High gain rectangular dielectric resonator antenna using uniaxial material at fundamental mode. *IEEE Trans. Antennas Propag.* **65**(1), 342–347 (2017)
28. S. Fakhte, I. Aryanian, L. Matekovits, Analysis and experiment of equilateral triangular uniaxial-anisotropic dielectric resonator antennas. *IEEE Access* **6**, 63071–63079 (2018)
29. S. Fakhte, H. Oraizi, L. Matekovits, Gain improvement of rectangular dielectric resonator antenna by engraving grooves on its side walls. *IEEE Antennas Wirel. Propag. Lett.* **16**, 2167–2170 (2017)
30. P.K. Gupta, A. Rajput, M. Mishra, B. Mukherjee, A compact low profile, wideband and high gain stacked dielectric resonator antenna. *Electromagnetics* **43**(3), 163–174 (2023)
31. K.W. Leung, K.M. Luk, E.K.N. Yung, S. Lai, Characteristics of a low-profile circular disk DR antenna with very high permittivity. *JET Electron. Lett.* **31**(6), 417–418 (1995)

32. K.P. Esselle, A low-profile rectangular dielectric-resonator antenna. *IEEE Trans. Antennas Propag.* **44**(9), 1296–1297 (1996)
33. E. Rodriguez-Villegas, S. Iranmanesh, S.A. Imtiaz, Wearable medical devices: High-level system design considerations and tradeoffs. *IEEE Solid-State Circuits Mag.* **10**(4), 43–52 (2018). <https://doi.org/10.1109/MSSC.2018.2867247>
34. M. Boyuan, J. Pan, E. Wang, Y. Luo, Conformal bent dielectric resonator antennas with curving ground plane. *IEEE Trans. Antennas Propag.* **67**(3), 1931–1936 (2019)
35. M. Boyuan, J. Pan, D. Yang, Y.X. Guo, Investigation on homogenization of flat and conformal stacked dielectric resonator antennas. *IEEE Trans. Antennas Propag.* **70**(2), 1482–1487 (2022)
36. M. Boyuan, J. Pan, E. Wang, D. Yang, Miniaturized conformal arc dielectric resonator antennas using dielectric and metallic loading. *IEEE Access* **7**, 139518–139525 (2019)
37. M. Boyuan, J. Pan, E. Wang, D. Yang, Estimation and utilization of ground effects on conformal dielectric resonator antennas. *IEEE Access* **7**, 162387–162394 (2019)
38. M. Mishra, A. Rajput, P.K. Gupta, B. Mukherjee, A low profile perturbed CDRA with convex conformal ground plane excited by differential feed. *AEU Int. J. Electron. Commun.* **173**, 155033 (2024) ISSN 1434-8411

# Reflectarray Antenna Designs



Ravi Kumar Arya

## 1 Introduction

Applications like radar, satellite communication, and long-distance communication have increased demand for high-gain antennas. Because of their distinct advantages, parabolic reflectors or antenna arrays have traditionally been used to meet the requirement for high gain. Because of their curved and electrically large surfaces, parabolic reflectors have large mass/volume ratios, which may make them unsuitable for some applications. Because high surface accuracy is required for these frequencies, parabolic antennas intended for high-frequency applications also require careful fabrication. On the other hand, the antenna arrays, while they have several advantageous characteristics, like their low profile and scan capability, also require large, costly electronic circuitry for beamforming, which can result in significant losses at higher frequencies, which raises concerns. Before going further into the chapter, we will discuss a few salient features of reflectarrays.

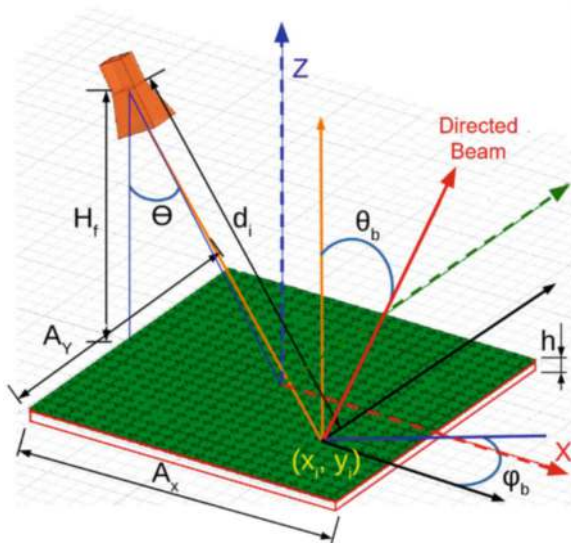
Reflectarray antennas [1–4] offer a unique approach to achieving high-gain performance. Unlike traditional parabolic reflectors, reflectarrays utilize a flat surface covered with precisely designed elements (often printed microstrip patches, dipoles, or rings) (refer to Fig. 1). These elements manipulate the phase of the reflected waves, effectively focusing on the outgoing beam in a desired direction. This innovative design offers a significant cost advantage over conventional antenna arrays. The phase shifting elements in a reflectarray can be fabricated using cost-effective printed circuit board (PCB) techniques, simplifying the manufacturing process compared to complex antenna networks. This combination of a flat surface

---

R. K. Arya (✉)

Xiangshan Laboratory, Zhongshan Institute of Changchun University of Science and Technology, Zhongshan, China

e-mail: [raviarya@cust.edu.cn](mailto:raviarya@cust.edu.cn)

**Fig. 1** Typical reflectarray

and PCB-based elements makes reflectarray antennas, a compelling solution for applications demanding high-gain performance in a compact, lightweight, and cost-effective package.

Reflectarrays offer several benefits compared to other types of antennas, including:

- *High Gain:* Reflectarrays can provide high gain, similar to reflector antennas depending upon their designs. This helps them to be employed for the applications where high gain is required such as in long-distance communication and radar systems.
- *Low Profile:* Reflectarrays can be designed to provide high gain with a low profile which helps them to be usable for specific applications where space or height is constrained, such as on aircraft or satellites.
- *Simple Feed System:* Compared to other antennas such as phased arrays, reflectarrays employ a simpler feed system.
- *Beam Shaping and Steering:* Reflectarrays can be customized to create specific shape beams as per particular applications such as pencil beams, etc. by changing the phase of the individual elements. If electronically controlled elements are used in reflectarray, the reflectarray can be made reconfigurable and can steer or shape the beam in different directions.
- *Lightweight:* Reflectarrays are generally low in weight as compared to conventional parabolic dish antennas, which makes them easy to install.
- *Frequency Agility:* In recent research works, there have been reflectarrays that can operate over a wide range of frequencies, which makes them usable for multiband or multipurpose applications.

- *Wideband Operation*: Recent advancements have also shown an improvement in reflectarray bandwidth. By using customized elements, reflectarrays have shown the potential to operate over a wider range of frequencies.
- *Easy Manufacturing*: Reflectarrays can be manufactured using traditional PCB techniques, which makes them cost-effective and easy to manufacture.
- *Ruggedness and Durability*: Reflectarrays are typically more rugged and durable as they do not employ any moving parts. It helps them to have high reliability in harsh environmental conditions.

Overall, reflectarrays provide a combination of performance, versatility, and practicality that makes them well suited for a wide range of communication, radar, and satellite applications.

This chapter introduces four distinct reflectarray designs, each offering unique advantages. The first two, categorized as metal-only reflectarray (MORA) antennas, utilize purely metallic elements for construction, eliminating the need for dielectric materials. Conversely, the remaining two reflectarrays leverage grounded dielectric elements to achieve broadband functionality. One of these broadband designs incorporates a phase-compensating flat lens to minimize the required maximum permittivity of the dielectric blocks. We will compare the performance of all four reflectarrays and highlight their benefits, particularly when compared to traditional narrowband designs that rely on resonant elements. Subsequent sections delve deeper into the details of these innovative reflectarray configurations.

## 2 Reflectarray Design

In the next sections, we present two distinct metal-only reflectarray (MORA) designs, both utilizing the same feed horn with a skew angle. The first MORA directs its beam in the specular direction, while the second design achieves broadside radiation. We will explore the specifics of these MORA configurations in subsequent sections.

The emergence of 3D printing has opened exciting possibilities for dielectric-based reflectarrays [5]. However, a key challenge lies in the limited permittivity range offered by current 3D printing materials. The first dielectric reflectarray design utilizes dielectric blocks backed by a ground plane, but this approach demands high permittivity values, which can be restrictive.

To address this limitation, we propose a second reflectarray incorporating a phase-compensating flat lens. This innovative design significantly reduces the required permittivity of the dielectric blocks, achieved by strategically placing the lens in front of the feed horn. We will delve deeper into the details of this approach later.

Before, discussing different types of these reflectarrays, it is important to discuss the typical process of designing conventional reflectarrays.



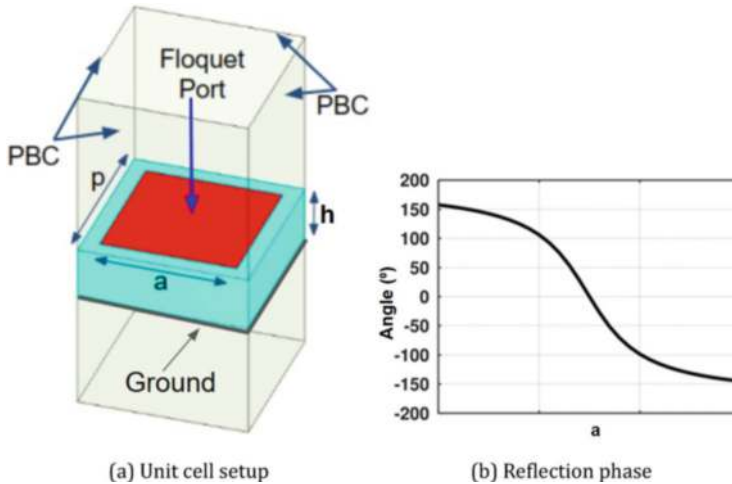


**Fig. 2** Typical reflectarray unit cell

## 2.1 Conventional Reflectarray Design Process

The conventional approach to reflectarray design, as outlined in [1–3], involves initially fabricating microstrip patches of various sizes (as depicted in Fig. 2a), shapes, and orientations on a dielectric substrate. This configuration enables local phase control (as illustrated in Fig. 2b) of the reflected wave when it is illuminated by an offset-fed horn (see Fig. 1), which illuminates the surface. Normally, a unit cell of specific dimensions is used as the reflecting element for controlling the reflected wave's phase. The patches in such reflectarray are separated from each other by unit cell periodicity and are supported by a dielectric layer.

Overall, designing a reflectarray involves several steps and considerations. It involves several steps:

- *Requirements Definition:* Determine the specifications and requirements of the reflectarray, including frequency of operation, gain, bandwidth, beamwidth, polarization, or any other parameters that are relevant to the desired application.
- *Substrate Selection:* Select a suitable substrate material for the reflectarray by choosing the dielectric constant, loss tangent, cost, and mechanical properties of the substrate.
- *Array Element Design:* Decide the type and shape of the array element based on desired radiation properties.
- *Element Parameters' Calculation:* After the array element is selected, use an electromagnetic simulation software to determine the dimensions of the array element with the desired phase distribution.
- *Phase Distribution Optimization:* Optimize array elements over the reflectarray surface so that they provide the desired phase distribution to steer the beam in

the desired direction. This optimization process may include fixing dimensions, positions, and phase shifts of the elements to minimize sidelobes, maximize gain, or get other desired performance goals.

- *Design Feed Network:* Design the convenient feed to illuminate the reflectarray.
- *Simulation and Performance Analysis:* Use electromagnetic simulation software such as CST Studio, Ansys HFSS, FEKO, etc. to simulate the reflectarray design to verify if it is providing the desired results. Analyze key performance metrics such as radiation patterns, bandwidth, gain, sidelobe levels, beamwidth, impedance matching, and efficiency to evaluate the design's performance against the specified requirements.
- *Prototype Fabrication and Testing:* Fabricate the reflectarray prototype using appropriate manufacturing techniques. Once fabricated, test the reflectarray prototype in an anechoic chamber or other controlled environment to validate its performance.
- *Iterative Optimization:* Iteratively refine the reflectarray design based on the similarity between simulation results and experimental measurements. Fine-tune the element parameters, feed design, and other factors to achieve the best possible performance within the given constraints.
- *Finalization and Documentation:* Finalize the reflectarray design, and document the specifications, simulation results, fabrication details, measurement setup, and testing steps for future reference and replication.

Throughout the design process, it is important to consider practical constraints such as material availability, manufacturing capabilities, cost, environmental factors, and measurement capabilities. It is worthwhile to consult electromagnetics, antenna design, and RF engineering experts to ensure a successful reflectarray design. Following the above steps, most conventional reflectarrays are designed. In the following sections, we discuss more about other innovative techniques to design different reflectarrays.

## 2.2 Offset-Fed Metal-Only Reflectarray Antennas

Recently, there has been a growing interest in metal-only reflectarray antennas due to their avoidance of dielectric materials, making them not only cost-effective but also less susceptible to environmental conditions when deployed in space. Several metal-only designs have been proposed by researchers, ranging from the earliest iteration [1] utilizing slot-type elements [6, 7] to more complex three-dimensional designs [8–11].

The design process of these reflectarrays commences with the placement of the feed horn. It is assumed that the feed horn illuminates the reflectarray surface at angles depicted in Figs. 1 and 3. Reflectarray elements situated at a height,  $h$ , from the ground plane are tasked with reflecting the incident field in a manner that directs the reflected beam toward the desired direction ( $\varphi_b, \theta_b$ ). For achieving a collimated

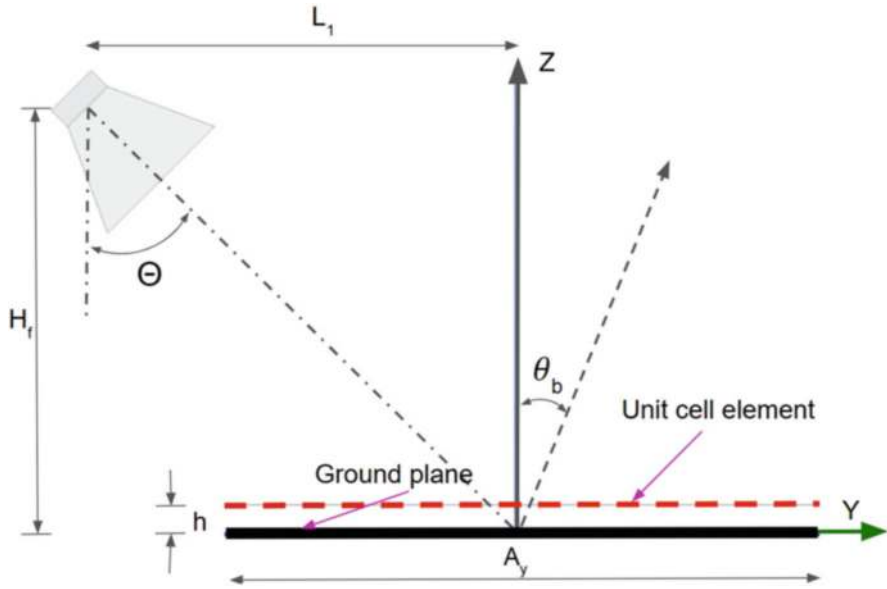


**Fig. 3** Typical metal-only reflectarray

beam in the  $(\varphi_b, \theta_b)$  direction, the progressive phase distribution required for these reflectarray elements can be mathematically expressed as [3]

$$\phi(x_i, y_i) = -k_0 x_i \sin \theta_b \cos \varphi_b - k_0 y_i \sin \theta_b \sin \varphi_b \quad (1)$$

where element  $i$ 's coordinates are denoted by  $\phi(x_i, y_i)$  and  $k_0$  denotes the propagation constant in vacuum.

The reflected field from the reflectarray is the desired field contributed from all the elements of the reflectarray. The phase of the reflected field at each element results from the sum of the incident phase and the phase shift introduced by each element, and we can express it as follows:

$$\phi(x_i, y_i) = -k_0 d_i + \phi_R(x_i, y_i) \quad (2)$$

where element  $i$  introduces phase shift of  $\phi_R(x_i, y_i)$  and  $d_i$  denotes the separation of the element to the phase center of the feed.

From equations (1) and (2), the phase shift needed at each element comes out to be

$$\phi_R(x_i, y_i) = k_0(d_i - \sin \theta_b(x_i \cos \varphi_b + y_i \sin \varphi_b)) \quad (3)$$

The reflectarray is made of many phasing elements. So, phasing element design constitutes a crucial aspect of reflectarray design.

The aperture efficiency of these reflectarrays is determined by computing the simulated gain using the following formula:

$$\eta = \frac{G\lambda^2}{4\pi A} \quad (4)$$

where  $A$  and  $G$  represent the physical area and gain of the reflectarray at the wavelength,  $\lambda$ .

### 2.2.1 Results

As previously noted, simulations were conducted for two offset-fed prototype reflectarrays, considering radiation in both normal and specular directions. For more details, please refer to [11–13]. The parameters for the reflectarray setup are as follows: The design frequency  $f$  is 35.6 GHz; the aperture dimensions are  $A_x \times A_y$ , where  $A_x = A_y = 96.83$  mm ( $11.5\lambda$ ); the tilt angle is represented by  $\Theta = 30^\circ$ ; the thickness is  $h = 0.787$  mm; and the height of the feed is  $H_f = 75$  mm ( $8.9\lambda$ ).

According to the simulations, the reflectarray, for the normal beam, achieved a simulated gain of 26.2 dBi at 35.6 GHz, with an aperture efficiency of 25.5%, calculated using equation (4), while the reflectarray for specular beam achieved a gain of 28 dBi at 35.6 GHz, with an aperture efficiency of 35.4% as discussed in [11–13].

## 2.3 Dielectric Reflectarray Designs

As compared to conventional reflectarray design, we introduce an alternate design to the conventional approach for designing dielectric reflectarray. This reflectarray design invokes the image principle to show the principle of the design, and it is similar to that of designing graded-index lenses [14]. We use offset-fed reflectarray design in this study as it is the most commonly used configuration in academia and industry.

We start the design process by first looking at the design of a transmitarray. Designing a transmitarray is easy as it uses the Ray Optics method. The design for the reflectarray can be easily formulated by taking out half of the transmitarray and replacing the other half with a PEC ground plane.

Initially, we begin by assuming that the feed horn illuminates the reflectarray surface at an angle  $\Theta$ , depicted in Fig. 4, as the first step. Next, we determine the phase distribution on the top surface of the reflectarray located at  $\Phi_{in}$ , when illuminated by the feed horn. We calculate the desired phase distribution at  $\Phi_{out}$ . By both these phase distributions, we can embed the dielectric blocks between  $\Phi_{in}$  and  $\Phi_{out}$  planes so that the compensating phase introduced by these dielectric blocks enforces the phase distribution at the exit aperture to the desired distribution

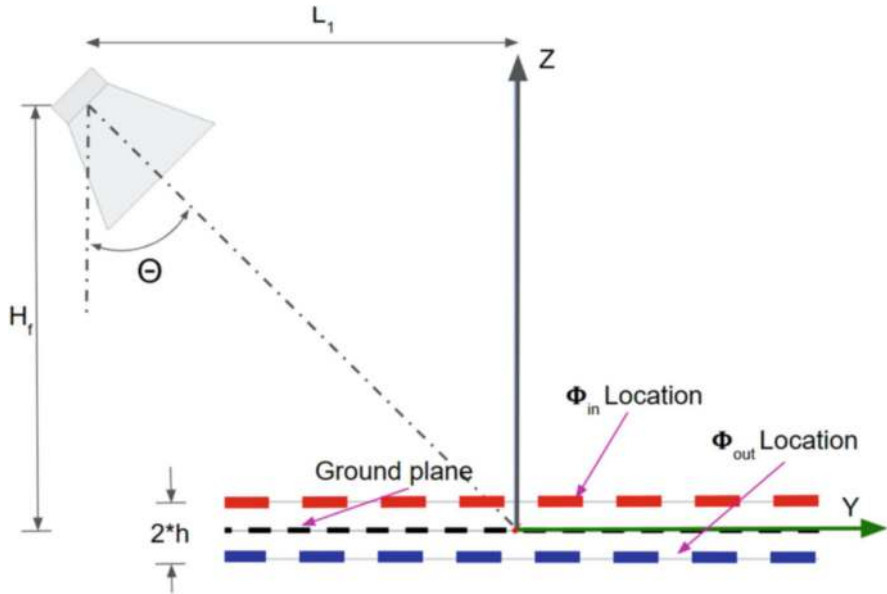


**Fig. 4** Location of the input and output aperture

calculated at the exit plane,  $\Phi_{out}$ . Once we place these dielectric blocks, it is similar to the design of a transmitarray only with the difference that the output beam is offset by an angle  $\Theta$  as compared to the normal incidence as is common with typical transmitarray.

Once the phase distribution at the input aperture,  $\Phi_{in}$ , and the desired phase distribution at the exit aperture,  $\Phi_{out}$ , are known, we can calculate the desired permittivity of the dielectric blocks as follows:

$$\Phi_{out} - \Phi_{in} = \frac{2\pi t}{\lambda_0} \sqrt{\epsilon_{rj}} \quad (5)$$

where  $\lambda_0$  is the free space wavelength,  $t$  is the thickness of the dielectric block, and  $\epsilon_{rj}$  is the dielectric constant of the  $j$ th block along  $y$ -axis.

We then calculate the values of  $\epsilon_{rj}$  needed at different locations of the reflectarray. The placement of these dielectric blocks completes our design for transmitarray and thus forms the transmitarray as shown in Fig. 5.

The transmitarray works as a preliminary design for the reflectarray. We convert it to the reflectarray by placing the PEC sheet at  $x$ - $y$  plane at  $z = 0$  mm and removing the part of the dielectric blocks below  $z = 0$  mm. The placement of PEC sheet at  $z = 0$  mm will reflect the incident beam from the feed horn in the specular direction. The final design of the converted reflectarray is shown in Fig. 6. This completes our design for the offset-fed dielectric reflectarray.

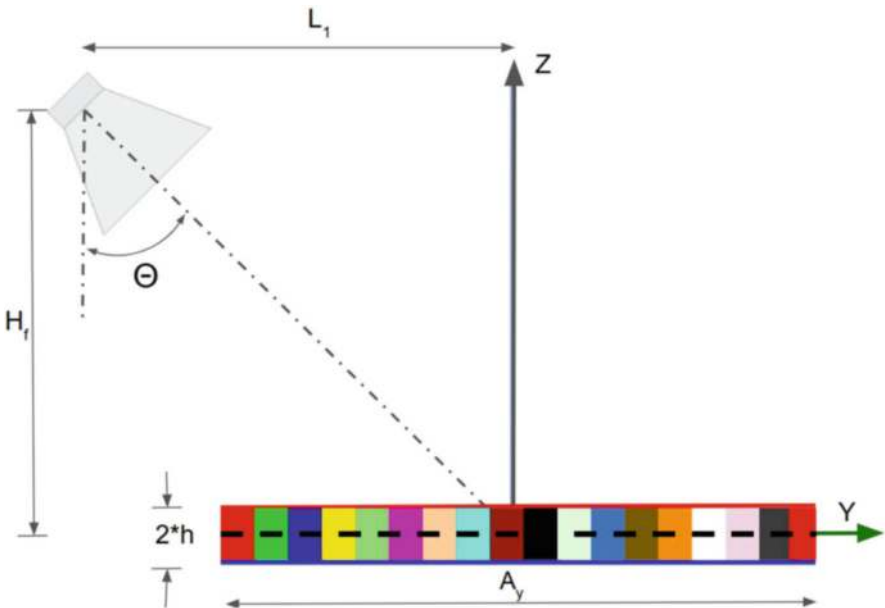


Fig. 5 Dielectric transmitarray

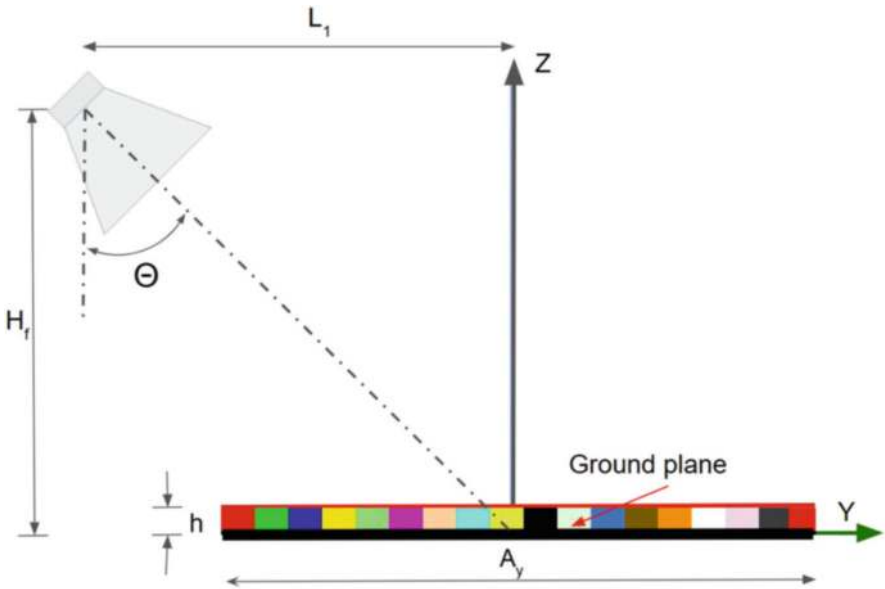
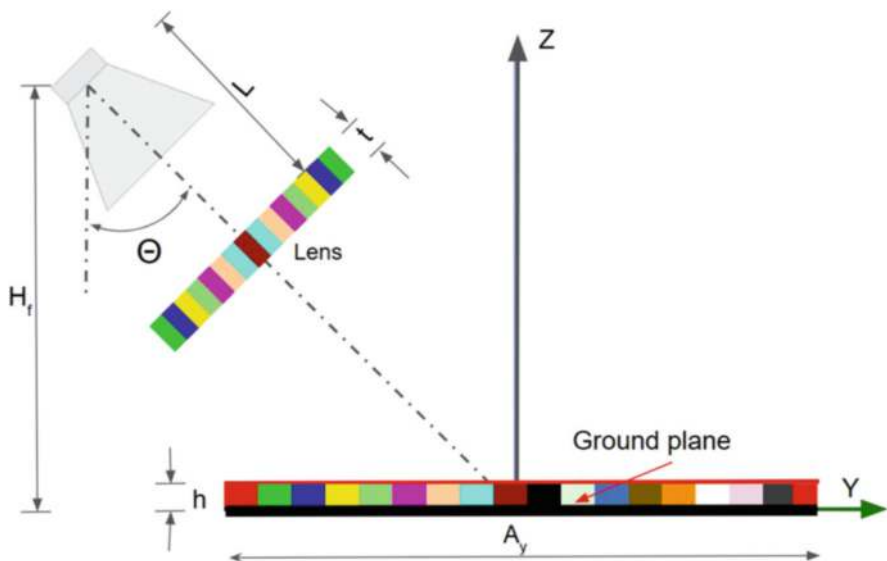


Fig. 6 Offset-fed dielectric reflectarray



**Fig. 7** Dielectric reflectarray with phase-compensating flat lens

We position different dielectric blocks above the ground plane to achieve the desired phase compensation. Each block measures  $x \times x$  with a height of  $h$  where both  $x$  and  $h$  are decided by reflectarray properties and frequency of operation. Normally, it is found that a design of this type needs a high value of dielectric constant for the dielectric blocks. However, obtaining materials that have such a vast expanse of values of permittivities for the reflectarray is difficult from the commercial off-the-shelf (COTS) materials. Even advanced techniques like 3D printing with air-void embedding [15] are not helpful in this scenario as the 3D printing materials with high  $\epsilon_r$  values are not easily available or are quite expensive. To reduce the maximum required value of the permittivity of the dielectric blocks, we propose a modified design by incorporating a lens as explained next.

In this design, we employ the same methodology as described earlier for the design process. However, for the second reflectarray, we maintain the same physical parameters while introducing a phase-compensating flat lens between the horn and the array. This lens aims to decrease the phase excursion of the spherical wave as it interacts with the dielectric blocks, as depicted in Fig. 7. With the inclusion of the lens, the maximum permittivity required for the dielectric blocks reduces to lower values as compared to when the lens is not used.

The desired values of permittivity in this design can be achieved by using the Dial-a-Dielectric (DaD) technique [16]. We can use ABS as printing material with printed conductive patches to realize desired permittivity values that otherwise cannot be achieved by 3D printing alone.

### 2.3.1 Results

The previous publications [11–13] demonstrated the effectiveness of the reflectarray design with the phase-compensating flat lens. It was found that it was possible to get a gain of 6 dB gain with the introduction of the phase-compensating flat lens. It was also found that dielectric constant values required by reflectarray were also decreased drastically by the introduction of the lens.

## 3 Conclusion

This chapter explored the design of four versatile reflectarray antennas. We began with two metal-only reflectarrays (MORAs). To showcase the design flexibility, one MORA directs its beam in the normal direction, while the other achieves a specular beam. Interestingly, the specular design boasts both higher gain and lower sidelobe levels compared to its normal beam counterpart.

Next, we ventured into dielectric reflectarrays, introducing two designs that both utilize dielectric blocks backed by a ground plane to achieve a specular beam. The key difference lies in the inclusion of a phase-compensating flat lens in one design. This lens offers significant advantages: It drastically reduces the maximum permittivity required for the dielectric blocks, making them more suitable for 3D printing and potentially lowering the overall antenna profile. However, the lens introduces phase shifts that necessitate adjustments to the permittivity values to maintain the desired specular beam direction.

## References

1. D. Berry, R. Malech, W. Kennedy, The reflectarray antenna. *IEEE Trans. Antennas Propag.* **11**(6), 645–651 (1963)
2. D.M. Pozar, S.D. Targonski, H.D. Syrigos, Design of millimeter wave microstrip reflectarrays. *IEEE Trans. Antennas Propag.* **45**(2), 287–296 (1997)
3. J. Huang, J.A. Encinar, *Reflectarray Antennas* (Wiley, 2008)
4. J. Budhu, Y. Rahmat-Samii, Understanding the appearance of specular reflection in offset fed reflectarray antennas, in *2011 IEEE International Symposium on Antennas and Propagation (APSURSI)* (IEEE, 2011), pp. 97–100
5. P. Nayeri, M. Liang, R. A. Sabory-Garcı, M. Tuo, F. Yang, M. Gehm, H. Xin, A. Z. Elsherbeni, et al., 3D printed dielectric reflectarrays: low-cost high-gain antennas at sub-millimeter waves. *IEEE Trans. Antennas Propag.* **62**(4), 2000–2008 (2014)
6. G. Carluccio, A. Mazzinghi, A. Freni. Design of complementary reflectarray. *Electron. Lett.* **50**(1), 16–17 (2014)
7. R. Deng, F. Yang, S. Xu, M. Li, A low-cost metal-only reflectarray using modified slot-type Phoenix element with 360° phase coverage. *IEEE Trans. Antennas Propag.* **64**(4), 1556–1560 (2016)
8. Y. H. Cho, W. J. Byun, M. S. Song, High gain metal-only reflectarray antenna composed of multiple rectangular grooves. *IEEE Trans. Antennas Propag.* **59**(12), 4559–4568 (2011)



9. W. Lee, M. Yi, J. So, Y. J. Yoon, Non-resonant conductor reflectarray element for linear reflection phase. *Electron. Lett.* **51**(9), 669–671 (2015)
10. H.-T. Chou, C.-Y. Lin, M.-H. Wu, A high efficient reflectarray antenna consisted of periodic all-metallic elements for the Ku-band DTV applications. *IEEE Antennas Wirel. Propag. Lett.* **14**, 1542–1545 (2015)
11. S.V. Pandey, *Techniques for Designing Microwave and Millimeter Wave Antennas and Components Using Artificially Engineered Materials and Metasurfaces*. PhD thesis, The Pennsylvania State University, 2017
12. R. Mittra, S. Pandey, R.K. Arya, Offset-fed metal-only reflectarray antenna designs, in *2017 Sixth Asia-Pacific Conference on Antennas and Propagation (APCAP)*, pp. 1–3 (2017)
13. S. Pandey, R.K. Arya, R. Mittra, S. Zhang, D. Cadman, W. Whittow, Y. Vardaxoglou, Offset-fed metal-only reflectarray antenna design using 3D-cross elements, in *2018 IEEE International Symposium on Antennas and Propagation & USNC/URSI National Radio Science Meeting*, pp. 1629–1630 (2018)
14. R.K. Arya, S. Pandey, R. Mittra, A technique for designing flat lenses using artificially engineered materials, in *2014 IEEE Antennas and Propagation Society International Symposium (APSURSI)* (IEEE, 2014), pp. 769–770
15. S. Zhang, R.K. Arya, S. Pandey, Y. Vardaxoglou, W. Whittow, R. Mittra, 3D-printed planar graded index lenses. *IET Microwaves Antennas Propag.* **10**(13), 1411–1419 (2016)
16. R.K. Arya, S. Zhang, Y. Vardaxoglou, W. Whittow, R. Mittra. 3D-printed millimeter wave lens antenna, in *2017 10th Global Symposium on Millimeter-Waves* (IEEE, 2017), pp. 172–174

# Antennas for Full-Duplex Communication: State of the Art and Way Forward



Jogesh Chandra Dash  and Debdeep Sarkar 

## 1 Introduction

In the coming years, wireless user traffic is expected to surge exponentially compared to the contemporary fifth-generation (5G) load. Therefore, it is expected to achieve twice the energy efficiency, 1 Tbps peak data rate, double the spectral efficiency, and 10 times reduced communication latency in 6G compared to 5G [1]. These requirements are crucial to enable futuristic applications such as extended reality, digital twin, holography, smart health care, autonomous vehicles, dense cellular connectivity, and many more. Thus, it is time to think beyond the existing communication system which works in the traditional half-duplex (HD) mode. HD mode of communication performs in either time-division duplexing (TDD) or frequency-division duplexing (FDD). These two duplexing techniques leverage the orthogonality of time/frequency resources at the expense of spectral efficiency [2]. On the other hand, in-band full-duplex (IBFD) communication has attracted significant attention due to its remarkable properties to deal with spectral scarcity. It, theoretically, doubles the spectral efficiency compared to the half-duplex system and reduces the communication latency due to its simultaneous transmission and reception over the same time and frequency slot. The schematic representation of the FD and HD communication system is shown in Fig. 1. However, the serious bottleneck associated with the IBFD system is the self-interference (SI) caused by

---

J. C. Dash

National Institute of Technology, Rourkela, Rourkela, Odisha, India  
e-mail: [dashjc@nitrkl.ac.in](mailto:dashjc@nitrkl.ac.in)

D. Sarkar (✉)

Indian Institute of Science Bangalore, Bengaluru, Karnataka, India  
e-mail: [debdeep@iisc.ac.in](mailto:debdeep@iisc.ac.in)

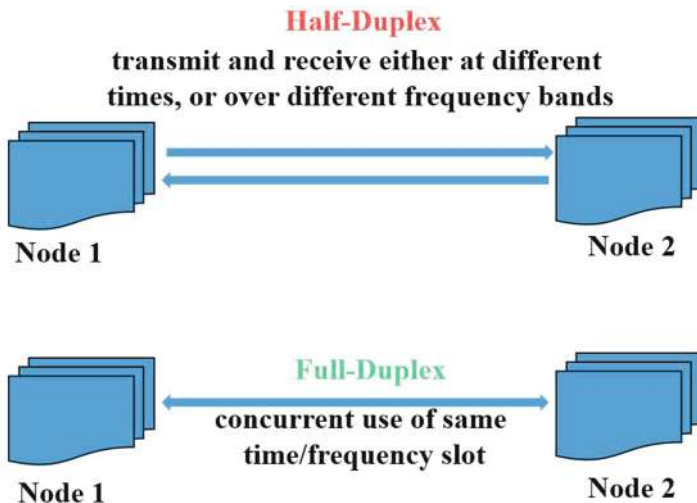


**Fig. 1** A schematic representation of HD and FD wireless communication systems

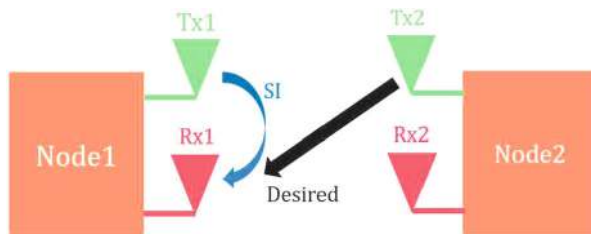


**Fig. 2** Schematic representation of SI signal and desired SoI in FD communication system

its transmitter signal into the receiver which prevents the reception of the actual signal of interest (SoI). The schematic representation of SI is provided in Fig. 2.

The SI signal is a very high-power signal, which can be over a million times stronger compared to SoI. It is reported that a conventional wireless communication system requires more than 100 dB of SI cancellation (SIC) to achieve a signal-to-interference noise ratio (SINR) similar to that of the HD communication system [3–6]. In this circumstance, for successful implementation of FD communication, it is highly essential to suppress the SI signal well below the receiver's thermal noise floor. To achieve the isolation level of more than 100 dB, SIC is performed jointly in three different stages, namely RF/antenna domain, analog domain, and digital domain.

A few recently reported analog and digital SIC techniques such as nonlinear SI cancellation using an auxiliary transmitter [7], a bandpass common-gate structure with high-Q selectivity [8], RF rejection by injecting a Tx signal replica into Rx and cancelling at a low-noise amplifier (LNA) [9–12], transmit SIC beamformer [13], basis function selection-based SIC [14], using variable fractional delay finite

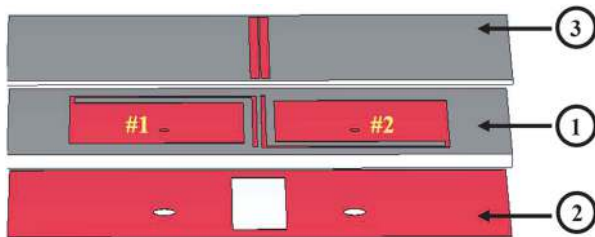
impulse response (FIR) filter [15], and digital SI canceller Antennas for Full-Duplex Communication: State of the Art and Way Forward using demodulation reference signal configuration [16], etc. are a few. However, analog/digital SIC techniques use additional circuitry and signal processing blocks, which leads to increased design complexity, power consumption, latency, and system cost. Therefore, a high degree of antenna domain SIC suppression can reduce the subsequent analog and digital domain cancellation load.

## 2 FD Antenna Design and SIC Techniques

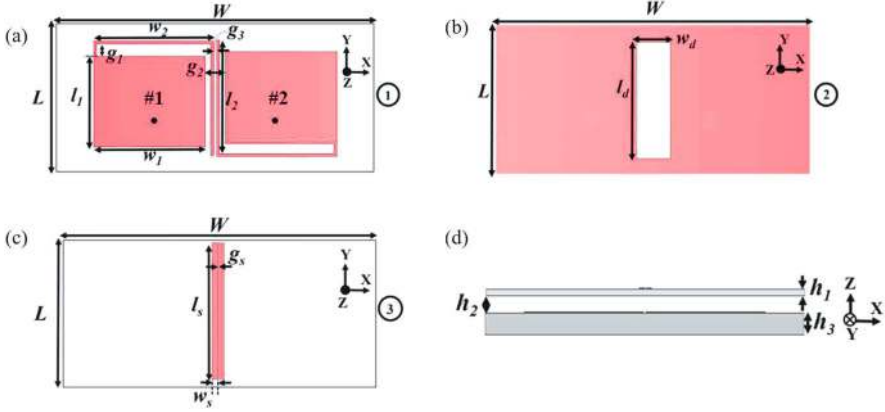
### 2.1 Layered Multi-radiator FD Antenna with SIC Using NFDS and DGS

Figure 3 shows the proposed two-port antenna that comprises a three-layer structure [17]. The coaxially fed microstrip patch antenna in Fig. 4a is designed on an RTD5880 substrate of 1.57 mm thickness, having  $\epsilon_r = 2.2$  and  $\tan \delta = 0.0009$ . An inverted L-shaped structure is connected from one end of the patch radiating edge and directed toward the non-radiating edge to create an asymmetry in the design, thereby reducing the inter-element H-plane coupling. A rectangular portion having the dimension of  $l_d \times w_d$  is etched from the ground plane to design a defected ground structure (DGS) (Fig. 4b). Another dielectric sheet RT5880LZ of 0.5 mm thickness having  $\epsilon_r = 1.96$  and  $\tan \delta = 0.0019$  is placed above the microstrip antenna at  $h_2$  height (Fig. 4c–d). Inspired by the antenna decoupling surface proposed in [18], two parallel microstrip lines are designed on that dielectric sheet immediately above the inter-element spacing and the near-field region, which act as NFDS. Note that the NFDS substrate should be low loss and its dielectric permittivity should be as low as possible to avoid the effect of dielectric loading on the antenna radiation performance. The resonant combination of DGS and the NFDS helps in reducing field coupling between the two nearby antennas.

A detailed analysis of the aforementioned decoupling mechanism by examining the field distribution has been provided in the subsequent section. It has been shown



**Fig. 3** Schematic diagram of proposed two-port antenna at 5.85 GHz



**Fig. 4** Proposed two-port antenna showing dimensions for individual layers in Fig. 3: (a) top layer, (b) middle layer, (c) ground plane, and (d) side view. Dimensions:  $L = 1.092\lambda_0$ ,  $W = 0.507\lambda_0$ ,  $l_1 = 0.31\lambda_0$ ,  $w_1 = 0.38\lambda_0$ ,  $l_2 = \lambda_0$ ,  $w_2 = 0.4\lambda_0$ ,  $g_1 = 0.039\lambda_0$ ,  $g_2 = 0.068\lambda_0$ ,  $g_3 \approx 0.01\lambda_0$ ,  $l_d = 0.394\lambda_0$ ,  $w_d = 0.117\lambda_0$ ,  $l_s = 0.478\lambda_0$ ,  $w_s = 0.018\lambda_0$ ,  $g_s = 0.00429\lambda_0$ ,  $h_1 = 0.0057\lambda_0$ ,  $h_2 = 0.0136\lambda_0$ ,  $h_3 = 0.03\lambda_0$

that the reduction of field coupling, both E- and H-fields, helps in reducing the mutual coupling between the nearby radiating elements to an extremely low value.

### 2.1.1 Explanation of Decoupling Mechanism in Proposed Two-Port Antenna

In this section, we present the design evolution of the proposed two-port antenna along with its decoupling mechanism. For each design stage, we examine the field distribution, mutual coupling ( $S_{21}/S_{12}$ ), and impedance matching ( $S_{11}$ ) levels and the 2D radiation pattern.

**Stage-0** Initially, an antenna system having two closely spaced ( $g_2 = 0.06\lambda_0$ ) microstrip patches (dimensions of  $l_1 \times w_1$  each) is designed (Fig. 5). The patch antenna works at 5.85 GHz LTE band with good impedance matching ( $|S_{11}| < -10$  dB). However, strong H- and E-field coupling between the nearby antennas ( $|S_{21}| = |S_{12}|$  about  $-11$  dB) can be observed (Fig. 5). The 2D radiation patterns (E-/H-plane) of antenna #1 and #2 at stage-0 are shown in Fig. 6a and b respectively. The patterns show a good cross-polar level (below  $-20$  dB) at both the E- and H-planes for two antenna elements.

**Stage-1** Next, the L-shaped structure of Fig. 4a is included to create an asymmetry in the microstrip antenna structure designed in stage-0 to reduce the mutual coupling (Fig. 7), which can be verified from the H-field distribution in Fig. 7. As compared to stage-0, stage-1 exhibits 8 dB increase in the isolation. The L-shaped structure increases the effective electrical length of individual antenna elements, causing a

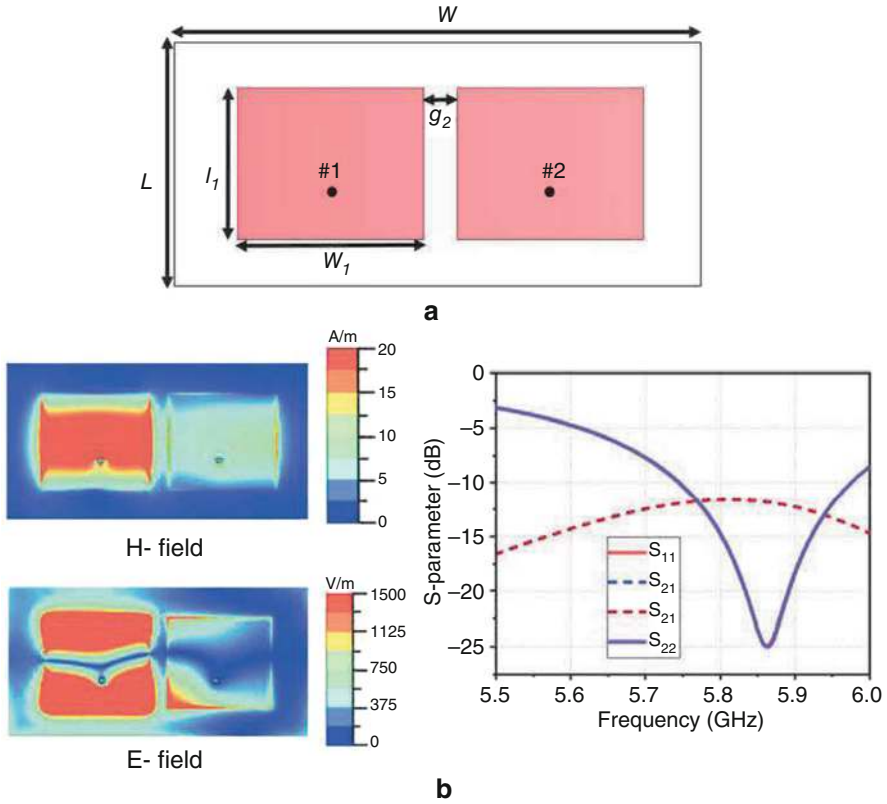


**Fig. 5** (a) Schematic of the proposed two-port antenna at stage 0, and (b) H- and E-field distribution on the patches of the stage-0 antenna configuration at 5.85 GHz, along with the frequency variation of S-parameters (port 1 is excited, while keeping port 2 terminated with matched load). Note that we have  $S_{11} = S_{22}$  due to structural symmetry (reciprocity ensures  $S_{12} = S_{21}$ )

shift in the operating frequency from 5.85 GHz at stage-0 to 5.75 GHz at stage-1. However, the asymmetry in the antenna design varies the individual antenna impedance matching, and the E-field coupling still exists as shown in Fig. 7. The 2D radiation pattern for the stage-1 antenna configuration is shown in Fig. 8. The asymmetry introduced in this stage increases the cross-polar level than the antenna configuration at stage-0. However, the cross-polar level is below  $-15$  dB at the broadside direction for both the antenna elements (see Fig. 8).

**Stage-2** Stage-2 incorporates both the DGS (Fig. 4b) and the NFDS (Fig. 4c) in conjunction with the asymmetric patch configuration of stage-1. DGS loading in the ground plane reduces the surface wave excitation thereby improving the cross-polar response (see Fig. 14), and the dimension of the DGS determines the stop-band effect by incorporating transmission zero at the frequency of interest [19, 20]. The

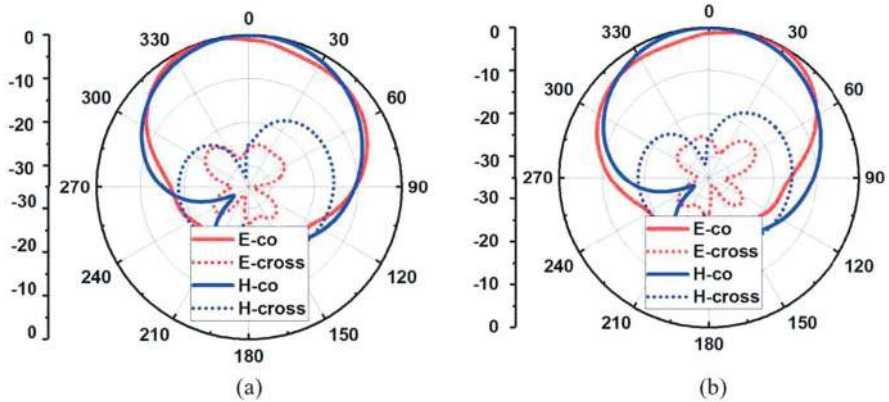


**Fig. 6** Simulated 2D radiation pattern at 5.85 GHz of antenna design stage-0 (Fig. 5): (a) Antenna #1 and (b) Antenna #2

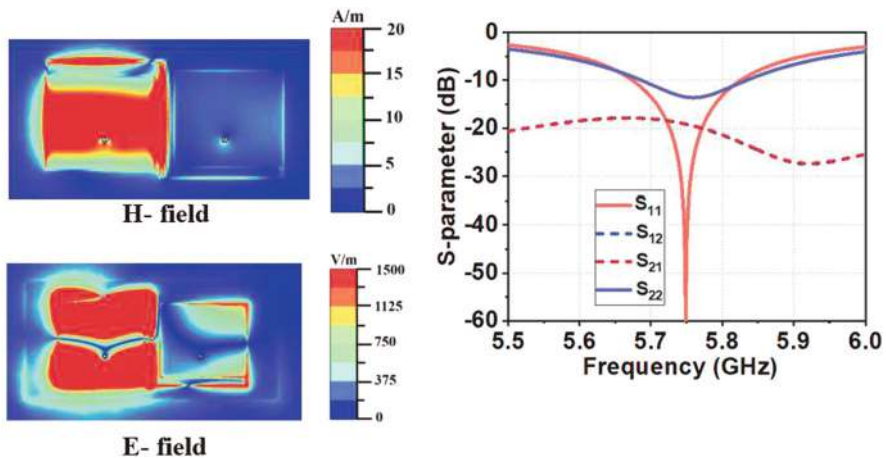


**Fig. 7** H- and E-field distribution on the patches of the stage-1 antenna configuration (see only Fig. 4a) at 5.85 GHz, along with the frequency variation of S-parameters (port 1 is excited while keeping port 2 terminated with matched load). Note that, due to structural asymmetry, we have  $S_{11} \neq S_{22}$  (reciprocity ensures  $S_{12} = S_{21}$ , as expected)

height between NFDS and the antenna ground plane determines the phase of the partially diffracted wave to cancel out the coupled wave. Also, the height between the defected ground and NFDS ensures an extremely low value of the inter-element mutual coupling. The dimensions of DGS and NFDS and the height between them are carefully decided using parametric analysis as shown in Fig. 9.

The parametric study is conducted for the DGS design parameters  $l_d$  and  $w_d$  and the NFDS design parameters  $l_s$ ,  $w_s$ , and  $h_2$ . It is observed that the variation of  $l_d$  and  $w_d$  has very little impact on impedance matching; however, these decide the

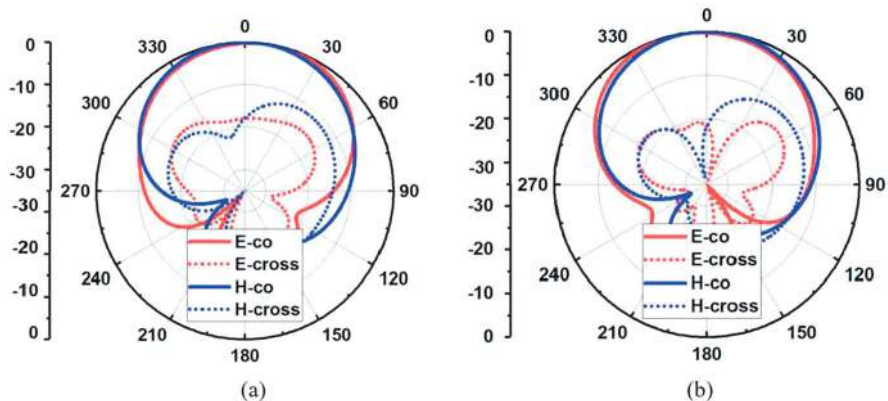


**Fig. 8** Simulated 2D radiation pattern at 5.7 GHz of antenna design stage-1 (Fig. 4a): (a) Antenna #1 and (b) Antenna #2

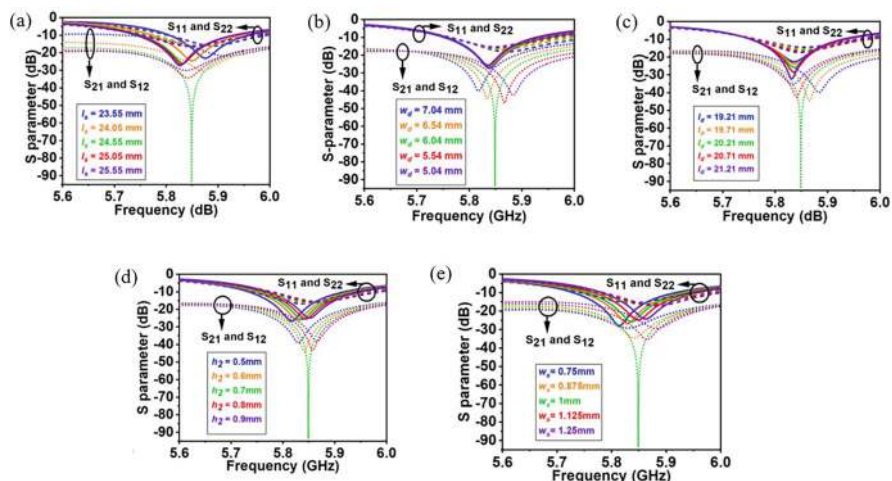


**Fig. 9** Studies on parameters: (a)  $l_d$ , (b)  $w_d$ , (c)  $l_s$ , (d)  $w_s$ , and (e)  $h_2$ , to understand the respective effects on S-parameter response of the proposed two-port antenna configuration

resonant frequency for  $S_{21}$  ( $S_{12}$ ). As shown in Fig. 9a and b, there is a gradual decrease (increase) in the frequency for the mutual coupling parameter with a gradual increase (decrease) in  $l_d$  ( $w_d$ ) values observed. On the other hand, the variation of NFDS design parameters ( $l_s$ ,  $w_s$ , and  $h_2$ ) alters the antenna operating frequency due to the superstrate loading effect. Moreover, the NFDS design parameters improve the mutual coupling performance at the frequency of interest as shown in Fig. 9c–e. The parametric study provides an intuition for NFDS design in the presence of DGS to reduce the mutual coupling. Moreover, the study of power flow between the antenna elements for different stages of antenna design



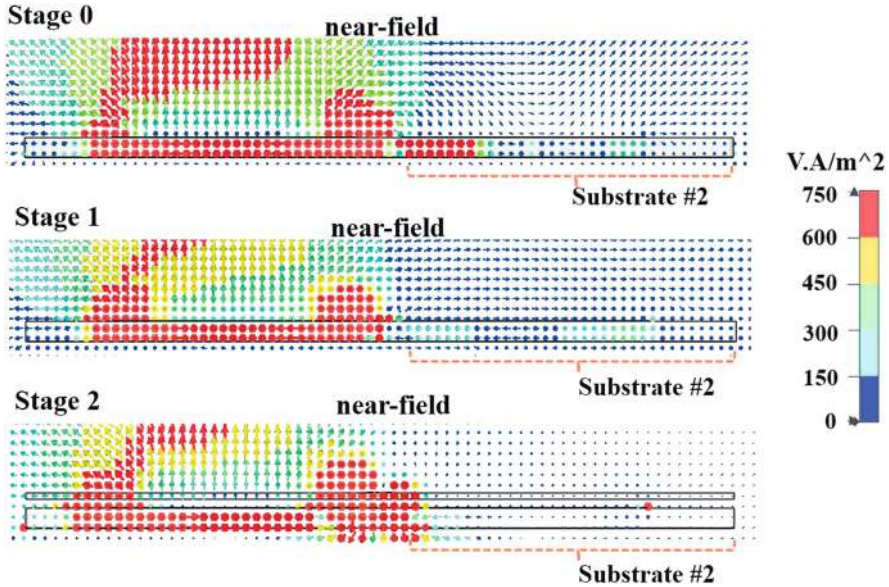


**Fig. 10** Schematic diagram of proposed two-port antenna at 5.85 GHz

is provided in Fig. 10. At design stage-0 (see Fig. 5), the closely spaced antenna elements create significant power flow between them through the substrate and in the near-field region (see Fig. 10) due to the absence of any decoupling technique. The asymmetry introduced at the stage-1 (Fig. 4a) antenna design reduces the power flow in the substrate region, from antenna #1 to antenna #2, compared to stage-0 (see Fig. 10). At stage-2 the use of DGS and NFDS along with the asymmetry introduced in stage-1 completely prevents the power flow both in the substrate region and in the near-field region of antenna #2 from antenna #1 (see Fig. 10).

The combined resonant effect of DGS and NFDS reduces both the H-field and E-field coupling between the nearby antennas as shown in Fig. 11. Consequently, the proposed technique exhibits the good impedance matching at 5.85 GHz desired operating frequency and reduces the mutual coupling between the nearby antennas having  $S_{11} < -10$  dB and  $S_{21}/S_{12} < -90$  dB, respectively, as shown in Fig. 11. Antenna #1 covers 5749 MHz–5949 MHz operating band having  $-10$  dB impedance bandwidth of 200 MHz, while antenna #2 covers 5762 MHz–5978 MHz operating band having  $-10$  dB impedance bandwidth 216 MHz. The overlapping bandwidth of the antenna is 187 MHz.

### 2.1.2 Prototype Fabrication and Measurement Results

Figure 12a–c depicts the fabricated antenna prototype. The superstrate with NFDS structure is supported, and height  $h_2$  is adjusted by four dielectric screws at four

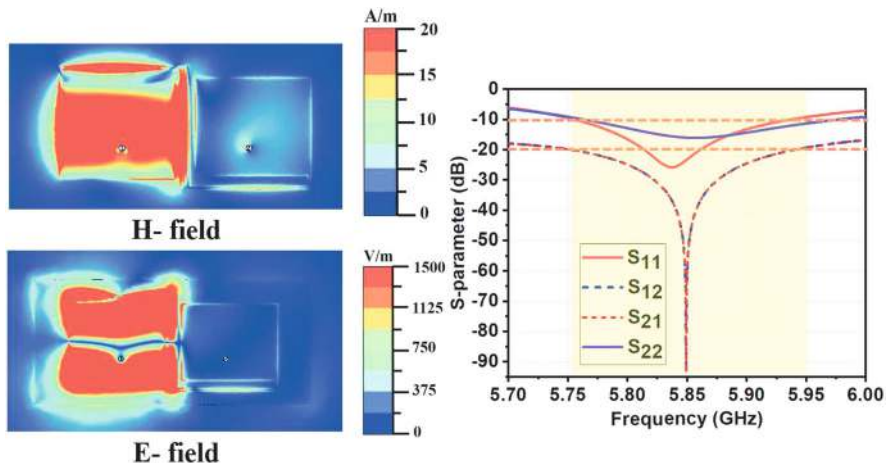


**Fig. 11** H- and E-field distribution on the patches of the stage-2 antenna configuration (see complete Fig. 3) at 5.85 GHz, along with the frequency variation of S-parameters (port 1 is excited while keeping port 2 terminated with matched load). Here, also, due to structural asymmetry, we have  $S_{11} \neq S_{22}$  (reciprocity ensures  $S_{12} = S_{21}$ , as expected)

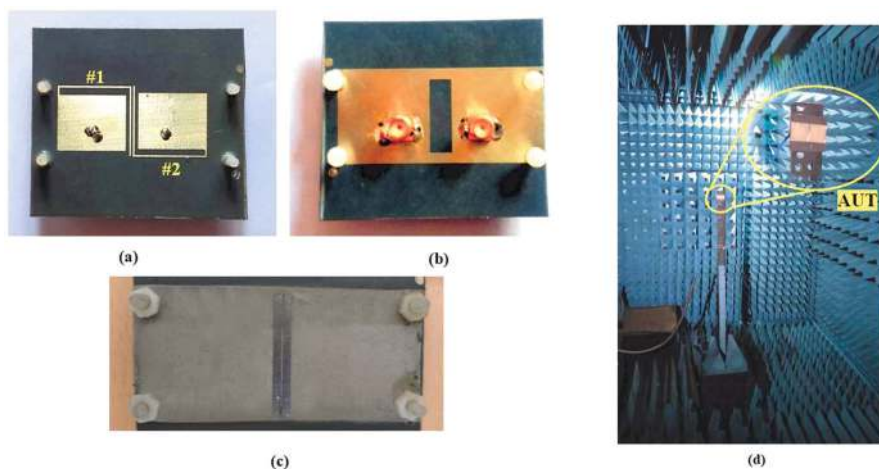


**Fig. 12** Fabricated proposed antenna prototype: (a) top view (without superstrate), (b) bottom view, (c) top view (with superstrate), and (d) far-field radiation pattern measurement setup in anechoic chamber

corners of the antenna (see Fig. 13). The S-parameters for the proposed two-port antenna are measured using Agilent N5230A PNA and compared with the simulation results (see Fig. 13). The measured inter-element isolation at the operating frequency is  $\approx 90$  dB. It is more than 25 dB over the complete operating band. The deviation in the S-parameter is due to the fabrication tolerances and surrounding

**Fig. 13** Frequency variation of simulated and measured S-parameters for the proposed antenna in Fig. 1

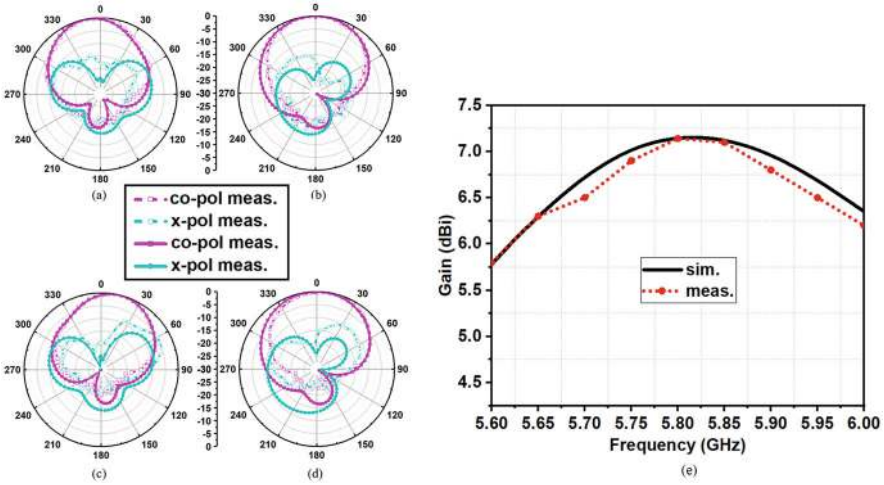
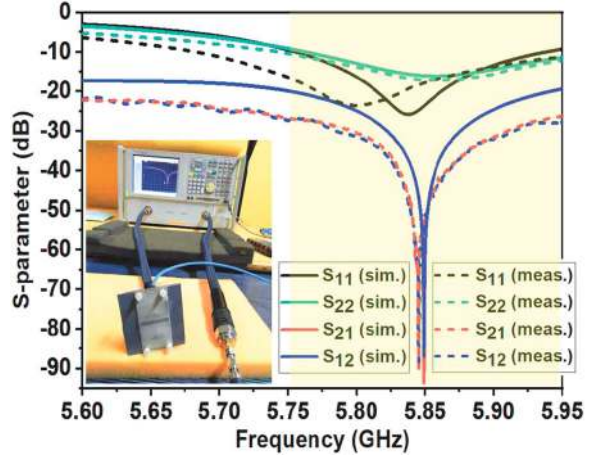


**Fig. 14** Simulated and measured patterns at 5.85 GHz: (a) E-plane (Antenna 1), (b) H-plane (Antenna 1), (c) E-plane (Antenna 2), (d) H-plane (Antenna 2), and (e) frequency variation of simulated and measured gain for the proposed antenna

effects. Figure 12d depicts the antenna far-field measurement setup. The measured and simulated far-field E-plane and H-plane co/cross-polar pattern is provided in Fig. 14. The proposed antenna exhibits a maximum gain of 7.11 dBi at  $10^\circ$  broadside tilt angle and 6.69 dBi gain at  $0^\circ$  broadside direction. The simulated and measured gain over frequency curve is provided in Fig. 15. A comparison study of these earlier published works with the proposed technique is provided in Table 1. The comparison study shows that the proposed technique exhibits maximum possible isolation ( $> 90$  dB) with very close inter-element spacing ( $\approx 0.01\lambda_0$ ) compared to the earlier published works. Moreover, the impedance bandwidth and the gain of

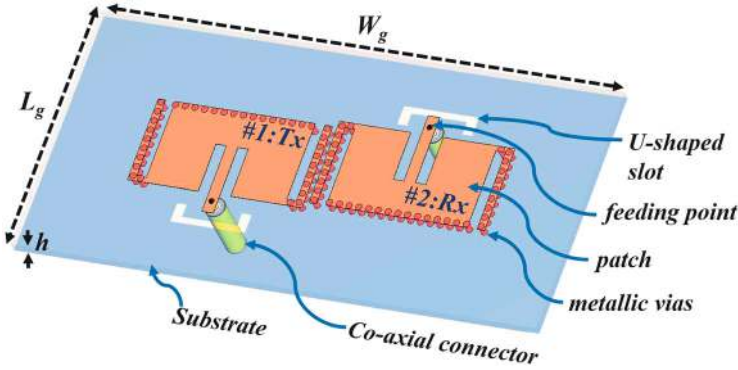


**Fig. 15** Schematic representation of SI signal and desired SoI in FD communication system

the proposed antenna are comparable with the earlier reported results as provided in Table 1.

## 2.2 Planar Multi-radiator FD Antenna with SIC Using Field Confinement Method

In this section, a multi-radiator FD antenna design is discussed where the planarity in design is achieved unlike section 2.1. The schematic of the proposed planar multi-radiator antenna is shown in Fig. 15 [31], where SIC is obtained using two techniques acting simultaneously such as the field confinement technique using metallic vias and stop-band characteristic by defected ground structure (DGS). The multi-radiator structure contains two half-mode microstrip patch radiating structures designed on an RTD 5880 substrate having  $\epsilon_r = 2.2$ ,  $\tan \delta = 0.0009$ , with an overall dimension  $L_g \times W_g \times h$  (38 mm  $\times$  80 mm  $\times$  1.6 mm). A detailed design evolution of the proposed FD antenna is shown in Fig. 16.

Initially, in stage-I of the design flow, two inset-fed microstrip patch antennas are designed having  $TM_{01}$  mode, and the corresponding antenna dimension is length ( $l_p = 16.2$  mm) and width ( $w_p = 20$  mm) of the patch, width of notch ( $g_1 = 0.625$  mm), width of microstrip feed-line ( $w_f = 2.75$  mm), and the inset depth ( $l_1 = 5$  mm) [32, 33]. The two antennas such as the transmitter (#1 :  $T_x$ ) and a receiver (#2 :  $R_x$ ) are placed adjacent to each other with  $180^\circ$  orientation with a separation  $g = 6$  mm as shown in Fig. 16. The antennas are designed at 5.9 GHz operating frequency as shown in the S-parameter ( $|S_{11}|$ ) curve in Fig. 17a. In contrast, the  $|S_{21}|$  parameter of  $-11.8$  dB between #1 :  $T_x$  and #2 :  $R_x$  as shown in Fig. 17b signifies high mutual coupling leading to high antenna domain SI due to proximity between the antennas having similar polarization state. To improve the inter-element isolation ( $|S_{21}|$ ) compared to stage-I, two metallic vias are placed at two adjacent sides of the

**Table 1** Comparison of proposed two-port antenna with other structures available in open literature

Ref.	Edge spacing ( $\lambda_0$ )	OF (GHz)	IBW (%)	Isolation (dB)	Decoupling technique	Max. Gain (dBi)
[21]	0.06	2.45	1.5	>25	Ring DGS	NA
[22]	0.135	5.8	NA	>24.5	Metamaterial structure	4
[23]	0.1	5.4	NA	>23	Modified-U shape DS	4.24
[24]	0.11	4.8	5.21	>16	SMLR	NA
[25]	0.07	3.5	2.8	>35	PCR	~6
[26]	0.13	5.25	2.6	>16	FSS	9
[27]	0.19	10	3	>37	Slot	
[28]	0.14	4	NA	>45	PBO	5.3
[29]	NA	2.4	9	>35	180 hybrid/ DGS	4
[30]	0.09	4.7	6.5	>50	PAC	~3
Prop.	$\approx 0.01$	5.85	3.41	>90	Asymmetry+DGS+NFDS	7.11

(OF: operating frequency and IBW: 10 dB impedance bandwidth)

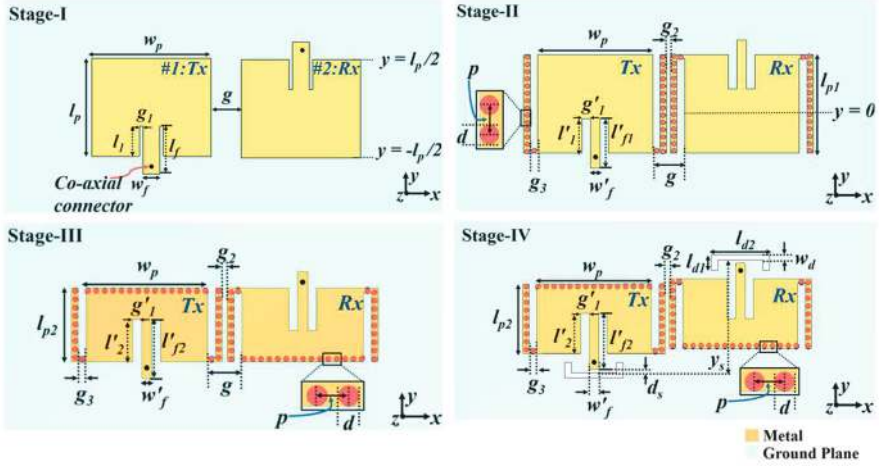


**Fig. 16** Design evolution of proposed planar multi-radiator FD antenna from stage-I to stage-IV

Tx and Rx microstrip antenna at  $y = -l_p/2$  and  $y = l_p/2$  of stage-I (see Fig. 16), in addition to a series of metallic vias at  $g_3$  distance away from the non-radiating edge as shown in stage-II of Fig. 16. The via diameter ( $d$ ) and the distance between two consecutive vias ( $p$ ) are 1 mm and 1.5 mm, respectively. This leads to a  $d/p$  value of approximately 0.66, which restricts the field coupling between radiating patches. On the other hand, it has been taken care of that the via positioning should not affect the antenna operating frequency and polarization state. The  $S_{11}$  plot for stage-II design in Fig. 17a shows an uninterrupted operating frequency of 5.9 GHz with improved  $S_{21}$  of  $-19$  dB, whereas a change in antenna bandwidth is observed. Furthermore, the surface current distributions in Fig. 18 for stage-I and stage-II show the unaffected polarization state.

In stage-III, another series of metallic vias is placed, having the same  $d/p$  ratio as in stage-I, at  $y = 0$  position, thereby reducing the antenna size. Furthermore, it changes the antenna operating mode from  $TM_{0,1}$  to  $TM_{0,1/2}$  at 5.9 GHz operating frequency and improves the antenna donation isolation to 31.5 dB (see Fig. 17b) due to the field confinement provided metallic via loading. Finally, in stage-IV two U-shaped slots are etched out from the ground near the feed line locations of the Tx and Rx antennas to further improve the antenna donation isolation. The slot design parameters such as slot-dimensions ( $l_{d1} = 3$  mm,  $l_{d2} = 11.5$  mm,  $w_d = 1$  mm), slot-position relative to the feed-line ( $d_s = 0.5$  mm), and the relative distance between two slots ( $y_s = 21.15$  mm) are optimized such that the Tx–Rx isolation is significantly enhanced to 87.08 dB compared to stage-III (Fig. 17b), without compromising on the  $|S_{11}|$  response (Fig. 17a).

Simulated Poynting power flow between the Tx and Rx antennas through the substrate for various design stages is provided in Fig. 19. This provides a clear visual understanding of the coupling between the Tx and Rx antennas. A gradual decrease



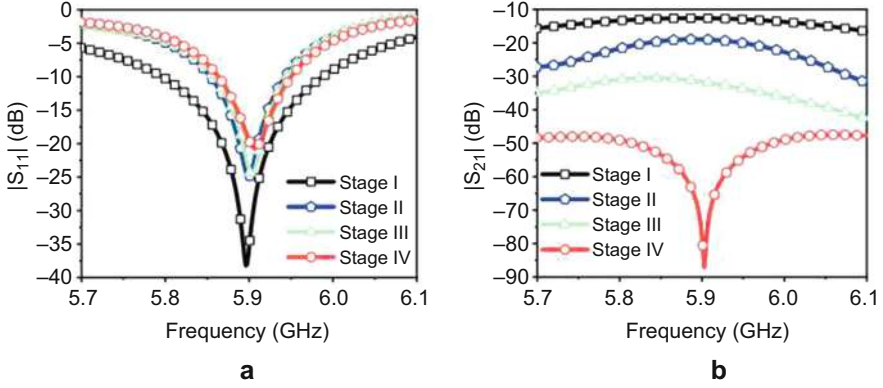


**Fig. 17** Simulated S-parameters response for stage-I to stage-IV as shown in Fig. 2: (a)  $|S_{11}| = |S_{22}|$  and (b)  $|S_{21}| = |S_{12}|$

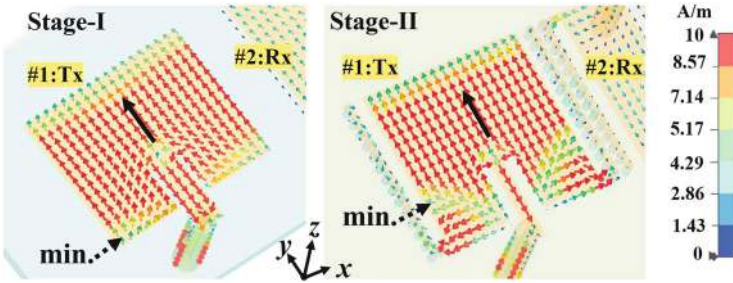


**Fig. 18** Schematic representation of SI signal and desired SoI in FD communication system

in the field coupling between the antennas can be observed in Fig. 19, where the field coupling is drastically reduced in stage-IV compared to stage-I. This validates the coupling S-parameter response provided in Fig. 17b. Table 2 provides a detailed account of the antenna's performance parameters during different design stages. The table shows an improvement in antenna domain isolation and efficiency at stage-IV compared to stage-I, without any impact on the antenna's operating frequency and cross-polar level. The miniaturization from  $TM_{0,1}$  mode to  $TM_{0,1/2}$  mode by via loading causes a decrease in impedance bandwidth and gain from stage-I to stage-IV. However, the obtained bandwidth and the antenna gain are sufficient to meet the application requirement of the IEEE 802.11p band, which is used for V2X-ITS (Intelligent Transportation System) applications around 5.9 GHz [34]. Table 3 compares the proposed work with some earlier published work, highlighting the distinct advantage of the proposed work. It provides maximum Tx–Rx isolation with a planar design, without the use of any conventional techniques such as complex feeding lines, circulators, hybrid networks, etc.

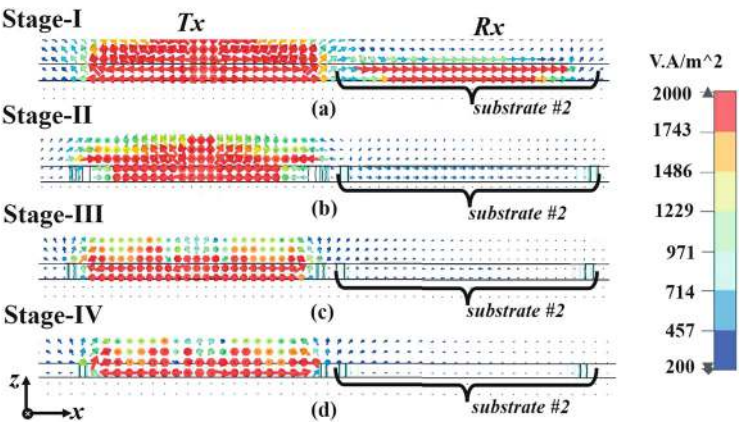


**Fig. 19** Poynting-vector distribution showing power flow between the Tx and Rx antennas of the proposed FD antenna for (a) Stage-I, (b) Stage-II, (c) Stage-III, and (d) Stage-IV. Here, Tx is excited, and Rx is terminated in matched load

**Table 2** Antenna performance at various design stages

Antenna	OF (GHz)	IBW (%)	PG (dBi)	TE (%)	Max. isolation (dB)	X-pol (dB)
Stage-I	5.9	3.38	7.65	88.5	11.8	>20
Stage-II	5.9	1.6	7.65	89.2	19	>20
Stage-III	5.9	1.6	6.2	90.5	31.5	>20
Stage-IV	5.9	1.6	5.63	90.5	87.08	>20

OF: Operating Frequency, IBW:  $-10$  dB Impedance Bandwidth, PG: Peak Gain, and TE: Total Efficiency

2.2.1 Parametric Studies and Experimental Results

A parametric study has been carried out to investigate the impact of various design parameters on the proposed design for stage-IV of Fig. 16. The study focuses on the effective length ( $l_d = l_{d1} + l_{d2}$ ), width ( $w_d$ ), and relative positions ( $d_s$  and  $y_s$ ) of two U-shaped slots as shown in Fig. 20. Increasing the values of  $l_d$  and  $w_d$  shifts the resonant band-stop  $|S_{21}|$  response toward lower frequencies, as shown in Fig. 20a and b. It is possible to customize the band-stop response at a desired frequency by keeping either  $w_d$  or  $l_d$  fixed and then varying the other. Refer to [40] for the equivalent circuit modeling of defected ground structures. As the distance between the two ground-perturbing slots ( $d_s$ ) and the width of the slots ( $y_s$ ) are reduced, they start to approach each other. This causes the effective mutual inductance of the slots to increase, which shifts the frequency response of the  $|S_{21}|$  band-stop toward lower frequencies. For more details, please refer to [41]. You can also see the graphs of this behavior in Fig. 20c and d. Figure 20 confirms that the  $|S_{11}|$ -characteristics remain unaffected by parametric variations, meaning that the mutual coupling response can



**Table 3** Comparison of proposed work with other structures available in open literature

[Ref.]	$f_0$ (GHz)	IBW (%)	Size ( $\lambda_0^3$ )	SIC method	Polarization	Isolation (dB)	Structure
[35]	2.45	4.1	0.106	BNF	Co-CP	> 47	Non-planar
[36]	2.44	4	0.03	QFN	Co-CP	> 40.6	Non-planar
[37]	2.45	11.7	0.029	Near-field cancellation	Co-LP	> 38	Non-planar
[38]	2.44	4.9	0.0025	Decoupling resonator	Co-LP	> 20	Non-planar
[39]	6.29	1.6	0.031	Two coupling path	Co-LP	> 40	Non-planar
Prop.	5.9	1.6	0.034	Field confinement	Co-LP	$\approx$ 90	Planar

$\lambda_0$ : free-space wavelength corresponding to  $f_0$ , BNF: Beamforming network, and QNF: Quadrature feeding network

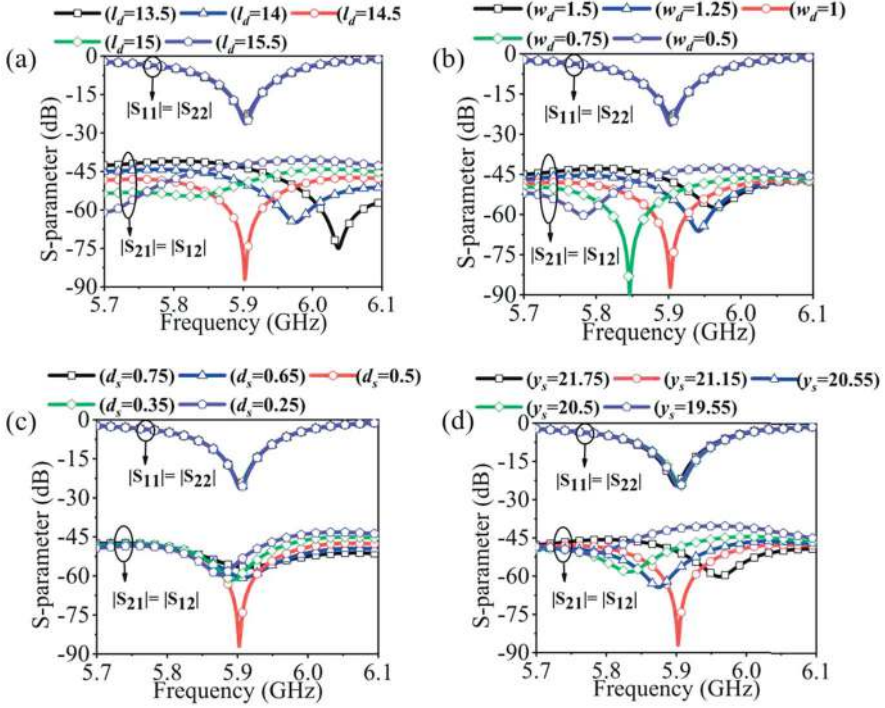


**Fig. 20** Parametric study of stage-IV design parameters: (a)  $l_d$ , (b)  $w_d$ , (c)  $d_s$ , and (d)  $y_s$  of Fig. 2 to observe the effect of parameter variation on FD antenna S-parameter (unit: mm)

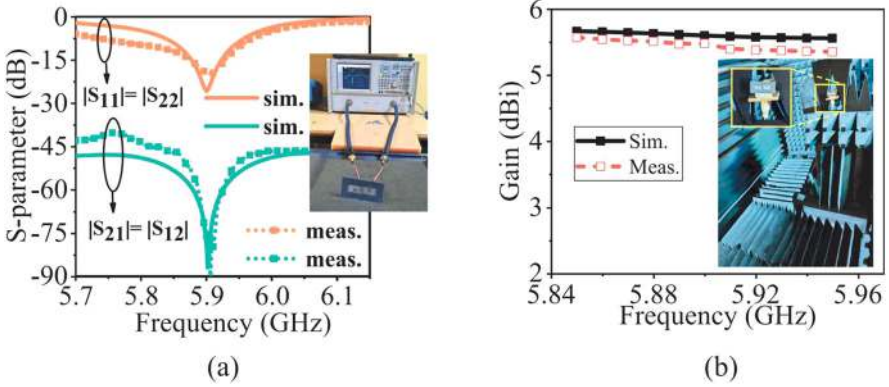
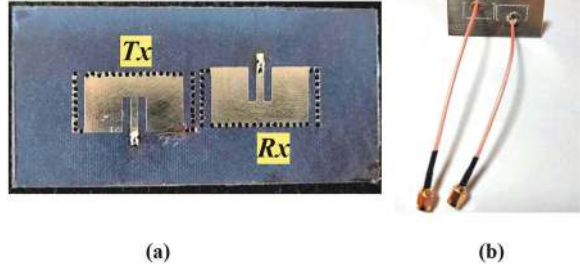
be fine-tuned without affecting the impedance matching performance. The results of the study provide a better understanding of the proposed design.

Figure 21 depicts the two-port FD antenna prototype. Figure 22 shows the corresponding S-parameter response and gain plot with far-field measurement setup in the anechoic chamber, while the inset displays the image of Agilent N5230A PNA. The S-parameters that were simulated and measured are in good agreement, as can be seen in Fig. 22a. The individual antenna gain is stable around 5.63 dBi in the operating band around 5.9 GHz, as shown in Fig. 22b. Both the simulated and measured 2D radiation patterns of the individual antenna element show an X-pol level of below 20 dB, as depicted in Fig. 23.

### 2.3 Planar Shared-Radiator FD Antenna with SIC Using Vias and Stub Resonator

Unlike Sects. 2.1 and 2.2, this section discusses a colinearly polarized shared-radiator (SR) FD antenna design where the planarity and further compactness with

**Fig. 21** Fabricated prototype of the proposed two-element FD antenna system of Fig. 1: (a) top view and (b) bottom view



**Fig. 22** Frequency variation of simulated and measured (a) S-parameters and (b) gain with far-field measurement setup in anechoic chamber of proposed FD antenna system as shown in Fig. 3

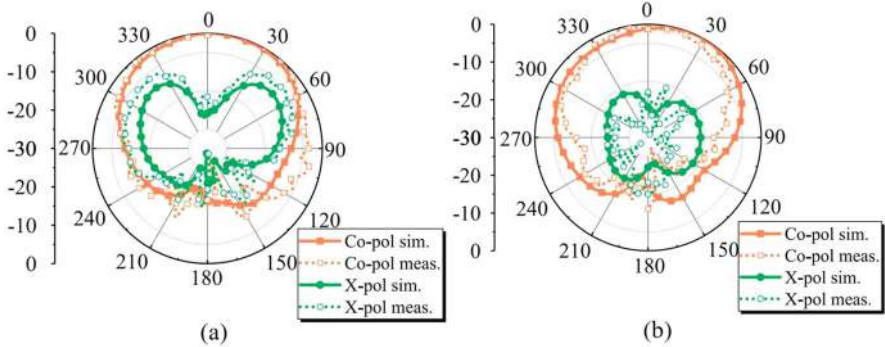


**Fig. 23** 2D radiation pattern of the Tx antenna of the two-element prototype of Fig. 1: (a) xoz-plane and (b) yoz-plane

simplicity in design are achieved. The schematic of the proposed SR-FD antenna is shown in Fig. 24 [42], where the SIC is achieved using via and stub resonator loading. The antenna is designed at 5.9 GHz operating frequency on a single Roger

**Fig. 24** 3D schematic design of the proposed shared-radiator FD antenna

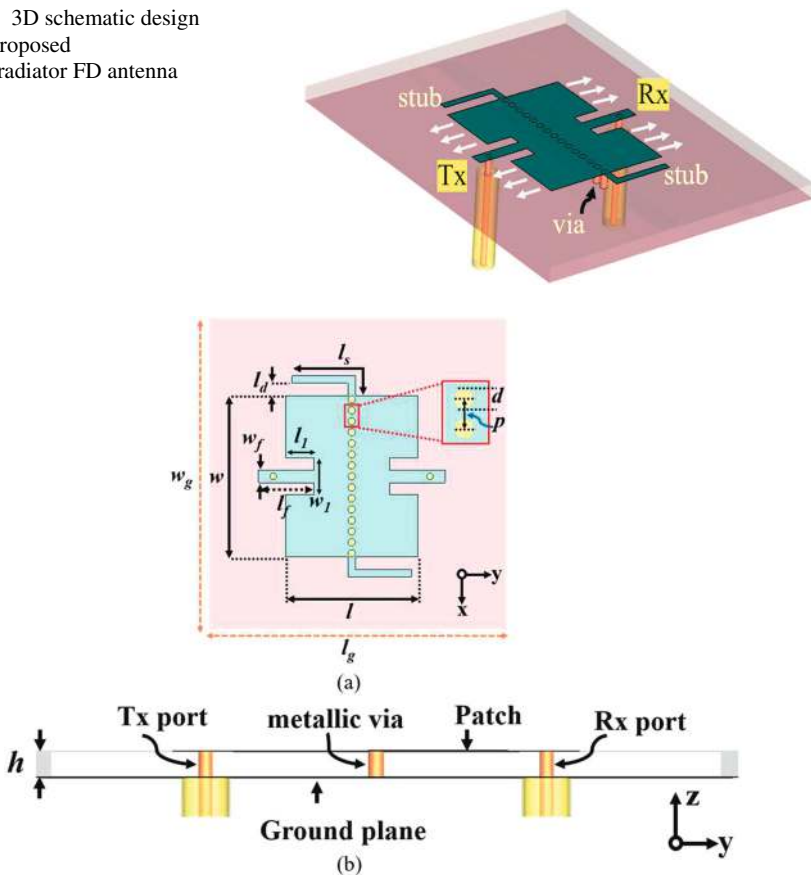


**Fig. 25** (a) Top and (b) cross-section view of the proposed SR-FD antenna. Dimensions:  $w_g = 1.024\lambda_0$ ,  $l_g = 0.841\lambda_0$ ,  $h = 0.031\lambda_0$ ,  $l_s = 0.222\lambda_0$ ,  $l_d = 0.033\lambda_0$ ,  $l = 0.353\lambda_0$ ,  $w = 0.432\lambda_0$ ,  $l_1 = 0.075\lambda_0$ ,  $w_1 = 0.098\lambda_0$ ,  $w_f = 0.034\lambda_0$  (where  $\lambda_0$  represents the free-space wavelength at 5.9 GHz operating frequency)

RTD5880 substrate ( $\epsilon_r = 2.2$ ,  $\tan \delta = 0.0009$ ) having  $l_g \times w_g \times h$  ( $0.841\lambda_0 \times 1.024\lambda_0 \times 0.031\lambda_0$ , where  $\lambda_0$  is the free-space wavelength at 5.9 GHz operating frequency), see Fig. 25. The rest of the design parameters are mentioned in Fig. 25. A detailed design evolution of the proposed antenna along with various performance parameters at different stages is shown in Fig. 26. The design evolution contains a comparative study of the E-field distribution, S-parameter response, and radiation pattern at different design stages, see Fig. 26.

Initially, in stage-1, a single microstrip structure is designed with two inset feeds at either end of the radiation edge, thereby providing a two-port configuration in a shared metallic structure, see Fig. 26. The two ports act as transmitter (Tx) and receiver (Rx) ports for an FD antenna system. The antenna dimensions having length

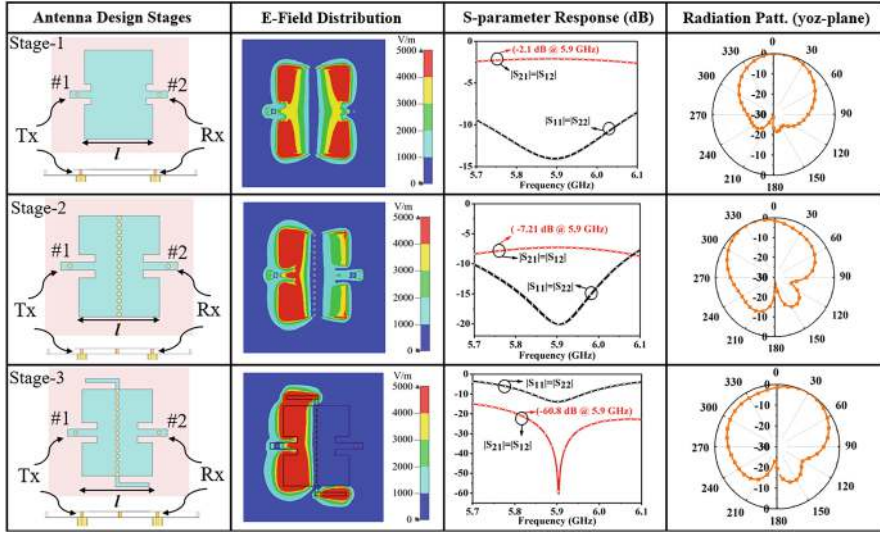


**Fig. 26** Design evolution of the proposed SR-FD antenna. (Note: (1) here E-field distribution corresponds to port #1:Tx excitation while port #2:Rx terminated to matched load, and (2) due to the identical radiation pattern for both Tx and Rx ports, the 2D pattern for only #1:Tx port is provided here)

( $l = 17.71$  mm) and width ( $w = 22$  mm) of patch, width of notch ( $w_1 = 5$  mm), width of microstrip feed-line ( $w_f = 1.75$  mm), and the inset depth ( $l_f = 5.5$  mm) are chosen [32] such that the antenna operates in  $TM_{1,0}$  fundamental modes at 5.9 GHz operating frequency. The S-parameter plot of the stage-1 design shows the good impedance matching of both Tx and Rx ports. However, unlike multi-radiator structures, the proposed FD antenna at stage-1 suffers from the extremely high mutual coupling between the Tx and Rx ports, as shown in E-field distribution in Fig. 26 and which also reflects in the S-parameter plot having  $S_{21} = -2.1$  dB. Here, the E-field of the SR-FD antenna is computed for the Tx port, while the Rx is terminated to match termination. The radiation pattern in stage-1 shows a stable response. To improve the Tx to Rx isolation, a series of metallic vias is placed at the center line of the SR-FD antenna as shown in the stage-2 design. The via loading makes the Tx and Rx ports operate at  $TM_{1/2,0}$  mode and reduces to mutual coupling  $S_{21} = -7.21$  dB, which is also visible in reducing the E-field coupling in the Rx port of stage-2 design compared to stage-1. However, the field suppression between the Tx and Rx is perfectly achieved which affects the modal purity and makes the radiation pattern tilt, as shown in the stage-2 design in Fig. 26. It has been taken care that the  $S_{11}$  parameter is unaffected by the via loading, and the updated design parameters at stage-2 are  $l = 17.5$  mm,  $w = 22$  mm,  $w_1 = 5$  mm,  $w_f = 1.75$  mm, and  $l_f = 3.55$  mm. Finally, in stage-3 two L-shaped microstrip stub resonators are designed at either side of the via loading such that the Tx and Rx isolation is significantly improved to  $-60.8$  dB, without affecting the antenna reflection

**Table 4** Antenna performance at various design stages

Antenna	$f_0$ (GHz)	IBW (%)	PRG (dBi)	TE (%)	Max. Isolation (dB)	X-pol (dB)
Stage-1	5.9	5.59	3.9	32.3	2.1	>18
Stage-2	5.9	6.05	6.19	76.9	7.21	>18
Stage-3	5.9	2.1	6.65	89.5	60.8	>18

$f_0$ : Operating frequency, IBW:  $-10$  dB Impedance bandwidth, PRG: Peak realized gain, and TE: Total efficiency (TE of a single antenna is computed while terminating the other antenna to a 50-ohm match load)

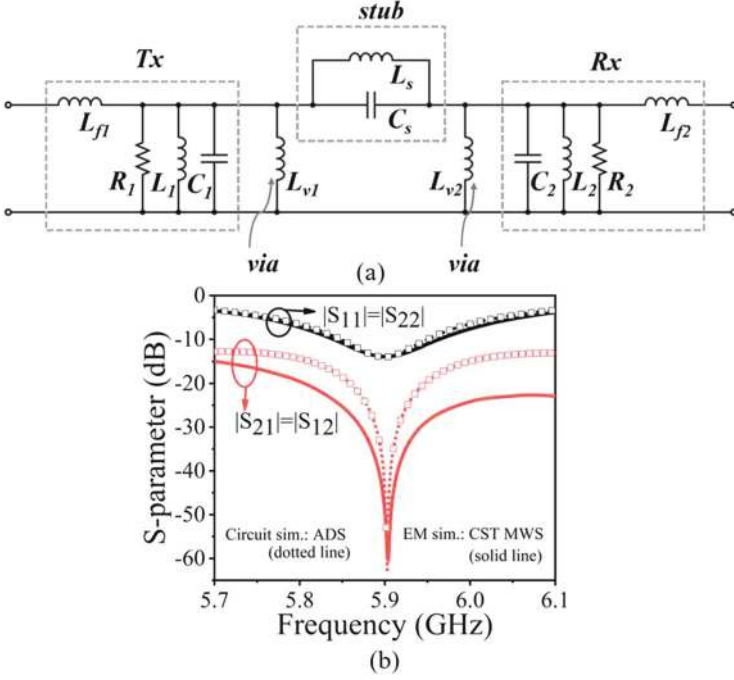
coefficient response, see Fig. 26. Here, the loaded stub resonators provide band-stop characteristics which are explained in the subsequent discussion. Furthermore, the E-field distribution in stage-3 depicts the significant coupling reduction near zero between the Tx and RX ports.

Table 4 shows the comparative study of various performance parameters at the three design stages. The Tx–Rx SIC or inter-element isolation is significantly improved from 2.1 dB in stage-1 to 60.8 dB in stage-3. Furthermore, a gradual increase in antenna gain and efficiency from stage-1 to stage-3 is also observed due to reduced Tx–Rx interference. The physical dimension reduction of individual antennas due to via loading results in a decrease of impedance bandwidth from 5.59% at stage-1 to 2.1% at stage-3 as shown in Table 4.

To provide a better insight into the stop-band response of L-shaped stub resonators, an equivalent circuit model is provided in Fig. 27a. Here, we use parallel *RCL* tank circuits to effectively represent the microstrip antennas. To represent the coaxial probes for the Tx and Rx ports, we use  $L_{f1}$  and  $L_{f2}$ , respectively. The  $L_{v1}$  and  $L_{v2}$  are used to represent the shorted vias. Finally, the *LC* tank circuit represents the L-shaped stub. The Keysight ADS software was used to verify the proposed equivalent circuit model. The lumped element circuit parameters are given in Fig. 27. Additionally, excellent agreement was observed when comparing the response generated by the ADS software with the EM simulation result, as demonstrated in Fig. 27b. Table 5 compares the proposed work with the other state-of-the-art counterparts in the open literature. This highlights the distinctness of the proposed work having a planar geometry with a shared-radiator structure. It is noticeable from the table that the proposed design achieves better inter-element isolation compared to its counterparts without using any conventional techniques, such as beamforming/feeding networks, bulky hybrid couplers, or circulators.

### 2.3.1 Parametric Studies and Experimental Results

In order to gain more understanding of the proposed FD antenna design, a parametric analysis for the following parameters: stub length ( $l_s$ ), the gap between the stub and the antenna's non-radiating edge ( $l_d$ ), and the distance between two consecutive vias ( $p$ ) are carried out. Refer to Fig. 28 for more details. It is evident that an increase in the value of  $l_s$  results in a reduction of the operating frequency and the corresponding stop-band response, as shown in Fig. 28a. This allows for



**Fig. 27** (a) Equivalent circuit model for the proposed SR-FD antenna (Design Stage: 3) and (b) comparison of S-parameter response of stage-3 SR-FD antenna using CST-MWS and ADS. ( $L_{f1} = L_{f2} = 0.44$  nH,  $L_1 = L_2 = 0.101$  nH,  $C_1 = C_2 = 0.101$  nH,  $C_1 = C_2 = 8.1$  pF,  $R_1 = R_2 = 83.05\Omega$ ,  $L_{v1} = L_{v2} = 1$  nH,  $L_s = 0.15$  nH,  $C_s = 4.847$  pF)

tuning the stop-band response based on the required operating band, providing high inter-port isolation flexibility. Furthermore, the value of  $l_s = 0.222\lambda_0 = 11.325$  mm is kept fixed, and the  $l_d$  variation is performed. Figure 28b depicts that the impedance matching is unaffected by the variation of  $l_d$ ; however, a small impact on the inter-port coupling is observed. Figure 28c illustrates the S-parameters response for changes in  $p$ . The response for  $p = 1$  and 1.5 mm is nearly identical, although choosing  $p = 1$  mm may result in a physical slot in the center line of the microstrip structure. A rise in  $p$  significantly amplifies the field coupling from port #1:Tx to #2:Rx, eventually resulting in a degraded response. This is clearly illustrated in Fig. 28c.

The prototype of the proposed SR-FD antenna is shown in Fig. 29. In Fig. 30a, the measured S-parameters (with an image of Agilent N5230A PNA in the inset) are presented along with the simulated values, which show good agreement. The simulated and measured peak-gain values' frequency variation can be seen in Fig. 30b (far-field measurement setup in the inset). One antenna of the FD system's simulated and measured 2D radiation patterns (with the other antenna port terminated with a matched load) shows a peak gain of 6.51 dBi at 5.9 GHz (refer to Fig. 30b), along with an X-pol level below  $-18$  dB (refer to Fig. 31).



**Table 5** Comparison of proposed work with other structures available in the open literature

[Ref]	$f_0$ (GHz)	BW (%)	Size ( $\lambda^3$ )	SIC method	Polarization	Isolation (dB)	Planar	SR
[35]	2.45	4.1	0.106	BNF	Co-CP	> 47	No	No
[32]	2.44	4	0.03	QFN	Co-CP	> 40.6	No	No
[37]	2.45	11.7	0.029	Near-field cancellation	Co-LP	> 38	No	No
[38]	2.44	4.9	0.0025	Decoupling resonator	Co-LP	> 20	No	Yes
[39]	6.29	1.6	0.031	Two coupling path	Co-LP	> 40	No	Yes
[43]	3.5	11.4	0.063	Mode cancellation	Co-LP	> 50	No	Yes
[44]	2.45	4.5	0.007	DGS	Co-LP	> 25	Yes	No
[17]	5.85	3.41	0.027	Asymmetry + DGS +NFDs	Co-LP	> 90	No	No
[31]	5.9	1.6	0.034	Field confinement	Co-LP	$\approx$ 90	Yes	No
Prop.	5.9	2.1	0.026	Vias and stub resonator	Co-LP	>60	Yes	Yes

$\lambda_0$ : free-space wavelength corresponding to  $f_0$ , BNF: Beamforming network, QNF: Quadrature feeding network, DGS: Defected ground structure, NFDs: Near-field decoupling structure, and SR: Shared radiator



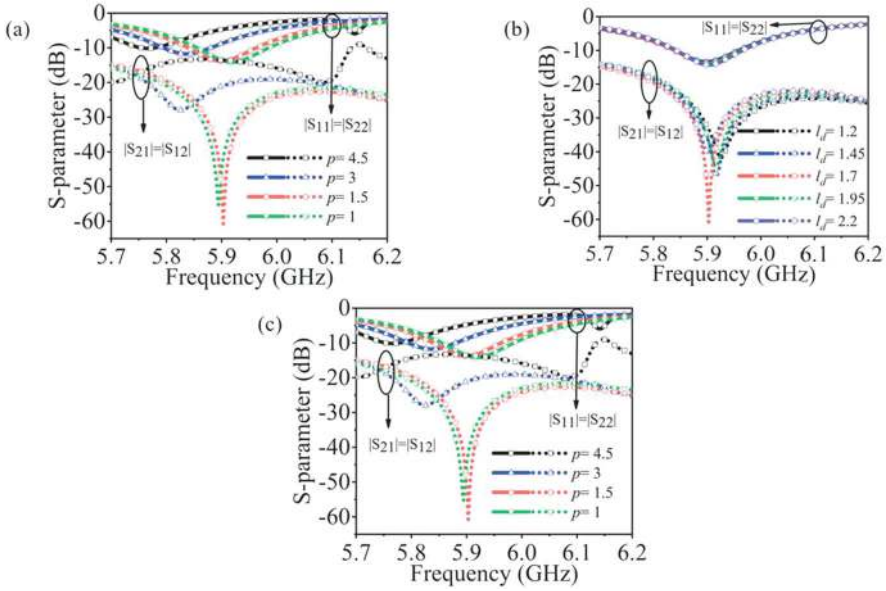
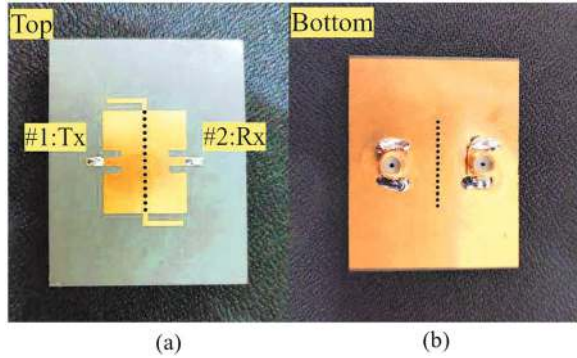


**Fig. 28** Parametric study of Stage-IV design parameters: (a)  $l_s$ , (b)  $l_d$ , and (c)  $p$  of Fig. 2 to observe the effect of parameter variation on FD antenna S-parameter (unit: mm)

**Fig. 29** Fabricated prototype of the proposed SR-FD antenna system of Fig. 1: (a) top view and (b) bottom view



### 3 Conclusion

Full-duplex-enabled antenna technology is emerging research for future wireless communication. In this chapter, we address the fundamental problem in full-duplex (FD) antenna systems, i.e., self-interference (SI), by providing various antenna design techniques. Chronologically, we discuss the three different state-of-the-art FD antenna designs along with SIC based on design complexity, compactness, and integrability. The initial FD antenna design uses three different techniques such as design asymmetry, near-field decoupling mechanism, and defective ground

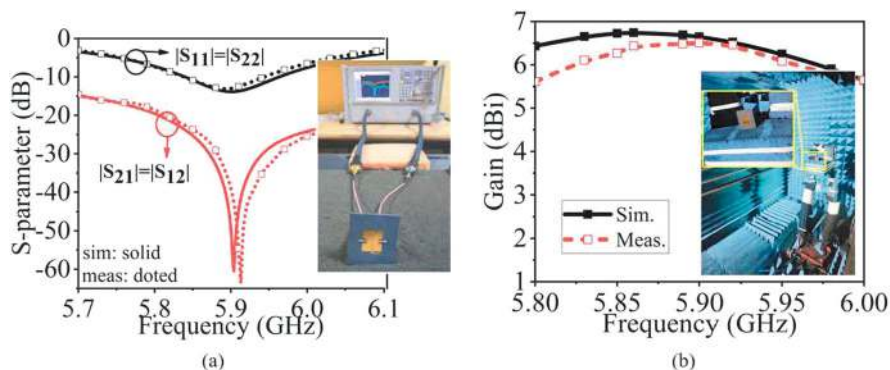


**Fig. 30** Frequency variation of simulated and measured (a) S-parameters and (b) gain with far-field measurement setup in anechoic chamber of proposed FD antenna system as shown in Fig. 1

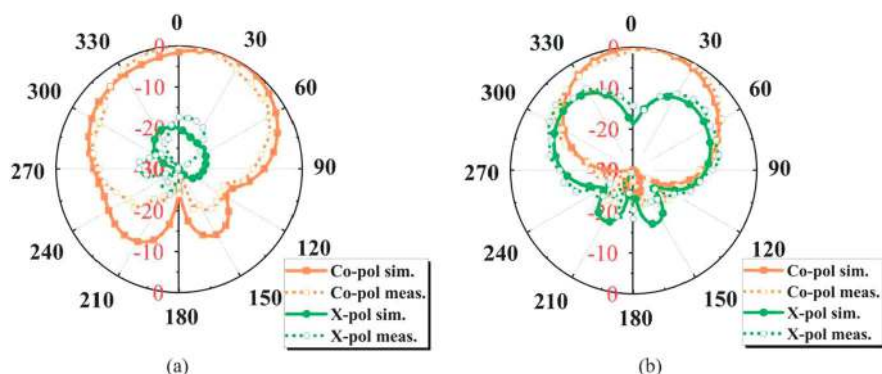


**Fig. 31** Fabricated prototype of the proposed SR-FD antenna system of Fig. 1: (a) top view and (b) bottom view

structure combinedly to suppress the SI level to  $\approx 90$  dB. However, this is a stacked design with a multi-radiator system. The second design uses the field confinement technique with a defected ground structure to reduce SI to nearly 90 dB having planar geometry with multi-radiator operation. The final design uses shorted vias with resonator loading, thereby surprising SI by 60 dB, where it is a planar design with shared-radiator operation.

## References

1. *6G The Next Hyper-Connected Experience for All*, White paper Samsung Research. [Online] Available: <https://research.samsung.com/next-generation-communications>
2. H. Holma, S. Heikkinen, O.-A. Lehtinen, A. Toskala, Interference considerations for the time division duplex mode of the UMTS Terrestrial Radio Access. *IEEE J. Sel. Areas Commun.* **18**(8), 1386–1393 (2000)

3. D. Kim, H. Lee, D. Hong, A survey of in-band full-duplex transmission: From the perspective of PHY and MAC layers. *IEEE Commun. Surv. Tutor.* **17**(4), 2017–2046 (2015)
4. A. Sabharwal, P. Schniter, D. Guo, D.W. Bliss, S. Rangarajan, R. Wichman, In-band full-duplex wireless: challenges and opportunities. *IEEE J. Sel. Areas Commun.* **32**(9), 1637–1652 (2014)
5. Z. Zhang, K. Long, A.V. Vasilakos, L. Hanzo, Full-duplex wireless communications: Challenges, solutions, and future research directions. *Proc. IEEE* **104**(7), 1369–1409 (2016)
6. H. Li et al., Self-interference cancellation enabling high-throughput short-reach wireless full-duplex communication. *IEEE Trans. Wirel. Commun.* **17**(10), 6475–6486 (2018). <https://doi.org/10.1109/TWC.2018.2859985>
7. T. Fukui, K. Komatsu, Y. Miyaji, H. Uehara, Analog self-interference cancellation using auxiliary transmitter considering IQ imbalance and amplifier nonlinearity. *IEEE Trans. Wirel. Commun.* **19**(11), 7439–7452 (2020)
8. H. Wang, Z. Wang, P. Heydari, An LO leakage suppression technique for blocker-tolerant wideband receivers with high-Q selectivity at RF input. *IEEE J. Solid State Circuits* **56**(6), 1682–1696 (2021)
9. K.E. Kolodziej, J.G. McMichael, B.T. Perry, Multitap RF canceller for in-band full-duplex wireless communications. *IEEE Trans. Wirel. Commun.* **15**(6), 4321–4334 (2016)
10. D. Korpi et al., Full-duplex mobile device: pushing the limits. *IEEE Commun. Mag.* **54**(9), 80–87 (2016)
11. T. Chen, J. Zhou, M.B. Dastjerdi, J. Diakonikolas, H. Krishnaswamy, G. Zussman, Demo abstract: Full-duplex with a compact frequency domain equalization-based RF canceller, in *Proc. IEEE Conf. Comput. Commun. Workshops*, May 2017, pp. 972–973
12. A. Nagulu, T. Chen, G. Zussman, H. Krishnaswamy, A single antenna full-duplex radio using a non-magnetic, CMOS circulator with in-built isolation tuning, in *Proc. IEEE Int. Conf. Commun. Workshops (ICC Workshops)*, May 2019, pp. 1–6
13. A. Liu, W. Sheng, T. Riihonen, Per-antenna self-interference cancellation beamforming design for digital phased array. *IEEE Signal Process. Lett.* **29**, 2442–2446 (2022)
14. K. Komatsu, Y. Miyaji, H. Uehara, Basis function selection of frequency-domain hammerstein self-interference canceller for in-band full-duplex wireless communications. *IEEE Trans. Wirel. Commun.* **17**(6), 3768–3780 (2018)
15. C. Li, H. Zhao, F. Wu, Y. Tang, Digital self-interference cancellation with variable fractional delay FIR filter for full-duplex radios. *IEEE Commun. Lett.* **22**(5), 1082–1085 (2018)
16. S. Mori, K. Mizutani, H. Harada, A digital self-interference cancellation scheme for in-band full-duplex-applied 5G system and its software-defined radio implementation. *IEEE Open J. Veh. Technol.* **4**, 444–456 (2023)
17. J.C. Dash, D. Sarkar, Microstrip patch antenna system with enhanced inter-port isolation for full-duplex/MIMO applications. *IEEE Access* **9**, 156222–156228 (2021)
18. K. Wu, C. Wei, X. Mei, Z. Zhang, Array-antenna decoupling surface. *IEEE Trans. Antennas Propag.* **65**(12), 6728–6738 (2017)
19. J.C. Dash et al., Design of dual band patch antenna with bandwidth enhancement using complementary defected ground structure, in *2nd International Conference on Contemporary Computing and Informatics (IC3I)*, pp. 271–274 (2016)
20. I. Bahl et al., *Microstrip Lines and Slotlines* (3rd edn.) (Artech, 2013)
21. R. Anitha et al., Enhanced isolation with defected ground structure in MIMO antenna. *Electron. Lett.* **50**(24), 1784–1786 (2014)
22. A. Iqbal et al., Metamaterial-based highly isolated MIMO antenna for portable wireless applications. *Electronics* **7**(10), 267 (2018)
23. A. Iqbal et al., Modified U-shaped resonator as decoupling structure in MIMO antenna. *Electronics* **7**(10), 267 (2020)
24. M. Alsathet et al., Implementation of slotted meander-line resonators for isolation enhancement in microstrip patch antenna arrays. *IEEE Antennas Wirel. Propag. Lett.* **12**, 15–18 (2013)
25. K.S. Vishvaksean, K. Mithra, R. Kalaiarasan, K.S. Raj, Mutual coupling reduction in microstrip patch antenna arrays using parallel coupled-line resonators. *IEEE Antennas Wirel. Propag. Lett.* **16**, 2146–2149 (2017)

26. T. Hassan, M.U. Khan, H. Attia, M.S. Sharawi, An FSS based correlation reduction technique for MIMO antennas. *IEEE Trans. Antennas Propag.* **66**(9), 4900–4905 (2018)
27. M. Kiani-Kharaji, H.R. Hassani, S. Mohammad-Ali-Nezhad, Wide scan phased array patch antenna with mutual coupling reduction. *IET Microw. Antennas Propag.* **12**(12), 1932–1938 (2018)
28. A. Ghadimi, V. Nayyeri, M. Khanjarian, M. Soleimani, O.M. Ramahi, A systematic approach for mutual coupling reduction between microstrip antennas using pixelization and binary optimization. *IEEE Antennas Wirel. Propag. Lett.* **19**(12), 2048–2052 (2020)
29. G. Makar, N. Tran, T. Karacolak, A high-isolation monopole array with ring hybrid feeding structure for in-band full-duplex systems. *IEEE Antennas Wirel. Propag. Lett.* **16**, 356–359 (2017)
30. J. Zhou et al., Integrated full duplex radios. *IEEE Commun. Mag.* **55**(4), 142–151 (2017)
31. J.C. Dash, D. Sarkar, A colinearly polarized full-duplex antenna with extremely high Tx–Rx isolation. *IEEE Antennas Wirel. Propag. Lett.* **21**(12), 2387–2391 (2022)
32. L.I. Babilio, M.A. Khayat, J.T. Williams, S.A. Long, The dependence of the input impedance on feed position of probe and microstrip line-fed patch antennas. *IEEE Trans. Antennas Propag.* **49**(1), 45–47 (2001)
33. C.A. Balanis, *Antenna Theory: Analysis and Design* (Wiley, Hoboken, NJ, 2016)
34. *Intelligent transport systems (ITS) usage*, report ITU-R M.2445-0, ITU-R (International Telecommunication Union, 2018). [Available Online]
35. J. Ha, M.A. Elmansouri, P. Valale Prasannakumar, D.S. Filipovic, Monostatic co-polarized full-duplex antenna with left- or right-hand circular polarization. *IEEE Trans. Antennas Propag.* **65**(10), 5103–5111 (2017)
36. D. Wu, Y. Sun, B. Wang, R. Lian, A compact, monostatic, co-circularly polarized simultaneous transmit and receive (STAR) antenna with high isolation. *IEEE Antennas Wirel. Propag. Lett.* **19**(7), 1127–1131 (2020)
37. D. Wu, Y. Zang, H. Luyen, M. Li, N. Behdad, A compact, low-profile simultaneous transmit and receive antenna with monopole-like radiation characteristics. *IEEE Antennas Wirel. Propag. Lett.* **18**(4), 611–615 (2019)
38. Y. He, Y. Li, Compact co-linearly polarized microstrip antenna with fence-strip resonator loading for in-band full-duplex systems. *IEEE Trans. Antennas Propag.* **69**(11), 7125–7133 (2021)
39. W. Zhang, J. Hu, Y. Li, Z. Zhang, Design of a stacked co-polarized full-duplex antenna with broadside radiation. *IEEE Trans. Antennas Propag.* **69**(11), 7111–7118 (2021)
40. D. Ahn, J.S. Park, C.S. Kim, J. Kim, Y. Qian, T. Itoh, A design of the low-pass filter using the novel microstrip defected ground structure. *IEEE Trans. Microwave Theory Tech.* **49**(1), 86–93 (2001)
41. C.S. Kim, J.S. Park, D. Ahn, J.B. Lim, A novel 1-D periodic defected ground structure for planar circuits. *IEEE Microwave Guid. Wave Lett.* **10**(4), 131–133 (2000)
42. J.C. Dash, D. Sarkar, A co-linearly polarized shared radiator-based full-duplex antenna with high Tx–Rx isolation using vias and stub resonator. *IEEE Trans. Circuits Syst. II Express Briefs* **70**(7), 2400–2404 (2023)
43. Y.-Z. Liang, F.-C. Chen, W.-F. Zeng, Q.-X. Chu, Design of self-decoupling dielectric resonator antenna with shared radiator. *IEEE Trans. Antennas Propag.* (2022). <https://doi.org/10.1109/TAP.2022.3217118>
44. K. Kumari, M. Saikia, R.K. Jaiswal, S. Malik, K.V. Srivastava, A compact, low-profile shorted TM  $1/2,0$  mode planar copolarized microstrip antenna for full-duplex systems. *IEEE Antennas Wireless Propag. Lett.* **21**(9), 1887–1891 (2022)

# Understanding Metasurface-Based Microwave Absorbers Using Transmission Line Theory



Debdeep Sarkar 

## 1 A Brief Historical Perspective on Microwave Absorbers and Anechoic Chambers

Electromagnetic (EM) wave absorbers and anechoic chambers are deployed by wireless system designers for measurement of a variety of antenna parameters like: impedance, gain, beamwidth, cross-polarization levels, radiation patterns, polarization states, monostatic and bistatic Radar cross sections, effective radiated power, boresight alignment, tracking error, etc. The term “Anechoic” means “free from echo,” where the echo can be of acoustic waves (e.g., sound waves) as well as EM waves (e.g., radio frequency signals). Anechoic chambers minimize the reflections of incident EM radiation through absorption as well as significantly reduce the external spurious EM interferences (EMI). Such chambers typically have minimum and maximum working frequencies around 30 MHz and 100 GHz, respectively. In the test region, such chambers can possess reflection levels as low as  $-70$  dB and high shielding isolation around 140 dB.

As discussed in [1], the first patented absorber using quarter-wavelength resonance concept around 2 GHz region was realized by Naamlouze Vennootschap Machinerieën in Netherlands, long back in 1936. During World War-II, more concerted efforts to achieve practical useful absorbers were carried out by both Germany and the USA. It is interesting to point out that, while the German research was focused on design of microwave absorbers for camouflaging Radars, the US research was more directed towards synthesis of absorbers for improvement of Radar performance by minimizing interfering reflections [1]. The German project bearing the code name “Schormteinfeger” (translating to “chimney sweep”) devel-

---

D. Sarkar (✉)

Indian Institute of Science, Bangalore, Karnataka, India

e-mail: [debdeep@iisc.ac.in](mailto:debdeep@iisc.ac.in)

oped multiple operational material for usage in camouflaging of submarine snorkels and periscopes. Among these methodologies, one was the “Jaumann” absorbers, which were rigid 3-inch thick broad-band material, constituted by alternate layers of rigid plastic and resistive sheets, having the ability to remain stable even after long exposures in submerged submarine environment. Such Jaumann absorbing layers effectively provided a reflection coefficient less than  $-20$  dB over the 2–15 GHz frequency range of about 2–15 GHz, for incident angles near the normal. During the period of 1941–1945, the US project led by Halpern at the Radiation Laboratory led to the evolution of Halpern-anti-radar-paint (HARP) materials, which can be more accurately described as rubber sheets rather than “paints” [1]. In addition to the HARP materials, design of the popular Salisbury screen absorber also came into the picture during this period. Salisbury showed that an efficient resonant absorber could be achieved by locating a suitable resistive sheet at a distance of quarter-wavelength from a reflecting surface. Using this Salisbury screen concept in a practical scenario, a US based Rubber company spearheaded the manufacture of special resistive cloth named as “Uskon Cloth.” For more discussions on the history of microwave absorbers, one must refer to [1].

When compared to other applications, more absorbers are deployed in Anechoic Chambers in modern times [2–4]. Figure 1 demonstrates the usage of pyramidal absorbers or Radar Absorbent Materials (RAMs) inside a representative Anechoic chamber. Typically, such pyramidal RAMs are made of rubberized foam material impregnated with controlled mixtures of carbon and iron. To be sufficiently lossy, RAM can be neither a good electrical conductor nor a good electrical insulator, as neither type actually absorbs any incident EM power. Typically, there is a grey paint that helps in protection of such delicate Pyramidal RAMs. In the GHz frequency range, ray-optical methods provide computationally efficient modeling approaches to evaluate the wave propagation in such electrically very large chambers. However,

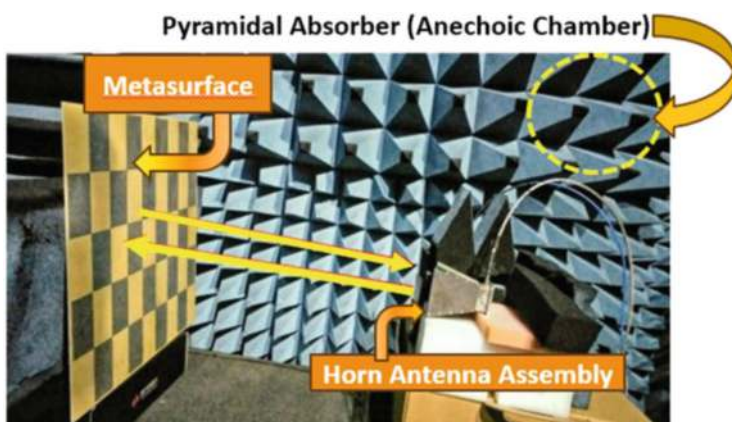


**Fig. 1** A photograph of Radar Cross Section (RCS) measurement setup inside Anechoic Chamber (Courtesy: Microwave Lab, Dept. of ECE, IISc Bangalore)



while pyramidal RAMs are extremely useful for building Anechoic chambers, many other applications demand the use of electrically thin and flat absorbing layers for the RCS reduction of structures. Hence, one needs to investigate the design of such thin EM absorbing layers, fundamentally motivated from the Salisbury screen and Jaumann layer principles.

## 2 Salisbury Screen and Its Analysis Using Plane Waves and Transmission Line Theory

As discussed in the previous section, a number of techniques have been proposed in the quest of controlling the reflection of EM waves from conducting bodies. The Salisbury screen is one such interesting solution, consisting of a thin resistive sheet mounted a quarter-wavelength above a conductor backing plate (see Fig. 2). In [5], the author provides insightful analytical treatment of multiple electric and magnetic Salisbury screens, which complements the computer code based trial-and-error approach for efficient design of Salisbury screens. To provide more insights into the Salisbury screen performance, we consider the case of a multi-layered media, illuminated by normally incident uniform plane wave from free-space (Fig. 3). In front of the semi-infinitely extended perfect electrical conductor (PEC) medium, we have two layers comprising of medium-1 (permittivity  $\varepsilon_1$ , permeability  $\mu_1$ , thickness  $h$ ) and medium-2 (permittivity  $\varepsilon_2$ , permeability  $\mu_2$ , thickness  $d$ ), respectively (Fig. 3). We assume both medium to be non-magnetic, implying  $\mu_1 = \mu_2 = \mu_0$ . Moreover, we consider that medium-1 is purely dielectric, whereas medium-2 has finite conductivity of  $\sigma_2$ .

The reflection coefficient  $\Gamma_{in}$  for the EM wave with the left-interface can be computed from plane wave and transmission line theory as [6]:

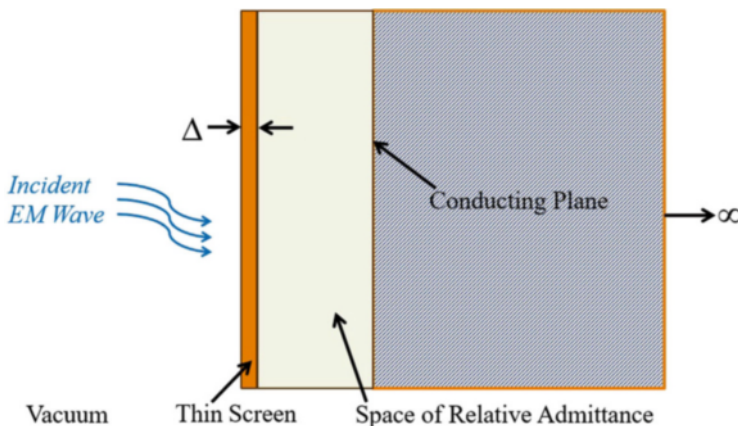
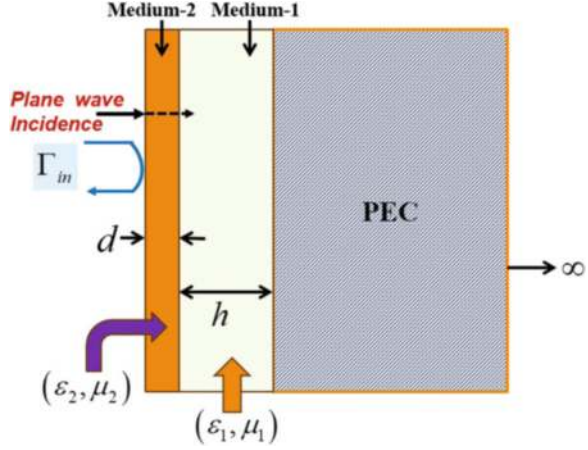


**Fig. 2** Schematic diagram of a Salisbury Screen (inspired from [5])

**Fig. 3** Schematic diagram of a semi-infinite multi-layered media illuminated by normally incident plane EM wave from free-space



$$\Gamma_{in} = \frac{\eta_{in,2} - \eta_0}{\eta_{in,2} + \eta_0}, \quad (1)$$

where  $\eta_0 = \sqrt{\mu_0/\epsilon_0}$  is the intrinsic impedance of free-space, and  $\eta_{in,2}$  is the input impedance for medium-2 backed by the medium-1 and PEC media, given by:

$$\eta_{in,2} = \eta_2 \left[ \frac{\eta_{in,1} + j\eta_2 \tan k_2 d}{\eta_2 + j\eta_{in,1} \tan k_2 d} \right]. \quad (2)$$

Here the quantities  $\eta_2$  and  $k_2$ , respectively, denote the intrinsic impedance and complex propagation constant for medium-2, given by:

$$\eta_2 = \sqrt{\mu_0/\epsilon_{c2}} \text{ and } k_2 = \omega\sqrt{\mu_0\epsilon_{c2}}, \quad (3)$$

where  $\epsilon_{c2}$  is the complex permittivity of medium-2:

$$\epsilon_{c2} = \epsilon_0\epsilon_{r2} + \frac{\sigma_2}{j\omega}. \quad (4)$$

Furthermore,  $\eta_{in,1}$  represents the input impedance experienced at the left-interface of medium-1 backed by PEC, which can be expressed as:

$$\eta_{in,1} = \eta_1 \left[ \frac{\eta_L + j\eta_1 \tan k_1 h}{\eta_1 + j\eta_L \tan k_1 h} \right], \quad (5)$$

where  $\eta_1$  and  $k_1$  represent the intrinsic impedance and complex propagation constant for medium-1, respectively:

$$\eta_1 = \sqrt{\mu_0/\epsilon_1} \text{ and } k_1 = \omega\sqrt{\mu_0\epsilon_1}. \quad (6)$$



Since the intrinsic impedance for the PEC medium is zero (i.e.,  $\eta_L = 0$ ), the above expression for  $\eta_{in,1}$  reduces to:

$$\eta_{in,1} = j\eta_1 \tan k_1 h \quad (7)$$

Once  $\Gamma_{in}$  is obtained from (1), for given values of  $\varepsilon_1$ ,  $\varepsilon_2$ ,  $\sigma_2$ ,  $d$  and  $h$ , we can compute the absorption coefficient  $A$  as:

$$A = 1 - |\Gamma_{in}|^2. \quad (8)$$

Note that, for semi-infinitely extended conductor media, there would be no transmission coefficient for consideration.

Considering the chosen set of parameters ( $h$ ,  $d$ ,  $\varepsilon_{r1}$ ,  $\varepsilon_{r2}$  and  $\sigma_1$ ), Fig. 4 represents the variation of  $R_{in} = \text{Re}(\eta_{in,2})$  and  $X_{in} = \text{Im}(\eta_{in,2})$  over the frequency range of 1–11 GHz, demonstrating the shunt resonance (i.e.,  $X_{in} = 0$ ) behavior near 6 GHz.

Figure 5 further showcase that the presence of a thin conductive layer leads to reduction of reflection coefficient (and enhancement of absorption) over a narrow bandwidth near the resonance frequency. To investigate the impact of various

**Fig. 4** Frequency variation of normalized  $\eta_{in,2}$  for the configuration of Fig. 3 with  $h = 3$  mm,  $\varepsilon_{r1} = 9$ ,  $d = 1$  mm,  $\varepsilon_{r2} = 12$ ,  $\sigma_2 = 3$  S/m. Here  $R_{in} = \text{Re}(\eta_{in,2})$  and  $X_{in} = \text{Im}(\eta_{in,2})$

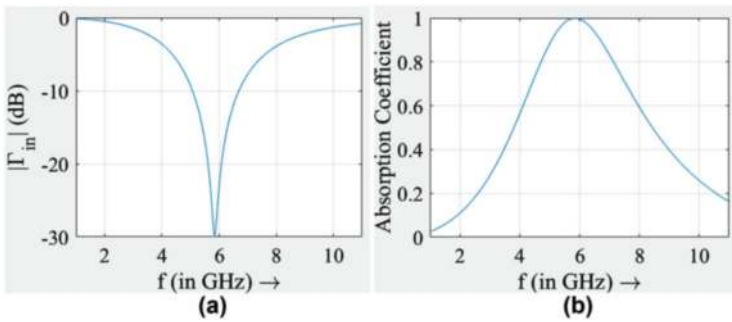
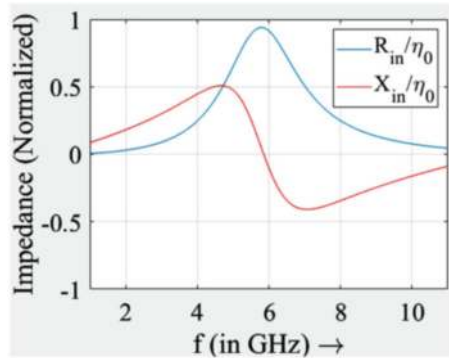
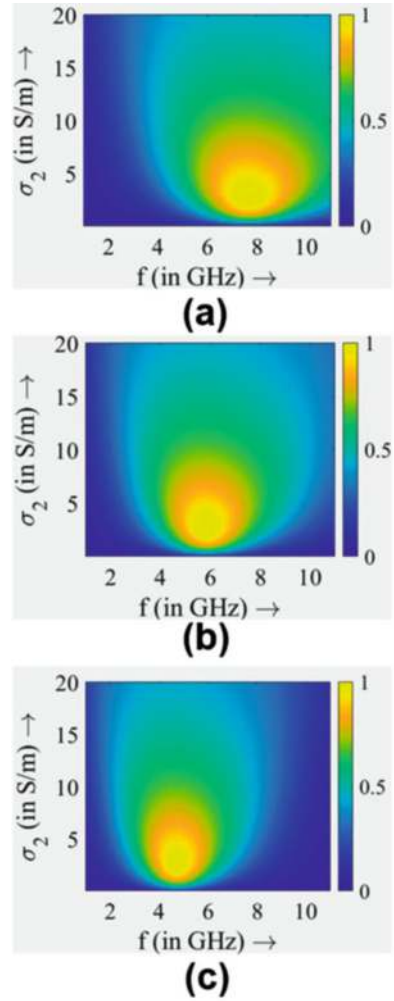


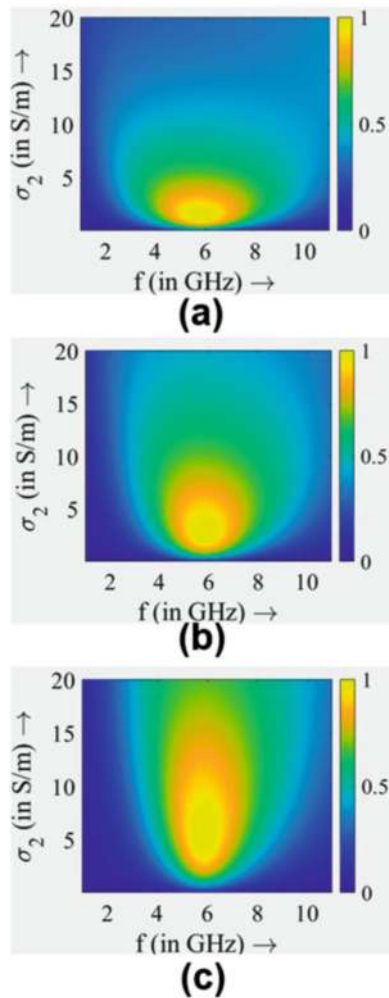
**Fig. 5** For the configuration of Fig. 3 with  $h = 3$  mm,  $\varepsilon_{r1} = 9$ ,  $d = 1$  mm,  $\varepsilon_{r2} = 12$ ,  $\sigma_2 = 3$  S/m: (a) reflection coefficient  $20 \log_{10} |\Gamma_{in}|$  (in dB) and (b) absorption coefficient  $A$  (in linear scale)

**Fig. 6** Simulated 2D distribution of absorption coefficient  $A$  for the configuration of Fig. 3 over the frequency range of 1–11 GHz and  $\sigma_2$ -range from 0.1–20 S/m, considering: (a)  $h = 2$  mm, (b)  $h = 3$  mm, and (c)  $h = 4$  mm. Rest of the parameters are kept as  $\epsilon_{r1} = 9$ ,  $d = 1$  mm,  $\epsilon_{r2} = 12$



parameters of the multi-layered Salisbury screen inspired configuration, we generate 2D plots of absorption coefficient with respect to frequency and conductivity values. Figure 6 shows that for increase in  $h$ , one shifts the absorption band to in lower frequency ranges. Moreover, Fig. 7 suggests that high dielectric constant and low thickness for medium-2 can ensure same absorption band for a wide range of conductivity values.

**Fig. 7** Simulated 2D distribution of absorption coefficient  $A$  for the configuration of Fig. 3 over the frequency range of 1–11 GHz and  $\sigma_2$ -range from 0.1–20 S/m, considering: (a)  $d = 2$  mm and  $\epsilon_{r2} = 6$ , (b)  $d = 1$  mm and  $\epsilon_{r2} = 12$ , (c)  $d = 0.5$  mm and  $\epsilon_{r2} = 24$ . Rest of the parameters are kept as  $\epsilon_{r1} = 9$ ,  $h = 3$  mm



### 3 Profile Reduction of Salisbury Screen Using Metasurfaces

#### 3.1 Concept of Jaumann Absorbers

As analyzed in the previous section, the classic Salisbury screen is probably the simplest of all absorbers (Fig. 2). In case of Salisbury screens, one places the resistive sheet a quarter-wavelength away from the metallic plate in order to be at the location with the maximum electric field. But this constraint on distance to be  $\lambda/4$  makes the combined configuration electrically thick, rendering it unsuitable for many applications. Moreover, while one can achieve a single reflection-zero to occur at a desired operating frequency of Salisbury screen, the  $|\Gamma_{in}| < -20$

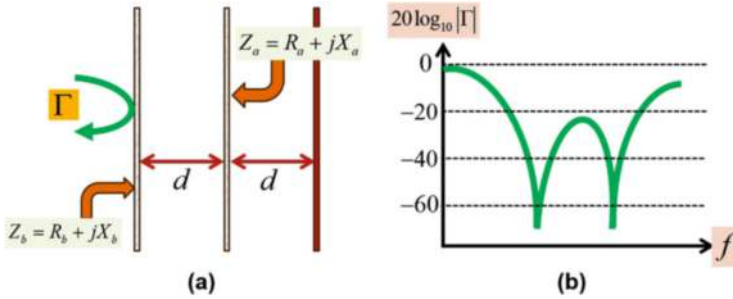


**Fig. 8** (a) Schematic diagram of two-sheet Jaumann Absorbers for wideband operation. (b) Representative frequency variation of reflection coefficient magnitude for such Jaumann absorbers

dB bandwidth of such an absorber is very low (typically  $< 20\%$ ). To enhance the bandwidth, one generally uses the concept of adding additional sheets, which leads to the formation of Jaumann absorber [7]. Furthermore, it is possible to add some capacitive reactance in series alongside the resistive components, such that one achieve bandwidth expansion with reduced inter-sheet spacing [7]. It is discussed in [7] that sheets equipped with shunt capacitive reactances can also reduce the inter-sheet spacing, but at the expense of shrunk absorption bandwidth.

Figure 8 demonstrates the configuration of an optimum Jaumann absorber designed using a simple two-sheet configuration, where both sheets have complex (capacitive) impedances [7]. Using the well-known “double-notch” concept, the authors demonstrate a  $|\Gamma_{in}| < -20$  dB bandwidth exceeding 100% using this two-sheet Jaumann absorber.

### 3.2 Synthesizing Electrically Thin Absorbers Using High-Impedance Metasurfaces

In the recent past, space-time metamaterials and metasurfaces have gained significant popularity for their diverse application areas ranging from antennas, frequency-selective surface (FSS) Radomes, superlenses to non-reciprocal circuits and reconfigurable intelligent surfaces (RIS) [8–18]. Spatial metamaterials and metasurfaces are generally constructed by a periodic array of sub-wavelength unit-cells, so that “effective homogeneity” condition is satisfied [19–21]. Historically speaking, one of the reasons behind the immense popularity of metamaterials is the *negative refraction*, which does not occur in “naturally” synthesized materials [19–21]. This negative refraction in metamaterials, which leads to “reversal of Snell’s law” and paves the way for Superlens design, is intrinsically connected to the of *backward waves* having anti-parallel group and phase-velocity (or oppositely pointed Poynting vector and propagation vector) [19]. While backward waves

can exist in different type of artificially engineered structures, their experimental verification in effectively homogeneous negative-index metamaterial medium was first carried out only couple of decades back, using the thin-wire(TW)-split ring resonator (SRR) arrays [19]. After that, researchers also demonstrated the backward wave phenomena in Composite Right Left Handed Transmission Lines (CRLH TL) [19–21]. Depending upon the unit-cell lumped parameters, the CRLH TLs can exhibit stop bands, which can be extended for 2D CRLH TL architectures. Note that, electromagnetic bandgap (EBG) structures, which are visually similar to the 2D CRLH TL configurations, can be realized by strategic placement of unit-cells (e.g., mushroom type configurations) to provide a stop-band for the surface-wave modes [19–21]. EBG metasurfaces have frequency dependent surface impedance features, which can be controlled by changing the properties (e.g., shape, size, lumped component loading) of the constituent sub-wavelength unit-cells. This opens up the possibility of synthesizing high-impedance surfaces (HIS) or artificial magnetic conductors (AMCs) [19–21].

Figure 9 illustrates the concept of traditional electric conductor and artificial magnetic conductors. In Fig. 9a, we show a PEC plate which provides a reflection coefficient  $\Gamma = -1$  [6]. Figure 9b demonstrates a two-dimensional (2D) array of several small flat inclusions (here, sub-wavelength square-shaped microstrip patches) distributed periodically near a flat surface. Such a 2D array of sub-wavelength patches can indeed behave as an frequency-selective surface (FSS) for an interacting incident EM wave interacts with it. One can electromagnetically characterize the 2D patch array as an anisotropic impedance tensor, whose values and specific forms are in general dependant on factors like frequency, incidence angle for impinging EM wave, shape, density, and size of the unit-cells (e.g.,  $a, b, g, w$  etc for Fig. 9b). Now, we can place this FSS (i.e., 2D array of square

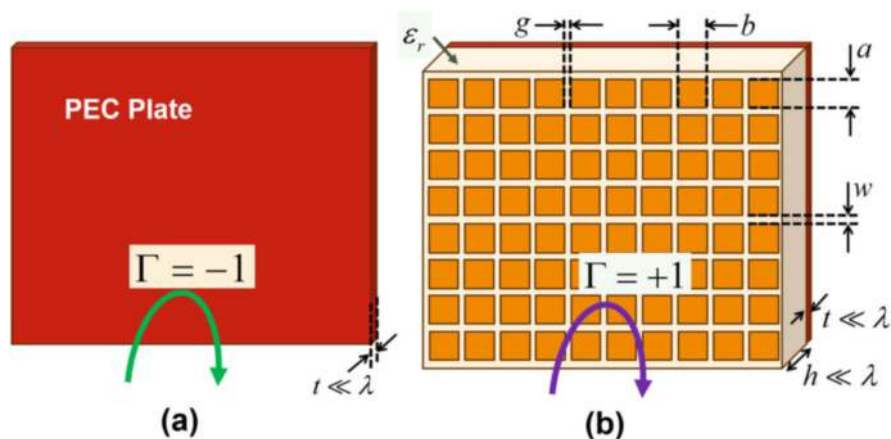


**Fig. 9** Schematic diagrams of: (a) Perfect electric conductor plate having reflection coefficient  $\Gamma = -1$ , (b) High impedance Metasurface configuration based on array of sub-wavelength square patches, displaying artificial magnetic conductor characteristics with  $\Gamma = +1$

patches) in front of a highly conductive metallic plate at a distance  $h$ , which is assumed to be much smaller than the operating wavelength (i.e.,  $h \ll \lambda$ ), along with a dielectric layer sandwiched between the FSS and the metal plate (Fig. 3b). Using transmission line theory, one can calculate the surface impedance at the top surface of this combined metasurface layer comprising of FSS, dielectric spacer and a ground plane [22]. It is showcased in [22] that one can realize the equivalent shunt impedance to attain very high values in a desired frequency range. This implies that the top-interface of the metasurface would have a reflectivity of  $\Gamma = +1$ .

Now, let us assume that a normally incident plane wave impinges upon this metasurface. Since  $\Gamma = +1$ , the total tangential component of the electric field and of the magnetic field on the top of this metasurface are, respectively,  $E_t^{\text{total}} \approx 2E_t^{\text{incident}}$  and  $H_t^{\text{total}} \approx 0$ , indicating that the metasurface will operate like a “magnetic wall.” Thus, unlike the case of a simple metallic ground plane (i.e., electric wall), here the tangential component of the total electric field becomes significant on the top surface. Therefore, if we can place a thin layer of resistive sheet on top of such high impedance metasurface, the high electric field intensity at the top layer would cause part of the incident energy to be dissipated on this resistive sheet. In this way, one can demonstrate by transmission line theory that the reflection coefficient can be significantly reduced. Clearly, it is possible to extend this argument for the scenarios with oblique incidence. This opens up the possibilities of reduction the reflection coefficient as well as the scattering cross section of such structures [22, 23].

### 3.3 Equivalent Circuit Model for Metasurface Absorbers

In [23], the authors describe a possible realization of metasurface-based microwave absorber around 2.45 GHz, where lumped resistors between the sub-wavelength metallic patches are used instead of resistive screens (see Fig. 10). Note that, the impedance of such a lossy FSS screen on the top layer can be represented through a series RLC circuit [24]:

$$Z_{FSS} = R + j\omega L + \frac{1}{j\omega C} = R - j \left( \frac{1 - \omega^2 LC}{\omega C} \right). \quad (9)$$

The surface impedance of the metasurface absorber can be calculated by considering the parallel connection between the FSS impedance and the surface impedance of thin grounded dielectric slab denoted by  $Z_d$  using the relation:

$$Z_R = \frac{Z_d Z_{FSS}}{Z_d + Z_{FSS}}, \quad (10)$$

where  $Z_d$  can be evaluated as:

$$Z_d = j Z_m^{TE, TM} \tan k_n d. \quad (11)$$

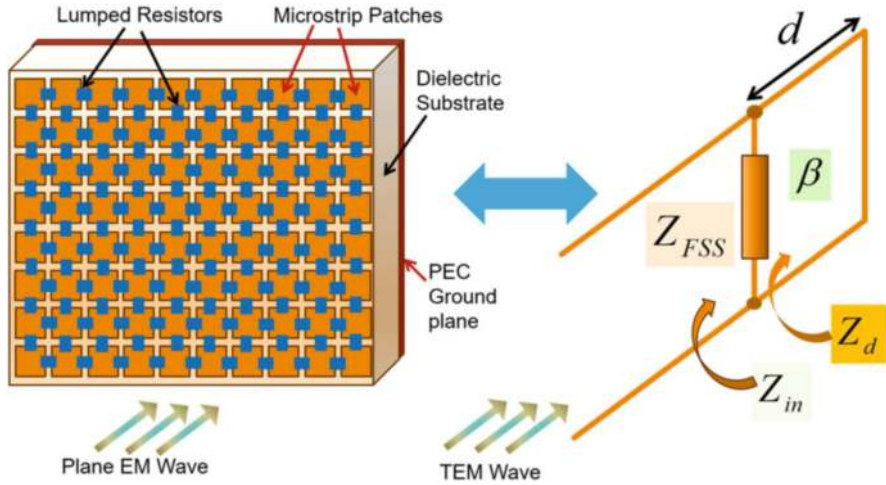


**Fig. 10** Artificial magnetic conductor with lumped resistor loading for metasurface absorber applications (inspired from [23]) along with its equivalent circuit model [24]

Here  $Z_m^{TE}$  and  $Z_m^{TM}$ , the characteristic impedances of the slab for TE and TM polarization, are computed via the following equations:

$$Z_m^{TE} = \frac{\omega \mu_r \mu_0}{k_n} \text{ and } Z_m^{TM} = \frac{k_n}{\omega \epsilon_r \epsilon_0}, \quad (12)$$

with  $k_n$  representing the propagation constant along the normal direction of the slab as:

$$k_n = \sqrt{k^2 - k_t^2}. \quad (13)$$

Here  $k_t = k_0 \sin \theta$ , with  $\theta$  being the incidence angle of the incoming wave with respect to the normal. Using analytical simplifications, one can find out the real and the imaginary parts of the input impedance  $Z_R$  as:

$$\text{Re} \{Z_R\} = \frac{R Z_d^2}{\left[ \frac{1 - \omega^2 LC}{\omega C} - Z_d \right]^2 + R^2} \quad (14)$$

$$\text{Im} \{Z_R\} = \frac{\left[ -\omega L Z_d + \frac{Z_d}{\omega C} \right] \cdot \left[ \frac{1 - \omega^2 LC}{\omega C} - Z_d \right] + R^2 Z_d}{\left[ \frac{1 - \omega^2 LC}{\omega C} - Z_d \right]^2 + R^2}. \quad (15)$$

When the inductive impedance of the substrate  $Z_d$  and the imaginary part of the FSS impedance  $(1 - \omega^2 LC)/\omega C$  become same, the parallel circuit resonates, making the

impedance purely real for thin substrates. In that case, we obtain:

$$\operatorname{Re}\{Z_R\} = \frac{\left(Z_m^{TE, TM}\right)^2 \tan^2 k_m^{TE, TM} d}{R}. \quad (16)$$

To absorb the incoming signal,  $\operatorname{Re}\{Z_R\}$  should match the free-space impedance  $\eta_0$ , which leads to the following expression of optimal FSS resistance  $R_{opt}$  as:

$$R_{opt} = \frac{\left(Z_m^{TE, TM}\right)^2 \tan^2 k_m^{TE, TM} d}{\eta_0^{TE, TM}}. \quad (17)$$

The equation (17) highlights that  $R_{opt}$  is strongly dependent on substrate permittivity as well as thickness. Now, to derive the optimal surface resistance  $R_{opt}$  from the equivalent circuit, one needs to formulate a relation between the lumped resistance of the equivalent circuit and the surface resistance of the FSS. Ideally,  $R_{opt}$  should be exactly equal to the resistance of the coating resistive ink, if it were uniform. However, for the FSS the coating resistive ink or lumped resistor locations can not be treated as uniform, which implies that  $R_{opt}$  will also dependent on unit-cell topology and shape, besides being controlled via substrate dielectric constant and thickness. More details on the design of equivalent circuit model of metasurface absorbers and their extension into wideband configurations are provided in [24–27].

## 4 RCS Reduction Using Metasurface Absorbers

As discussed earlier in Sect. 3.2, electrically thin metasurface-based absorbing screens can potentially reduce the scattering cross section compared to a conducting screen of same dimension. In [28–31], various metasurface-assisted techniques (EM wave absorption, scattering cancellation, polarization conversion, etc.) for narrowband as well as wideband radar cross section (RCS) reduction are discussed. In this section, we demonstrate this RCS reduction using metasurface absorbers, using full-wave simulations via CST Microwave Studio.

For the RCS analysis, we choose the printed square loop-based narrowband metasurface absorber as discussed in [26]. The dimensions for the four-fold symmetric polarization-insensitive unit-cell are provided in the caption of Fig. 11. The substrate chosen is FR4-Epoxy with  $\epsilon_r = 4.25$  and  $\tan \delta = 0.02$ . Using the periodic boundary condition in CST-MWS we carry out the simulation of S-parameters over the frequency range of 5–7 GHz first, considering orthogonal polarization states (Mode-1 and Mode-2 as indicated in Fig. 11b). Figure 12 corroborates the results in [26], indicating that co-polar reflection coefficient has dipped to  $-13.18$  dB around 6.1 GHz, indicating the existence of narrowband absorption around it. Figure 12 further confirms that negligible polarization conversion is occurring between mode-1 to



**Fig. 11** (a) Schematic diagram of the square-loop unit-cell with dimensional parameters with  $a = 7.5$  mm,  $w = 0.2$  mm,  $p = 10$  mm and  $h = 1$  mm chosen same as those in [26]. (b) Orthogonal polarization states considered for excitation of the unit-cell array by incident EM wave

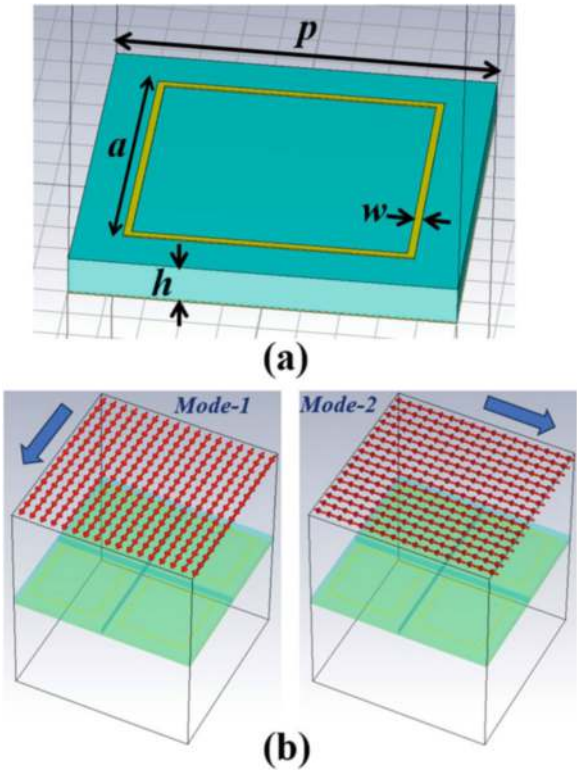
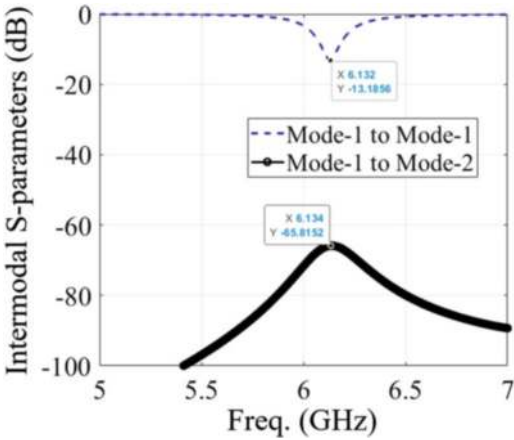


**Fig. 12** Frequency variation of inter-modal S-parameter magnitude, demonstrating possible mode-conversion using the square-loop unit-cell based metasurface (see Fig. 11)



mode-2, as the simulated transmission coefficient is only  $-65.81$  dB in magnitude at 6.1 GHz.

Next we evaluate the RCS characteristics for a finite metasurface structure consisting of square-loop arrays. It is well-known that RCS or  $\sigma(\theta, \phi)$  provides

a measure of the scattering properties of a specific radar target, and is computed by the formula:

$$\sigma(\theta, \phi) = 4\pi \frac{\text{Power Radiated Per Unit Solid Angle}}{\text{Irradiance due to incoming Plane Wave}} \quad (18)$$

Note that, here “irradiance” stands for incoming power per unit area. RCS generally depends on the incident wave properties like polarization, propagation angle ( $\theta, \phi$ ), operation frequency, as well as the target material characteristics, shape, size, etc.

Radar engineers generally use the notions of “monostatic RCS” and “bistatic RCS” which differ with respect to the relative alignment of excitation and probe direction. For a monostatic RCS, the probe direction for the scattered radiation is always same with the propagation direction of the incoming exciting plane wave. Therefore, monostatic RCS computation requires a sweep of the exciting plane wave. Each recorded data point quantifies the probability of backscattering by the target for an excitation of a plane wave from the respective direction. On the other hand for the bistatic RCS, the exciting plane wave direction is fixed and probes the probability of scattering in all other direction (not only backscattering). To calculate a bistatic RCS using CST-MWs, one must define a farfield/RCS monitor as well as a fixed plane wave excitation. The total RCS is typically defined as the ratio of the *scattered power* to the intensity of the incident plane wave. For our case, we evaluate the monostatic RCS at the resonance frequency for the finite sized absorber configuration in Fig. 13 comprising of  $12 \times 12$  array of square-loop unit-cells. Figures 14 and 15 highlight that the use of absorptive metasurface has significantly reduced the RCS by more than 15 dB around the broadside direction. Figure 15

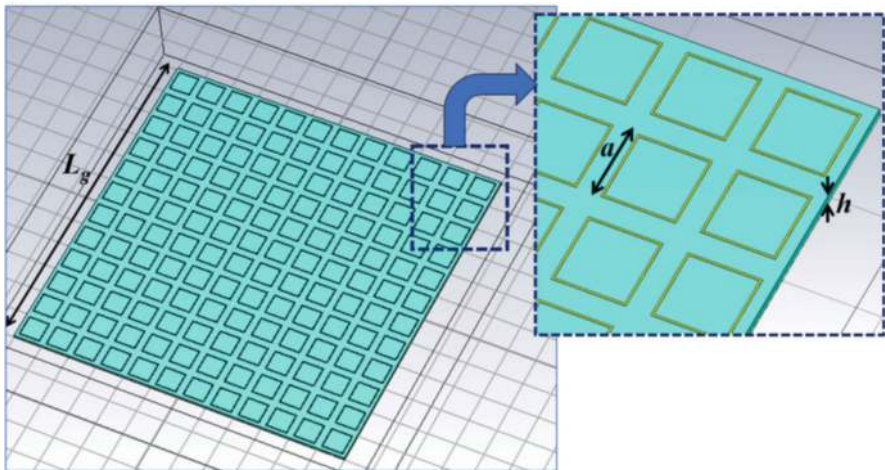


**Fig. 13** Schematic diagram of an  $N \times N$  array ( $N = 12$ ) of square-loop unit-cells (shown in Zoomed view) placed along the  $xy$ -plane, with  $a = 7.5$  mm,  $w = 0.2$  mm,  $p = 12.5$  mm and  $h = 1$  mm. Note that, the entire metasurface occupies a physical area of  $L_{g2} \times L_{g2}$ , where  $L_{g2} = Np$

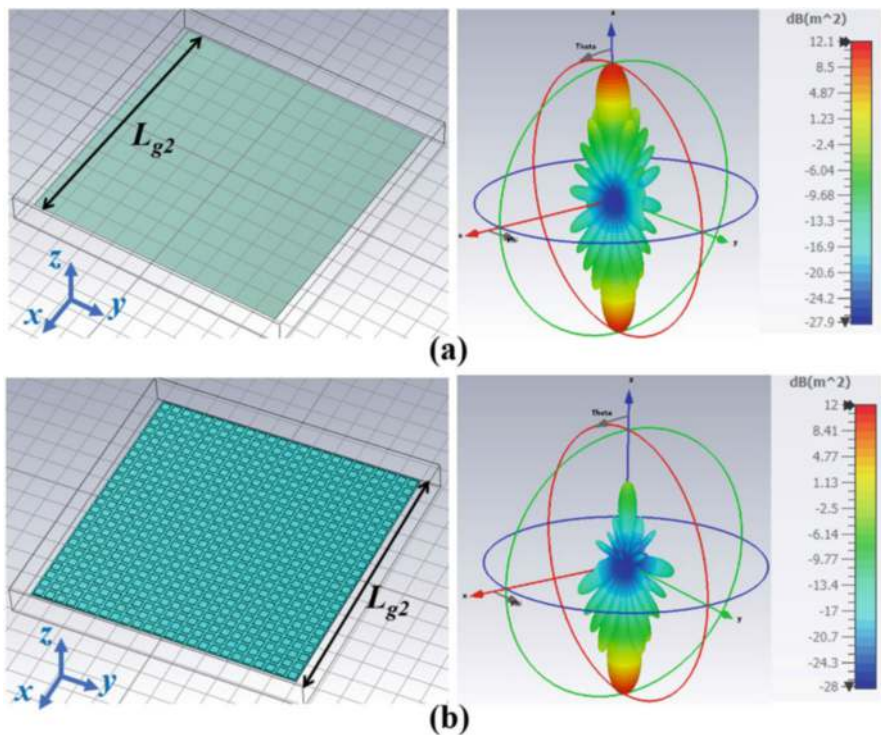
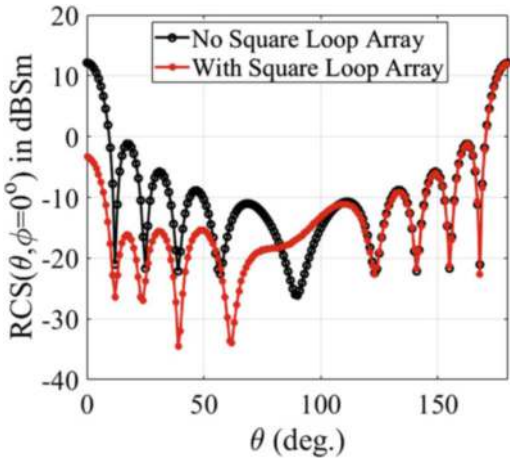


**Fig. 14** Simulated angular RCS pattern at the resonance frequency for: (a) only PEC plate (i.e., no square-loop array), (b) absorbing metasurface (i.e., with square-loop array) as shown in Fig. 13

**Fig. 15** Variation of simulated RCS at the resonance frequency with respect to  $\theta$  for  $\phi = 0^\circ$ , considering only PEC plate (i.e., no square-loop array) along with absorbing metasurface (i.e., with square-loop array)



further highlights that the RCS reduction performance is reasonably stable for a wide angular range.

## 5 Conclusion

In this chapter, we highlight the usage of artificially engineered metasurfaces with judiciously tailored surface impedance values for EM absorption and consequent RCS reduction of targets. One must note here that this idea of realizing absorptive metasurfaces via a combined high impedance metasurface with a resistive layer on top [22, 23], is simply the extension from single-screen Salisbury screens. However, these metasurface absorbers provide additional advantage in terms of the electrical profile miniaturization and weight reduction of absorbing layers. Using Transmission line theory, we demonstrate the possibility of using equivalent circuit models for prediction of Metasurface absorber performance. Using multi-layered metasurface-based absorbing screens, it is possible to enhance the operational bandwidth to cover the Radar bands from 2–18 GHz. Furthermore, use of polarization-insensitive unit-cells can help to achieve stable RCS reduction performance over a wide range of incidence angles.

## References

1. W. Emerson, Electromagnetic wave absorbers and anechoic chambers through the years. *IEEE Trans. Antennas Propag.* **21**(4), 484–490 (1973)
2. W. Sun, K. Liu, C. Balanis, Analysis of singly and doubly periodic absorbers by frequency-domain finite difference method. *IEEE Trans. Antennas Propag.* **44**(6), 798–805 (1996)
3. V. Rodriguez, Basic rules for indoor anechoic chamber design. *IEEE Antennas Propag. Mag.* **58**(6), 82–93 (2016)
4. Q. Xu, Y. Huang, X. Zhu, L. Xing, P. Duxbury, J. Noonan, Building a better anechoic chamber: a geometric optics-based systematic solution, simulated and verified. *IEEE Antennas Propag. Mag.* **58**(2), 94–119 (2016)
5. R.L. Fante, M.T. McCormack, Reflection properties of the Salisbury screen. *IEEE Trans. Antennas Propag.* **36**(10), 1443–1454 (1988)
6. D.K. Cheng, *Field and Wave Electromagnetics* (2nd edn.) (Pearson Education Asia Ltd, 2006)
7. E.F. Knott, C.D. Lunden, The two-sheet capacitive Jaumann absorber. *IEEE Trans. Antennas Propag.* **43**(11), 1339–1343 (1995)
8. J.B. Pendry, A.J. Holden, W.J. Stewart, I. Youngs, Extremely low frequency plasmons in metallic mesostructures. *Phys. Rev. Lett.* **76**(25), 4773–4776 (1996)
9. J.B. Pendry, A.J. Holden, D.J. Robbins, W.J. Stewart, Low frequency plasmons in thin-wire structures. *J. Phys. Condens. Matter* **10**(22), 4785–4809 (1998)
10. J.B. Pendry, A.J. Holden, D.J. Robbins, W.J. Stewart, Magnetism from conductors and enhanced nonlinear phenomena. *IEEE Trans. Microwave Theory Tech.* **47**(11), 2075–2084 (1999)
11. D.R. Smith, W.J. Padilla, D.C. Vier, S.C. Nemat-Nasser, S. Schultz, Composite medium with simultaneously negative permeability and permittivity. *Phys. Rev. Lett.* **84**(18), 4184–4187 (2000)

12. D. Sarkar, *FDTD Analysis of Guided Electromagnetic Wave Interaction with Time Modulated Dielectric Medium*. SpringerBriefs in Electrical and Computer Engineering (Springer, Singapore, 2022)
13. A. Kumar, J.C. Dash, D. Sarkar, Computational techniques for design and analysis of time-varying capacitor loaded transmission lines using FDTD and simulink. *IEEE J. Multiscale Multiphys. Comput. Tech.* **7**, 228–235 (2022)
14. R. Malleboina, J.C. Dash, A. Lemma, D. Sarkar, On the aperture size of digitally coded metasurfaces for beam steering applications using anomalous reflection, in *Proceedings of International Microwave and Antenna Symposium (IMAS)*, Cairo, Egypt, pp. 255–258 (2023). <https://doi.org/10.1109/IMAS55807.2023.10066942>
15. R. Malleboina, J.C. Dash, D. Sarkar, Design of anomalous reflectors by phase gradient unit cell-based digitally coded metasurface. *IEEE Antennas Wirel. Propag. Lett.* **22**(9), 2305–2309 (2023)
16. A. Kumar, D. Sarkar, FDTD analysis of space-time metamaterials using modulated TVTLs for frequency translation, mixing and non-reciprocity, in *Proceedings of 53rd European Microwave Conference (EuMC)*, Berlin, Germany, pp. 311–314 (2023). <https://doi.org/10.23919/EuMC58039.2023.10290288>
17. R. Malleboina, D. Sarkar, Coded metasurfaces for two-dimensional steering and splitting of incident radiation, in *Proceedings of Microwave, Antennas, and Propagation Conference (MAPCON)*, Ahmedabad, Gujarat, India (2023)
18. Y. Chandrakapure, A. Kumar, Easha, D. Sarkar, G. Banerjee, Time-modulated metasurface for spoofing doppler radar, in *Proceedings of Microwave, Antennas, and Propagation Conference (MAPCON)*, Ahmedabad, Gujarat, India (2023)
19. S.A. Ramakrishna, T.M. Grzegorzczak, *Physics and Applications of Negative Refractive Index Materials* (CRC Press, Taylor & Francis Group and SPIE Press, 2009)
20. G.V. Eleftheriades, K.G. Balmain, *Negative Refraction Metamaterials: Fundamental Principles and Applications* (IEEE, Wiley, Hoboken, NJ, 2005)
21. C. Caloz, T. Itoh, *Electromagnetic Metamaterials: Transmission Line Theory and Microwave Applications, The Engineering Approach* (Wiley, Hoboken, NJ, 2006)
22. N. Engheta, Thin absorbing screen using metamaterial surfaces. *Proc. IEEE Int. Symp. Antennas Propag.* **2**, 392–395 (2002)
23. H. Mosallaei, K. Sarabandi, A one-layer ultra-thin meta-surface absorber, in *Proc. IEEE Int. Symp. on Antennas Propag.* (2005)
24. F. Costa, A. Monorchio, G. Manara, Analysis and design of ultra thin electromagnetic absorbers comprising resistively loaded high impedance surfaces. *IEEE Trans. Antennas Propag.* **58**(5), 1551–1558 (2010)
25. F. Costa, S. Genovesi, A. Monorchio, G. Manara, A circuit-based model for the interpretation of perfect metamaterial absorbers. *IEEE Trans. Antennas Propag.* **61**(3), 1201–1209 (2013)
26. S. Ghosh, K.V. Srivastava, An equivalent circuit model of FSS based metamaterial absorber using coupled line theory. *IEEE Antennas Wirel. Propag. Lett.* **14**, 511–514 (2015)
27. Z. Yao, S. Xiao, Y. Li, B. Wang, On the design of wideband absorber based on multilayer and multiresonant FSS array. *IEEE Antennas Wirel. Propag. Lett.* **20**(3), 284–288 (2021)
28. M. Paquay, J.C. Iriarte, I. Ederra, R. Gonzalo, P. de-Maagt, Thin AMC structure for radar cross-section reduction. *IEEE Trans. Antennas Propag.* **55**(12), 3630–3638 (2007)
29. A. Murugesan, K.T. Selvan, A.K. Iyer, K.V. Srivastava, A. Alphones, A review of metasurface-assisted RCS reduction techniques. *Prog. Electromagn. Res. B* **94**, 75–103 (2021)
30. E. Ameri, S. Esmaeli, S. Sedighy, Ultra wideband radar cross section reduction by using polarization conversion metasurfaces. *Sci. Rep.* **9**, 478 (2019). <https://doi.org/10.1038/s41598-018-36542-6>
31. A. Dhumal, M.S. Bisht, A. Bhardwaj, M. Saikia, S. Malik, K.V. Srivastava, Screen printed polarization independent microwave absorber for wideband RCS reduction. *IEEE Trans. Electromagn. Compat.* **65**(1), 96–103 (2023)

# Frequency-Selective Surface and Its Applications in Radome Technology



Saptarshi Ghosh

## 1 Introduction

Since the last few decades, frequency-selective surfaces (FSSs) have drawn significant research attention due to their potential applications [1–3]. It is believed that Franklin and Maroni invented the concept of using FSS structures in a parabolic reflector by using half-wavelength wire sections [4]. With time, several other applications of FSS have been developed, and its importance has subsequently been increased. In the early days, FSS structures have mainly been used as spatial filters, where some of the frequency bands (in-band frequency) are allowed for transmission through the geometry, while others (out-of-band frequency) are reflected. Later, FSS designs have further been employed in different applications, such as the reduction of radar cross section (RCS) in defense [5], electromagnetic (EM) shielding in commercial devices [6], radomes in aerospace sectors [7], improvement in antenna performance [8], etc. They have also been exploited in various technologically advanced areas, such as artificial magnetic conductors [9], high impedance surfaces [10], digitally coding metasurfaces [11], reconfigurable intelligent surfaces [12], etc.

FSSs are periodic structures of metal-dielectric patterns in one- or two-dimensional arrays often realized on planar configurations. The metallic patterns are generally printed on either single or both sides of the dielectric. Traditional FSS patterns are designed using various elements, such as patch, dipole, slot, ring, loop, etc., a glimpse of which is shown in Fig. 1. Various commercially available substrates are used as dielectrics, such as FR4, RT Duroid, Taconic, etc., depending

---

S. Ghosh (✉)

Department of Electrical Engineering, Indian Institute of Technology Indore, Indore,  
Madhya Pradesh, India  
e-mail: [sghosh@iiti.ac.in](mailto:sghosh@iiti.ac.in)



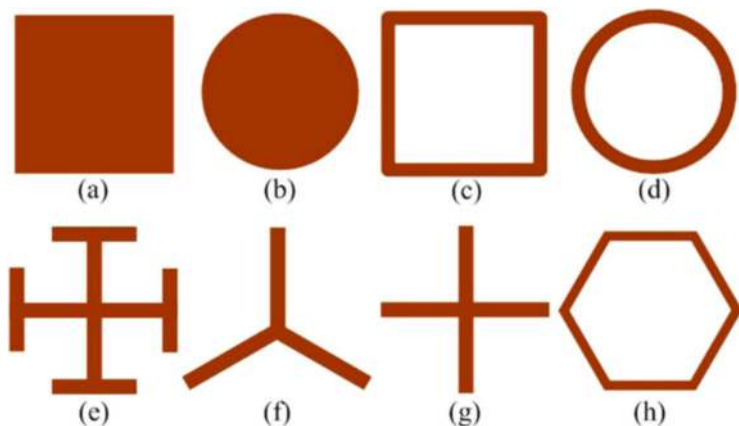


**Fig. 1** Different types of FSS elements widely used over past decades: (a) square patch, (b) circular patch, (c) square loop, (d) circular loop, (e) Jerusalem cross, (f) tripole element, (g) cross dipole, and (h) hexagonal loop

on their applications and frequencies of operation. Multilayer designs are also developed, where multiple dielectric layers are combined to achieve desired EM responses.

The basic principle of an FSS geometry can be explained by the resonance phenomenon. When a plane EM wave is incident on an FSS, the structure resonates at a specific frequency, which depends on the metallic patterns present in one period (unit cell), material properties of the constituent substrates, as well as the orientation of the incident EM wave. The shapes of the metallic elements and their spacing control the effective inductance and capacitance, respectively, of the design, whereas the polarization and incident angle govern the exposure of the incident wave on the structure. A brief overview of two different types of FSS designs is provided here.

Two complementary planar arrays, an array of patches and an array of slots, are considered to show the basic characteristics of FSS designs. A simple FSS structure consisting of a periodic array of metallic patches, as shown in Fig. 2a, has a low-pass characteristic [13–15]. While impinged by a plane EM wave, this FSS geometry transmits the lower-frequency components (but reflects the higher frequencies), thereby exhibiting a low-pass filter behavior. The complementary structure, an array of metallic slots, has a large inductive effect due to its topology (and a small capacitive effect) and therefore exhibits a high-pass filter response as observed in Fig. 2b. When these two types of geometries are combined in a single design (by printing on the opposite sides of a dielectric substrate), the structure will exhibit a bandpass or bandstop filter response. Designs can be modified to include both inductance and capacitance in the same layer, and the filtering characteristic can be achieved from a single metallic layer geometry. As per requirement, FSS geometries can also be converted to an absorber, polarizer, or rasorber by selectively designing the metallic patterns and regulating the transmission and reflection properties.

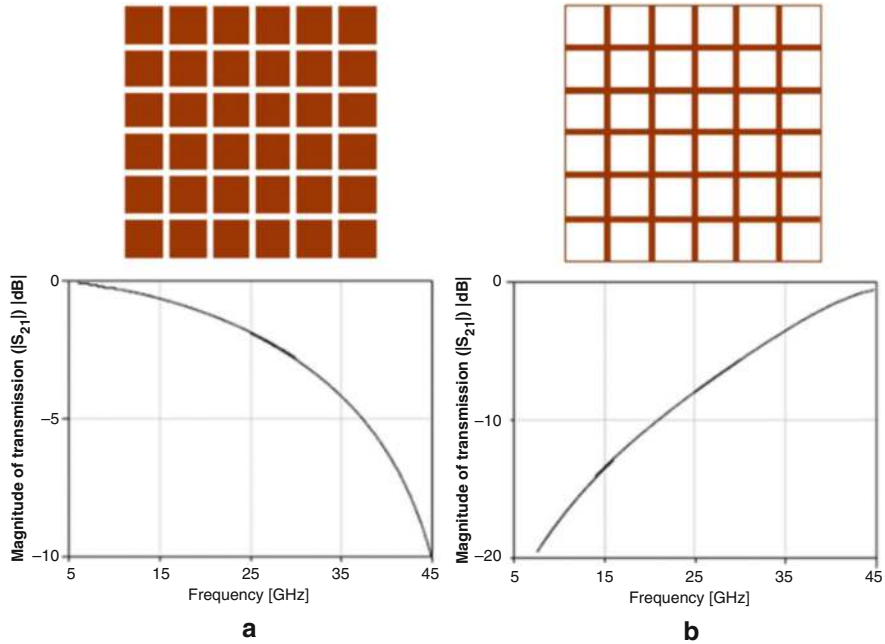


**Fig. 2** Two periodic geometries are considered for exhibiting the frequency selective operation of FSS structures, (a) metallic patches and (b) slots (or wire-grids), along with their transmission coefficients. The patches exhibit a low-pass response, and the slots exhibit a high-pass behavior

## 2 Equivalent Circuit Analysis

Figure 3a shows the schematic view of the array structure of an FSS-based structure. The proposed design consists of a cross-dipole geometry printed in a periodic pattern on the top side of a dielectric substrate, whereas the back side is empty. When the structure is illuminated by a plane EM wave, one part of the incident wave is reflected from the top surface, and the other part is transmitted through the geometry, with an assumption that the signals are not attenuated in the dielectric. The side view of the geometry is depicted in Fig. 3b.

An equivalent circuit model is devised for the structure, as shown in Fig. 3c, and it is observed that the top FSS provides a series  $R$ - $L$ - $C$  circuit and the dielectric is represented by a transmission line. The air medium present in the surroundings is marked as an impedance ( $Z_0$ ) of 377 ohm. In the design, the top surface inductance ( $L$ ) is provided by the metallic pattern of the cross dipole, the capacitance ( $C$ ) is obtained due to the gaps between the neighboring unit cells, and the resistance ( $R$ ) results owing to finite conductivity of the metal. The electric field is oriented in the vertical direction, which will create a time-varying magnetic flux generated along the cross-dipole length and subsequently results in the inductance. In contrast, a gap between the successive cross-dipoles exhibits the required capacitance.



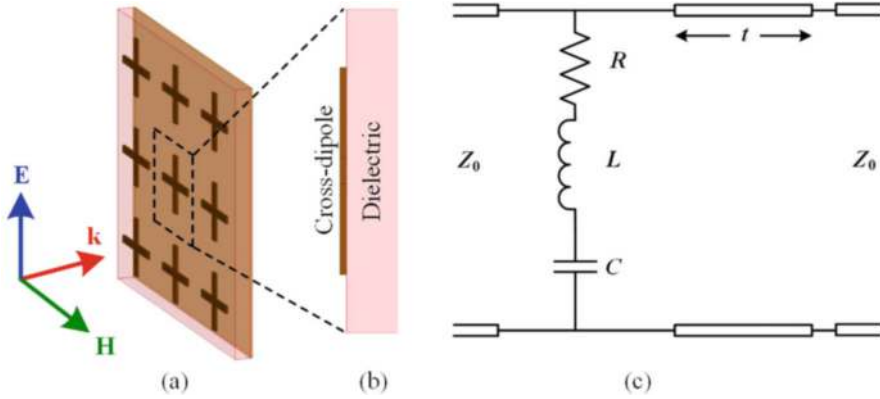


**Fig. 3** (a) Schematic diagram of an FSS-based geometry. (b) Side view of the unit cell geometry. (c) Equivalent circuit model of the structure

Hence, the input impedance of the structure according to the circuit model can be expressed as:

$$Z_{in} = \{R + j\omega L + 1/j\omega C\} \parallel Z_d$$

where  $Z_d$  is the impedance of the dielectric substrate terminated by an infinitely large air spacer. Therefore, by varying different parameters of the FSS design as well as substrate properties, the input impedance of the structure ( $Z_{in}$ ) can be precisely tuned to a high or low impedance value, and consequently, a bandstop or bandpass filter structure can be realized at a particular frequency.

It is noteworthy that the horizontal length of the cross dipole doesn't participate in the calculation of the resonance frequency, since no current flows through this segment under this condition. However, when the electric field is orthogonally incident (i.e., a horizontally oriented E-field), the horizontal dipole will provide the requisite inductance, and the vertical dipole will become inactive. Thus, the metallic pattern is made of two dipoles, one of which contributes to the resonance for the horizontal E-field, while the other participates for the vertical E-field. This further confirms the fact that the performance of an FSS geometry depends on the properties as well as the direction of the incident EM wave.

### 3 Radome Structure

A radome is a structural enclosure that protects a set of electronic equipment. In earlier days, the radome was constructed of materials transparent to radio-frequency (RF) signals, such that the impinging EM wave can get transmitted through the

radome structure and interact with inside electronic devices without any attenuation. Several types of radomes have been developed based on their applications, such as stationary radomes and dynamic radomes. Stationary radomes are used over grounded or fixed structures, like radomes at the Cryptologic Operations Center in Japan, whereas dynamic radomes are used in aircraft, missiles, and defense sectors. Those radomes not only protect the antennas and other electronic equipment mounted on the outer bodies of aircraft from weather but also conceal the equipment from view.

To achieve the maximum transfer of RF signal while passing through the radome material, two criteria should be simultaneously satisfied [16]: one, the input impedance of the radome structure should be matched to that of the free space such that the incoming EM wave encounters a minimal reflection, and second, the radome should be built with low-loss materials, such that the insertion loss will be very small and the RF signal passes unattenuated.

To achieve the first condition, one sample radome structure is drawn in Fig. 4 along with its side view. The structure is assumed to be made of a single-layer material having a relative permittivity of  $\epsilon_2$ , a relative permeability of  $\mu_2$ , and an intrinsic impedance of  $\eta_2$ . Air is present on both sides of the radome material (medium 1 and medium 3). Then, the wave impedance ( $Z_2$ ) of medium 2 at the left interface ( $z = 0$ ) can be derived in Eq. (1):

$$Z_2(0) = \eta_2 \frac{\eta_3 \cos \beta_2 d + j \eta_2 \sin \beta_2 d}{\eta_2 \cos \beta_2 d + j \eta_3 \sin \beta_2 d} \quad (1)$$

where  $\beta_2$  is the phase constant and  $d$  is the thickness of the radome material. The EM wave will transmit from medium 1 to medium 2 without any reflection if the wave impedance at the interface [ $Z_2(0)$ ] matches with that of the intrinsic impedance of air ( $\eta_1 = 377 \text{ ohm}$ ); i.e.,  $Z_2(0)$  should be equal to  $\eta_1$ . While solving Eq. (1) using this condition, two solutions are generated:

Solution 1:  $d = \lambda_g/2$ , when  $\eta_1 = \eta_3$ , i.e., similar material (air) is present on both sides of the radome.

Solution 2:  $d = (\lambda_g + 1)/4$ , when  $\eta_2 = \sqrt{\eta_1 \eta_3}$  and  $\eta_1 \neq \eta_3$ , i.e., different materials are present on different sides of the radome; one example is when the inside of the radome is filled up with some different materials.

Here,  $\lambda_g$  corresponds to the guided wavelength, expressed as  $\lambda_g = \lambda_0/\sqrt{\epsilon_r}$ , where  $\lambda_g$  is free space wavelength and  $\epsilon_r$  is relative permittivity of the radome material.

To achieve the second condition, the materials should be of low loss, like polycarbonate, ABS, Flexiglass, or composites, which have very small dielectric loss tangents (in the order of 0.0005). With these two conditions (impedance matching and low-loss materials), the radome will exhibit minimal reflection and absorption behavior, and the maximum RF signal will get transmitted through the material from one side to another, thereby representing an all-pass filter response.

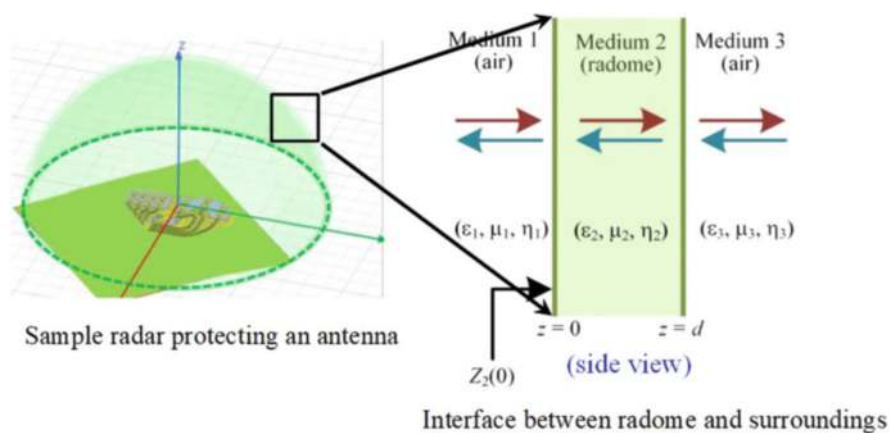


**Fig. 4** One radome structure and its side view, showing the impedance matching concept

## 4 FSS-Based Radome Structure

With the advent of technology, radome structures have been integrated with advanced features. Earlier radomes are meant to transmit EM waves over a wide frequency band, thereby posing a security threat to the aircraft and other moving objects. In particular, when a stealth aircraft is flying during a coveted mission, the signal radiated by the antenna mounted inside the radome can easily be detected by the enemy radars and will pose a security threat. To resolve this problem, the radome can be covered with a metal sheet, but this will completely block communication. Hence, researchers have started using a bandpass filter geometry on the top of a radome structure, such that only the intended signal will be passed through the radome and make communication with the antennas underneath, whereas unwanted signals will get reflected from the radome surface and get scattered in different directions [17, 18]. Thus, a bandpass filter-based radome structure has become a widely popular research topic in stealth applications.

Figure 5 illustrates the schematic diagram of a bandpass filter-based radome structure. As shown in the side view, the radome geometry is designed such that the RF signal impinging at a particular frequency ( $f_0$ ) will get transmitted through the radome without any attenuation, whereas the out-of-band frequencies ( $f_0 \pm \Delta f$ ) are reflected from the radome surface. There exist several techniques to design a bandpass filter; however, the FSS concept is widely used for filter applications owing to its simple design procedure, low-cost fabrication, and wide adaptability. An FSS geometry can be mounted on a radome structure, and the frequency response of such FSS-based radomes can be precisely controlled as per the requirement.

Figure 6 illustrates a scenario where an FSS-based periodic geometry is wrapped on a radome structure. The design of the FSS geometry and the radome materials will be selected such that only the intended frequency will be transmitted across the

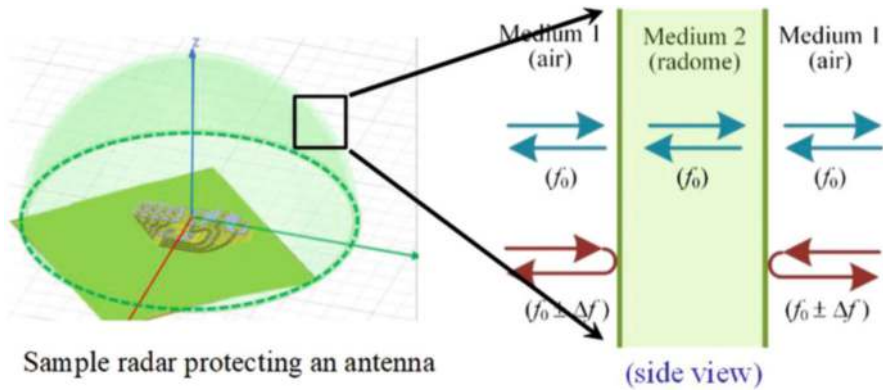


Fig. 5 An improved radome structure with a bandpass filter characteristic

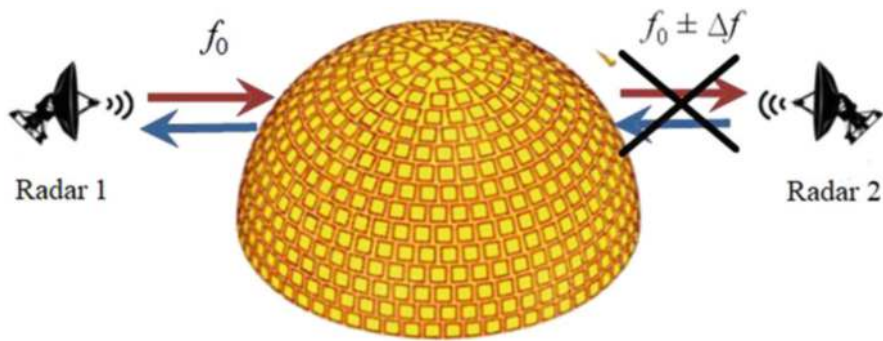


Fig. 6 A schematic diagram presenting an FSS-based radome with its applications

radome (from inside to outside and vice versa), whereas out-of-band frequencies will be reflected from the surface. By articulately designing the surface, the reflected signal can be scattered in different directions, and the radar cross-section (RCS) signature can be significantly reduced for the radome structure.

## 5 Literature Review of FSS-Based Radome

In the last few years, numerous FSS-based radome structures have been designed with various characteristics across different frequency bands. Some of the radomes are developed on planar surfaces, whereas some others are designed on non-planar surfaces [19]. Some structures are built with multiband operations [20], and few radomes are developed for wideband operations [21]. One of the radome structures, presented in Ref. [22], has been described in brief to explain the FSS-based radome mechanism.

The proposed radome structure is developed on a conical surface aiming to operate at 6 GHz. One monopole antenna is also designed at around 6 GHz to demonstrate the radome performance. The concept is numerically simulated and experimentally demonstrated. Initially, one planar FSS structure has been designed based on the aperture-coupled resonator concept, where three metallic layers are used along with two intermediate dielectric layers. The top and bottom metallic patterns are of patch shape, whereas the middle layer is of slot type. Such a patch-slot-patch combination exhibits a second-order filter characteristic with a highly selective filtering property. Once the filter response is obtained at around 6 GHz, the geometry has been conformed to a conical shape, with a height of 99.56 mm and a half-angle of  $41.04^\circ$ .

Afterward, a monopole antenna operating at 6 GHz with a reflecting ground plane is developed. The antenna geometry offers a good radiation performance with an omnidirectional radiation pattern in a standalone condition, and the reflection coefficient is relatively wide centering around 6 GHz. However, when the antenna element is covered by the conical radome, the reflection coefficient of the antenna and radome combination has been greatly changed. The input bandwidth becomes much narrower along with a high roll-off factor at the two ends. At the designed band, the antenna's performance remains almost similar to that of the original monopole antenna, whereas its out-of-band response is greatly suppressed. Thus, the presented radome structure allows for transmission of RF signals at around 6 GHz, whereas out-of-band signals are either suppressed or reflected from its surface, thereby ensuring high security for the electronic equipment enclosing the radome. The performance of the structure has successfully been validated by carrying out full-wave simulation and free space measurement.

## 6 Conclusion

A review of FSS-based radome designs and their operating mechanism has been presented in this chapter. Initially, a brief description of FSS structures has been provided, and later, the concept is explained with the help of an equivalent circuit model. Afterward, the need for FSS in radome designs is emphasized followed by the literature review of one FSS-based radome structure.

This chapter will be immensely beneficial to the readers in understanding the radome structures and their working principles. Several unexplored topics on radome concept, including absorptive radomes and reconfigurable radomes, can be investigated, and this chapter can act as a guide.

## References

1. T.K. Wu, *Frequency Selective Surface and Grid Array* (Wiley, New York, 1995)
2. J.C. Vardaxoglou, *Frequency Selective Surfaces: Analysis and Design*, 1st edn. (Wiley, New York, 1997)

3. B.A. Munk, *Frequency Selective Surfaces: Theory and Design*, 1st edn. (Wiley, New York, 2000)
4. G. Marconi, C. S. Franklin, *Reflector for Use in Wireless Telegraphy and Telephony*, U.S. Patent, 1,301,473, (1919)
5. M. Gustafsson, RCS reduction of integrated antenna arrays with resistive sheets. *J. Electromagn. Waves Appl.* **20**(1), 27–40 (2006)
6. W.F. Bahret, The beginnings of stealth technology. *IEEE Trans. Aerosp. Electron. Syst.* **29**(4), 1377–1385 (1993)
7. S. Narayan, G. Gulati, B. Sangeetha, R.U. Nair, Novel metamaterial-element-based FSS for airborne radome applications. *IEEE Trans. Antennas Propag.* **66**(9), 4695–4707 (2018)
8. S.H. Abadi, K. Ghaemi, N. Behdad, Ultra-wideband, true-time delay reflectarray antennas using ground-plane-backed, miniaturized element frequency selective surfaces. *IEEE Trans. Antennas Propag.* **63**(2), 534–542 (2015)
9. G.M. Monorchio, L. Lanuzza, Synthesis of artificial magnetic conductors by using multilayered frequency selective surfaces. *IEEE Antennas Wirel. Propag. Lett.* **1**, 196–199 (2002)
10. F. Costa, A. Monorchio, G. Manara, Analysis and design of ultrathin electromagnetic absorbers comprising resistively loaded high impedance surfaces. *IEEE Trans. Antennas Propag.* **58**(5), 1551–1558 (2010)
11. L.G. da Silva, S.A. Cerqueira, Wide incident angle digital coding metasurface applied to reconfigurable intelligent surfaces, in *2021 Antenna Measurement Techniques Association Symposium (AMTA), Daytona Beach, FL, USA*, (2021), pp. 1–5
12. S. Dey, M.A. Shukoor, Implementation of 3-Bit reconfigurable intelligent surface for sub-6 GHz range based on modified square loop FSS and tunable varactors, in *IEEE Microwaves, Antennas, and Propagation Conference (MAPCON), Bangalore, India*, (2022), pp. 973–977
13. S.W. Lee, G. Zarrillo, C.L. Law, Simple formulas for transmission through periodic metal grids or plates. *IEEE Trans. Antennas Propag.* **30**, 904–909 (1982)
14. R. Mittra, C. Chan, T. Cwik, Techniques for analyzing frequency selective surfaces- a review. *IEEE Proc.* **76**(23), 1593–1615 (1988)
15. F. Bayatpur, *Metamaterial-Inspired Frequency-Selective Surfaces*, PhD thesis, (University of Michigan, 2009)
16. M. Pozar, *Microwave Engineering*, 3rd edn. (Wiley, Hoboken, 2005)
17. G. Qian et al., Switchable broadband dual-polarized frequency-selective rasorber/absorber. *IEEE Antennas Wirel. Propag. Lett.* **18**(12), 2508–2512 (2019)
18. M. Tang, D.-F. Zhou, Q.-K. Liu, Z.-N. Yao, Q. Liu, Low-profile FSS-based polarization-insensitive rasorber with switchable transmission band. *IEEE Antennas Wirel. Propag. Lett.* **20**(6), 1038–1042 (2021)
19. A. Gouda, S. Ghosh, An analytical study of curved frequency selective surfaces for shielding applications. *Microw. Opt. Technol. Lett.* **65**(2), 3139–3146 (2023)
20. A. Sharma, S. Malik, S. Ghosh, K.V. Srivastava, A miniaturized frequency selective rasorber with independently regulated selective dual-transmission response. *IEEE Antennas Wirel. Propag. Lett.* **21**(2), 257–261 (2022)
21. S.C. Bakshi, D. Mitra, F.L. Teixeira, Wide-angle broadband rasorber for switchable and conformal application. *IEEE Trans. Microwave Theory Tech.* **69**(2), 1205–1216 (2021)
22. H. Zhou et al., Filter-antenna consisting of conical FSS radome and monopole antenna. *IEEE Trans. Antennas Propag.* **60**(6), 3040–3045 (2012)

# Algorithmic Applications for Massive MIMO Technology



Sai Mitheran, T. N. Ram, Debrup Mukherjee, and Hemant Kumar

## 1 Introduction

With the rise of 5G and 6G technology, wireless communication systems are subjected to growing demands for vast network capacity while maintaining low latency and increased availability. The idea behind massive multiple-input multiple-output (MIMO) evolved with the global bandwidth shortage, grouping antennas at both the transmitting and the receiving end to improve energy efficiency and increase spectral efficiency [1]. Keeping up with various factors such as increased peak data rates, connection density, and spectrum usage while ensuring minimum latency remains a challenge for MIMO technology [2]. This technology is focal to the wireless sector, as it emphasizes the union of antennas, radios, and spectrum to serve the high-speed and capacity requirements of 5G. The extra antennas used by massive MIMO help focus energy to increase throughput/efficiency with simple processing. The advantages that it encompasses, such as the significant multiplexing gain from extra antennas and beamforming, enable the usage of sensors with improved data rates and reliability. Further, it also makes it possible to sense data from concurrent sensors with reduced latency [2]. Consequently, this technology has been applied in real-time solutions that call for smart sensor applications, such as in smart grids [3], smart antennas [4], smart environmental monitoring [5], autonomous vehicles [6], and remote healthcare [7]. Massive MIMO design is currently the most heavily researched field in antenna design. In [8], the authors

---

Sai Mitheran and T. N. Ram have contributed equally.

---

S. Mitheran · T. N. Ram · D. Mukherjee · H. Kumar (✉)

Department, National Institute of Technology Tiruchirappalli, Tiruchirappalli, Tamil Nadu, India  
e-mail: [hemant@nitt.edu](mailto:hemant@nitt.edu)

have explored the optimal number of antennas, active users, and transmit power of a MIMO system. The design of cost- and energy-efficient massive MIMO arrays is explored in [9]. In [10], the problem of pilot beam pattern design for channel estimation is studied, and a novel algorithm for the same is proposed.

As other domains and interdisciplinary venues such as augmented reality (AR), virtual reality (VR), and Internet of Things (IoT) developed, early MIMO systems were unable to meet requirements such as that of spectral efficiency for hassle-free usage. The Massive MIMO theory addressed the rising influx in wireless data traffic [1]. These systems were validated to ensure indoor and outdoor operational efficiency and robust operation that requires low-complexity radio frequency and baseband circuit. The success of this technology and the attraction it gained for 5G was bound to its successful hardware implementation, which was built with low-complexity and low-cost hardware for both digital baseband and analog radio-frequency (RF) chains. In addition, several advancements focusing on algorithms [11], such as precoding, detection, and scheduling, have been designed to reduce cost and power, allowing optimal operational conditions that enable its widespread use. MIMO is also used in radar, which has made its presence crucial in several applications. In [12], the authors have explored the benefits of having a large number of virtual spatial antenna channels [13]. proposes a novel MIMO radar positioning scheme for automatic guided vehicles.

Several approaches in the past have been aimed at improving the diversity of applications involving massive MIMO technology [14, 15]. These attempts illustrate that algorithms intertwined with such technology can benefit research and its applications by creating a broader impact. Hence, this chapter contributes to an experimental overview of designing algorithms from both software paradigms that are leveraged to provide solutions for various applications involving massive MIMO technology and antenna design in 5G systems—specifically:

- A novel rule-based algorithm for obstacle detection—involving massive MIMO radar and the theory of cognition (Software 1.0). This algorithm is very efficient in terms of space and time complexity.
- Learning algorithms for MIMO-based antenna applications—machine learning and deep learning algorithms used for human activity classification, using human movement data captured by a radar device (Software 2.0).

## 2 Proposed Algorithms in MIMO Applications

This section illustrates the applications of algorithms from both software paradigms to massive MIMO radar technology, to provide an overview of the multifarious domains to which the union of the aforementioned methods can prove to be beneficial. The significance of combining algorithmic design with massive MIMO technology is demonstrated in terms of both Software 1.0 and Software 2.0.



Software 1.0 refers to the traditional software development paradigm involving conventional data structures, systems, and algorithms [16]. It involves explicit algorithmic programming, wherein the code directly controls the functioning of the software. All the code written in this work is primarily categorized under this particular paradigm: written in various languages such as Python and C++. Here, the individual focuses on defining a set of rules in program space that entails instructions to be compiled into a binary and then executed.

Software 2.0 is associated with specifying a given goal on the behavior of a program. The algorithmic rules are not explicitly defined by the programmer, but the “code” originates from the computations involved. A typical example of the code in this paradigm can be observed embedded in the weights of a neural network. Unlike rule-based instructions, this paradigm consists of many factors, such as the collected dataset (labeled/unlabeled) and the network architecture, which acts as the skeleton within which the weights are filled. It has a broader range of applications in speech recognition [17], games [18], computer vision [19], graphics [20], etc. Although it has certain disadvantages in terms of lacking intuitiveness and being vulnerable to adversarial attacks, they have proven to be better in practice, having advantages such as portability and efficiency.

## ***2.1 Obstacle Detection: Rule-Based Approach***

Obstacle detection is a critical component of self-driving cars. This technology calls for an intelligent radar system for sensing the environment. A cognitive radar (CR) system senses the environment, learns from it, and makes judgments depending on what it has learned. However, for CR to be useful, an antenna that offers a high waveform diversity at the transmitter is needed. MMIMO radar is a perfect candidate for this purpose. Besides providing a high degree of freedom, massive MIMO also provides high spectral efficiency by allowing its antenna array to focus beams in some desired directions. In [21], the authors have presented a reinforcement-learning-based approach for CR System. This sub-section presents a novel rule-based (Software 1.0) algorithm for the CR system.

### **2.1.1 Problem Definition**

Consider a massive MIMO radar with  $N_T$  transmitter and  $N_R$  receiver antennas, both of which are uniform linear arrays with  $\lambda/2$  spacing between them, where  $\lambda$  is the operating wavelength. Let  $s(t) \in \mathbb{C}^{N_T}$  be the transmitted signal from all  $N_T$  transmitter antennas, where

$$s(t) = W\Phi(t)$$

$s(t)$  is a result of the linear combination of  $N_T$  independent orthonormal signals  $\Phi(t) \in \mathbb{C}^N_T$  and  $W = [w_1, w_2 \dots w_{N_T}]^T \in \mathbb{C}^N_T \times \mathbb{C}^N_T$  is the beamforming weight matrix.

Let  $y \in \mathbb{C}^N_R \times \mathbb{C}^N_T$  be the received signal, and from [21],

$$y = \alpha h(\theta) + c$$

where  $c \in \mathbb{C}^N_R \times \mathbb{C}^N_T$  is the spatially colored disturbance vector and  $\alpha \in \mathbb{C}$  is a deterministic unknown variable that accounts for two-way path loss. From [21, 22], it can be written

$$h(\theta) = (W^T a_T(\theta)) \otimes a_R(\theta)$$

where  $\otimes$  signifies Kronecker product and  $a_T(\theta)$  and  $a_R(\theta)$  are the array manifold vectors of the transmitter and receiver, respectively.

$a(\theta) = [1, e^{\frac{j(2\pi d)}{\lambda} \sin(\theta)}, \dots, e^{\frac{j(2\pi d)}{\lambda} (N_T-1) \sin(\theta)}]^T$  and  $a_R(\theta)$  is defined in a similar manner. Also, the beam pattern can be expressed as  $B(\theta) = a_T^T(\theta) (WW^H) a_T^*(\theta)$  [21–23].

### 2.1.2 Detection of Target

The received signal is processed by spatial filters, which divides the radar field of view into  $L$  different angle bins. The system transmits  $K$  different pulses  $k \in \{1, \dots, K\}$ . Let  $y_l^k$  be the received signal for the  $k^{th}$  pulse  $k = 1, \dots, K$ , at  $l^{th}$  bin  $l = 1, \dots, L$ . There are two cases for the received signal:

$$(I) : y_l^k = c_l^k$$

$$(II) : y_l^k = \alpha h_l^k + c_l^k$$

Case (I) happens when there is no target in the angle bin, and the radar receives only noise. Case (II) is when there is a target in the bin. To differentiate the two cases, a test statistic  $\Lambda$  is required. Using [12],

$$\Lambda_l^k = \frac{2 |(h_l^k)^H y_l^k|^2}{(h_l^k)^H \hat{\Gamma} (h_l^k)} \quad (1)$$

where  $\hat{\Gamma}$  is the estimate of  $\Gamma$ . Using the assumption that  $c_l^k$  is a stationary discrete and circular complex valued process,  $\Gamma = E \{(c_l^k) (c_l^k)^H\}$ .  $\Lambda_l^k > \lambda$  corresponds to case (II) and  $\Lambda_l^k < \lambda$  to case (I) where  $\lambda$  is the operating wavelength [12, 21].

### 2.1.3 An Algorithm for Cognition

If a radar is cognitive, it learns from the pulses previously sent. In this case, the beamforming weight matrix  $\mathbf{W}$  is updated each time a pulse arrives at the receiver. This is done in such a way that more power is focused on angle bins where target was detected.

An algorithm to change  $\mathbf{W}$  matrix to focus more power on certain angle bins is presented in [21]. Let  $\mathbf{W}_k$  be the updated  $\mathbf{W}$  matrix after the  $k$ th pulse that was sent arrives. Before the first pulse is transmitted, the beamforming weight matrix is identity matrix ( $\mathbf{W}_0 = \mathbf{I}$ ). When  $k$ th pulse arrives,  $\Delta_I^k$  is calculated for all the bins using the formula in (II-A2). Using this estimate, the radar can find the bins where the target is present. The  $\mathbf{W}$  matrix is then updated such that more power is transmitted to these bins.

A radar was simulated, and the target was present at  $-30^\circ$  with respect to the radar. It was made cognitive using Algorithm 1, and the results are shown in Fig. 1. The graph compares the antenna beam when the first pulse is sent and the beam after the 50th pulse was sent as a function of the azimuth angle from the antenna, showing that the radar focuses more power at the direction of the target.

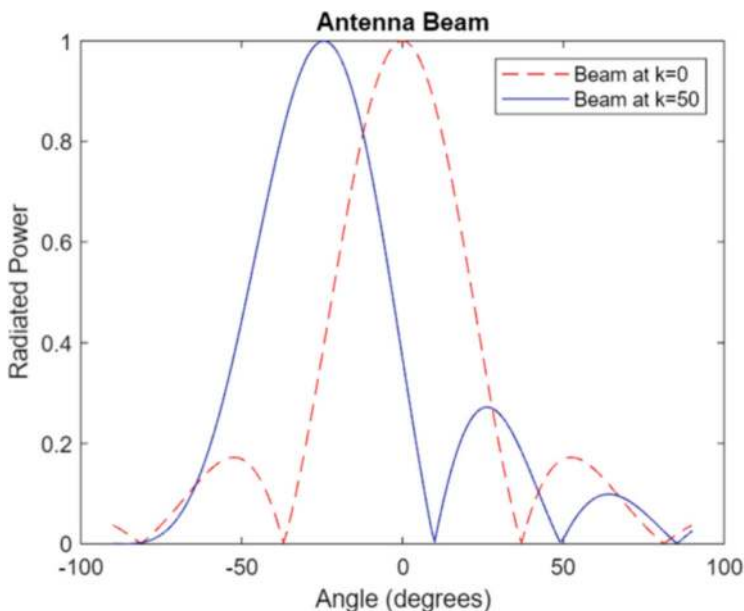


**Fig. 1** The dashed red line shows the antenna beam pattern when the first pulse was sent. The solid blue line represents the beam pattern after the 50th pulse was sent

**Algorithm 1: Algorithm for Cognitive Radar**

```

1: Initialize  $DP = 0L$ ,  $K = 50$ ,  $W0 = I$ 
2: for each time step  $k$  do
3:   for  $l = 1 \rightarrow L$  do
4:     Calculate  $\Lambda k l$ 
5:   end for
6:   if  $k == 1$  then
7:     for  $l = 1 \rightarrow L$  do  $DP(l) \leftarrow \Lambda k l$ 
8:   end for
9:   else
10:    for  $l = 1 \rightarrow L$  do  $DP(l) \leftarrow DP(l) \cdot (k - 1) + \Lambda k l k$ 
11:   end for
12:   end if
13:   Find  $W_{k+1}$  by focusing more power on angle bins  $l \in \{l: DP(l) > \lambda\}$ 
14: end for

```

**2.2 Human Activity Classification: Learning-Based Approach**

This sub-section employs machine learning (ML) and deep learning (DL) algorithms for massive MIMO radars, aiding commercial applications. The experimental analysis of human activity classification has been conducted using a publicly available dataset [24]. The proposed hypothesis aims to develop high-efficiency methods with minimal processing time while outperforming previously proposed methods applied for the task at hand. The activities provided in the dataset include walking, running, and jumping. The data has been carefully curated by Davoli et al. [24], where a single-radar device is used to measure the activity of one person in front of it, avoiding angular information. A single transmitter-receiver pair is employed ( $N_T = N_R = 1$ ), with defined parameters for the transmitted waveform upon verification, some of which include bandwidth  $B = 1.0$  GHz, reset time  $T_R = 32\mu s$ ,  $N_C = 128$  chirp signals, and a chirp interval  $T = 128\mu s$ .

The dataset employed for analyzing various ML algorithms consists of features extracted from the radar data, as mentioned in [24], and numeric labels for classes. Further, to evaluate the DL algorithm, normalized spectrogram data is obtained in the form of images of size  $512 \times 53$  (Fig. 2), representative of the measured radar data. Since the objective is to classify the data points into one of  $N$  classes (where  $N = 3$ ), this can be formulated as a simple multi-class classification problem.

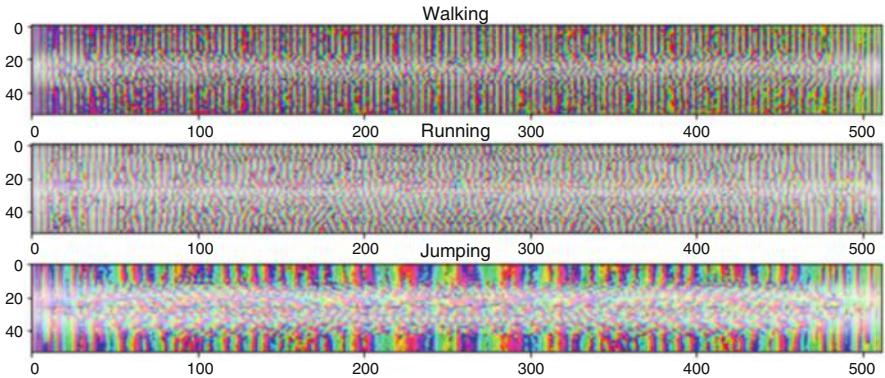


**Fig. 2** Normalized spectrogram

**Table 1** Comparison of the performance of common ml algorithms in terms of accuracy, following a 80-20 train-test split

Algorithm	Accuracy	Algorithm	Accuracy
Ada Boost Classifier	0.94	Label Propagation	0.97
Bagging Classifier	0.87	Label Spreading	0.97
Bernoulli NB	0.3	Linear Discriminant Analysis	0.98
Calibrated Classifier CV	0.93	Linear SVC	0.96
Complement NB	0.63	Logistic Regression	0.96
Decision Tree Classifier	0.97	Logistic Regression CV	0.93
Extra Tree Classifier	0.8	MLP Classifier	0.97
Extra Trees Classifier	0.97	Multi nomial NB	0.93
Gaussian NB	0.93	Nearest Centroid	0.96
Gaussian Process Classifier	0.97	Nu SVC	0.93
Gradient Boosting Classifier	0.96	Passive Aggressive Classifier	0.64
Hist Gradient Boosting Classifier	0.93	Perceptron	0.94
K Neighbors Classifier	0.94	Quadratic Discriminant Analysis	0.93
Random Forest Classifier	0.95	Radius Neighbors Classifier	0.91
Ridge Classifier	0.97	SGD Classifier	0.76
Ridge Classifier CV	0.96	SVC	0.97

**2.2.1 Analysis of Machine Learning Algorithms**

An extensive survey of different ML algorithms is presented, typically used for classification tasks as shown in Table 1. The algorithms are readily available for implementation through the scikit-learn library [25]. From the results obtained, it can be inferred that the performance of most algorithms is reasonable, with the exception of a few baselines such as Bernoulli NB, which is suitable for discrete data, and complement NB, commonly adopted for imbalanced datasets. These algorithms rely on precomputed features that have already been extracted, simply

leveraging the patterns in the feature distribution to classify the activity according to its class. As a result, the performance of the ML algorithms is nearly on par with the data-driven feature-extractor explained in the next section.

### 2.2.2 Analysis of Deep Learning Algorithms

Upon obtaining the normalized spectrogram, data in the form of images, as shown in Fig. 2, a convolutional neural network (CNN) is designed to classify the recorded activity as detected by the radar device. Although this method does not utilize precomputed features as the ML algorithms illustrated above, the superior ability of CNN to extract features from raw data contributes to the performance gain. The spectrogram data is complex valued and incompatible with preliminary architectural modules available in the PyTorch [26] deep learning framework. Hence, complex-valued operations are implemented, as elucidated by Trabelsi et al. [27] using the Python programming language and PyTorch. Specifically, this paper implements Complex Convolution, Complex Rectified Linear Units (ReLU), Complex Max Pooling, and Complex Fully Connected (Linear) layers, using a wrapper function for existing modules, as shown in Algorithm 2.

#### Algorithm 2: Pseudocode for Complex Module Wrapper [27]

```

1: import torch.nn as nn
2: def wrapper fn (m1:nn.Module, m2:nn.Module, input)
3: # m1 and m2 are module pairs, (nn.Conv2d, etc)
4: real = m1(input.real) - m2(input.imag) # Re(output)
5: imag = m1(input.imag) + m2(input.real) # Im(output)
6: return real + i · imag # Complex operation of input module

```

The standard block consisting of five operations (ABCDE) is repeated 5 times, with the combinations for each pass as per the operations legend shown in Fig. 3. The kernel size for the single stride convolutions is specified as  $m \times n$ , and the max-pooling layers use a  $2 \times 2$  kernel. The ReLU [28] activation is adopted as the real counterpart [27] of the activation layers, which help in introducing sparsity. Given very few data points and the over-parameterized network, sparsity arises when the inputs are negative and aid the model's learning process to prevent overfitting on the training split. Max pooling is used to scale down the spatial dimensions of the feature maps, to reduce the compute and network's number of parameters. To train the CNN with the spectrogram images, a standard train/test split of 80:20 is used, with a batch size of 8 for 50 epochs. For the optimization of the neural network, the SGD [29] optimizer is employed, with a learning rate of  $\alpha = 0.01$  and a momentum of  $\beta = 0.9$ . The standard multi-class classification cross-entropy loss function is used.

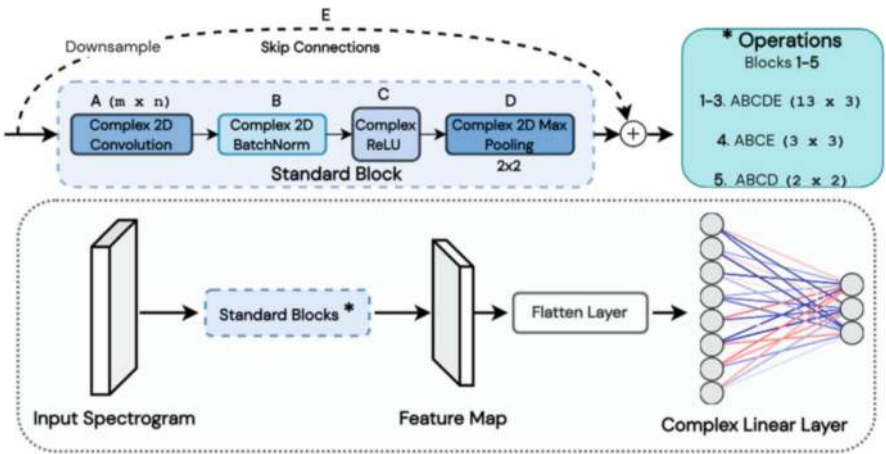


**Fig. 3** Overall architecture of the CNN, standard block, and the sequence of standard block operations for all five blocks

**Table 2** Performance analysis of the convolutional neural network in terms of accuracy and compute

Metric	Value
Training time	22 s
Number of parameters in the model	16,467
FLOPS	0.126G
Test accuracy	98.6%

The results obtained are provided in Table 2. Classification accuracy is reported on the testing set to account for model performance. As this is achieved with minimal compute overhead, the number of model parameters and Giga FLOPS (floating-point operations per second) is calculated. The training time reported is the time taken to optimize the CNN for convergence with the available labeled data samples, which is quite optimal for adaptation across datasets. The number of parameters refers to all the weight and bias matrices that represent the layers of the CNN. Given the minimal number of parameters and FLOPS, the importance of such vital applications using MMIMO technology is undeniable, having the ability to scale up and maintain computational efficiency while still providing promising results.

### 3 Conclusion

This chapter inspects and analyzes various algorithmic applications that can be exploited to produce advancements in massive MIMO applications for 5G systems, including antenna design. Specifically, it presents an experimental overview of leveraging the two software paradigms, namely, Software 1.0 (rule-based algo-

rithms) and Software 2.0 (intelligent learning-based algorithms), to aid developments in massive MIMO technology and its use cases. Firstly, this chapter proposes an obstacle detection algorithm using a novel rule-based method, with the potential to be employed in autonomous vehicles. This method involves massive MIMO radar and the theory of cognition. Further, machine learning and deep learning algorithms are employed for human activity classification, using human movement data captured by a radar device. The performance of the proposed algorithms for the tasks at hand demonstrates the scope for the development of massive MIMO systems using algorithmic design. The authors of this work hope to encourage future work on accelerating massive MIMO applications by harnessing advancements from other inter-disciplinary avenues.

## References

1. N.H.M. Adnan, I.M. Rafiqul, A.Z. Alam, Massive mimo for fifth generation (5g): Opportunities and challenges, in *International Conference on Computer and Communication Engineering (ICCC)*, vol. 2016, (2016), pp. 47–52
2. R. Chataut, R. Akl, Massive MIMO systems for 5g and beyond networks—Overview, recent trends, challenges, and future research direction. *Sensors* **20**(10) (2020). Available <https://www.mdpi.com/1424-8220/20/10/2753>
3. J. Jiang, H. Sun, W.-Y. Chiu, Energy efficient massive MIMO system design for smart grid communications, in *2016 IEEE International Conference on Communications Workshops (ICC)*, (2016), pp. 337–341
4. T. Kaiser, *Smart Antennas: State of the Art* (Hindawi Publishing Corporation, 2005)
5. H. Yuan, Z. Yin, C. Zhao, Z. Yang, S. Gao, S. Zhao, L. Xu, T. Tan, Y. Fang, Evaluation of smart environmental protection systems and novel UV-oriented solution for integration, resilience, inclusiveness and sustainability, in *2020 5th International Conference on Universal Village (UV)*, (2020), pp. 1–77
6. S. Sun, A.P. Petropulu, H.V. Poor, MIMO radar for advanced driver-assistance systems and autonomous driving: Advantages and challenges. *IEEE Signal Process. Mag.* **37**(4), 98–117 (2020)
7. J. Kim, D. Han, J.-M. Chung, Virtual MIMO based wireless communication for remote medical condition monitoring, in *International Conference on Smart Homes and Health Telematics*, (Springer, 2010), pp. 259–262
8. E. Bjornson, L. Sanguinetti, J. Hoydis, M. Debbah, Optimal design of energy-efficient multi-user MIMO systems: Is massive MIMO the answer? *IEEE Trans. Wirel. Commun.* **14**(6), 3059–3075 (2015)
9. A. Puglielli, A. Townley, G. LaCaille, V. Milovanovic, P. Lu, K. Trot-skovsky, A. Whitcombe, N. Narevsky, G. Wright, T. Courtade, E. Alon, B. Nikolic, A.M. Niknejad, Design of energy- and cost-efficient massive MIMO arrays. *Proc. IEEE* **104**(3), 586–606 (2016)
10. S. Noh, M.D. Zoltowski, Y. Sung, D.J. Love, Pilot beam pattern design for channel estimation in massive MIMO systems. *IEEE J. Sel. Top. Sign. Proces.* **8**(5), 787–801 (2014)
11. D. Borges, P. Montezuma, R. Dinis, M. Beko, Massive MIMO techniques for 5g and beyond—opportunities and challenges. *Electronics* **10**(14) (2021). Available: <https://www.mdpi.com/2079-9292/10/14/1667>
12. S. Fortunati, L. Sanguinetti, F. Gini, M.S. Greco, B. Himed, Massive MIMO radar for target detection. *IEEE Trans. Signal Process.* **68**, 859–871 (2020)



13. Z. Chen, X. He, Z. Cao, Y. Jin, J. Li, Position estimation of automatic-guided vehicle based on MIMO antenna array. *Electronics* **7**(9) (2018) Available: <https://www.mdpi.com/2079-9292/7/9/193>
14. M.A. Albreem, M. Juntti, S. Shahabuddin, Massive MIMO detection techniques: A survey. *IEEE Commun. Surv. Tutorials* **21**(4), 3109–3132 (2019)
15. W. Ajib, D. Haccoun, An overview of scheduling algorithms in MIMO-based fourth-generation wireless systems. *IEEE Netw.* **19**(5), 43–48 (2005)
16. A. Karpathy, Software 2.0 (2021). Available: <https://karpathy.medium.com/software-2-0-a64152b37c35>
17. A. Amberkar, P. Awasarmol, G. Deshmukh, P. Dave, Speech recognition using recurrent neural networks, in *2018 International Conference on Current Trends Towards Converging Technologies (ICCTCT)*, (IEEE, 2018), pp. 1–4
18. G.N. Yannakakis, J. Togelius, *Artificial Intelligence and Games* (Springer, 2018)
19. D. Forsyth, J. Ponce, *Computer Vision: A Modern Approach* (Prentice hall, 2011)
20. H. Samet, R.E. Webber, Hierarchical data structures and algorithms for computer graphics. i. Fundamentals. *IEEE Comput. Graph. Appl.* **8**(3), 48–68 (1988)
21. A.M. Ahmed, A.A. Ahmad, S. Fortunati, A. Sezgin, M.S. Greco, F. Gini, A reinforcement learning based approach for multitarget detection in massive MIMO radar. *IEEE Trans. Aerosp. Electron. Syst.* **57**(5), 2622–2636 (2021)
22. B. Friedlander, On transmit beamforming for MIMO radar. *IEEE Trans. Aerosp. Electron. Syst.* **48**, 3376–3388 (2012)
23. J. Li, P. Stoica, MIMO radar with colocated antennas. *IEEE Signal Process. Mag.* **24**(5), 106–114 (2007)
24. A. Davoli, G. Guerzoni, G.M. Vitetta, Machine learning and deep learning techniques for colocated MIMO radars: A tutorial overview. *IEEE Access* **9**, 33704–33755 (2021)
25. F. Pedregosa, G. Varoquaux, A. Gramfort, V. Michel, B. Thirion, O. Grisel, M. Blondel, P. Prettenhofer, R. Weiss, V. Dubourg, J. Vanderplas, A. Passos, D. Cournapeau, M. Brucher, M. Perrot, E. Duchesnay, Scikit-learn: Machine learning in python. *J. Mach. Learn. Res.* **12**, 2825–2830 (2011)
26. A. Paszke, S. Gross, F. Massa, A. Lerer, J. Bradbury, G. Chanan, T. Killeen, Z. Lin, N. Gimelshein, L. Antiga, A. Desmaison, A. Kopf, E. Yang, Z. DeVito, M. Raison, A. Tejani, S. Chilamkurthy, B. Steiner, L. Fang, J. Bai, S. Chintala, PyTorch: An imperative style, high-performance deep learning library, in *Advances in Neural Information Processing Systems* 32, ed. by H. Wallach, H. Larochelle, A. Beygelzimer, F. d’Alche-Buc, E. Fox, R. Garnett, (Curran Associates, Inc., 2019), pp. 8024–8035. Available: <http://papers.neurips.cc/paper/9015-pytorch-an-imperative-style-high-performance-deep-learning-library.pdf>
27. C. Trabelsi, O. Bilaniuk, Y. Zhang, D. Serdyuk, S. Subramanian, J. F. Santos, S. Mehri, N. Rostamzadeh, Y. Bengio, and C. J. Pal, “Deep Complex Networks,” 2018
28. V. Nair, G.E. Hinton, Rectified linear units improve restricted Boltzmann machines, in *Proceedings of the 27th International Conference on International Conference on Machine Learning, ser. ICML’10. Madison, WI, USA: Omnipress*, (2010), pp. 807–814
29. S. Ruder, An overview of gradient descent optimization algorithms. arXiv preprint arXiv, 1609.04747 (2016)



## 1 Linear Basis Regression Using Parametric Approach

Consider the input random vectors be represented as  $\mathbf{x}$  and the corresponding observed noisy output variable be represented as  $t$ . Let  $\mathbf{x}_1, \mathbf{x}_2 \dots \mathbf{x}_N$  are the outcome of the input random vector  $\mathbf{x}$  and the corresponding noisy outcome of the output random variable  $t$  be represented as  $t_1, t_2 \dots t_N$  respectively (refer Fig. 1). There is the hidden parametric relationship between the input vector  $\mathbf{x}$  and the noisy observation  $\mathbf{t}$  is represented as  $y(\mathbf{x})$ . The requirement is to obtain the parametric model that describes the empirical relationship as described below.

$$y(\mathbf{x}) = \mathbf{w}^T \phi(\mathbf{x}) \quad (1)$$

$$y(\mathbf{x}) = w_0 f_0(\mathbf{x}) + w_1 f_1(\mathbf{x}) + \dots + w_{M-1} f_{M-1}(\mathbf{x}) \quad (2)$$

Data-driven model  $y(\mathbf{x})$  involves obtaining  $w_0, w_1, \dots w_{M-1}$  using the training set  $\mathbf{x}_1, \dots \mathbf{x}_N, t_1, \dots t_N$  with predefined selection of basis functions  $f_0(\mathbf{x}), f_1(\mathbf{x}), f_2(\mathbf{x}) \dots f_{M-1}(\mathbf{x})$ . The training set satisfies the following set of equations.

$$\mathbf{t}_1 = w_0 f_0(\mathbf{x}_1) + w_1 f_1(\mathbf{x}_1) + \dots + w_{M-1} f_{M-1}(\mathbf{x}_1) + \epsilon \quad (3)$$

$$\mathbf{t}_2 = w_0 f_0(\mathbf{x}_2) + w_1 f_1(\mathbf{x}_2) + \dots + w_{M-1} f_{M-1}(\mathbf{x}_2) + \epsilon \quad (4)$$

$$\dots \quad (5)$$

$$\mathbf{t}_N = w_0 f_0(\mathbf{x}_N) + w_1 f_1(\mathbf{x}_N) + \dots + w_{M-1} f_{M-1}(\mathbf{x}_N) + \epsilon \quad (6)$$

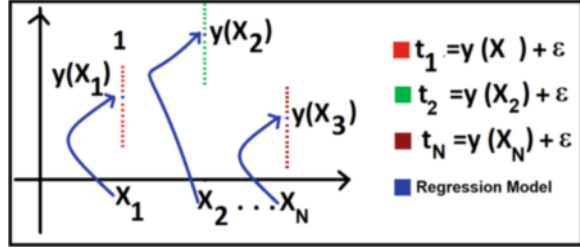
---

E. S. Gopi (✉)

National Institute of Technology, Tiruchirappalli, Tamil Nadu, India

e-mail: [esgopi@nitt.edu](mailto:esgopi@nitt.edu)

**Fig. 1** Illustration of Linear regression



$\epsilon$  is the random variable that follows Gaussian distribution with mean 0 and variance  $\sigma_N^2$ . Since the functions  $f_0(\mathbf{x})$ ,  $f_1(\mathbf{x})$ ,  $f_2(\mathbf{x}) \dots f_{M-1}(\mathbf{x})$  are fixed, the likelihood function of  $f(t_i/\mathbf{w})$  follows Gaussian density function with mean

$\mathbf{w}^T \mathbf{f}(\mathbf{x}_i)$  (constant) and variance  $\sigma_N^2$ . The unknown vector  $\mathbf{w} = \begin{bmatrix} w_0 \\ w_1 \\ \dots \\ w_{M-1} \end{bmatrix}$  is

estimated as follows. Refer Fig. 1 for illustration of Linear regression model.

### 1.1 Least Square Technique

In this technique, the unknown vector  $\mathbf{w}$  is estimated by minimizing the  $\|\mathbf{t} - \mathbf{F}\mathbf{w}\|^2$ ,

where  $\mathbf{t} = \begin{bmatrix} t_0 \\ t_1 \\ \dots \\ t_{N-1} \end{bmatrix}$  and  $\mathbf{F} = \begin{bmatrix} f_0(\mathbf{x}_0) & f_1(\mathbf{x}_0) & \dots & f_{M-1}(\mathbf{x}_0) \\ f_0(\mathbf{x}_1) & f_1(\mathbf{x}_1) & \dots & f_{M-1}(\mathbf{x}_1) \\ \dots & \dots & \dots & \dots \\ f_0(\mathbf{x}_{N-1}) & f_1(\mathbf{x}_{N-1}) & \dots & f_{M-1}(\mathbf{x}_{N-1}) \end{bmatrix}$ . This is obtained as follows. Let us represent  $\mathbf{f}_i = \begin{bmatrix} f_i(\mathbf{x}_0) \\ f_i(\mathbf{x}_1) \\ \dots \\ f_i(\mathbf{x}_{N-1}) \end{bmatrix}$ .

Thus we can estimate  $\mathbf{w}$  such that  $\|\mathbf{t} - w_0\mathbf{f}_0 - w_1\mathbf{f}_1 - \dots w_{M-1}\mathbf{f}_{M-1}\|^2$  is minimized. The vector  $w_0\mathbf{f}_0 + w_1\mathbf{f}_1 + \dots w_{M-1}\mathbf{f}_{M-1}$  lies in the vector space  $V$  spanned by the vectors  $\mathbf{f}_0, \mathbf{f}_1, \dots, \mathbf{f}_{M-1}$  and are chosen such that magnitude of the vector  $\mathbf{e} = (\mathbf{t} - w_0\mathbf{f}_0 - w_1\mathbf{f}_1 - \dots w_{M-1}\mathbf{f}_{M-1})$  is minimized. This happens when the error vector  $\mathbf{e}$  is orthogonal to the vector space  $V$ . Every error vector  $\mathbf{e}$  is orthogonal to every individual vectors than spans the space  $V$  (refer Fig. 2). i.e.  $\mathbf{e}^T \mathbf{f}_i = \mathbf{f}_i^T \mathbf{e} = 0 \forall i = 1, \dots, N$

$$\begin{aligned} \mathbf{f}_1^T (\mathbf{t} - w_0\mathbf{f}_0 - w_1\mathbf{f}_1 - \dots w_{M-1}\mathbf{f}_{M-1}) &= 0 \\ \Rightarrow \mathbf{f}_0^T \mathbf{t} &= \mathbf{f}_0^T (w_0\mathbf{f}_0 + w_1\mathbf{f}_1 + \dots w_{M-1}\mathbf{f}_{M-1}) \\ \mathbf{f}_1^T \mathbf{t} &= \mathbf{f}_1^T (w_0\mathbf{f}_0 + w_1\mathbf{f}_1 + \dots w_{M-1}\mathbf{f}_{M-1}) \\ \mathbf{f}_2^T \mathbf{t} &= \mathbf{f}_2^T (w_0\mathbf{f}_0 + w_1\mathbf{f}_1 + \dots w_{M-1}\mathbf{f}_{M-1}) \end{aligned}$$

**Fig. 2** Illustration of Least Square Technique

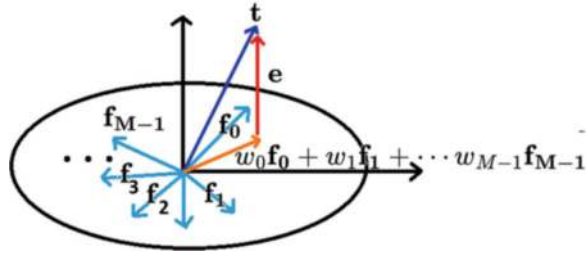
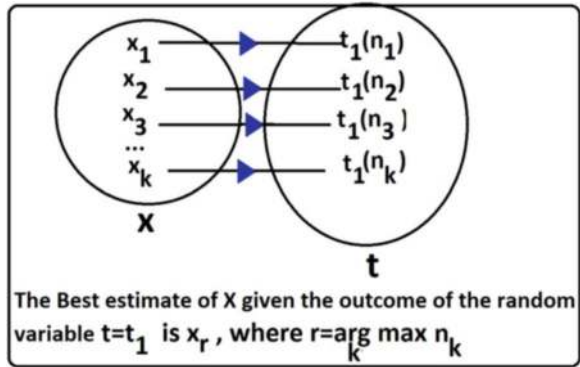


**Fig. 3** Illustration of Maximum Likelihood estimation



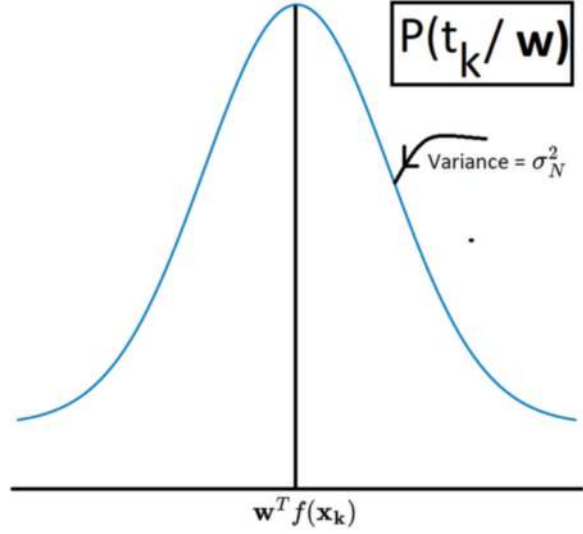
$$\begin{aligned} \dots \\ \mathbf{f}_{N-1}^T \mathbf{t} &= \mathbf{f}_{N-1}^T (w_0 \mathbf{f}_0 + w_1 \mathbf{f}_1 + \dots + w_{M-1} \mathbf{f}_{M-1}) \\ \Rightarrow \mathbf{w} &= (\mathbf{F}^T \mathbf{F})^{-1} \mathbf{F}^T \mathbf{t} \end{aligned}$$

## 1.2 Maximum Likelihood Estimation

Consider the outcome of the random vector  $\mathbf{x}$ ,  $\mathbf{x}_1$  ends up with the outcome of the random variable  $t$  as  $t_1, n_1$  number of times. Let outcome of the random vector  $\mathbf{x}$ ,  $\mathbf{x}_2$  ends up with the outcome of the random variable  $t$  as  $t_1, n_2$  number of times. Similarly outcome of the random vector  $\mathbf{x}$ ,  $\mathbf{x}_k$  ends up with the outcome of the random variable  $t$  as  $t_1, n_k$  number of times. Then the estimate of  $\mathbf{x}$  given the outcome of the random variable  $t$  as  $t_1$  is obtained as  $x_r$ , where  $r = \arg_m \max n_m$  (refer Fig. 3).

The unknown vector  $\mathbf{w}$  is estimated by maximizing the likelihood function  $p(\mathbf{t}/\mathbf{w}) = p(t_0/\mathbf{w})p(t_1/\mathbf{w})p(t_3/\mathbf{w}) \dots p(t_{N-1}/\mathbf{w})$ . with density function  $p(t_k/\mathbf{w})$  follows Gaussian distributed with mean  $\mathbf{w}^T \mathbf{f}(\mathbf{x}_k)$  with  $k = 0 \dots N - 1$  with variance  $\sigma_N^2$ . Thus  $p(\mathbf{t}/\mathbf{w})$  is given as follows.

**Fig. 4** Illustration of Likelihood function



$$p(\mathbf{t}/\mathbf{w}) = \left(\frac{1}{2\pi\sigma_N^2}\right)^{\frac{N}{2}} \prod_{i=0}^{N-1} e^{-\frac{(t_i - \mathbf{w}^T f(\mathbf{x}_i))^2}{2\sigma_N^2}} \quad (7)$$

Refer Fig. 4 for the illustration of Likelihood function. Since logarithm function is the increasing function. Maximizing  $p(\mathbf{t}/\mathbf{w})$  is equivalent to maximizing  $\log(p(\mathbf{t}/\mathbf{w}))$ , which is further interpreted as minimizing the following.

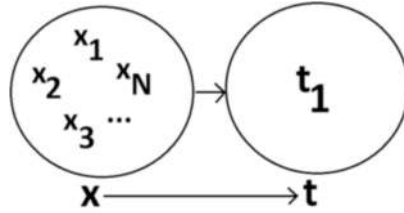
$$\sum_{i=0}^{N-1} (t_i - \mathbf{w}^T f(\mathbf{x}_i))^2. \quad (8)$$

This is the Least Square technique for estimating the vector  $\mathbf{w}$  and hence  $\mathbf{w}$  is estimated as  $\Rightarrow \mathbf{w} = (\mathbf{F}^T \mathbf{F})^{-1} \mathbf{F}^T \mathbf{t}$ . The Maximum Likelihood estimation of the vector  $\mathbf{w}$  in regression model  $t_k = \mathbf{w}^T f(\mathbf{x}_k) + \epsilon$  ends up with Least square estimation if  $\epsilon$  follows Gaussian distributed.

### 1.3 Bayes Technique

Let  $\mathbf{x}_1, \mathbf{x}_2, \dots, \mathbf{x}_N$  be the outcomes of the random vector  $\mathbf{x}$  that ends up with identical outcome of the random variable  $t$  as  $t_1$ . Then the best estimate of  $\mathbf{x}$  given the observation of the outcome of the random variable  $\mathbf{t}$  are obtained as one of the following. (refer Fig. 5)

**Fig. 5** Illustration of Conditional Mean, Median and Mean estimates, MMAE, MAP estimation



Given the outcome of the random variable  $t$  as  $t_1$ , the corresponding best estimate of the random variable  $X$  is obtained as the following.

Mean of  $\{x_1, x_2, x_3, \dots, x_N\} \Rightarrow$  Conditional Mean Estimate

Median of  $\{x_1, x_2, x_3, \dots, x_N\} \Rightarrow$  Conditional Median Estimate

Mode of  $\{x_1, x_2, x_3, \dots, x_N\} \Rightarrow$  Conditional Mode Estimate

1. Mean of  $x_1, x_2, x_3, \dots, x_N$  is known as conditional mean estimate. This is otherwise known as Minimum Mean Square Estimation (MMSE).
2. Median of  $x_1, x_2, x_3, \dots, x_N$  is known as conditional median estimate. This is otherwise known as Minimum Mean Absolute Error Estimation (MMAE).
3. Mode of  $x_1, x_2, x_3, \dots, x_N$  is known as Conditional mode estimate. This is otherwise known as Maximum a posteriori density estimation (MAP).

The posterior density function  $p(\mathbf{w}/\mathbf{t})$  is computed as follows.

$$p(\mathbf{w}/\mathbf{t}) = \frac{p(\mathbf{t}/\mathbf{w})p(\mathbf{w})}{\int p(\mathbf{t}/\mathbf{w})p(\mathbf{w})d\mathbf{w}} \quad (9)$$

If  $\mathbf{w}$  follows Gaussian distribution with mean as the zero vector and co-variance matrix  $\sigma_N^2 \mathbf{I}$ , where  $\mathbf{I}$  is the Identity matrix.

It can be shown that  $p(\mathbf{w}/\mathbf{t})$  follows Multivariate Gaussian distributed with mean vector  $(\mathbf{F}^T \mathbf{F} + \frac{\sigma_N^2}{\sigma_w^2} \mathbf{I})^{-1} \mathbf{F}^T \mathbf{t}$  and Co-variance matrix  $(\mathbf{F}^T \mathbf{F} + \frac{\sigma_N^2}{\sigma_w^2} \mathbf{I})^{-1}$ .

The random vector  $\mathbf{w}$  is estimated as the conditional mean/conditional median/conditional mode of the posterior density function  $p(\mathbf{w}/\mathbf{t})$  and is given as the following. (refer Fig. 6)  $\mathbf{w} = (\mathbf{F}^T \mathbf{F} + \frac{\sigma_N^2}{\sigma_w^2} \mathbf{I})^{-1} \mathbf{F}^T \mathbf{t}$ .

## 2 Gaussian Smoothing

From least square technique (refer section 1.1), the regression model is obtained as the following.

$$y(\mathbf{x}_{\text{test}}) = \mathbf{w}^T \mathbf{f}(\mathbf{x}_{\text{test}}) = \mathbf{f}(\mathbf{x}_{\text{test}})^T \mathbf{w} \quad (10)$$

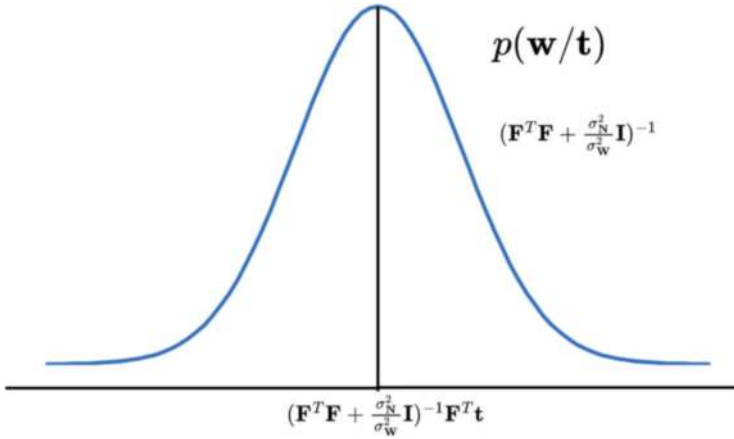


**Fig. 6** Illustration of Linear regression

where

$$\mathbf{w} = (\mathbf{F}^T \mathbf{F})^{-1} \mathbf{F}^T \mathbf{t} \quad (11)$$

$$\text{and } \mathbf{f}(\mathbf{x}_{\text{test}}) = \begin{bmatrix} f_0(\mathbf{x}_{\text{test}}) \\ f_1(\mathbf{x}_{\text{test}}) \\ \vdots \\ f_{M-1}(\mathbf{x}_{\text{test}}) \end{bmatrix}$$

$$\Rightarrow y(\mathbf{x}_{\text{test}}) = \mathbf{f}(\mathbf{x}_{\text{test}})^T ((\mathbf{F}^T \mathbf{F})^{-1} \mathbf{F}^T \mathbf{t}) \quad (12)$$

$$\Rightarrow y(\mathbf{x}_{\text{test}}) = \sum_{i=1}^{i=N} k(\mathbf{x}_{\text{test}}, \mathbf{x}_i) t_i \quad (13)$$

where  $k(\mathbf{x}_{\text{test}}, \mathbf{x}_i)$  is the kernel function given as the following.

$$k(\mathbf{x}_{\text{test}}, \mathbf{x}_i) = \sum_{i=1}^{i=N} \mathbf{f}(\mathbf{x}_{\text{test}})^T (F^T F)^{-1} \mathbf{f}(\mathbf{x}_{\text{test}}) \quad (14)$$

Refer Fig. 7 for illustration (14).

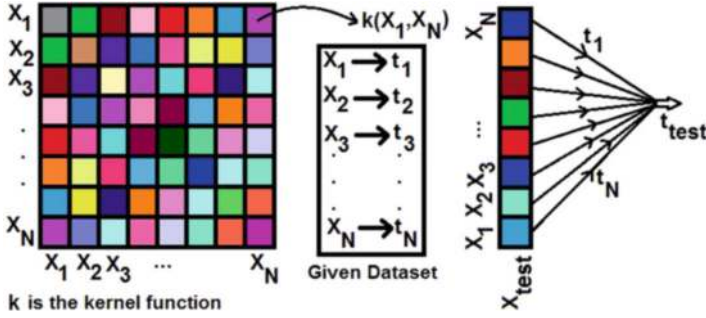


Fig. 7 Illustration of Kernel smoothing technique for regression

### 3 Gaussian Process Technique

In this technique the training data observation data  $t_n$  corresponding to the input vector  $\mathbf{x}_n$  is modeled as Gaussian distributed with mean  $\phi(\mathbf{x}_n)$  and variance  $\sigma_N^2$ . The idea behind Gaussian process based estimation of the target corresponding to the test input vector  $\mathbf{x}_{\text{test}}$  is to obtain the conditional density function  $f(t_{\text{test}}/t_1 t_2 \dots \mathbf{x}_1 \mathbf{x}_2 \dots \mathbf{x}_N \mathbf{x}_{\text{test}})$  and the mean of the obtained density function is declared as the estimate. It can be shown that the density function  $f(t_{\text{test}}/t_1 t_2 \dots \mathbf{x}_1 \mathbf{x}_2 \dots \mathbf{x}_N \mathbf{x}_{\text{test}})$  follows Gaussian distributed with mean and variance computed as follows. Let  $k(\mathbf{x}_i, \mathbf{x}_j) = E(\Phi_{\mathbf{x}_i}, \Phi_{\mathbf{x}_j}) = k_{ij}$ , where  $E(\cdot)$

is the Expectation operator. The co-variance matrix of the vector  $\mathbf{t} = \begin{bmatrix} t_1 \\ t_2 \\ \dots \\ t_N \end{bmatrix}$  is

given as the following.  $\mathbf{C}_t = \begin{bmatrix} k_{11} + \sigma_N^2 & k_{12} & \dots & k_{1N} \\ k_{21} & k_{22} + \sigma_N^2 & \dots & k_{2N} \\ \dots & \dots & \dots & \dots \\ k_{N1} & k_{N2} & \dots & k_{NN} + \sigma_N^2 \end{bmatrix}$ .

Let  $\mathbf{k} = \begin{bmatrix} \mathbf{k}_{\text{test},1} \\ \mathbf{k}_{\text{test},2} \\ \dots \\ \mathbf{k}_{\text{test},N} \end{bmatrix}$  and  $\sigma^2 = \mathbf{k}_{\text{test},\text{test}}$ . The a posterior density function

$f(t_{\text{test}}/t_1 t_2 \dots \mathbf{x}_1 \mathbf{x}_2 \dots \mathbf{x}_N \mathbf{x}_{\text{test}})$  follows Gaussian distributed with mean  $\mathbf{k}^T \mathbf{C}_t^{-1} \mathbf{t}$  and variance  $\sigma^2 - \mathbf{k}^T \mathbf{C}_t^{-1} \mathbf{k}$ . Thus the estimate corresponding to random vector  $\mathbf{x}_{\text{test}}$  is given as the following.  $\mathbf{k}^T \mathbf{C}_t^{-1} \mathbf{t}$  Refer Fig. 8 for the illustration of the Gaussian process.



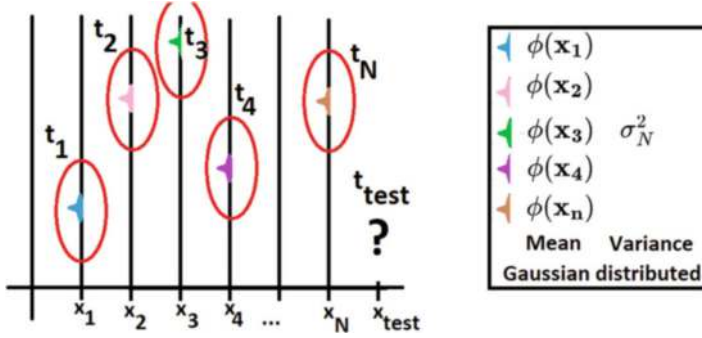


Fig. 8 Illustration of Gaussian Process

#### 4 Intuitive Understanding on the Impact of Number of Data on Estimating $w$

Given the dataset, it is understood that every outcome of the random vector  $w$  ends up with individual regression model. For the arbitrary testing vector  $x_{test}$ , the outcome of the random vector  $t_{test}$  is obtained as follows.

$$t_{test} = w^T f(x_{test}) + \epsilon \quad (15)$$

In this  $f(x_{test})$  is fixed, the predicted value  $t_{test}$  depends upon the choice of  $w$  and  $\epsilon$ . It can be shown that the density function  $t_{test}$  follows Gaussian with mean vector  $(F^T F + \frac{\sigma_N^2}{\sigma_w^2} I)^{-1} F^T t$  and variance  $f(x_{test})^T (F^T F + \frac{\sigma_N^2}{\sigma_w^2} I)^{-1} f(x_{test}) + \frac{1}{\beta}$ . It is understood that the size of the matrix  $F$  is  $N \times M$ . It can also be shown that the variance of the predictive variable  $t_{test}$  decreases as  $N$  increases and as  $N$  tends to  $\infty$ , the variance tends to  $\frac{1}{\beta}$ . Refer Fig. 9 for the illustration. In this case, it is understood that the value of  $\sigma_N^2$ .

#### 5 Conclusion

In this chapter, we have discussed the basic data-driven model establishing the relationship between the random vector  $x$  (input) and the target scalar  $t$  (output) using various regression techniques. Other techniques like Evidence approximation, Approximate inference techniques, Artificial Neural Networks, and Deep learning regression techniques [1–4] are recommended for further reading on this topic.

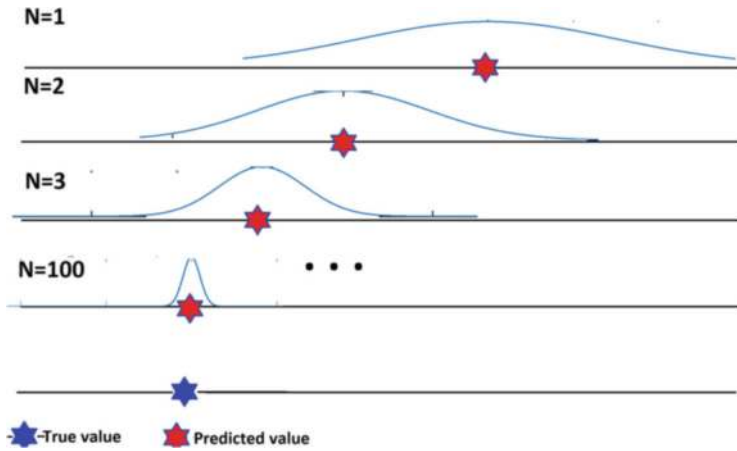


**Fig. 9** Illustration that the variance of the density function of the predictive distribution  $t_{test}$  decreases as the number of training data increases. Also mean of the predictive distribution  $t_{test}$  converges to the true value as the number of training data increases

## References

1. L. Cheng, F. Yin, S. Theodoridis, S. Chatzis T.-H. Chang, Rethinking Bayesian learning for data analysis: The art of prior and inference in sparsity-aware modeling. *IEEE Signal Process. Mag.* **39**(6), 18–52 (2022)
2. C.M. Bishop, *Pattern Recognition and Machine Learning* (Springer, 2006)
3. E.S. Gopi, *Pattern Recognition and Computational Intelligence Techniques Using Matlab* (Springer, 2020)
4. I. Goodfellow, Y. Bengio, A. Courville, *Deep Learning* (The MIT Press, Cambridge, MA, London (2016)

# Index

## A

Additive manufacturing, 107, 109, 111  
Algorithm design and analysis, 176, 181–183

## B

Bandwidth, 4, 12, 13, 18, 19, 24, 29–31, 37–41, 45, 49, 51, 52, 54, 55, 57–59, 61, 66–68, 71, 83, 85–91, 93–96, 98, 100, 102, 104, 109–111, 126, 128, 130–133, 139, 151, 154, 162, 172, 175, 180  
Broadband antennas, 68

## C

Characteristic impedance, 8–9, 157  
Characteristic modes, 37, 39, 40, 84, 85  
Circuit theory, 4–6  
Compact antennas, 29, 55–56  
Compact size, 45, 83, 84, 90  
Conformal, 65, 70, 71, 74, 83, 93–104  
Co-polarization, 60, 99

## D

Dielectric resonator antennas (DRAs), 83–91, 93  
Dipole antennas, 17, 23, 29–42, 70, 73, 95  
Directivity, 7, 18, 19, 23–25, 94  
Distributed components, 7–8  
Driven element, 55–58, 60, 61  
Dual-mode, 30–41

## E

Efficiency, 37, 38, 40, 42, 45, 52–55, 60–62, 65, 66, 71, 72, 83, 85, 87, 90, 91, 93, 95, 99, 102, 111, 113, 119, 132, 139, 175–177, 183  
Electrically small antennas (ESAs), 45–62  
Equivalent circuit, 133, 139, 140, 156–158, 167–168, 172

## F

Field theory, 6, 10  
Finite circular ground, 17–26  
5G communication, 13, 52, 119, 175  
Frequency-selective surface (FSS), 70, 74, 130, 154–158, 165–172  
Full-duplex, 119–143

## G

Gaussian process, 181, 193–194

## H

High-gain antennas, 107

## I

Intelligent Transportation System (ITS), 132  
Internet of Things (IoT), 13, 45, 67, 96, 176

**K**

Kernel smoothing, 193

**L**

Linear regression, 188, 192  
 Low-profile, 65, 90, 93–104, 107, 108  
 Lumped components, 3, 155

**M**

Machine learning (ML), 176, 180–182, 184  
 Metal-only reflectarray (MORA), 109, 111–113, 117  
 Metasurface, 147–162, 165  
 Microstrip antenna, 29, 66, 83, 84, 121, 122, 131, 139  
 Microwave absorber, 147–162  
 Microwaves, 1–14, 65, 83, 84  
 mm waves, 1–14, 83, 95  
 Mode compression, 29–42  
 Modes, 12, 29–37, 39–41, 84–86, 89, 93, 95, 96, 99, 119, 129, 131, 132, 138, 141, 155, 191  
 Monopole, 17–26, 46–50, 52, 55, 56, 61, 66, 68, 85, 86, 172  
 Multi-mode, 30–41  
 Multiple input-multiple output (MIMO), 13, 84, 175–184  
 Mutual coupling, 122, 124–126, 129, 133, 138

**O**

Omnidirectional radiation, 29, 52, 60, 172

**P**

Periodic structures, 165  
 Perturbation, 89, 93, 96–99, 104

**R**

Radar, 2, 3, 10–11, 89, 91, 96, 107–109, 147, 160, 162, 170, 176–180, 182, 184

Radar cross-section (RCS), 7, 11, 147–149, 158–162, 165, 171  
 Radio frequency (RF), 1–14, 66, 67, 71, 73, 111, 120, 147, 168–170, 172, 176  
 Radome, 154, 165–172  
 Reader antennas, 67–69  
 Reflectarray, 107–117  
 Resonance, 10, 14, 31, 46–52, 55, 57, 58, 61, 84, 151, 166, 168  
 Resonance frequency, 17–24, 61, 151, 160, 168  
 Resonating modes, 53, 54, 57–59, 61

**S**

Satellite communications, 12, 89, 91, 107  
 Self-interference cancellation, 120–129, 135–142  
 Skin depth, 7  
 Stub loading, 31–33, 38  
 Stub resonators, 45, 46, 135–142

**T**

Tag antennas, 67–70, 73  
 Textile, 65–77  
 3D printing, 109, 116, 117  
 Transmission line, 6–9, 46, 49, 73, 147–162, 167  
 Transmitarray, 113–115

**U**

UHF-RFID, 67–70, 73, 75, 77  
 Unit cell, 94, 110, 154, 155, 158–160, 162, 166–168

**V**

V2X, 132

**W**

Wireless systems, 1, 7, 10, 12, 73, 147